

Doctoral Dissertation (Censored)

博士論文（要約）

**Study of VHE Gamma-ray Emission from  
Active Galactic Nucleus 1ES 1959+650  
with the MAGIC Telescopes**

(MAGIC 望遠鏡による活動銀河核 1ES 1959+650 からの  
超高エネルギーガンマ線放射の研究)

**A Dissertation Submitted for the Degree of Doctor of Philosophy**

December 2022

令和 4 年 1 2 月 博士（理学）申請

Department of Physics, Graduate School of Science,

The University of Tokyo

東京大学大学院理学系研究科物理学専攻

Shunsuke Sakurai

櫻井 駿介

# **Study of VHE Gamma-ray Emission from Active Galactic Nucleus 1ES 1959+650 with the MAGIC Telescopes**

Shunsuke Sakurai

February 15, 2023



---

## List of Abbreviation

**AGN** Active Galactic Nuclei

**BAT** Burst Alart Telescope

**DC** Direct Current

**DCF** Discrete Correlation Function

**EAS** Extensive Air Shower

**EBL** Extra Gelectic Background

**HE** High Energy

**IACT** Imaging Atmospheric Cherenkov Telescope

**LAT** Large Area Telescope

**MAGIC** Major Atmospheric Gamma Imaging Telescope

**MRK** Markarian

**MWL** Multiwavelength

**NSB** Night Sky Background

**OVRO** Owens Valley Radio Obsevaroty

**PMT** Photo-Multiplier Tube

**SED** Spectral Energy Distribution

**SMBH** Super Massive Black Hole

**ToO** Target of Oppotunity

**UVOT** Ultraviolet and Optical Telescope

**VHE** Very High Energy

**XRT** X-ray Telescope

**p.e.** photoelectron

## Abstract

Very high-energy gamma-ray astronomy is a field trying to reveal the nature of the extreme phenomenon in the universe using gamma rays at the energy above a few tens of GeV. The science topics are not only astronomical objects but also fundamental physics, such as dark matter search and the validation of special relativity.

High-energy astronomical objects are considered candidates for the origin of cosmic rays and have been studied by electromagnetic observations. In the case of blazars, the source that emission from the relativistic jet is a major component, and it is the dominant source in the gamma-ray sky. Thus was considered one of the plausible candidates. Two bumps can characterize the emission from blazars. The synchrotron emission can explain the low-energy bump. However, the origin of the high-energy component is still controversial. Hadronic models, such as proton synchrotron and pion decay, have also been tested thus far for several sources, but no clear evidence has been confirmed.

Inverse Compton emission by relativistic electrons has successfully explained the blazar emissions, but recent observation results imply more complex emission models. High angular-resolution radio observation also suggests the relativistic jets have structured morphology. For the above reasons, one needs to study emission models with a novel perspective to understand the blazar emission deeply. Especially long-term monitoring can be performed for only a few sources due to the limited sensitivity of the telescopes. The VHE emission from most blazars is only detectable when a flaring episode happens. Thus only a few sources are always detectable by VHE gamma rays. They have to be close and bright in VHE gamma rays. The subclass of blazars, BL Lacertae (BL Lac) object, is a good target; famous sources are Markarian 421, 501, and 1ES 1959+650. The multiwavelength monitoring of Markarian sources has been conducted actively thus far, but 1ES1959+650 was not. The high-peak frequency BL Lac object 1ES1959+650 is a somewhat old object in VHE gamma-ray but has some fascinating history. The most exciting report from the source was an orphan gamma-ray flare, which was a gamma-ray flare independent from the other wavelength. The observation has led to some hadronic models but no neutrino detection in the past.

In this study, I analyzed five-year MAGIC data observing 1ES 1959+650 and multi-wavelength observations in the same period. MAGIC data required dedicated analysis methods because half of the data was taken under the moonlight. The reconstructed light curve showed a trend getting lower flux with some flaring episodes after the 2016 flare. Spectral shapes were different from 2016 and 2017 onward.

On top of that, multiwavelength analyses were performed to understand electromagnetic emission through radio to gamma rays. The multiwavelength light curves showed unique features in each energy band. I performed a detailed multiwavelength temporal analysis and spectral modeling to reveal the nature of complex behavior from radio to gamma rays. Flux correlation between X-ray and VHE Gamma-ray showed a strong correlation changing in time. In order to understand the nature of the complicated flux correlation, I performed modeling of spectral energy distribution for the selected periods with a one-zone synchrotron self-Compton (SSC) model. The result suggests the difference in the magnetic field in the emission region might cause the flux correlation in time. I concluded

that the complex behavior of blazar could be explained with the one-zone SSC model, but one needs further improvement in the instruments and analysis technique. In addition, more complex emission models should be tested in the future.

This thesis has three parts and twelve sections. Part I mainly introduced the fundamental physics and history of the field. Section 1 gives you a summary of gamma-ray astronomy and cosmic-ray physics. Section 2 explains physical processes frequently appearing in the detection technique and physical interpretations of blazars. Finally, section 3 introduces active galactic nuclei and blazars, an extragalactic source with relativistic jets.

Part II demonstrates the study of a recent five-year VHE gamma-ray observation of 1ES1959+650 with the MAGIC telescopes. Section 5 shows what the motivation for my research is. In section 6, the previous studies of 1ES 1959+650 are summarized. In section 7, the details of the MAGIC telescopes are introduced. At last, Section 8 gives the analysis method and result along with the actual analysis steps.

Part III discusses multiwavelength analysis with MAGIC and other wavelength data. Section 9 reports multiwavelength instruments and data analyses. Next, section 10 shows the temporal analysis using multiwavelength light curves. Section 11 explains multiwavelength spectral modeling with a one-zone SSC model. In the end, section 12 summarizes the research and gives prospects.

# Contents

<b>Abstract</b>	<b>3</b>
<b>I. Introduction</b>	<b>9</b>
<b>1. Astroparticle Physics</b>	<b>10</b>
1.1. Cosmic Rays and their Origins . . . . .	10
1.2. Gamma-ray Astrophysics . . . . .	13
<b>2. Physical Process</b>	<b>14</b>
2.1. Emissions . . . . .	14
2.1.1. Ionization Loss . . . . .	14
2.1.2. Bremsstrahlung . . . . .	16
2.1.3. Synchrotron Radiation . . . . .	16
2.1.4. Thomson and Compton scattering . . . . .	18
2.1.5. Inverse Compton scattering . . . . .	19
2.1.6. Cherenkov Radiation . . . . .	20
2.2. Interactions . . . . .	20
2.2.1. Electron-positron Pair Production . . . . .	21
2.2.2. Pion Decay . . . . .	23
2.2.3. Hadronic Interactions . . . . .	24
<b>3. Active Galactic Nuclei</b>	<b>26</b>
3.1. AGN Classification and Unified model . . . . .	26
3.2. Blazar . . . . .	27
3.2.1. BL Lacertae type object . . . . .	27
3.2.2. Flat Spectrum Radio Quasar . . . . .	27
3.3. Emission models . . . . .	28
3.3.1. One-zone model . . . . .	28
3.3.2. Complex models . . . . .	31
3.4. Typical TeV Blazars . . . . .	32
<b>II. Study of VHE Gamma-ray Emission from Active Galactic Nucleus 1ES 1959+650 with the MAGIC telescopes</b>	<b>36</b>
<b>4. Motivation</b>	<b>37</b>
<b>5. 1ES 1959+650</b>	<b>37</b>
5.1. Distance, Location, and Central core . . . . .	37
5.2. Morphology . . . . .	38
5.3. Neutrino observation . . . . .	39

5.4. Past multiwavelength campaigns . . . . .	40
<b>6. Major Atmospheric Gamma Imaging Cherenkov Telescope</b>	<b>42</b>
6.1. Observation principals . . . . .	42
6.1.1. Electromagnetic shower . . . . .	42
6.1.2. Hadronic shower . . . . .	43
6.1.3. Atmospheric Cherenkov light . . . . .	44
6.2. Instrument . . . . .	45
6.2.1. Reflector . . . . .	46
6.2.2. PMT Camera . . . . .	47
6.2.3. Event Trigger and Data Aquision . . . . .	48
6.2.4. Auxicially systems . . . . .	50
6.2.5. Performance . . . . .	51
<b>7. Observation and Data Analysis</b>	<b>54</b>
7.1. Observation and Data selection . . . . .	54
7.1.1. Observation mode . . . . .	54
7.1.2. Data Selection . . . . .	55
7.2. Data Analysis . . . . .	60
7.2.1. Software . . . . .	60
7.2.2. Signal calibration . . . . .	61
7.2.3. Image Cleaning . . . . .	62
7.2.4. Hillas parametrization . . . . .	64
7.2.5. Event reconstruction . . . . .	65
7.2.6. Signal detection . . . . .	65
7.2.7. Flux derivation . . . . .	66
7.2.8. Combining the different analysis levels . . . . .	66
7.2.9. Unfolding and forward-unfolding . . . . .	68
<b>8. Analysis Results</b>	<b>70</b>
8.1. Analysis Results . . . . .	70
8.1.1. Light curve . . . . .	70
8.1.2. Bayesian block analysis . . . . .	70
8.1.3. Spectral energy distribution . . . . .	74
<b>9. Summary of MAGIC analysis result</b>	<b>82</b>
 <b>III. Study of Temporal Variabilities and Emission Models of 1ES 1959+650 with Multiwavelength data</b>	 <b>83</b>
<b>10. Multiwavelength Instruments</b>	<b>84</b>
10.1. <i>Fermi</i> Large Area Telescope . . . . .	84
10.1.1. Performance . . . . .	85

10.1.2. Analysis Software . . . . .	89
10.1.3. Data Selection . . . . .	89
10.1.4. Photon Reconstruction . . . . .	89
10.1.5. Binned Likelihood Analysis . . . . .	90
10.1.6. Light curves . . . . .	91
10.1.7. Spectral Energy Distrubution . . . . .	92
10.2. <i>Swift</i> X-Ray Telescope . . . . .	96
10.2.1. Software . . . . .	97
10.2.2. Calibration . . . . .	97
10.2.3. Data Selection . . . . .	97
10.2.4. Aperture photometry . . . . .	98
10.2.5. Background Reduction . . . . .	99
10.2.6. Spectral analysis . . . . .	101
10.2.7. Light curve . . . . .	102
10.2.8. Spectral analysis . . . . .	107
10.3. <i>Swift</i> Burst Alert Telescope . . . . .	116
10.3.1. Light curve . . . . .	117
10.4. <i>Swift</i> Ultra Violet and Optical Telescope . . . . .	118
10.4.1. Light curve . . . . .	119
10.5. Tuorla observatory . . . . .	120
10.5.1. Light curve . . . . .	120
10.5.2. SED . . . . .	121
10.6. Owens Valley Radio Observatory . . . . .	123
10.6.1. Light curve . . . . .	125
10.6.2. SED . . . . .	126
<b>11. Temporal Analysis with Multiwavelength light curves</b>	<b>128</b>
11.1. Variability in Blazar emission . . . . .	129
11.2. Multiwavelength Temporal Analysis . . . . .	130
11.2.1. Fractional variability . . . . .	130
11.2.2. Simultaneous flux correlation . . . . .	132
11.2.3. Discrete Correlation Function (DCF) . . . . .	133
11.3. Summary and Discussion of the Temporal Analysis . . . . .	140
<b>12. Evaluation of temporal variability with one-zone SSC model</b>	<b>141</b>
12.1. Multiwavelength Spectral Energy Distribution modeling . . . . .	141
12.2. Discussion and Summary . . . . .	147
12.3. Comparison with the previous study . . . . .	151
<b>13. Conclusion and Future prospect</b>	<b>155</b>
<b>A. Spectral function</b>	<b>157</b>
A.1. Power law . . . . .	157
A.2. Log Parabola . . . . .	157

A.3. Power-law with exponential cutoff . . . . .	157
<b>B. Discrete Correlation Functions</b>	<b>159</b>
<b>C. Systematic effect of coincidence windows in the flux correlation</b>	<b>170</b>
<b>D. Flux correlations</b>	<b>171</b>
<b>References</b>	<b>182</b>
<b>Acknowledgement</b>	<b>187</b>

# **Part I.**

## **Introduction**



# 1. Astroparticle Physics

## 1.1. Cosmic Rays and their Origins

Victor Hess has discovered high-energy particles coming from outer space, and they are called cosmic rays ([Hess, 2018](#)). Some elementary particles, such as positron and muon, also were discovered from cosmic rays, and cosmic-ray physics has been developed historically as a part of elementary particle physics. Although more than 100 years have passed since the cosmic-ray discovery, the precise understanding of the origin of cosmic rays is still not yet done, primarily high-energy domain. As shown in figure [1.1](#), several experiments confirmed that the particles have energy well beyond the energy produced by the artificial particle accelerator. Acceleration sites and mechanisms of such high-energy particles are one of the biggest problems in astrophysics.

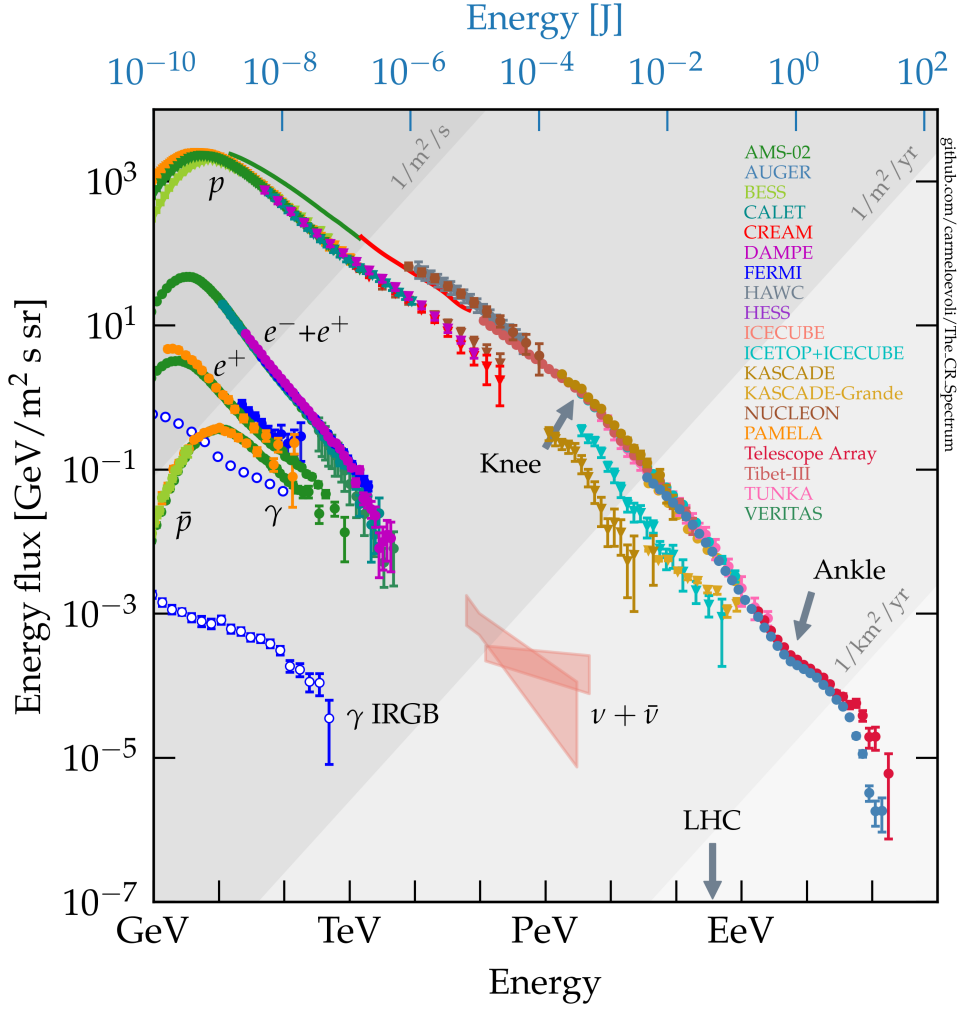


Figure 1.1: Cosmic-ray spectra made by [Evoli \(2020\)](#). The continuum starting from 10 GeV to  $10^{20}$  eV is the total cosmic-ray spectrum. The spectrum has several energies where the spectral index changes; Knee and Ankle are shown. Measurements of each particle are annotated;  $\gamma$  IRGB is an abbreviation of an isotropic diffuse gamma-ray background. LHC represents the maximum energy in the target rest frame.

Although we have not fully understood the origin of cosmic rays, the cosmic-ray spectra have been measured precisely at the energy for more than 20 orders of magnitudes. Figure 1.1 shows various cosmic-ray spectra from 1 GeV to  $10^{20}$  eV, and we know that the power-law spectrum with the index  $\sim -2.7$  can roughly explain the spectra in the whole energy range. Moreover, more precise structures are known, called "knee" and "ankle."

Those energies are considered the point where the cosmic-ray spectra from different origins are superposed. The knee at around  $10^{15}$  eV is close to the high-energy limit of the galactic origin cosmic rays, and the ankle is the region extra-galactic cosmic rays being dominated. Moreover, the energy from  $10^{16}$  eV to  $10^{18}$  eV is a transition region

from galactic origin to the extra-galactic cosmic rays. This interpretation is based on the relation of maximum energy and acceleration-site size. Figure 1.2 is the so-called Hillas plot showing the relation between the maximum energy, magnetic field, and acceleration region size. The high-energy astronomical objects are shown with their typical size and magnetic field. Although scientists frequently study those objects, we still do not have clear evidence of cosmic-ray acceleration.

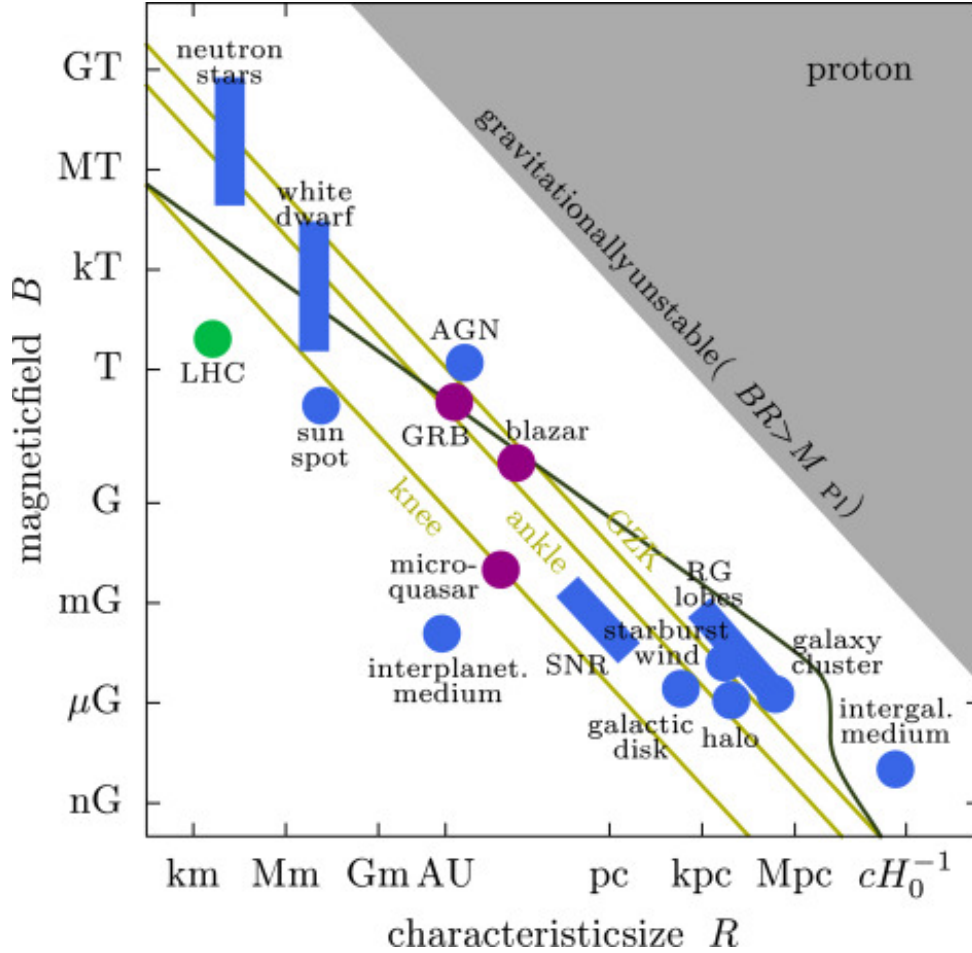


Figure 1.2: Hillas plot: The maximum energy depends on magnetic field and acceleration size. Solid lines with "knee", "ankle" and "GZK" show the maximum energy of photon under the certain magnetic field and the certain size of accelerators (Dova, 2015)

The crucial points of the measurement of the cosmic ray are magnetic fields and statistics. At low energy, the Larmor radius becomes small; thus, particles quickly lose their arrival directional information. This makes observation challenging to estimate the origin of low-energy particles. On the other hand, the number of arriving particles is relatively small at the highest energy. Even using the  $\text{km}^2$  instrument, the arriving particle rate is one per century. Therefore, the statistical discussion is difficult to estimate the origin.

Then can we not reveal the origin of cosmic rays? The answer is yes, we can. The indirect approaches using photons and neutrinos were developed to manage the problems. According to the fundamental interactions discussed in section 2, cosmic rays produce secondary particles. Photons and neutrinos produced by the interactions can propagate toward the earth.

Those neutral particles are a good probe to study the cosmic-ray origin; then, the individual field was developed. Gamma-ray astronomy is one of the fields motivated by cosmic-ray physics.

## 1.2. Gamma-ray Astrophysics

The gamma-ray astronomy was developed to detect the high-energy photons produced via the interaction between cosmic-rays and interstellar medium. Gamma-ray astrophysics has a broad subjects in high-energy astrophysics and elementary physics. Most of them are related to the origin of cosmic ray as mentioned in above. Pulsars, Supernova remnants, Active galactic nuclei, are gamma ray bursts are major target of the filed. On top of that, a dark matter search and a test of Lorentz invariance violation using gamma rays are also subjects.

The first gamma-ray satellite Explore 11 was launched in 1961, and later Whipple telescope was built in 1968 (Kildea et al., 2007). However, significant progress has been made by CGRO launched 1991, EGRET, which is onboard gamma-ray telescope

Fermi-LAT opened an new window for high-energy gamma-ray astronomy. The number of detected source is being increased, now it reaches 5000 sources (Abdollahi et al., 2020).

This enable us to perform big data science such is performed in optical astronomy. On the other hand, the very high-energy gamma-ray astronomy, it mainly focus on gamma rays above 100 GeV still being developed. The number of source is around 200, this implies we need more sensitivity to detect the sources which already detected in the high-energy gamma-ray.

Imaging Atmospheric Cherenkov Telescope (IACT) is main instrument for ground-based gamma-ray astronomy. The telescope observes gamma rays via Cherenkov lights produced by secondary charged particles initiated by gamma rays.

On top of the IACT, surface detector arrays also work as gamma-ray telescope; they are also being operated such as HAWC, LHAASO, Tibet AS- $\gamma$  (Smith, 2015; Cao et al., 2019; Amenomori et al., 1992). Especially, LHAASO found a PeV gamma-ray, or ultra-high-energy gamma-ray detected then opened the new field. On one hand, the PeV gamma-ray from the galactic object is suggesting the PeV accelerator in out galaxy (Amenomori et al., 2021), but on the other hand there is no clue for the origin of ultra high-energy cosmic rays (UHECR).

## 2. Physical Process

Accelerated charged particles affect the surrounding electromagnetic field, and the changes propagate as electromagnetic waves. The energy-loss rate of charged particles can be evaluated using Larmor's formula:

$$-\frac{dE}{dt} = \frac{q^2 \gamma^4}{6\pi \varepsilon_0 c_0^3} \left[ a^2 + \gamma^2 (\vec{\beta} \cdot \vec{a}) \right], \quad (2.1)$$

where  $q = ze$  is the charge of accelerated particles<sup>1</sup>,  $\varepsilon_0$  is the vacuum permittivity<sup>2</sup>,  $c_0$  is the speed of light in vacuum<sup>3</sup>,  $\vec{\beta} = \vec{v}/c_0$  and  $\beta = |\vec{\beta}|$  is the particle velocity normalized by  $c_0$ ,  $\gamma = 1/\sqrt{1 - \beta^2}$  is Lorentz factor, and  $a = |\vec{a}|$  is the acceleration of particles. See some textbooks, e.g., Longair (2011) or Rybicki & Lightman (1986), for detailed algebra.

As seen from equation 2.1, the acceleration of the particle characterizes the energy-loss rate. When the force acting on the particle is apparent, the concrete form of energy-loss rate can be assessed, and through Fourier transformation, a spectrum of the radiation can also be obtained. Subsequent sections introduce properties such as energy-loss rate and cross sections for radiation processes, which play an important role in our understanding of high-energy celestial objects.

### 2.1. Emissions

This chapter discusses the standard radiative processes in high-energy astronomy. The criteria for radiation and interaction are ambiguous, but for this chapter, radiation is defined as a physical process in which charged particles lose energy through electromagnetic interactions. Each radiative process is discussed in terms of its energy loss, and its spectrum is also discussed for the most important ones.

#### 2.1.1. Ionization Loss

In matter, a charged particle interacts with the bound electrons of atoms and loses its energy through the Coulomb force. This process is called ionization loss because the bound electrons gain energy and are excited or ionized. The following equation expresses ionization loss:

$$-\frac{dE}{d\xi} = \frac{q^2 e^2}{4\pi^2 \varepsilon_0^2 m_e v^2} \frac{N_A Z}{A} f(v, Z), \quad (2.2)$$

where  $\xi = \rho x$  is a radiation length or a depth,  $N_A$  is the Avogadro number<sup>4</sup>,  $A$  is a mass number,  $Z$  is an atomic number, and  $m_e$  is the electron mass<sup>5</sup>. In addition,  $f(v, Z)$  is a

<sup>1</sup> $e = 1.602\,176\,634 \times 10^{-19}$  C from CODATA

<sup>2</sup> $\varepsilon_0 = (8.854\,187\,812\,8 \pm 0.000\,000\,001\,3) \times 10^{-12}$  C<sup>2</sup> kg<sup>-1</sup> m<sup>-3</sup> s<sup>2</sup> from CODATA

<sup>3</sup> $c_0 = 2.997\,924\,58 \times 10^8$  m s<sup>-1</sup> =  $2.997\,924\,58 \times 10^{10}$  cm s<sup>-1</sup> from CODATA

<sup>4</sup> $N_A = 6.022\,140\,76 \times 10^{23}$  mol<sup>-1</sup> from CODATA

<sup>5</sup> $m_e = (9.109\,383\,701\,5 \pm 0.000\,000\,002\,8) \times 10^{-31}$  kg =  $(510.998\,950\,00 \pm 0.000\,000\,15)$  keV from CODATA

function that expresses the dependency in velocity, and this term varies by calculation; for example, in Longair (2011),  $f(v, Z) = \ln(2\gamma^2 m_e v^2 / \bar{I}(Z)) - \beta^2$ . This equation, also called the Bethe-Bloch equation, describes the energy loss by a charged particle in matters. Figure 2.1 shows the approximate form of the Bethe-Bloch equation, where the energy loss varies inversely with the square of the velocity at low energies and is approximately constant at high energies. Thus, the energy lost by a charged particle with relativistic velocity is approximately proportional to the radiation length. The energy loss at its lowest value is independent of the mass of the charged particle and depends only on its velocity, and this difference can be used to determine the particle species. Also, since the mass in the equation is the particle's mass receiving the energy, the ionization loss to the nucleus can be neglected in most cases.

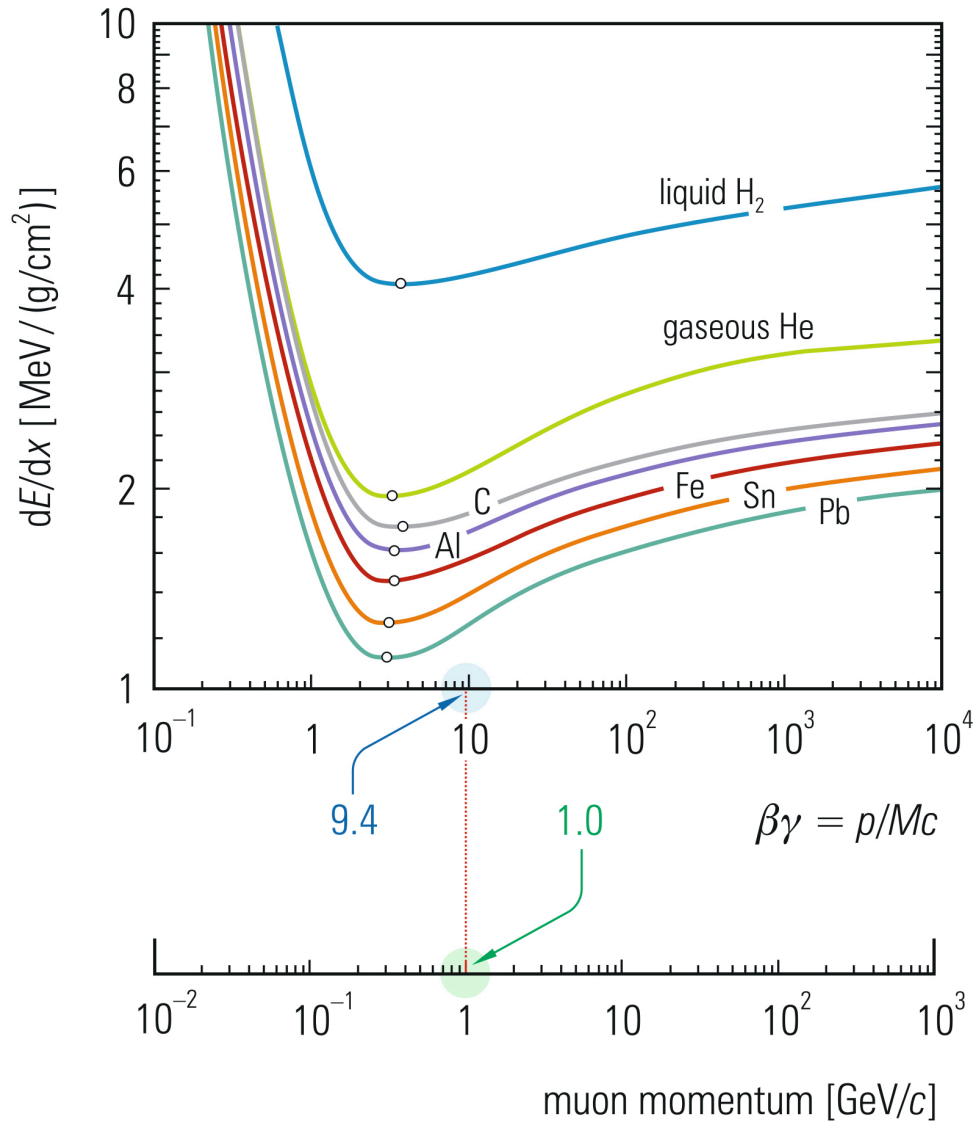


Figure 2.1: Ionization loss in several materials (Gruppen, 2020).

### 2.1.2. Bremsstrahlung

Bremsstrahlung is mediated by Coulomb forces, as is ionization loss, but the electron loses energy due to radiation. Bremsstrahlung in matter can be calculated by considering the acceleration due to the Coulomb force using Larmor's formula introduced in Eq 2.1.

$$-\frac{dE}{dt} = \frac{Z^2 e^2 q^4 N_e E}{12\pi^3 \epsilon_0^3 c_0^4 \hbar} \ln \left( \frac{192}{Z^{1/3}} \right) \quad (2.3)$$

Where  $N$  is the number density of nuclei, and  $\hbar$  is Dirac's constant<sup>6</sup>. Although some detail calculations vary equation 2.3, the critical feature is that the energy-loss rate is proportional to  $Z^2$  and  $E$ .

Detailed calculations depend on the material, but in the relativistic limit, the energy loss is proportional to the energy. This increases more slowly than, for example, synchrotron radiation, which will be more dominant in high energy. The energy loss per radiation length is expressed by the equation Since the energy loss is proportional to energy, we also know that the energy decreases exponentially, and the distance until the energy reaches  $1/e$  is called the radiation length. The radiation length is important when considering the development of charged-particle showers.

Another important perspective of Bremsstrahlung is, the critical energy  $E_{\text{crit}}$ . The critical energy is the energy the energy-loss of Bremsstrahlung equals the one of ionization-loss. For the air,  $E_{\text{crit}} \sim 87 \text{ MeV}$ . When the particles lose energy down to 87 MeV, the particle shower stops its development.

### 2.1.3. Synchrotron Radiation

Charged particles in a magnetic field undergo a rotational motion under the Lorentz force  $q\vec{v} \times \vec{B}$ . At this time, acceleration is generated as a centripetal force, and energy is radiated in response to the rotational motion. This motion is called gyroscopic motion and is characterized by gyroscopic radius  $r_{\text{gyro}} = \gamma m v_{\perp} / e |\vec{B}|$  and gyroscopic frequency  $\omega_{\text{gyro}} = |q| |\vec{B}| / \gamma m$ . Typical values under a magnetic field of 1 Gauss are;

$$\nu_{\text{gyro}} = \frac{\omega_{\text{gyro}}}{2\pi} = 2.799 \frac{|z|}{\gamma} \left( \frac{B}{1 \text{ G}} \right) \left( \frac{m}{m_e} \right)^{-1} \text{ MHz} \quad (2.4)$$

$$r_{\text{gyro}} = 17.045 \frac{\gamma}{|z|} \left( \frac{m}{m_e} \right) \left( \frac{B}{1 \text{ G}} \right)^{-1} \beta \sin \alpha \text{ m} \quad (2.5)$$

If the velocity of the particle is small, its radiation is called cyclotron radiation, and radiation is produced at a frequency corresponding to the gyro frequency. When the velocity is relativistic, its radiation spectrum becomes continuous and is called synchrotron radiation. In this section we discuss the spectrum of synchrotron radiation and its characteristics. Charged particles in a magnetic field receive the Lorentz force and produce

---

<sup>6</sup> $\hbar = 6.626\,070\,15 \times 10^{-34} \text{ kg m}^2, \hbar = h/2\pi$

circular motion. The circular motion is called gyro motion and is characterized by the gyro radius and gyro frequency .

**Energy-loss rate** The energy loss rate due to synchrotron radiation is derived by substituting the acceleration into equation 2.1. The acceleration is perpendicular to the velocity. Thus the  $a = evB \sin \alpha / \gamma m$ . Therefore the energy-loss rate is;

$$\begin{aligned} -\frac{dE}{dt} &= 2z^4 \left( \frac{e^4}{6\pi\epsilon_0^2 m_e^2 c_0^4} \right) c_0 \left( \frac{m_e}{m} \right)^2 \left( \frac{B^2}{2\mu_0} \right) \gamma^2 \beta^2 \sin^2 \alpha \\ &= 2z^4 \sigma_T c_0 \left( \frac{m_e}{m} \right)^2 U_B \gamma^2 \beta^2 \sin^2 \alpha \end{aligned} \quad (2.6)$$

$$-\left\langle \frac{dE}{dt} \right\rangle = \frac{4}{3} z^4 \sigma_T c_0 U_B \gamma^2 \beta^2 \quad (2.7)$$

Where the  $\sigma_T = e^4 / 6\pi\epsilon_0^2 m_e^2 c_0^4$  is thomson cross section, and  $U_B = B^2 / 2\mu_0$  is the magnetic energy density. One should know that the energy-loss rate is proportional to the square of a magnetic field and the Lorentz factor.

**Energy spectrum** One can compute the energy spectrum via Fourier transformation of equation 2.7. The energy spectrum from a single particle is;

$$I_{\perp}(\omega) = \frac{\sqrt{3}q^2\gamma \sin \alpha}{8\pi\epsilon_0 c_0} [F(\psi) + G(\psi)] \quad (2.8)$$

$$I_{\parallel}(\omega) = \frac{\sqrt{3}q^2\gamma \sin \alpha}{8\pi\epsilon_0 c_0} [F(\psi) - G(\psi)] \quad (2.9)$$

Where  $I(\omega) = dE/d\omega$  is the energy emitted per frequency<sup>7</sup>.  $F(\psi) = \psi \int_{\psi}^{\infty} K_{5/3}(z) dz$  is the integration of modified vessel function of order 5/3 and  $G(\psi) = \psi K_{2/3}(\psi)$ . The spectral shape depends on  $F(\psi)$ , and  $\psi$  is normalized frequency defined as  $\psi = \nu / \nu_{\text{crit}}$ . The critical frequency;

$$\nu_{\text{crit}} = \frac{\omega_{\text{crit}}}{2\pi} = \frac{3}{2} \gamma^3 \nu_{\text{gyro}} \sin \alpha \quad (2.10)$$

$$\psi \propto \nu / B \gamma^2 \Leftrightarrow \gamma \propto \left( \frac{\nu}{B\psi} \right)^{1/2} \quad (2.11)$$

---

<sup>7</sup>  $\int_0^{\infty} \frac{dE}{dt} dt = \int_0^{\infty} I(\omega) d\omega$



characterize a spectrum. by considering emission per orbital period  $\tau_{\text{gyro}} = \nu_{\text{gyro}}^{-1} = 2\pi\gamma m/|q|\vec{B}|$ , one can evaluate total emitted energy per frequency per time  $j(\omega)$ .

$$\begin{aligned} -\frac{d^2E}{dt d\omega} &= j(\omega) = \frac{I_{\perp}(\omega) + I_{\parallel}(\omega)}{\tau_{\text{gyro}}} \\ &= \frac{\sqrt{3}q^3 B \sin \alpha}{16\pi^2 \varepsilon_0 m c_0} F(\psi) \end{aligned} \quad (2.12)$$

The spectrum can be expressed approximately as follows;

$$F(\psi) \propto \begin{cases} \psi^{1/3} & \psi \ll 1 \\ \psi^{1/2} \exp(-\psi) & \psi \gg 1 \end{cases} \quad (2.13)$$

One can confirm that the synchrotron spectrum follows a power-law function and a power-law function with an exponential cutoff from equation 2.19. And the  $F(\psi)$  shows maximum values at  $\psi \sim 0.29$ .

For the application in astrophysics, the synchrotron emission from the electron population is also essential. From theoretical prediction and observational results, it is believed that electrons follow a power-law distribution. Assume the electron differential number spectrum follows  $dN \propto \gamma^{-p} d\gamma$ . Combining it with equation 2.9, the energy spectra from the power-law electrons is;

$$\begin{aligned} -\frac{d^2E}{dt d\omega} &= \int j(\psi) \frac{dN}{d\gamma} d\gamma \\ &\propto \int B F(\psi) \gamma^{-p} d\gamma \sim \int B \psi \nu^{-p/2+1/2} B^{p/2-1/2} \psi^{p/2-3/2} d\psi \\ &\propto \omega^{-(p-1)/2} B^{(p+1)/2} \end{aligned} \quad (2.14)$$

Thus, emissions from the power-law distributed electron also follow the power-law function with index  $(p-1)/2$  and also depends on  $B^{(p+1)/2}$ . at low energy, electron absorb synchrotron radiation it self. The phenomenon is called synchrotron self absorption.

#### 2.1.4. Thomson and Compton scattering

The scattering of photons by a stationary electron is known as Thomson scattering. Through Thomson scattering, photons do not change their energy. The differential cross-section of Thomson scattering is;

$$\frac{d\sigma_T}{d\Omega} = \frac{3}{16} (1 + \cos^2 \chi) \quad (2.15)$$

and the total cross-section is;

$$\sigma_T = \frac{8\pi}{3} r_e^2 = \frac{e^4}{6\pi\epsilon_0^2 m^2 c^4} = 6.652\,458\,7 \times 10^{-29} \text{ m}^2. \quad (2.16)$$

This coefficient often appears when one considers particle interactions.

For high-energy photons, we can not ignore the inelasticity of the scattering. The scattering considering the energy transfer is called Compton scattering, which is more important in the astronomical application. From the energy-momentum conservation law, the scattered photon energy  $E_{S,ph}$  can be described as;

$$E_{S,ph} = \frac{E_{ph}}{1 + \epsilon(1 - \cos \chi)} \quad (2.17)$$

where  $\epsilon = E_{ph}/m_e c_0^2$ . Thus, when energy is smaller than the electron rest mass, the scattered energy does not change as discussed for Thomson scattering.

Moreover, the cross-section also needs to be modified for the high-energy photons. The precise cross-section is famous as the Klein-Nishina cross-section;

$$\sigma_{KN} = \frac{3\sigma_T}{8\epsilon} \left\{ \left[ 1 - \frac{2(\epsilon + 1)}{\epsilon^2} \right] \ln(2\epsilon + 1) + 0.5 + 0.25\epsilon^{-1} - \frac{1}{2(2\epsilon + 1)^2} \right\} \quad (2.18)$$

and for the low-energy ( $\epsilon \ll 1$ ) and high-energy limit ( $\epsilon \gg 1$ ),

$$\sigma_{KN} \sim \begin{cases} \sigma_T(1 - 2\epsilon) & \text{for } \epsilon \ll 1 \\ \frac{3\sigma_T}{8\epsilon} (\ln 2\epsilon + 1) & \text{for } \epsilon \gg 1 \end{cases} \quad (2.19)$$

Thus, the cross-section decreases at highest energy and it gives the limit in the inverse-compton scattering.

### 2.1.5. Inverse Compton scattering

In the previous section, I introduced the scattering of electrons by photons. However, the opposite scattering process by high-energy electrons is known as Inverse Compton scattering. Inverse Compton scattering is important when considering the high-energy emission of the blazar. The characteristics of the emission can be derived by combining a usual Thomson scattering and Lorentz transformation. When the electron has energy  $\gamma mc^2$ , the scattering photon energy in the electron rest frame is;

$$E_{sc} = \gamma E'_{sc} (1 + \beta \cos \chi') \quad (2.20)$$

Thus one can compute a scattering using the photon energy  $E''$ . As far as  $E''$  is smaller than the electron rest mass, the scattered photon energy is also  $E''$ . Repeating the Lorentz

transformation into the laboratory frame gives the scattered photon energy as below.

$$\begin{aligned} E' &= E'_{\text{sc}} \\ &= \gamma E(1 - \beta \cos \chi) \end{aligned} \quad (2.21)$$

$$E_{\text{sc}} = \gamma^2 E(1 + \beta \cos \chi')(1 - \beta \cos \chi) \quad (2.22)$$

Thus, the maximum photon energy will be  $4\gamma^2 E$  in the thomson regime.

The energy-loss rate due to Inverse Compton scattering is

$$-\left(\frac{dE}{dt}\right) = \frac{4}{3}\sigma_T c \beta^2 \gamma^2 U_{\text{ph}} \quad (2.23)$$

### 2.1.6. Cherenkov Radiation

In matter, the speed of light decreases by the amount of the refractive index. On the other hand, particles with sufficiently large energy can move beyond the speed of light in matter, and electromagnetic waves are also emitted at such times. This radiation is called Cherenkov radiation and is similar to shock waves in air. Because the velocity of the particles must exceed the speed of light in matter, the

$$v > \frac{c_0}{n} \Leftrightarrow \beta > \frac{1}{n} \quad (2.24)$$

Radiation is produced only when The radiation is strongly forward in the direction of the particle's motion, and its radiation angle is  $\cos \theta = 1/n\beta$  and the minimum radiation angle can be obtained when  $\beta = 1$ :

$$\theta_{\text{min}} = \arccos 1/n \quad (2.25)$$

The spectra of cherenkov radiation is

$$I(\omega) = \frac{\omega q^2 v}{4\pi\epsilon_0 c_0^3} \left(1 - \frac{1}{n^2 \beta^2}\right). \quad (2.26)$$

Hence the spectral shape shows higher energy emitted in the higher frequency, but in reality, the spectrum has a peak around  $\lambda = 300 \text{ nm}$  due to the atmospheric absorption.

## 2.2. Interactions

The previous section gives the physical processes that produce photons. On the contrary, this section explains various interactions describing more than two particles or producing non-photon particles.

### 2.2.1. Electron-positron Pair Production

Photons interact with each other to produce electron-positron pairs. Electron-positron pairs can also be produced by annihilating other particles, but we discuss only those caused by photons. This process can occur in various situations since photons can also interact with Coulomb fields, such as those of atomic nuclei.

This reaction is also critical for observing gamma rays since it is an absorption reaction. High-energy gamma rays interact with low-energy gamma rays emitted from stars and galaxies and are absorbed before they reach Earth. From the energy conservation law,

$$\begin{aligned} s^2 &= 2E_{\text{ph},1}E_{\text{ph},2}(1 - \mu) = 4E_e^{*2} \\ &\geq 4m_e^2c_0^4 \end{aligned} \quad (2.27)$$

should be satisfied, where  $E_{\text{ph},1}$  and  $E_{\text{ph},2}$  are photon energies of high-energy(= 1) and low-energy(= 2); and  $E_e^* = \gamma^*m_e c_0^2$  is the electron energy in the center-of-mass frame. Thus,

$$E_{\text{ph},1}E_{\text{ph},2} \geq \frac{2m_e^2c_0^4}{(1 - \mu)} \geq m_e^2c_0^4 \quad (2.28)$$

is a threshold condition for the interaction. From the condition, a high-energy photon of 1 TeV will interact with and be absorbed by low-energy photons with energies above 0.26 eV. Figure 2.2 shows historical extragalactic background light (EBL) studies (Franceschini, A. et al., 2008; Gilmore et al., 2012; Domínguez et al., 2011). Because of the bump around  $1 \mu\text{m}$ , corresponds to  $1.24 \text{ eV}^8$ , high-energy gamma rays are strongly absorbed and need to be corrected to know the intrinsic flux of gamma-ray source.

---

<sup>8</sup> $\lambda = 1240 * 1 \text{ eV/E [nm]}$

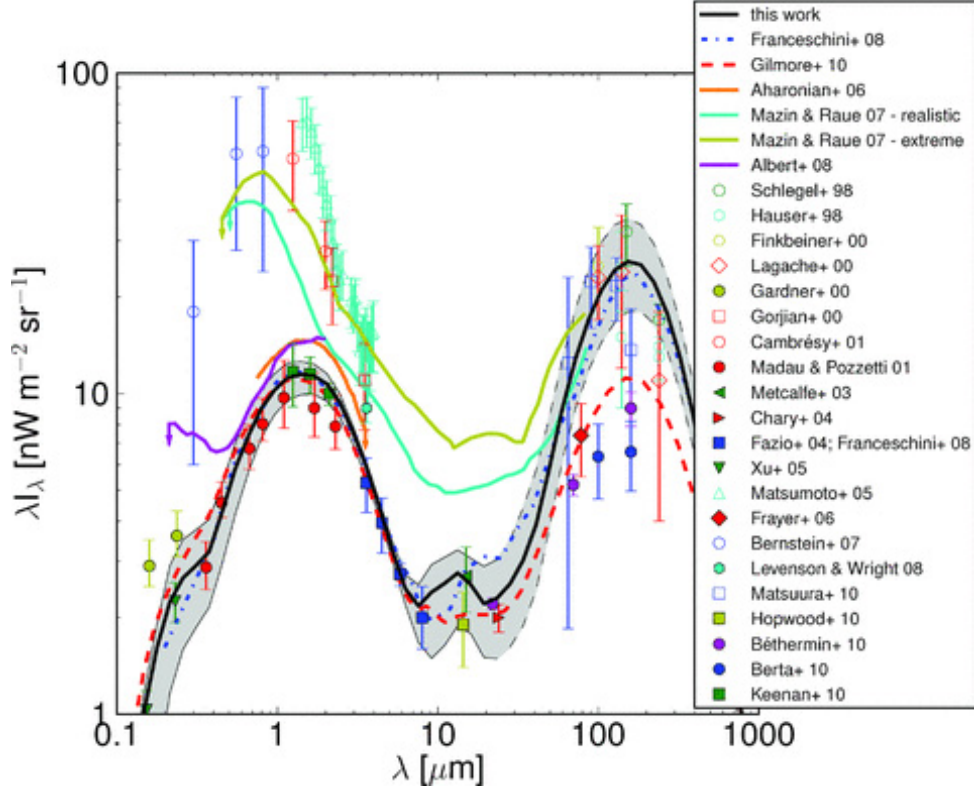


Figure 2.2: Extragalactic background light (Dom nguez et al., 2011).

$$\sigma_{\gamma\gamma}(\beta^*) = \frac{3}{16}\sigma_T(1 - \beta^{*2}) \left[ (3 - \beta^{*4}) \ln \left( \frac{1 + \beta^*}{1 - \beta^*} \right) - 2\beta^*(2 - \beta^{*2}) \right] \quad (2.29)$$

$$= \frac{3}{8}\sigma_T \begin{cases} \beta^* & \text{for } \beta^* \ll 1 \\ (1 - \beta^{*2}) \left\{ \ln \left( \frac{4}{1 - \beta^{*2}} \right) - 1 \right\} & \text{for } \beta^* \sim 1 \end{cases} \quad (2.30)$$

Interactions through the Coulomb field include:

$$\gamma + Z \rightarrow Z + e^+ + e^-, \quad (2.31)$$

$$(2.32)$$

$$\gamma + e^\pm \rightarrow e^\pm + e^+ + e^-. \quad (2.33)$$

$$(2.34)$$

Equation 2.32 is the interaction with nucleus and 2.34 is the one with electrons. Corresponding cross-sections are defined using the ratio of photon energy to electron mass

energy  $\epsilon' = E'_{\text{ph}}/m_e c^2$  as:

$$\sigma_{e^\pm\gamma}(\epsilon') = \frac{3}{8\pi}\alpha\sigma_T \begin{cases} \frac{\sqrt{\pi}}{324}(\epsilon' - 4)^2 & \text{for } \epsilon' - 4 \ll 1 \\ \frac{28}{9}\{\ln(\epsilon')\} - \frac{218}{27} & \text{for } \epsilon' \gg 4 \end{cases} \quad (2.35)$$

$$\sigma_{Z\gamma}(\epsilon') = \frac{3}{8\pi}\alpha\sigma_T Z^2 \begin{cases} \frac{2\pi}{3}(\epsilon' - 2)^2 & \text{for } \epsilon' - 2 \ll 1 \\ \frac{28}{9}\{\ln(2\epsilon')\} - \frac{218}{27} & \text{for } \epsilon' \gg 2 \end{cases} \quad (2.36)$$

The energy range is defined by the energy-momentum conservation law. The threshold energy is  $\epsilon' = 4$  and  $\epsilon' \sim 2$ , respectively (Krolik, 2021). As you can see from formulae, the pair creation with nucleus works more stronger. For the air shower development discussed in the later section, the repetition of the pair production and Bremsstrahlung are main process of making an electromagnetic shower.

### 2.2.2. Pion Decay

Pion decays are introduced to understand the development of atmospheric showers and to explain hadronic emissions in celestial objects. In this section, after introducing pion decays, we discuss the gamma rays expected from the decays.

First, the neutral pion undergoes the following decay with probability 98.8%, producing two gamma rays.

$$\pi^0 \rightarrow 2\gamma. \quad (2.37)$$

The neutral-pion lifetime is  $\tau_{\pi^0} = 8.43 \times 10^{-17}$  s and its mass is  $m_{\pi^0} = 134.98 \text{ MeV}/c_0^2$  (PDG et al., 2022).

In atmospheric showers, the hadronic shower will have a small electromagnetic shower because the pions produced by the interaction of cosmic rays and the atmospheric nuclei emit gamma rays. In the radiation of celestial objects, pions are produced by the reaction of cosmic rays with interstellar gas or low-energy photons and thus are the source of gamma-ray emission.

If the gamma rays are produced isotropically in a rest system of neutral pion, their angular distribution will be

$$\frac{dN}{d\cos\theta'} = \frac{1}{2}. \quad (2.38)$$

Moreover, the photons per energy is defined as follows:

$$\begin{aligned} \frac{dN}{dE_{\text{ph}}} &= \frac{dN}{d\cos\theta'} \frac{d\cos\theta'}{dE_{\text{ph}}} \\ &= \frac{2}{E_\pi \beta_\pi}. \end{aligned} \quad (2.39)$$

Assuming that the particle distribution of neutral pion is  $dN_\pi/dE_\pi \propto E_\pi^{-\Gamma_\pi}$ , the particle

distribution of gamma rays can be estimated:

$$\begin{aligned}\frac{dN_\gamma}{dE_\gamma} &= \int \frac{dN}{dE_{\text{ph}}} \frac{dN_\pi}{dE_\pi} dE_\pi \\ &= \int \frac{2}{E_\pi \beta_\pi} \frac{dN_\pi}{dE_\pi} dE_\pi,\end{aligned}\tag{2.40}$$

$$\propto \frac{dN_\pi}{dE_\pi} \quad \text{for } \beta_\pi \gg 1.\tag{2.41}$$

Thus the particle distribution of photons has the same index of neutral pion.

Next, in the case of charged pions, they decay into muons accompanied by neutrinos. The decay probability at this time is 99.988 %.

$$\pi^+ \rightarrow \mu^+ + \nu_\mu\tag{2.42}$$

$$\pi^- \rightarrow \mu^- + \bar{\nu}_\mu\tag{2.43}$$

Their lifetime is  $\tau_{\pi^\pm} = 2.60 \times 10^{-8}$  s and their mass is  $m_{\pi^\pm} = 139.57 \text{ MeV}/c_0^2$  (PDG et al., 2022).

Muons also decay further into electrons:

$$\mu^+ \rightarrow e^+ + \bar{\nu}_\mu + \nu_e\tag{2.44}$$

$$\mu^- \rightarrow e^- + \bar{\nu}_e + \nu_\mu\tag{2.45}$$

Muon lifetime is  $\tau_\mu = 2.197 \mu\text{s}$  and the mass is  $m_\mu = 105.66 \text{ MeV}/c_0^2$ . Muons have sufficiently long lifetimes  $\gamma_\mu c_0 \tau_\mu \sim 0.66 \gamma_\mu \text{ km}$  to reach the surface without decay if they have relativistic velocities. Therefore, in experiments using atmospheric showers, muons are used to discriminate between hadronic showers and gamma-ray showers.

### 2.2.3. Hadronic Interactions

Hadronic interaction also plays a important role in the high energy astronomy and it's observation. However, the interaction between nucleus follows strong interaction, hence it is quite difficult to derive analytical result. Therefore, experiment to measure the cross section has been done historically. Despite that, the interaction model at highest energy is not known well. This makes things difficult for the several aspects.

There are several interaction induced by high-energy cosmic rays:

$$p_{\text{inj}} + A \rightarrow A' + p + n + \pi^{0/+/-} + K^{0/+/-} + \dots\tag{2.46}$$

$$p + \gamma \rightarrow p' + e^+ + e^-\tag{2.47}$$

$$p + \gamma \rightarrow n + \pi^+\tag{2.48}$$

$$p + \gamma \rightarrow \Delta^{++} + \pi^-\tag{2.49}$$

$$p + \gamma \rightarrow \Delta^0 + \pi^+\tag{2.50}$$

In each interaction, the chain of reaction continues. For the pions and kaons, they will

decay in to the muons and neutrinos. Once electromagnetic component are produced, the electromagnetic interaction cascade occurs in the chain. Some of them are also introduced when one consider the hadronic emission models. For example, gamma-ray emission from supernova remnant is well explained by the interaction between high-energy protons and the interstellar gas.



### 3. Active Galactic Nuclei

#### 3.1. AGN Classification and Unified model

It is known that some of galaxies have supermassive black holes (SMBH) at the center of the galaxies. Some of those black holes are active, the gasses surrounding SMBH are accreting into the core produce strong emission, which sometimes exceed the luminosity of the whole galaxy. Such a luminous core is called Active Galactic Nuclei (AGN).

On top of that, there are many kinds of classification exist in the AGN. As one example, if the radio emission is strong, this is called Radio Galaxy and if it looks like a star (a point source), it called Quasars. Currently, the difference in those categories is due to the apparent effect causing by the viewing angle. Those scenario is called as unified model as shown in figure 3.1, and it is moderately believed among the community.

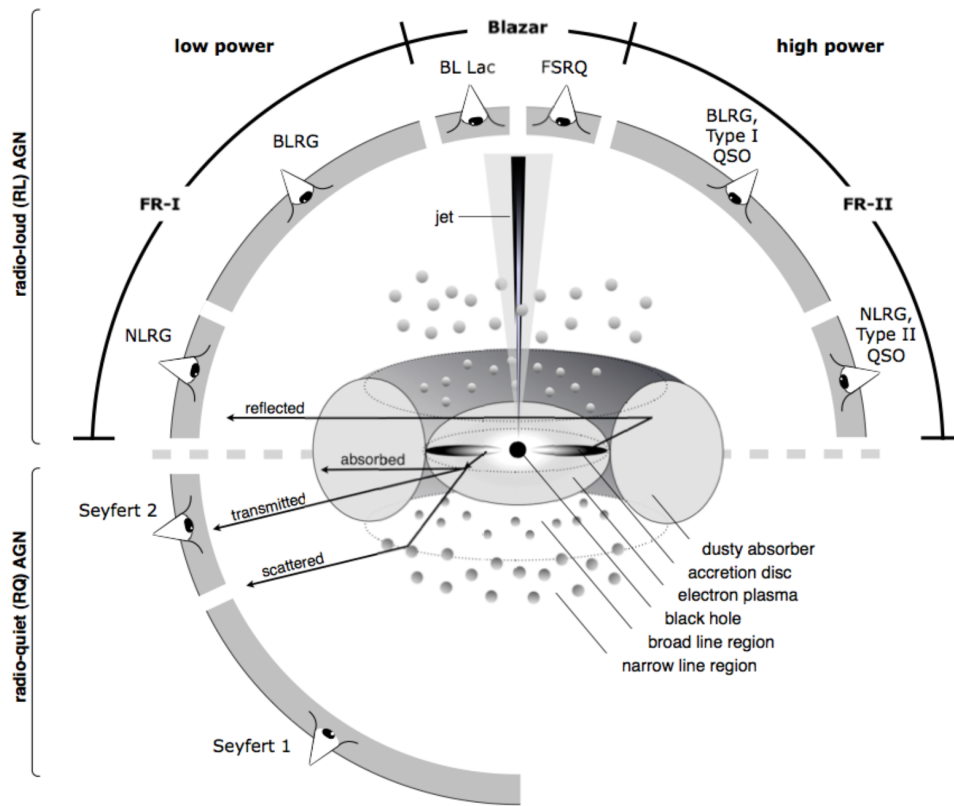


Figure 3.1: Unified model. The model assumes that AGNs have intrinsically same properties, but they look different due to the difference of the observational angle (Britto et al., 2016).

Moreover, some of AGNs have the collimated outflows and they are observed by the radio and optical emissions. This outflow from the center of the galaxy is called jet. The relativistic motion was confirmed from the observation of relativistic apparent speed motion. Thus the jet is also known as the relativistic jet. At least some of AGN has a jet.

If the jetted emission is lying along the perpendicular line of site, this is considered a Radio Galaxy, which is bright on the radio and makes it easy to see the whole jet structure. On the other hand, the opposite situation happens by chance. It is known as blazars. The emission is amplified by the relativistic effect.

### 3.2. Blazar

As explained in the above, some AGNs have jets, which is relativistic flow from the centre. If the direction of relativistic bulk motion is pointed toward us, the emissions are magnified by the effect of special relativity. This is called as doppler boosting. Here I will skip the calculation, but as a result, the observed photon energy will be changed as follows:

$$E_{\text{obs}} = \frac{E_{\text{emi}}}{\Gamma(1 - \beta \cos \theta)} \quad (3.1)$$

$$\delta_D := \frac{1}{\Gamma(1 - \beta_{\Gamma} \cos \theta)} \quad (3.2)$$

$$\Gamma := \frac{1}{\sqrt{1 - \beta_{\Gamma}^2}} \quad (3.3)$$

$$\beta_{\Gamma, \text{app}} := \frac{\beta_{\Gamma} \sin \theta}{1 - \beta_{\Gamma} \cos \theta} \quad (3.4)$$

The apparent speed  $\beta_{\Gamma, \text{app}}$  takes a maximum value of  $\beta_{\Gamma, \text{app}, \text{max}} = \Gamma \beta_{\Gamma} = \sqrt{\Gamma^2 - 1}$  when  $\cos \theta = \beta_{\Gamma}$ , and  $\Gamma = \delta_D$  is also satisfied.

From the radio observation, typical value of  $\delta_D$  from the measurements are roughly 10 (Lioudakis et al., 2018). On the other hand, some blazar modeling suggests larger doppler factors, such as  $\delta_D \sim 30$ . This contradiction is known issue in the field.

#### 3.2.1. BL Lacertae type object

BL Lacertae (BLLac) type object is main subclass of blazar showing no emission lines in the optical band. It is believed that no gas clouds exist around the SMBH. The well known BLLac type sources are Markarian 421 and 501. They locates relatively close enough to detect with even poor sensitivity, thus it has been studied from the beginning of the gamma-ray history.

#### 3.2.2. Flat Spectrum Radio Quasar

Flat Spectrum Radio Quasars (FSRQs) are an another subclass of blazars. The optical spectra shows broad and narrow emission lines, thus it is considered that the ionized gas exists around the SMBH. Emissions from those clouds will be a seed of inverse Compton scattering. Thus the high-energy emission from the FSRQ blazars often introduce dust clouds and dust torus in the modeling and shows bright gamma-ray flux.

### 3.3. Emission models

The electromagnetic emission from blazar has "two bump" structure in the spectral energy distribution. Low-energy peak are considered as Synchrotron emission from high-energy electron. This is because the source shows polarized mission in optical band. On the other hand, the high-energy peak, which is energy above X-ray or Gamma-ray, is still controversial. The leptonic model naturally introduced in the modeling is inverse compton scattering. For BLLac sources, the synchrotron self-Compton scattering will explains the snapshot of the Spectral Energy Distribution (SED). The synchrotron self-Compton model is often called one-zone SSC.

#### 3.3.1. One-zone model

A one-zone model is often used to explain the blazar emission, especially BL Lac type objects. Among the emission models, synchrotron self-Compton (SSC) model is often used. However, the synchrotron emission from proton is also included here. The one-zone model requires some uniform single emission region despite the leptonic origin or hadronic origin. To model the emission, electron (or charged particle) distribution and environmental parameters should be given. The electrons are often modeled by a power-law distribution or distributions having additional parameters, e.g., broken power-law, log-parabola (See Appendix A). The normalization defines how many electrons exist inside the emission regions and one need to specify the energy range of electrons as shown in figure 3.2.

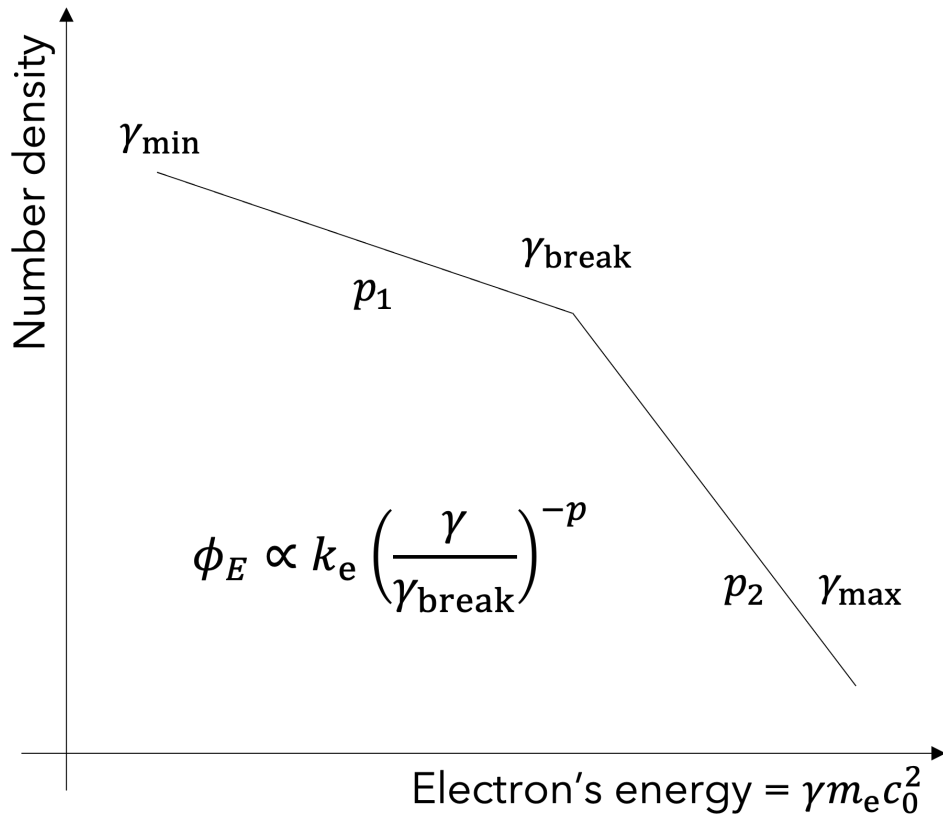


Figure 3.2: Electron distribution assumed in the emission model. In this study, it is assumed that electrons follow the power-law distribution which has a break at certain energy, called broken power-law.

The electrons are confined in magnetized spherical region at the jet rest frame, and the region is moving with relativistic speed. Thus, the magnetic field  $B$ , the emission region scale  $R_{blob}$ , and bulk Lorentz factor  $\Gamma_{Bulk}$  characterize the emission region as shown in figure 3.3.

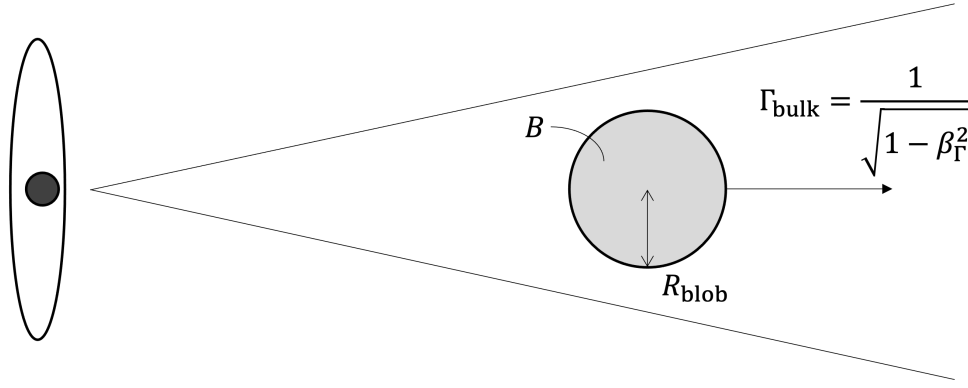


Figure 3.3: Relativistic jet and emission region. The emission region exists inside the jet, and filled by electron as shown in figure 3.2.

Though the Doppler boosting factor  $\delta_D$  is defined in equation 3.1, the observing angle  $\theta$  is unknown in most cases. Thus we assume the ideal observing angle  $\theta$  to satisfy  $\Gamma_{\text{Bulk}} \sim \delta_D$ . The apparent effects are summarized in figure 3.4.

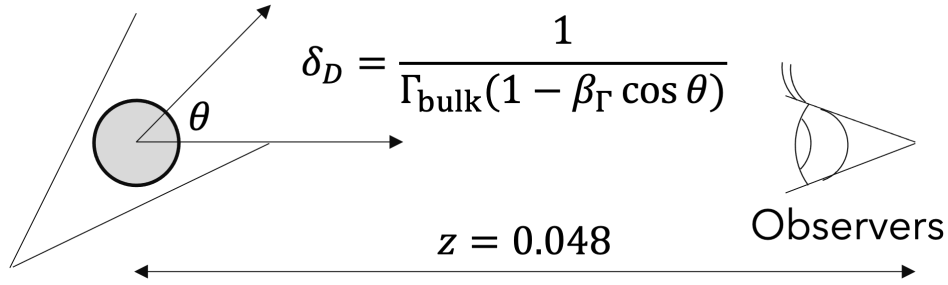


Figure 3.4: Doppler effect. Emission from the region inside the jet will be boosted by Doppler factor  $\delta_D$ . Redshift also affects in the observation, but it is small enough if it is compared with Doppler boosting.

The minimum parameters are  $k_e$ ,  $E_{\min} = \gamma_{\min} mc^2$ ,  $E_{\max} = \gamma_{\max} mc^2$ ,  $p$ ,  $B$ ,  $\delta$ ,  $R$ . Those parameters degenerate each other; thus, one needs to constrain some of those parameters.

Figure 3.5 represents how the one-zone SSC model change its shape and normalization. Some parameters have similar dependency for the apparent spectral shape, thus modeling is not easy.

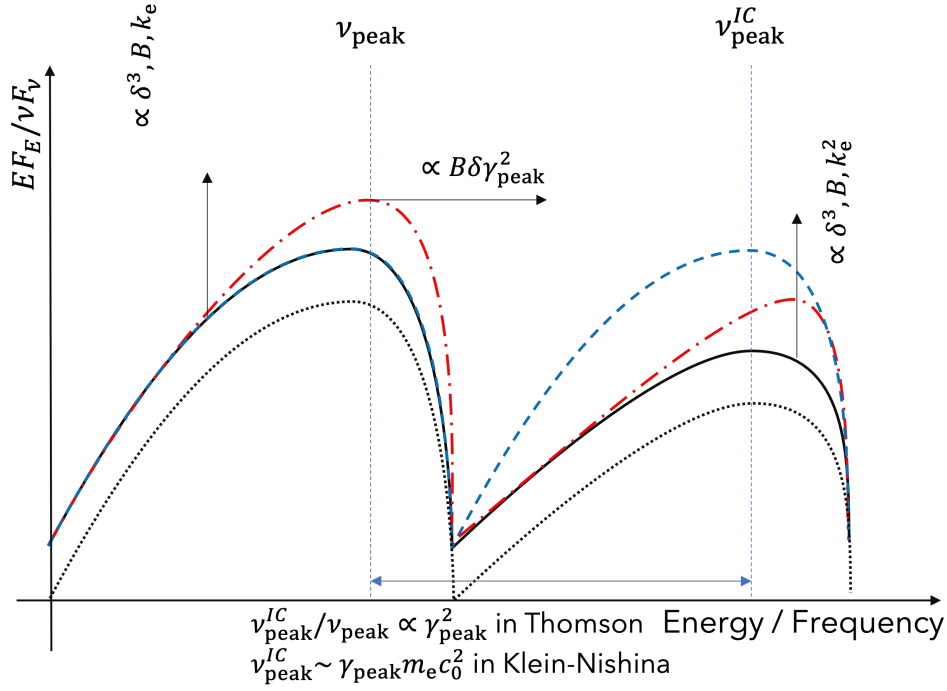


Figure 3.5: One-zone SSC model with modeling parameters. Dependencies of spectral normalization and shape on modeling parameters are shown. Magnetic field  $B$ , Doppler factor  $\delta_D$ , and the electron density  $k_e$  would change normalization. Magnetic field  $B$  and Doppler factor  $\delta_D$  shifts whole spectra. Relation between synchrotron peak and inverse Compton peak are also shown. Lines show patterns of possible variability. Red dotted-dashed line represents variability around the peaks, blue dashed line demonstrates the variability changing a ratio between low-energy and high-energy bump. black dotted line indicates the variability in a flux normalization

### 3.3.2. Complex models

At some blazars, the one-zone model does not work well. Therefore, more complex models assuming several regions are introduced. Furthermore, in the modeling of FSRQs, the additional photon fields are considered to explain the emissions (Hayashida et al., 2012). Ionized gas clouds become the source of low-energy photons, then those photons are scattered by the electrons inside the jet. It enables constraining the circumstance materials around the SMBHs. However, those intense photon-field work as gamma-ray absorbers, and the observed gamma-ray flux is reduced.

Another model is the spine-sheath model. The jet has a layer structure, so-called spine, and sheath. The inner jet, the spine, is faster than the outer jet, the sheath. Both layers make synchrotron emissions and produce inverse Compton scattering each other. The strong motivation for introducing the spine-sheath model is the observation of Radio galaxies by the VLBI technique (Hada, 2017). The edge-bright structure suggests that internal structure exists inside a jet.

Although there are several reasons to introduce complex model to explain the emission of blazars, the modeling is still challenging without many assumption. This is because the number of parameters easily increase by considering additional components.

### 3.4. Typical TeV Blazars

There are few well-known blazars in TeV band. In this section, I will introduce most famous blazars, Markarian 421 and 501. They are good object because they were quite deeply studied.

Markarian 421 is the closest blazar and has been discovered in VHE gamma rays in 1992. Figure 3.6 shows long-term averaged spectral energy distribution (SED) reported in [Abdo et al. \(2011a\)](#). The spectrum has straight slope from radio to optical, and low-energy peak locates around a few keV. The high-energy peak consists from GeV and TeV gamma rays. One-zone SSC model succeeded to explain the emission.

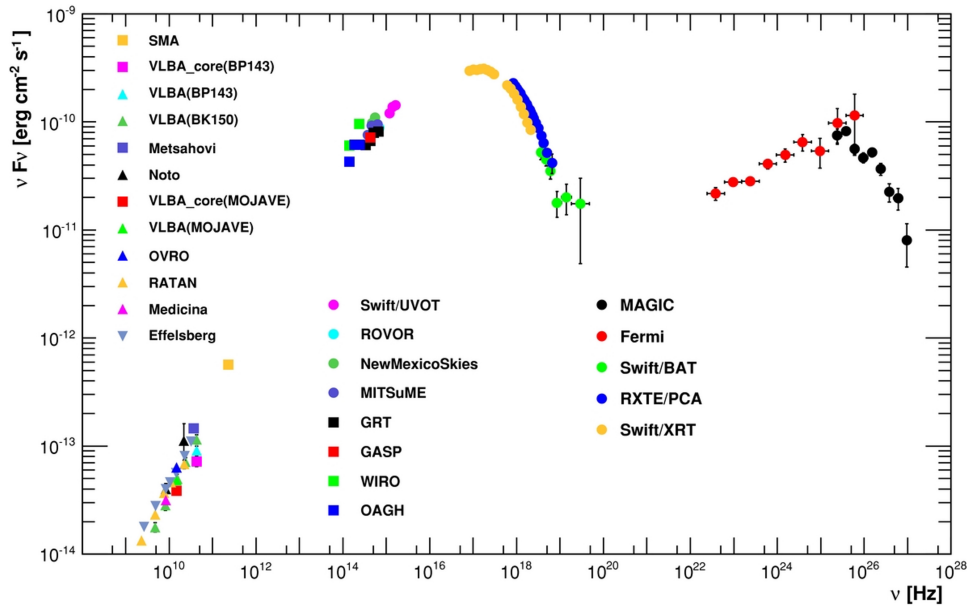


Figure 3.6: Averaged spectral energy distribution of Markarian 421 ([Abdo et al., 2011a](#)). Whole emission can be characterized with two bumps.

However, a gamma-ray flare which is not naturally expected from one-zone SSC was observed in [Acciari et al. \(2011\)](#). Figure shows multiwavelength (MWL) light curves in [Acciari et al. \(2011\)](#). X-ray and Gamma-ray light curves showed strong independent flaring period individually.

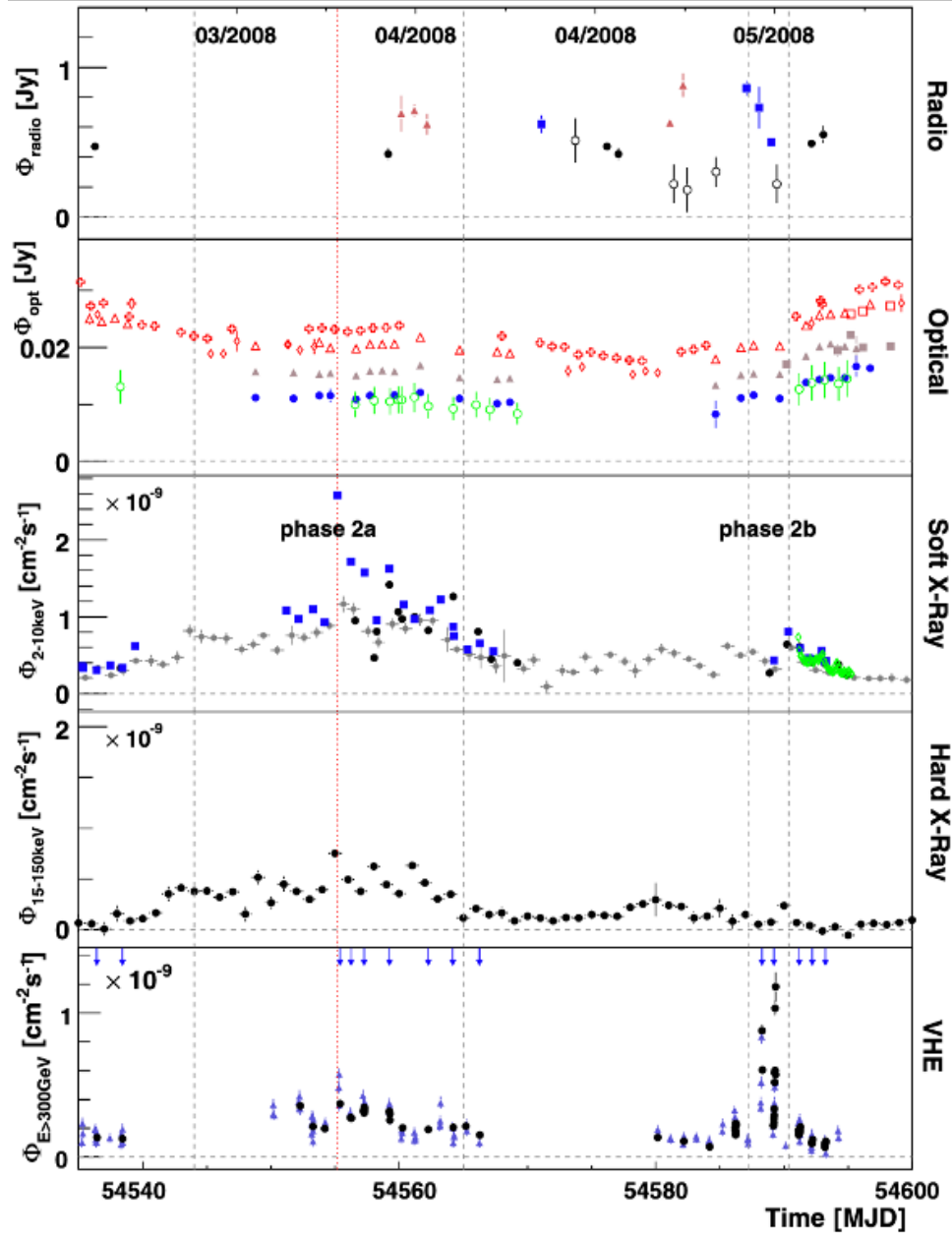


Figure 3.7: Multiwavelength light curves for several months (Acciari et al., 2011). X-ray and Gamma-ray light curves showed flaring episodes individually. In phase 2a, X-ray light curve showed flaring episode while VHE gamma-ray showed a flare alone in phase 2b.

Markarian 501 is the second closest TeV blazar discovered in VHE range in 1996. Figure 3.8 shows MWL SED published in Abdo et al. (2011b). It can also be explained with one-zone SSC model except thermal emission at optical band. It is called big blue bump, and believed that emission comes from accretion disks.



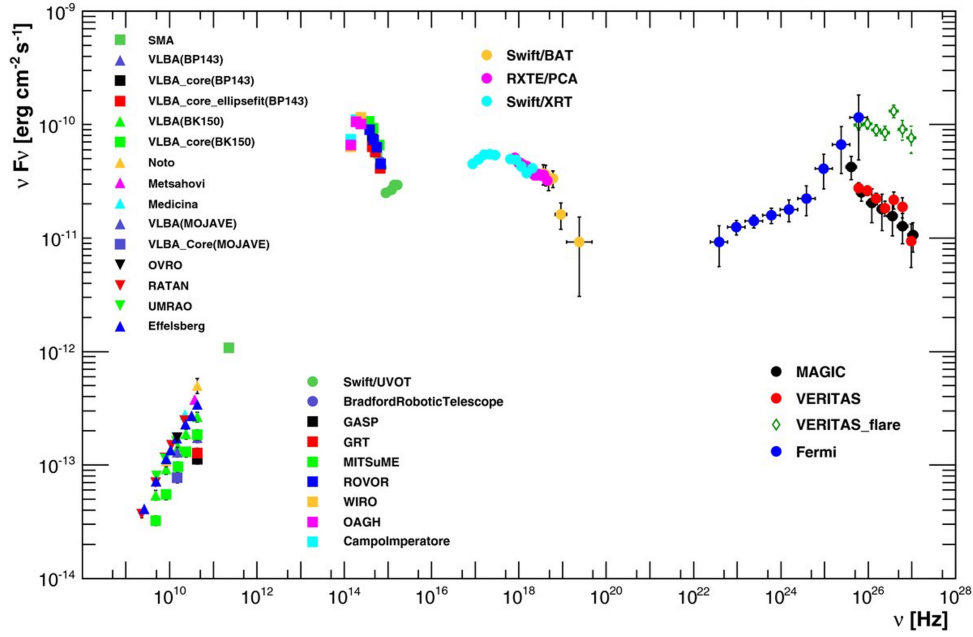


Figure 3.8: Averaged spectral energy distribution of Markarian 501 (Abdo et al., 2011b). Whole emission can be characterized with two bumps with a thermal emission at optical band. It is considered as emission from accretion disk around SMBH.

For Markarian 501, unusual structure in TeV spectra was found (MAGIC Collaboration: et al., 2020). One possible scenario is the pile up in the electron distribution. It is not found in the other sources.

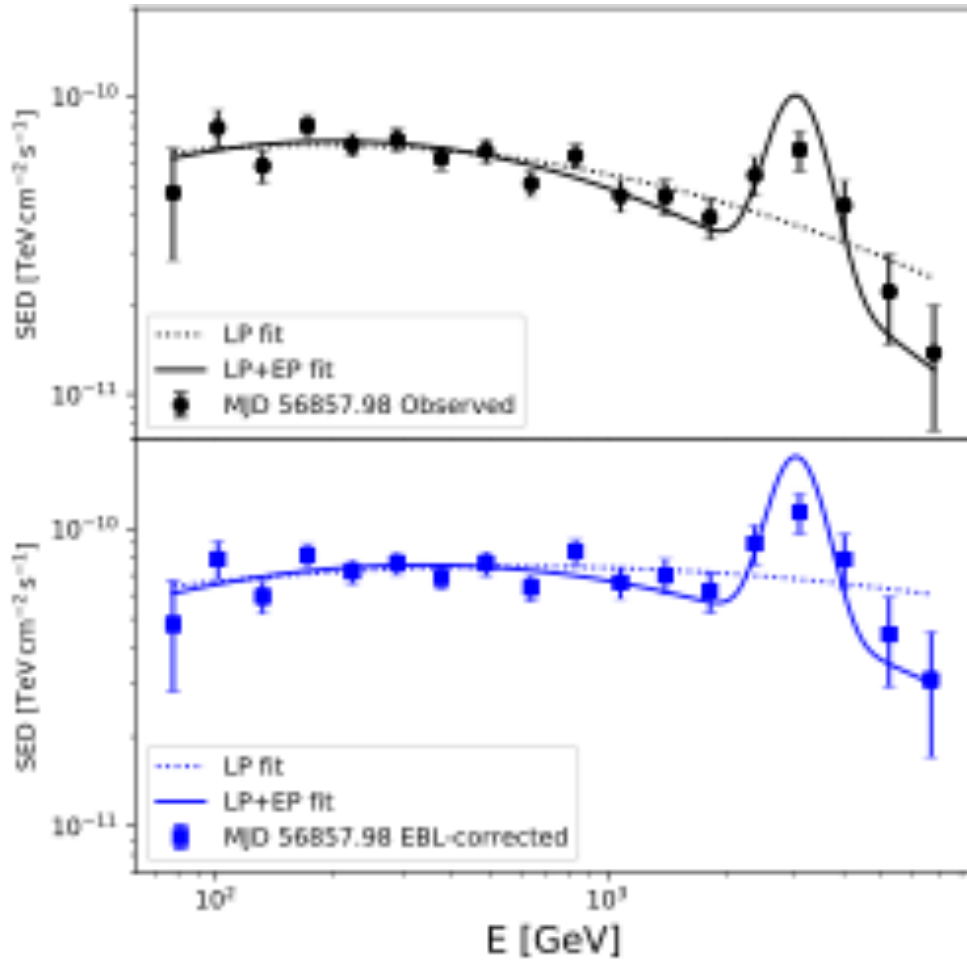


Figure 3.9: Spectral energy distribution of Markarian 501 at X-ray maximum state in 2014 (MAGIC Collaboration: et al., 2020). Narrow peak structure appeared in TeV spectra

As shown in the above, the classical TeV blazar was successfully modeled with a simple, one-zone SSC emission model. But some recent observation showed unexpected result with the simple SSC model. The one-zone SSC model has to be modified or complex model should be introduced as a standard emission model.

**Part II.**  
**Study of VHE Gamma-ray Emission**  
**from Active Galactic Nucleus**  
**1ES 1959+650 with the MAGIC**  
**telescopes**

## 4. Motivation

Blazar has been studied since about 30 years ago with TeV gamma-rays. This is because TeV gamma-ray is critical energy band for the near blazars, such as BL Lac type object, and blazars are most dominant source in the TeV gamma-ray sky.

Historically, blazars were detected when flares happen, and a one-zone SSC model worked well for a short-term data. However, as discussed in the previous section, we might need to modify the simplest model to explain the anomalies in observations.

One solution is introducing a complex model. Complex model such as two-zone model can explain data better than one-zone SSC (MAGIC Collaboration et al., 2020a). However, the complex model requires more information than one-zone model, thus the observation will be challenging. How about the hadronic models? Although IceCube detected neutrino coinciding a gamma-ray flare from TXS0506, no clear conclusion was obtained regarding the hadronic model Cerruti et al. (2018). The pure hadronic model seems to be constrained by x-ray flux, and it seems hadronic component is not dominant contribution in the emission. Many research are trying to propose a reasonable emission model, but no clear answer was obtained thus far.

Including temporal variability might be able to improve situation in the blazar modeling. In the current modeling, only some paper tries time-dependent spectral modeling, especially for short-term data (e.g., Asano & Hayashida (2018)). Moreover, taking long-term data is also difficult due to the instrumental sensitivity. However, 1ES 1959+650, one of the bright blazar was monitored by MAGIC during past five-years. Quick look of the monitoring data showed interesting flux correlation with X-ray and Gamma-ray, This allow us to discuss temporal evolution of the source.

I considered this is a good chance of testing long-term variability with spectral model. Thus I tried MWL modeling with MAGIC VHE-gamma ray data considering with Multiwavelength (MWL) temporal behaviors.

## 5. 1ES 1959+650

1ES 1959+650 is a BL Lac-type object known as a classical TeV blazar. The source was discovered in the *Einstein* Slew Survey reported by Elvis et al. (1992), and the source was later identified as BL Lac object (Schachter et al., 1993). In the VHE gamma-ray band, Utah Seven Telescope Array detected the source in 1993, and HEGRA confirmed it in 2001 (Nishiyama, 1999; Horns, 2003).

The source has been historically studied as a typical source in TeV gamma-ray sky and a hadronic source candidate. This section will introduce basic properties and previous studies as prior knowledge of this research.

### 5.1. Distance, Location, and Central core

1ES 1959+650 is one of the second brightest gamma-ray sources in the northern hemisphere. The coordinate is RA of 19:59:59.85 and DEC +65:08:54.65 in the J2000 coor-

dinate, and this corresponds to the galactic longitude 98.00 deg and the galactic latitude 17.67 deg. Due to its location, the source is only observable in summer with ideal conditions from the northern hemisphere.

The distance to the source is a redshift  $z = 0.048$ , reported by [Perlman et al. \(1996\)](#). The central mass of the core object is about  $10^8 M_{\text{sun}}$ , according to previous studies, e.g., [Wu et al. \(2002\)](#).

As shown in Figures 5.1, its optical spectra have no emission lines known as BL Lac-type objects. Some absorption lines are due to the atmosphere, which is not intrinsic. This is because continuum emission from the jet is too bright and hides emissions from the host galaxy. In addition, featureless spectra indicate no foreground matters for the optical line emission, such as ionized clouds.

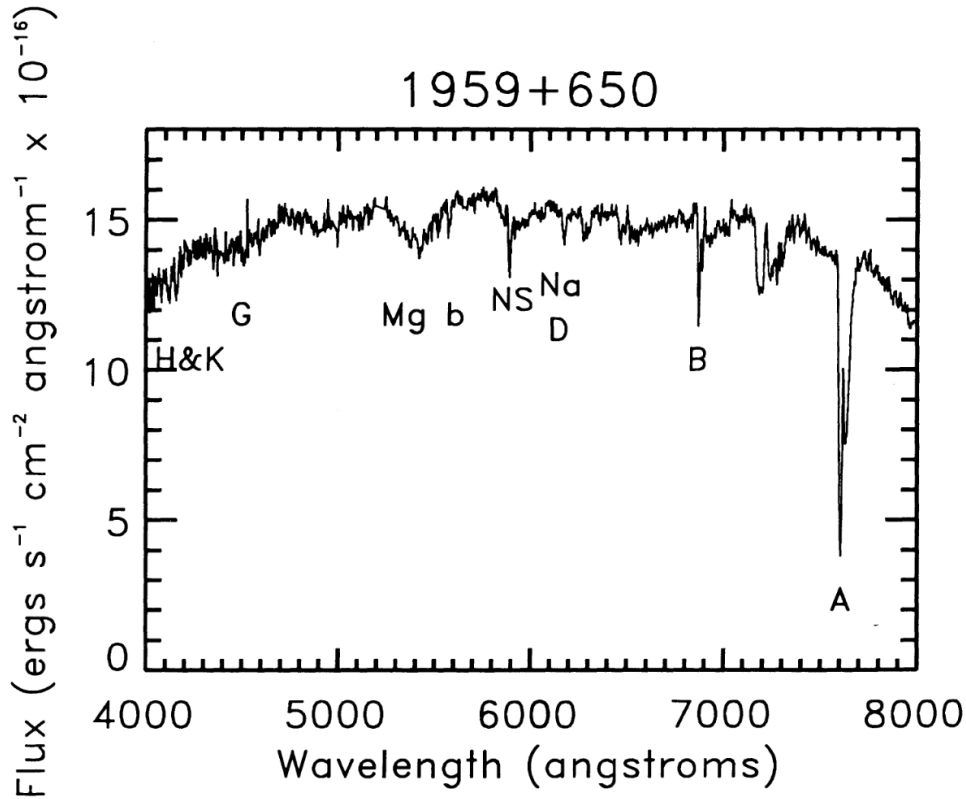


Figure 5.1: Spectra from [Schachter et al. \(1993\)](#).

## 5.2. Morphology

The jet structure was measured by VLBA between 2008 and 2009 at 43 GHz ([Piner et al., 2010](#)) and also in 1999 and 2000 at 15 GHz ([Piner et al., 2008](#); [Piner & Edwards, 2004](#)). Two circular components were found in the observation, and the apparent speed of one of the components, C2, was measured, as shown in figure 5.2. The apparent speed is  $0.1c$  during ten years, and no counter jet has been confirmed thus far.

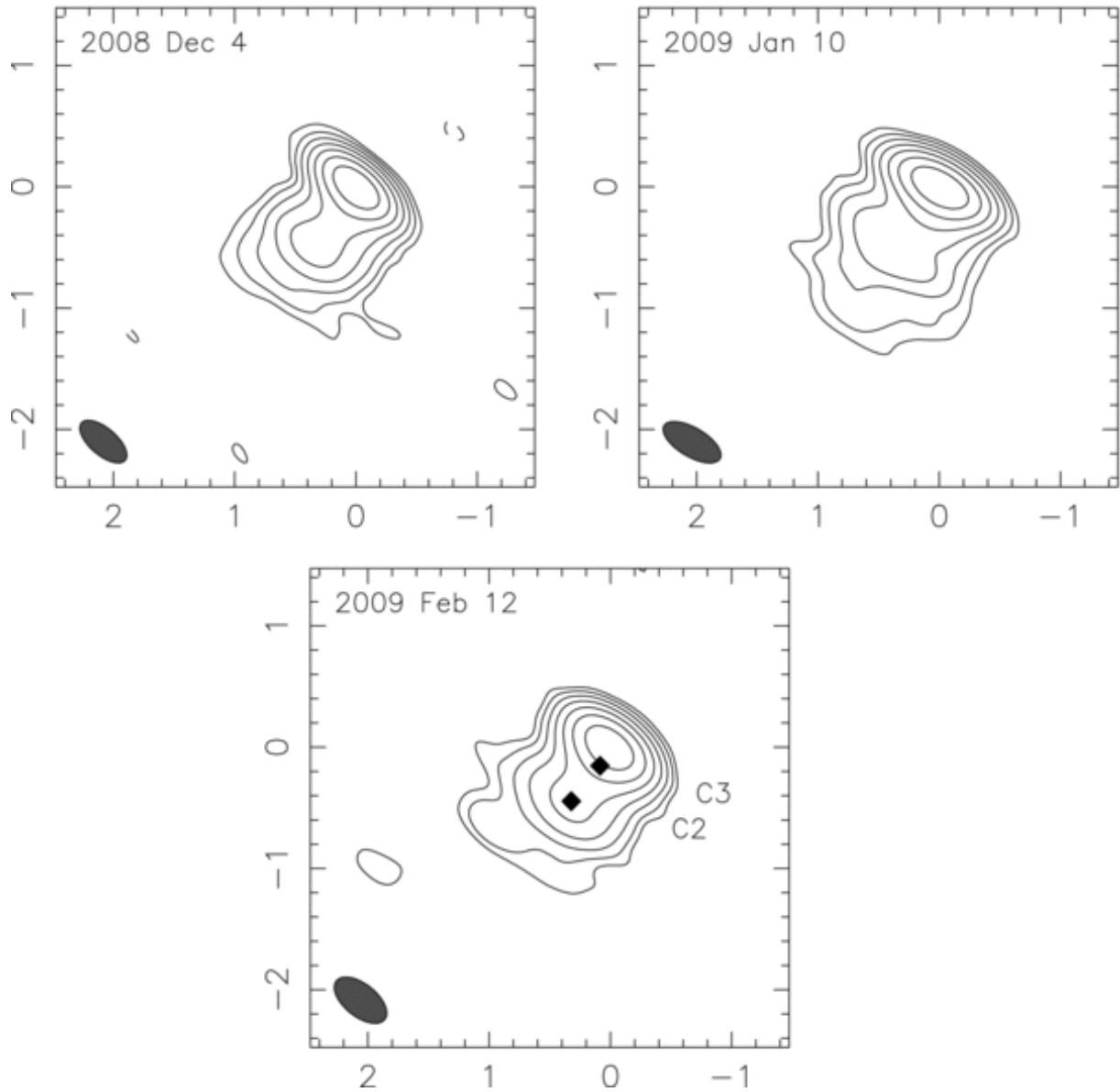


Figure 5.2: Radio morphology (Piner et al., 2010). No counter jet was observed.

The source is not currently monitored by the VLBI campaign. So no latest morphological information from radio observation.

### 5.3. Neutrino observation

The source was tested as a hadronic origin historically. This is because AMANDA has reported two neutrino candidates from the direction of 1ES 1959+650 coinciding with the orphan gamma-ray flare (Bernardini, 2005). The significance of the two events is low, but they led the discussion for the hadronic emission model. Later, in response to the 2016 flare, another neutrino search has conducted using IceCube data, although no significant

excess was found (Kintscher et al., 2017).

## 5.4. Past multiwavelength campaigns

Several multiwavelength studies have been conducted since its discovery.

In 2002, the source showed the prominent VHE gamma-ray flare above 600 GeV and 2 TeV. The flux reached three times higher than Crab Nebula in VHE gamma-ray band. However, the X-ray flux did not change coinciding with the VHE flare. This gamma-ray flare was named Orphan flare and it had led several discussion about the mechanism (Krawczynski et al., 2004). On top of that, neutrino candidate reported from AMANDA. At that time, orphan flare is unique property of the 1ES1959+650, however similar features were found in the other sources later (e.g., Acciari et al. (2011)). This behavior is not expected well by the simple one-zone model.

After the 2002 flare, the third generation IACTs were built and took over the observation. However no remarkable events were found until the source showed flare in 2016.

MAGIC telescope reported three times Crab Nebula flux above 300 GeV in 2016 (MAGIC Collaboration et al., 2020b). The source showed quite hard spectra in both Gamma-ray and X-ray band. At that time, VERITAS and FACT also reported the increased flux.

This study is connected period including the 2016 data. Thus it is also tried to understand nature of the 2016 flare.

Concerning the spectral modelings in previous studies, I summarized the modeling parameters in the table 5.1 and 5.2. One can see that there are many combinations of the parameters to explain the emission.

Table 5.1: One-zone SSC phenomenological parameters in previous studies.

Model	$B$	$R$	$\Gamma$	$\theta$	$\delta$
—	[G]	$[\times 10^{15} \text{cm}]$	—	[deg]	—
MAGIC Collaboration et al. (2020b)	0.10 to 0.25	0.7 to 1	—	—	40 to 60
MAGIC Collaboration et al. (2020b)	0.2 to 0.4	0.8 to 1	—	—	30 to 50
MAGIC Collaboration et al. (2020a)	0.06	7.2	—	—	41
MAGIC Collaboration et al. (2020a)	0.06	5.5	—	—	30
MAGIC Collaboration et al. (2020a)	0.07	4.3	—	—	31
Tagliaferri, G. et al. (2003)	0.9	9	14	3.1	17.8
Tagliaferri, G. et al. (2003)	0.8	9	14	3.1	17.8

Table 5.2: One-zone SSC's electron parameters in previous studies.

Model	$\gamma_{\min}$ [ $\times 10^3$ ]	$\gamma_{\text{break}}$ [ $\times 10^5$ ]	$\gamma_{\max}$ [ $\times 10^6$ ]	$n_1$	$n_2$
—	—	—	—	—	—
MAGIC Collaboration et al. (2020b)	0.7	4 to 10	1 to 7		
MAGIC Collaboration et al. (2020b)	0.3 to 0.7	1 to 5	1 to 7		
MAGIC Collaboration et al. (2020a)	0.4	0.07	0.45	1.98	2.7
MAGIC Collaboration et al. (2020a)	0.5	0.6	0.80	2.0	2.85
MAGIC Collaboration et al. (2020a)	1.0	0.6	1.5	1.95	2.8
Tagliaferri, G. et al. (2003)	12	0.4	—	3.8	—
Tagliaferri, G. et al. (2003)	7.0	0.5	—	3.6	—

Figure 5.3 shows spectral energy distribution in Backes (2012). Comparing with Markarian 501 and 421, the spectral shape of high energy component looks flat. This is not normal if we consider inverse Compton emission from electrons. Thus two-zone emission model was also proposed to explain the SED.

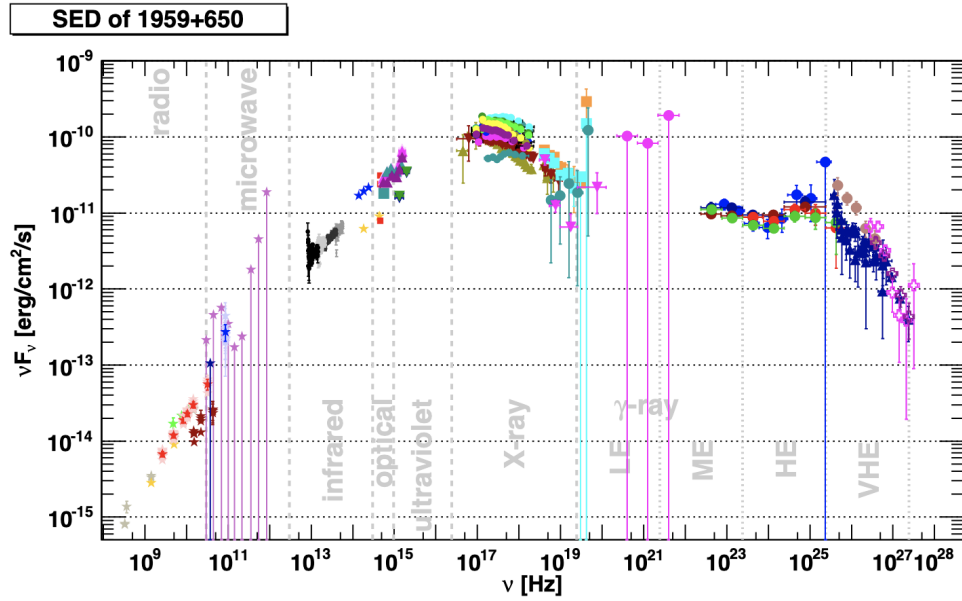


Figure 5.3: Spectral energy distribution reported in Backes (2012)



## 6. Major Atmospheric Gamma Imaging Cherenkov Telescope

### 6.1. Observation principals

When high-energy particles enter the atmosphere, they interact with atmospheric nuclei and are absorbed or decay before they reach the ground. Therefore, a technique using secondary particles produced from primary particles was developed and is now in use. This section describes the properties of these secondary particles, known as extensive air shower (EAS), and their relevance to gamma-ray observations.

#### 6.1.1. Electromagnetic shower

First, consider the case in which the primary particles are gamma rays. If gamma rays arrive on earth, they interact with the nuclei in the air. When the particles are sufficiently energetic, the electron-positron pair production becomes dominant. The electrons produced are also high energy enough and radiate bremsstrahlung by the electric field of the air nucleus.

As those two reactions are repeated, the number of particles doubles per a reaction, producing a population of charged particles and gamma rays. The phenomenon is called an electromagnetic (EM) shower, and the one triggered by gamma rays or electrons is known as an electromagnetic shower. The shower development continues as long as those two interactions are dominant. The minimum energy for the interaction is called critical energy, roughly 86 MeV for electron bremsstrahlung and roughly 1MeV for pair production. As shown in figure 6.1, the interaction length of bremsstrahlung and pair creation differs by just a factor of 9/7. Thus simple shower development model known as Heitler model can explain the EM shower development (Matthews, 2005).

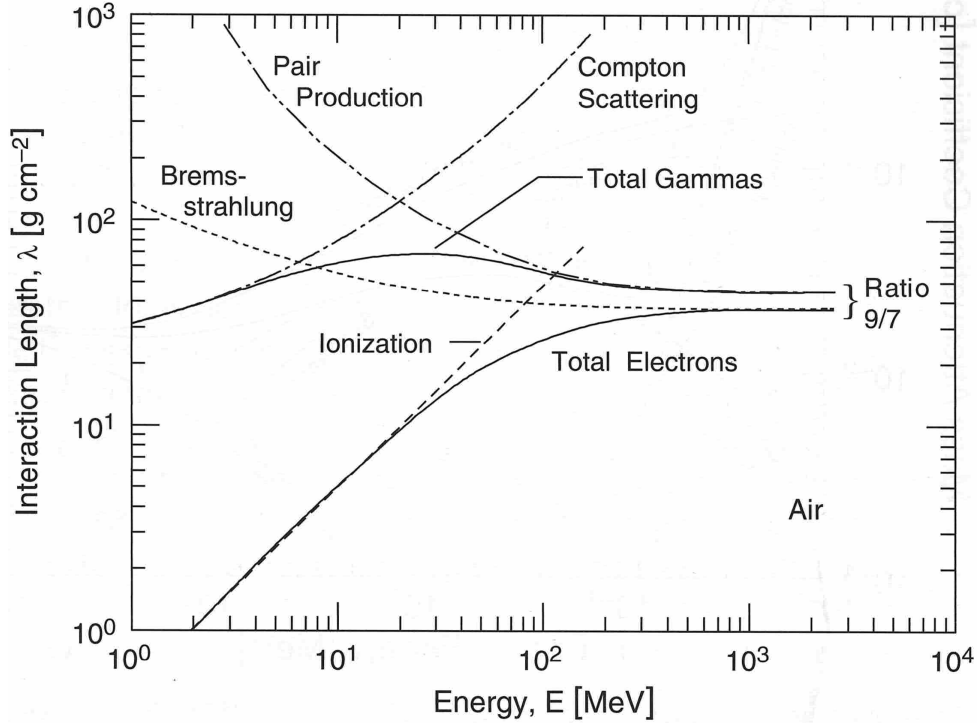


Figure 6.1: Interaction length of photons and electrons. Bremsstrahlung and pair production shows similar interaction length at higher energy.

### 6.1.2. Hadronic shower

Extensive air shower initiated by cosmic-rays are called hadronic shower. Because of the interaction relating strong interaction, the various kinds of particles are produced. The dominant particles are pions, and they decay into muons and electrons later. Many body interaction make transverse momentum, thus EAS has wider structure than the EM shower. This difference enable us distinguish the EM shower and hadronic shower from the cherenkov image observed by the imaging telescope. Figure 6.2 shows simulated EM shower and hadronic shower. One can see small shower inside the hadronic shower, they sometime mimic the EM-shower like signal for the telescope. Thus event classification is important to remove the cosmic-ray induced backgrounds.

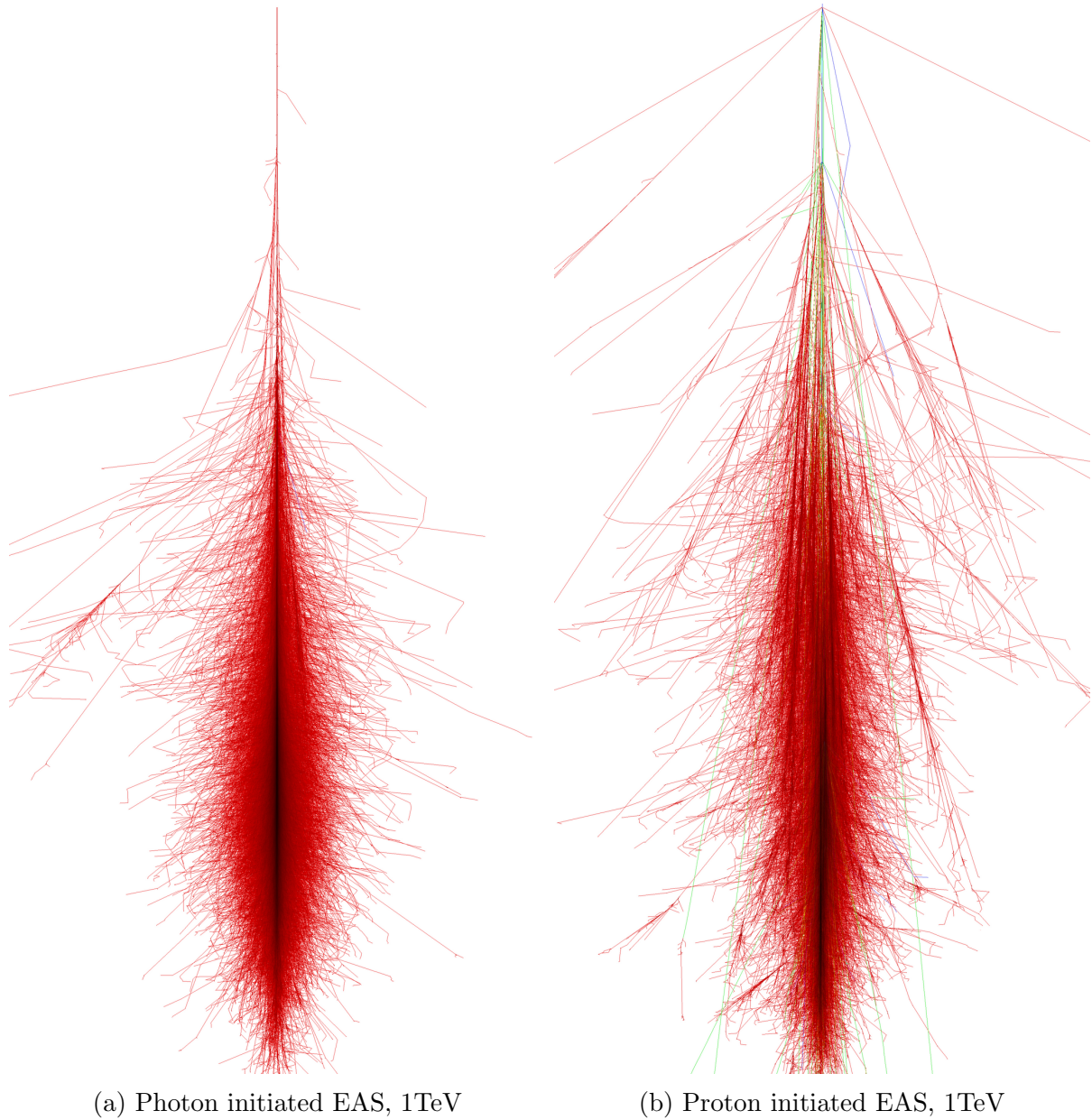


Figure 6.2: Simulated EAS initiated by photons and protons, Credit: <https://www.iap.kit.edu/corsika/>

### 6.1.3. Atmospheric Cherenkov light

As discussed in the previous section, charged particle faster than the speed of light in the matter radiate cherenkov radiation. Because the atmosphere has a structure, the refractive index also vary on the altitude. Figure 6.3 shows the cherenkov angle dependency with various altitude. The cherenkov light emitted at shower maximum ( $\sim$  altitude 10 km) and near the ground have different Cherenkov angle, thus this will make a shower image on the telescope camera.

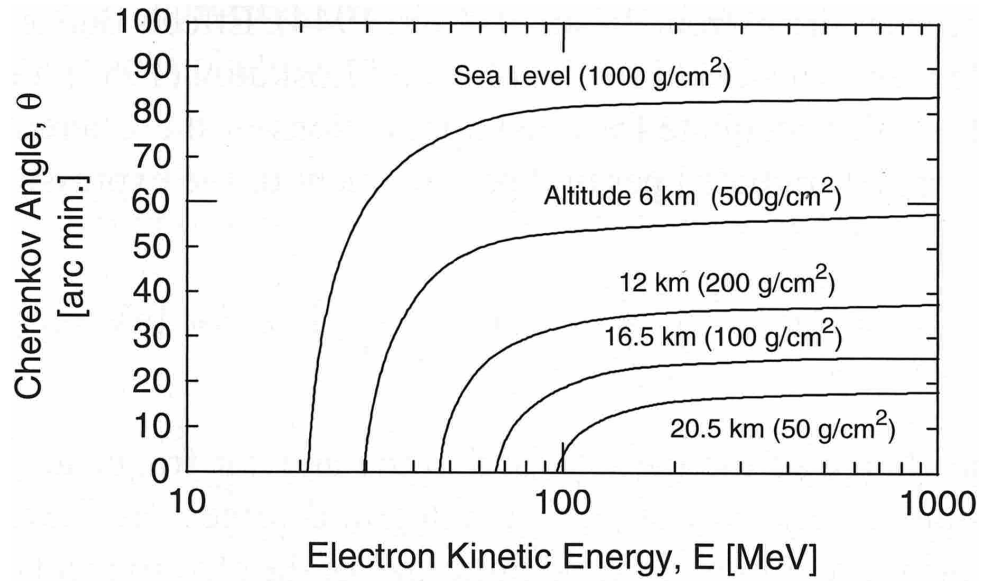


Figure 6.3: Cherenkov angle

Detecting those cherenkov light by telescope, one can detect gamma rays from the ground.

## 6.2. Instrument

Figure 6.4 shows Major Atmospheric Gamma Imaging Cherenkov (hereafter MAGIC), an Imaging Atmospheric-Cherenkov Telescope (IACT) facility. The MAGIC is composed of two 17-m diameter telescopes, which are MAGIC I and MAGIC II. Both telescopes locates at 2200 m above sea level and the Roque de los Muchachos Observatory (ORM) in the Canary Islands, Spain. MAGIC contributes to the VHE gamma-ray astronomy with H.E.S.S. and VERITAS experiments ([Hinton, 2004](#); [Krennrich et al., 2004](#)).



Figure 6.4: MAGIC telescopes. MAGIC II locates in the front, and MAGIC I locates in the back. MAGIC I was built in 2004, and MAGIC II was built in 2009. Both telescopes were upgraded to uniform their performance in 2011 - 2012 (Aleksić et al., 2016a).

The key features of MAGIC are a large-area reflector, a high-sensitivity camera, and high-speed slewing. Those features were designed to detect emissions of Gamma-Ray Bursts (GRB) from the ground. This section introduces the components of MAGIC telescopes used in this study.

### 6.2.1. Reflector

The 17-m diameter reflector comprises more than 200 segmented mirrors arranged following the parabolic shape. The diameter is larger than H.E.S.S. and VERITAS telescopes because MAGIC aims to observe a faint Cherenkov light, whose intensity decreases depending on the incident gamma-ray energy. Figure 6.5 shows the sketch of reflecting light by a parabolic reflector.

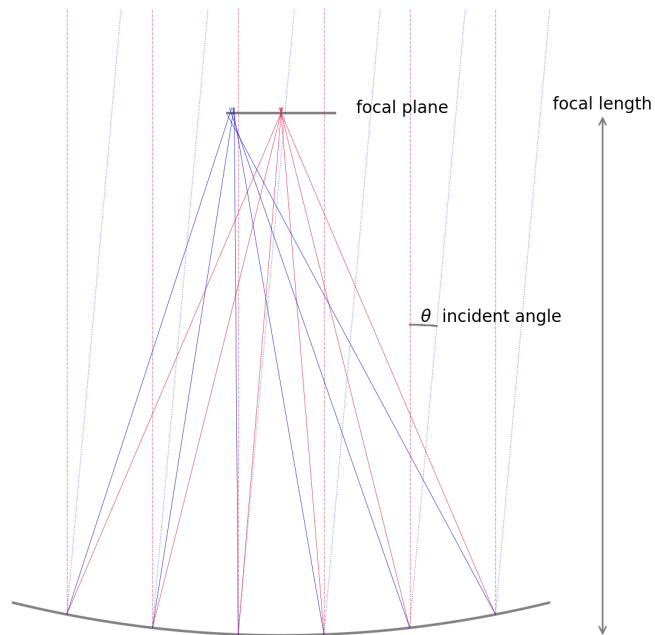


Figure 6.5: Sketch of parabolic reflector and reflected light. The focusing point of incident light with offset angle  $\theta$  is displaced from the center. Thus Cherenkov light emitted from the different heights will be focused at the different positions on the focal plane (camera).

The light parallel to the telescope axis is focused onto the center of the PMT camera. If the light incidents with angle  $\theta$ , the focus position is displaced from the center. Where  $f$  is the focal length of each spherical segmented mirror,  $f = 1.03D$ , and  $D$  is the reflector's diameter. Thus, the reflector works as a converter between the incident angle and camera position. It explains that the Cherenkov image from the EAS will make an elliptical shape on the focal plane because the light emitted at different heights enters with different incident angles.

### 6.2.2. PMT Camera

The Cherenkov light focused by the reflector is converted into an electric signal with Photo Multiplier Tube (PMT) camera, as shown in figure 6.6. Cherenkov light from the EAS is very faint and fast (a few ns width). Moreover, the background light from stars



and the moon (Night Sky Background light, NSB) continuously enters the PMTs. Their relative contribution will increase when the telescope observes low-energy gamma rays. To remove the NSB noise efficiently, MAGIC stores waveforms of PMT signals as raw observational data. The photon converted into an electron (called photo-electron) at the surface of PMT is sent to the trigger electronics and Data acquisition (DAQ) electronics after the amplification inside PMTs.

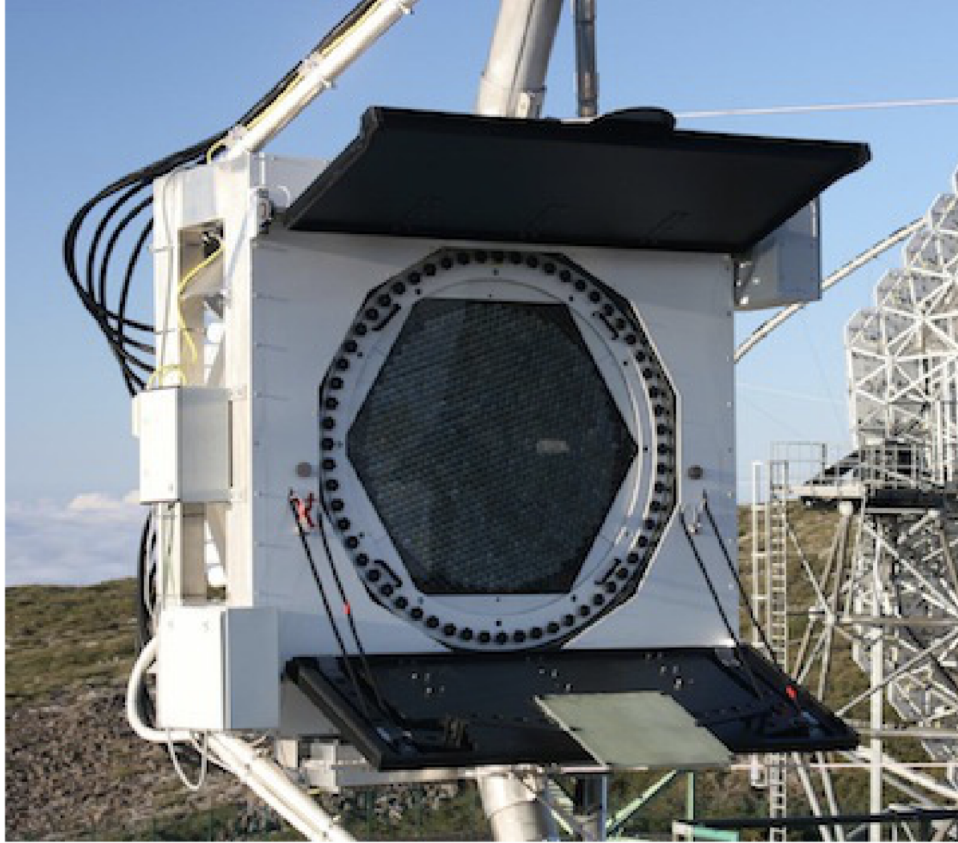


Figure 6.6: MAGIC I Camera, PMT Camera consists of 1039 PMTs (Nakajima et al., 2013).

### 6.2.3. Event Trigger and Data Aquisition

The signals sent from the PMT camera are divided into two pathways. The one goes to a trigger circuit, which decides if data is saved, and the decision is based on the signal intensity of several pixels. Figure 6.7 shows the camera pixels and areas used in the trigger.

The standard triggering algorithm is called Nearest Neighbor (NN) method. The algorithm judges whether the nearest pixel's sum exceeds the predefined limit (roughly four photo-electron) for available pairs inside each hexagonal area, as shown in figure 6.7. MAGIC uses three neighbors for the standard observation. Once specific pixels satisfy the threshold, an event trigger is issued. A data acquisition electronics receiving the event

trigger start saving waveforms (Tridon et al., 2009).

The waveforms on the whole camera are kept on the sampling circuit, DRS4 Ritt (2008), for a short moment. The chip was developed for the MEG experiment ??, and conducting GHz waveform sampling. MAGIC DAQ system adopts a 1.64GHz sampling frequency to sample data. As soon as DAQ electronics receive the event trigger, waveforms kept in DRS4 chips are sent to ADC and recorded to the storage disk. In the end, data analysis can be performed.

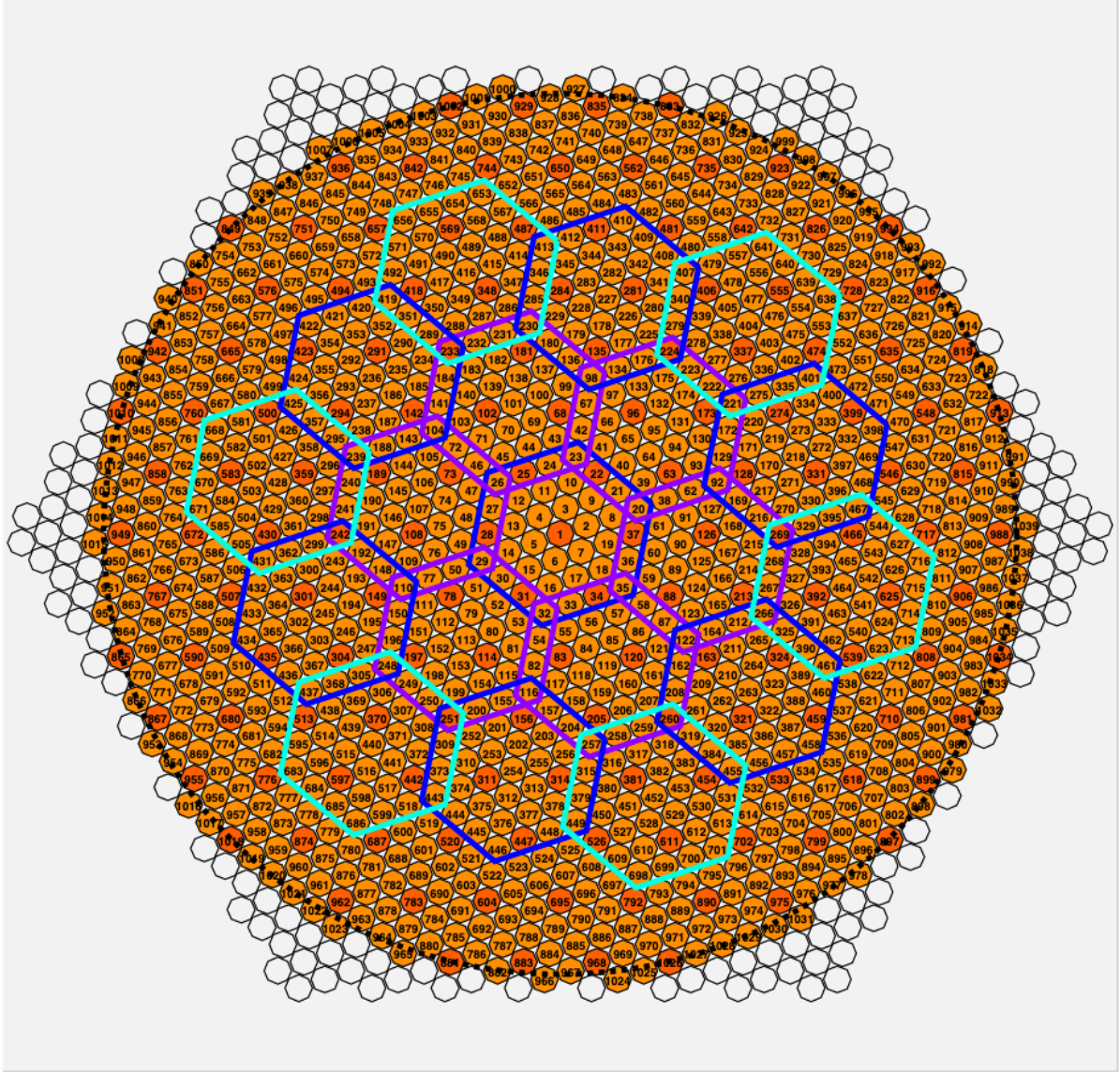


Figure 6.7: MAGIC I Camera pixel arrangement and triggering regions. Blue, cyan, and purple hexagons are each triggering region. Overlapping pixels are used in each region(Cortina et al., 2009).



### 6.2.4. Auxiliarily systems

In this subsection, I introduce the MAGIC subsystems that play an important role in the analysis. It does not directly participate in the data taking, but it is critical for taking good quality data.

**Calibration laser** MAGIC equipped the laser for the camera calibration at the center of the dish (Schweizer et al., 2002). The events taken with the calibration laser are used to correct the PMT gain. During the observation, the interleaved calibration events are taken, and a dedicated run is taken before the observing a specific source. Those events are used to compute the conversion factor from the ADC count to the number of photo-electrons.

**LiDAR** MAGIC has a hand-made LiDAR (abbreviation of Light Detection And Ranging) to determine an atmospheric transmittance. MAGIC LiDAR can extract atmospheric conditions by measuring Rayleigh scattering light. During MAGIC observations, LiDAR observes the point close to the source which MAGIC observes. Figure 6.8 shows a sketch of the MAGIC LiDAR. LiDAR shoots a laser pulse every 5 mins, with a 1000 Hz frequency.

From the distribution of the collected light, one can estimate the absorption coefficient at arbitral height from the MAGIC site. MAGIC analysis currently implements energy correction using the LiDAR measurement. However, I did not use the correction in the later analysis step because most of the data in 2016 had no valid lidar information.

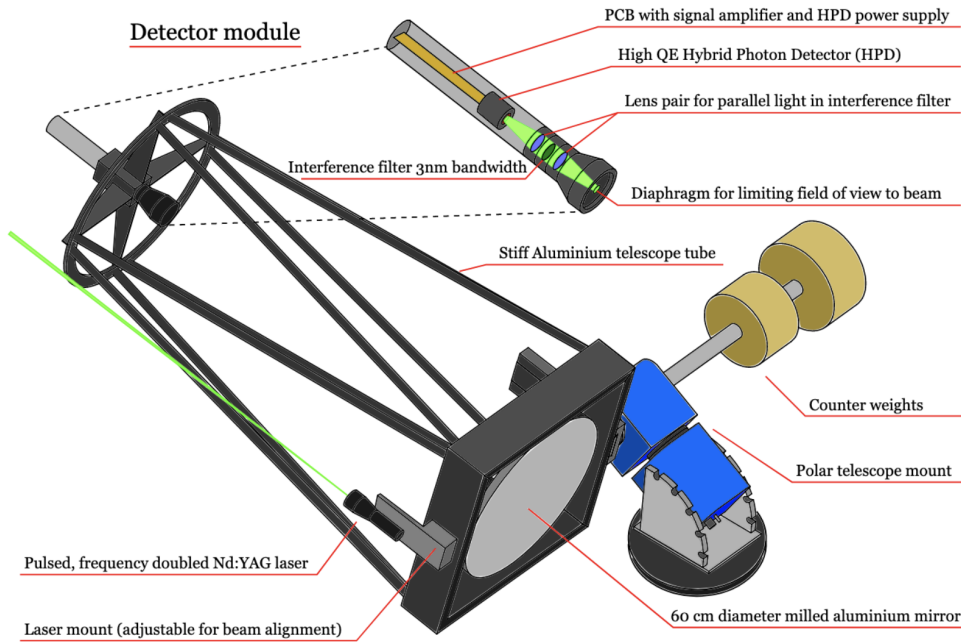


Figure 6.8: MAGIC LiDAR. It able to measure an atmospheric transmittance by collecting Rayleigh scattering light emitted from the Nd:YAG laser (Fruck et al., 2014).

The computation of the aerosol transmittance from the observation site is done at the `quate` program. See section 7.1.2 for details.

**Starguider camera** To correct the actual pointing position, the star guider camera at the center of the reflector dish observes the night sky continuously. In this study, I used the number of stars to select good-quality data when LiDAR was not correctly working. It is based on my assumption that if the sky is not clear, observed stars changes. The wavelengths of Cherenkov light and light observed by the star guider camera are not identical. Therefore the number of stars is not a physically meaningful parameter, but it is helpful to perform rough data selection. See a detailed study regarding the selection using the number of stars.

### 6.2.5. Performance

This section provides an instrumental performance of the MAGIC telescopes. However, the performance of the atmospheric Cherenkov telescope is strongly affected by the zenith angle and analysis method as described in the later section. Thus, the standard performance for low zenith observation is mentioned in the following sections.

**Energy bias and resolution** The energy range of MAGIC telescopes is about 50 GeV to 20 TeV for the low-zenith standard analysis. However, the very large zenith observation can raise the upper energy limit to 100 TeV (MAGIC Collaboration et al., 2020c). After the parameter cut, the lower energy threshold rises to about 75 GeV. The peak of survived gamma-ray energy distribution defines this analysis threshold.

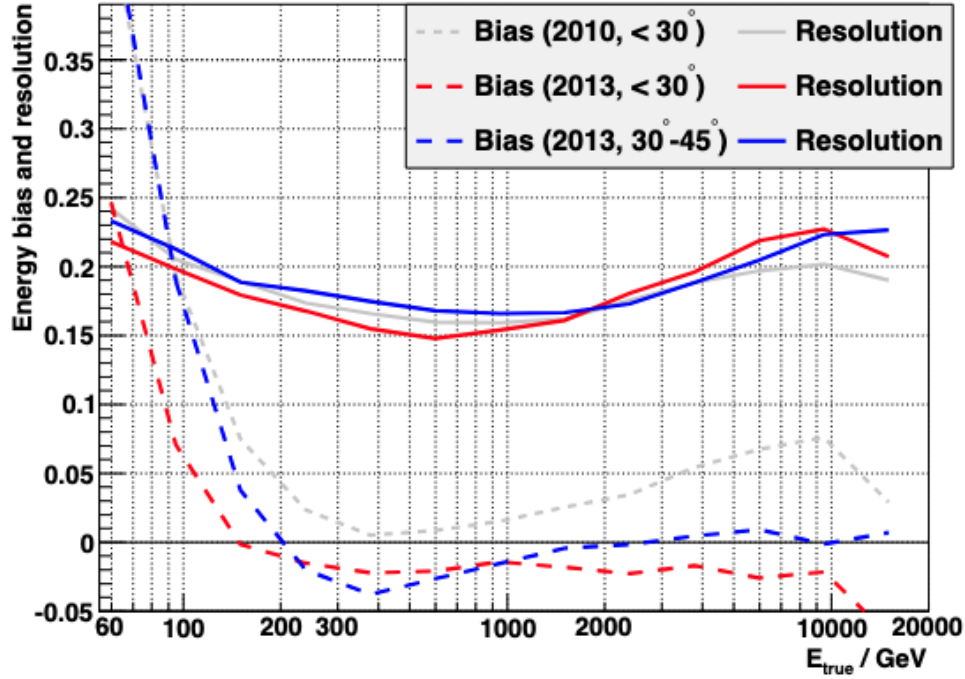


Figure 6.9: MAGIC Energy reconstruction performance (Aleksić et al., 2016b). Colors show different zenith angle range or different periods.

The energy resolution and bias are summarized in figure 6.9. The bias is less than 5 % above 200 GeV, and the resolution is at most 25 % at the edge of the energy range.

**Angular performance** The angular resolution is defined by the spread of the gamma-ray direction from the point source as shown in 6.10. The calculation assumes one sigma of the gaussian distribution. The value is 0.07 deg at 250 GeV. With more high energy, the resolution improves up to 0.04 deg.

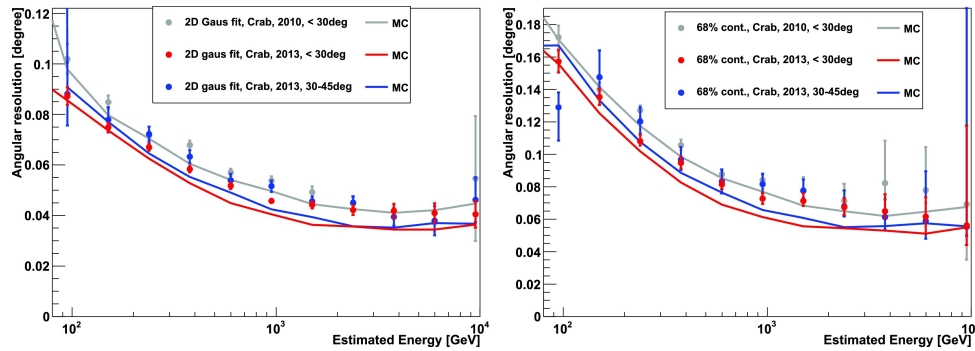


Figure 6.10: MAGIC Angular resolution performance (Aleksić et al., 2016b). Left: angular resolution is defined by a sigma of 2D gaussian function, Right: 68% containment radius versus the reconstructed energy. Colors show different zenith angle range or different periods.

**Effective area** the effective area is the total area to be used in the gamma-ray detection. Thus, the effective area depends on instrumental design and analysis method. If the efficiency of gamma-ray reconstruction is quite well, the effective area almost equal to the size of a telescope array. Typical effective area is approximately  $10^5 \text{ m}^2$

**Sensitivity** Figure 6.11 shows the differential sensitivity curve in Crab Unit (C.U.) and around 1 TeV, sensitivity reaches 1 %. The sensitivity is roughly proportional  $\sqrt{t_{\text{obs}}}$ , thus for 1 hour of observation, the sensitivity will degrade by a factor of seven. Therefore the source has a differential flux about 10 % C.U. at 1 TeV can be detected in one hour. This is nearly the flux of low state 1ES1959+650, and the only few sources that can be monitored with current VHE gamma-ray telescopes.

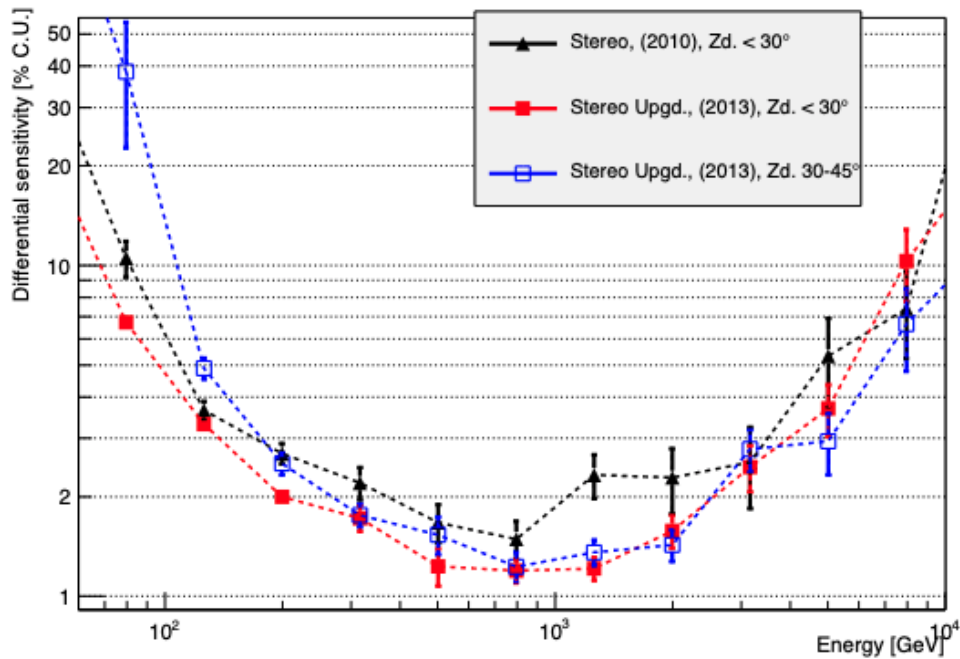


Figure 6.11: MAGIC differential Sensitivity curve for 50 hour observation (Aleksić et al., 2016b)

## 7. Observation and Data Analysis

### 7.1. Observation and Data selection

During the 5-year period from 2015, MAGIC observed 1ES1959+650 for a total of about 300 hours. In order to increase the observation time as much as possible, MAGIC also conducted observations under moonlight. In order to accurately reconstruct the gamma-ray flux from these observations, a dedicated analysis method must be applied. In this section, we discuss the details of the observations made by MAGIC and the selection of the data to be analyzed.

#### 7.1.1. Observation mode

In the gamma-ray observation through Cherenkov light, the hadronic shower will be major background events in the triggered data. To eliminate those background contamination, additional observation was required. Currently, special observation method, wobble observation was established and commonly used in the field. In the wobble observation, the observational target is placed on the place where is slightly separated from the center of the camera as shown in figure 7.1.

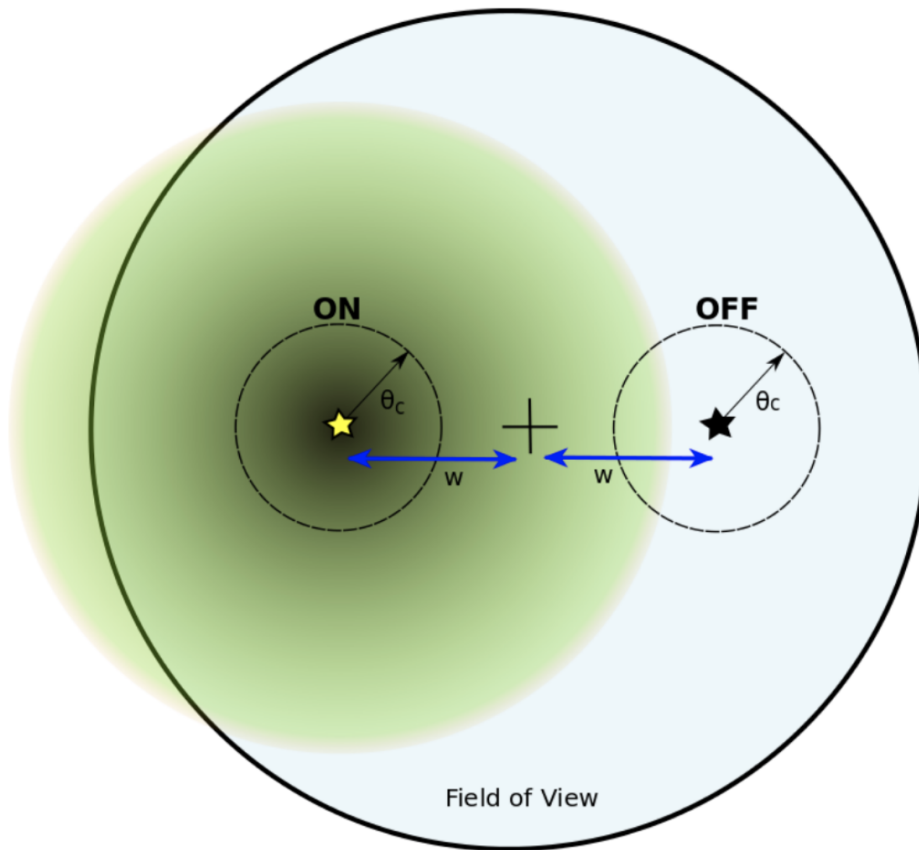


Figure 7.1: Schematic view of wobble observation.

In addition, another observation is performed for the symmetrical place on the camera. The pair of observation provides ON-OFF subtraction on the same region camera. It means, one can eliminate the effect, such as non-uniformity of the camera, when analyze data. Moreover, Wobble observation twice efficient if it compares with legacy ON-OFF observation if one perform ON-OFF subtraction from a single observation.

### 7.1.2. Data Selection

The gamma-ray observation by imaging atmospheric cherenkov telescope is significantly affected by the atmospheric condition because of its observation principals. In order to guarantee the quality of observed data, data selection plays important role for the IACT data analysis. Especially, to study a variability of the source, fluctuation due to the data selection might become critical. In this study, I used three parameters to select the data as explained below. From the beginning of 2015 to till the end of 2019, the 1230 observations were performed for 1ES1959+650. This section gives information about how to select good-quality data which can be used in the analysis.

**Average current** In this study, data from MAGIC observations between 2015 and 2020 were used; in 2015, 1ES1959+650 was not subject to steady-state observations, so observations were conducted primarily as ToO observations, which detect light intensification or receive information from other telescopes. From 2016 onward, steady-state observations were proposed and carried out. The observation continued until the end of 2020. However, for 2018, the observing approach was such that observations were made in situations where other objects could not be observed because the priority of the observations was lowered. In addition, many of the 1ES1959+650 observations in both periods were conducted in moonlight, as many celestial objects prefer to be observed in a non-moon environment.

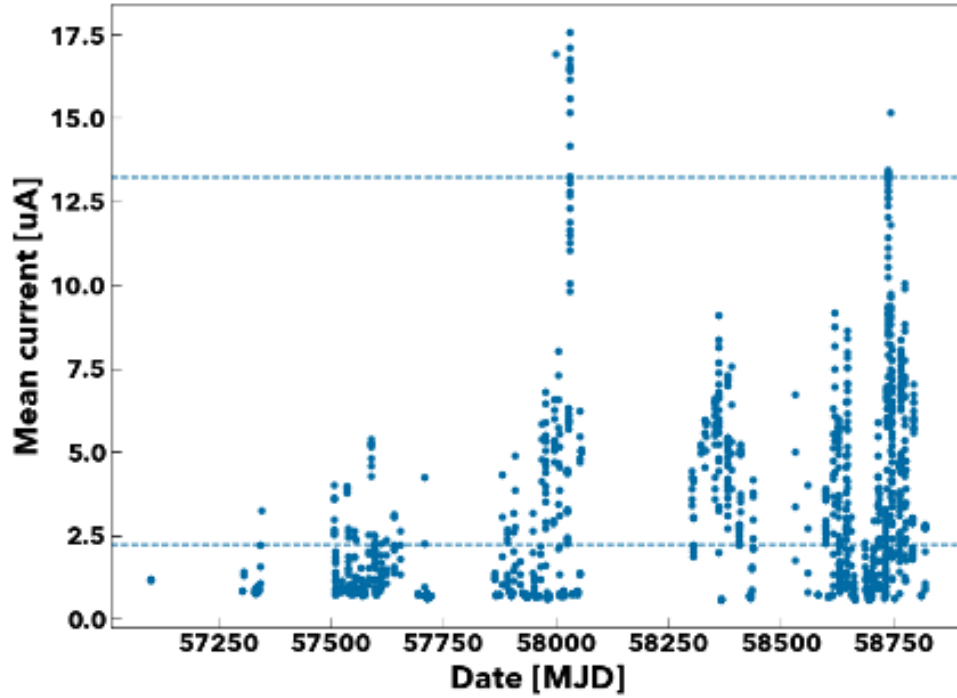


Figure 7.2: Average current on the MAGIC I camera. Upper horizontal dashed line indicate the maximum value of current which studied in previous study. Lower dashed line represents the maximum current of standard data selection

Figure 7.2 shows the average current values of the PMT on the camera for each run of about 15 minutes. The upper dashed line indicates the value where the moon analysis method has not been investigated in previous study, and the lower line indicates the current value at the limit where the usual analysis can be applied. In order to properly handle these data, it is necessary to remove the noise that increases due to the moonlight. Runs beyond the upper line totaled 21 runs and were excluded from the analysis.

**Zenith** The performance of IACT changes depends on the observing angle from the ground. Especially low energy gamma-ray detection efficiency be worse and vise versa for high-energy gamma rays because of the thickness of the atmosphere. The zenith angle of 1ES1959+650 will not be less than 35 degree due to the location on the sky. If the zenith angle of the source exceed 62 degrees, the energy threshold defined by the survived gamma-rays become rapidly worse. Thus I excluded observation has the zenith angle more than 62 degrees.

As explained in the observation principle, MAGIC observes gamma rays by measuring Cherenkov radiation originating from atmospheric showers. The distance from the telescope to the point of maximum development of the atmospheric shower is geometrically multiplied by  $1/\cos\theta$ , depending on the observation angle  $\theta$ . The Cherenkov pool drawn by the Cherenkov light from the shower grows while the density of Cherenkov photons decreases, so the detection efficiency of low-energy gamma rays decreases and the energy

threshold of the telescope increases. To guarantee an energy threshold of 300 GeV, the zenith angle is capped at 62 degrees.

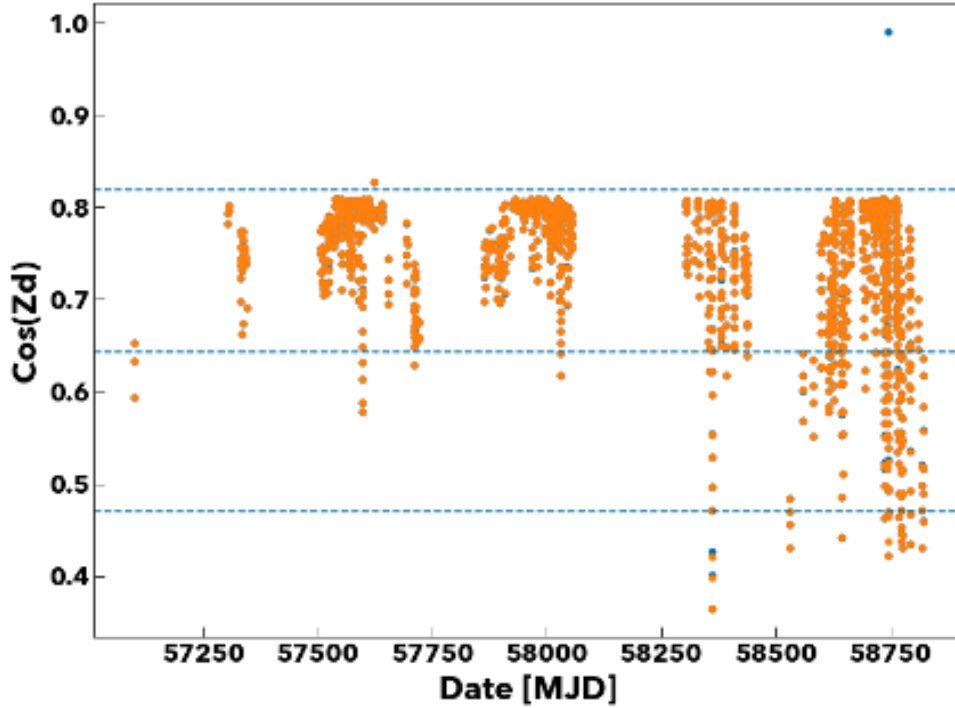


Figure 7.3: Average zenith angle during a observation. Different colors show each MAGIC telescope.

Figure 7.3 shows the average zenith angle ( $Z_d$ ) for each Run, expressed as  $\cos(Z_d)$ . The different colors indicate the difference between the two MAGIC telescopes. The horizontal wavy lines correspond to 35, 50, and 62 degrees from the top. This celestial object is always observed at a zenith angle of 35 degrees or more due to its position on the celestial sphere and the observation site. There are two Runs with smaller zenith angles, neither of which was used in the analysis. Runs with very large zenith angles were excluded from the analysis. Such runs totaled 19 runs. In addition to this, a total of 49 runs were excluded from the observed data for the purpose of testing the triggering method, etc., taking advantage of the fact that 1ES1959+650 is a bright celestial object.

**Atmospheric transmission** The atmospheric transmission values are measured by hand-made LiDAR during the observation. The transmission value is used to exclude data having a bad quality of atmosphere. In this study, I adopt the value the transmission above 9 km must larger equals 60 % for the light curve and 80 % for the spectra respectively.

Selection by atmospheric transparency was performed on the data after completing the above selections. In this study, atmospheric transparency at 9 km from LiDAR measured by MAGIC-LiDAR, which is located at the MAGIC observation site, was used. According to previous studies, when the atmospheric transparency is below 80%, a correction that



takes atmospheric transparency into account is mandatory. On the other hand, as shown in figure 7.4, the data from this study shows that there are many data points below 80% as well as some points showing 0.0.

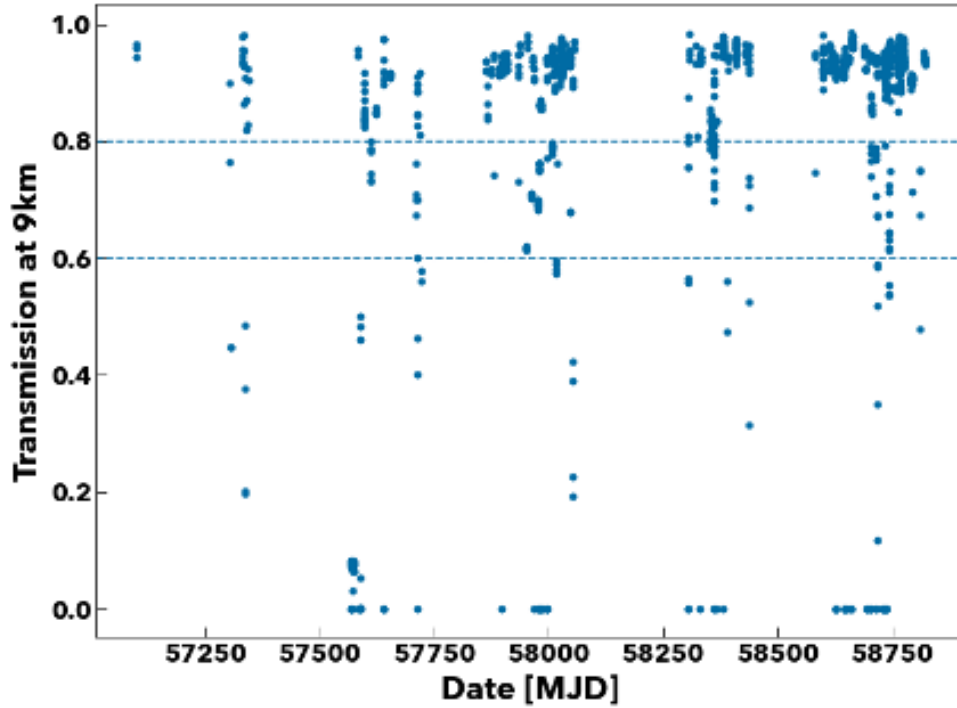


Figure 7.4: Atmospheric transmittance above 9km from MAGIC LiDAR. Two horizontal lines correspond to atmospheric transmittance 80% and 60% respectively.

**Number of stars** LiDAR did not work properly sometimes. For such a data, there is no clue to estimate the atmospheric conditions. Trigger event rate is commonly used to check the data quality as a rough estimator, but it's not good indicator for this study. This is because, for the moon data, trigger rate is continuously change due to the moonlight. Thus I checked the relation between the good-LiDAR transmission and the number of stars confirmed by the starguider camera. According to the 1ES1959 data, the number of stars more than 20 guarantees the transmission above 80%. Based on the study, I selected data with the number of stars when LiDAR spectra had a problem.

Such a point corresponds to a case where the direction of the LiDAR indicator differs by more than 5 degrees during the observation. Also, the figure does not show the case of a run with no LiDAR operation throughout the night. In order to utilize such data with minimal arbitrariness, the number of stars detected by the StarGuider camera was used as a supplementary indicator in this study.

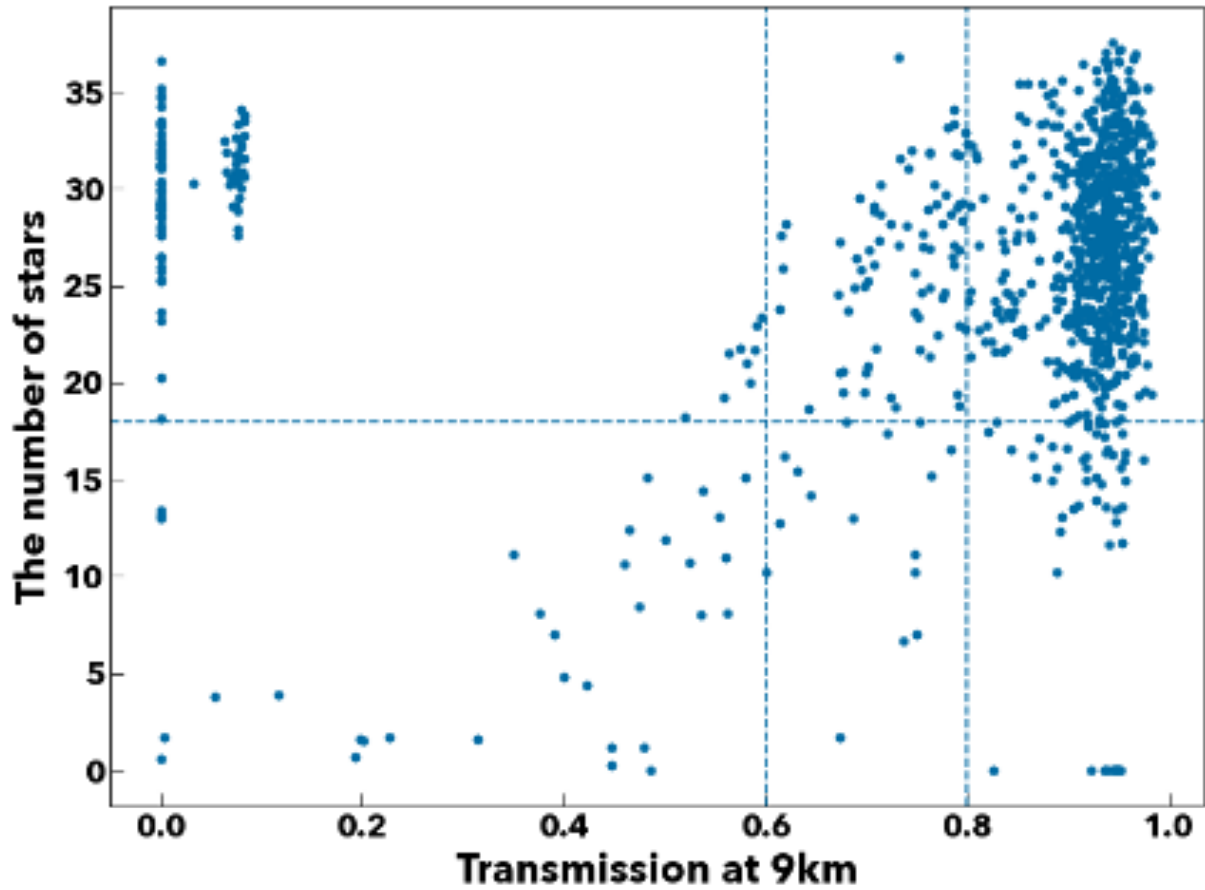


Figure 7.5: Number of stars identified by star-guider camera.

Figure 7.5 shows the relationship between the atmospheric transparency measured by LiDAR at 9 km and the number of stars detected by the Star Guider camera. The data where the atmospheric transparency was not measured properly is located in the upper left corner of the figure. On the other hand, for data with a horizontal axis in the range of 0.8 to 1.0, i.e., data with good atmospheric transparency, the number of detected stars is distributed around about 30. Modeling this distribution with a Gaussian distribution, the mean and standard deviation could be approximated by 26 and 2.5, respectively, so  $\mu - 3\sigma = 18.5$  18 was used as the threshold value. The figure shows a horizontal line at the point where the number of stars corresponds to 18, and when combined with the LiDAR measurements, it is expected that limiting the number of stars to 18 or more would result in an atmospheric transparency of at least 50%. For the data for which this cut had to be adapted, additional detailed data quality was checked. The validity of the data selection using the number of stars was confirmed by using the same technique with data from the Crab nebula, a standard source of TeV gamma rays, whose spectra are consistent with previous studies.

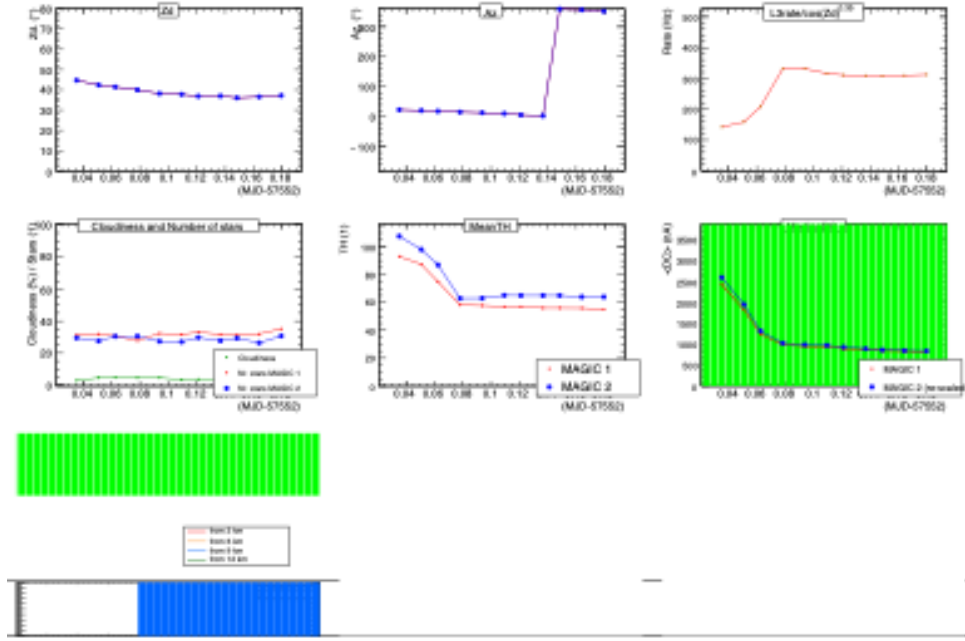


Figure 7.6: Data quality check plot.

Figure 7.6 shows, as an example, the data quality on June 13, 2016. The middle left shows the number of stars, which is well greater than 18. As a result of the above data selection, 1103 runs were finally selected as good quality data. The total observation time is approximately 328 hours, of which 160 hours were made under moonlight. Please refer to the analysis section for a description of the analysis performed to make the moonlight data usable.

As a result of data selection, the 1085 runs out of 1230 observation were survived after cut. The total survived observation time is approximately 300 hours. Among them, half of observation was done moderate or strong moon condition. For such data, without dedicated analysis, the reconstructed spectra and flux would be wrong. Thus I performed the dedicated analysis from the image cleaning step as discussed in (Ahnen et al., 2017).

## 7.2. Data Analysis

### 7.2.1. Software

Standard analysis software **MARS** was used to reconstruct gamma-ray events and a compute gamma-ray flux (Moralejo et al., 2009). The software based on C++ and ROOT, and **MARS** provides the spectra and the light curve as final products. The software version was V2-19-14, and V2-19-20 was also used to check the software systematic difference.

Figure 7.7 shows a whole structure of **MAGIC** data analysis chain. In the following sections, I will provide the details of each step and analysis results.

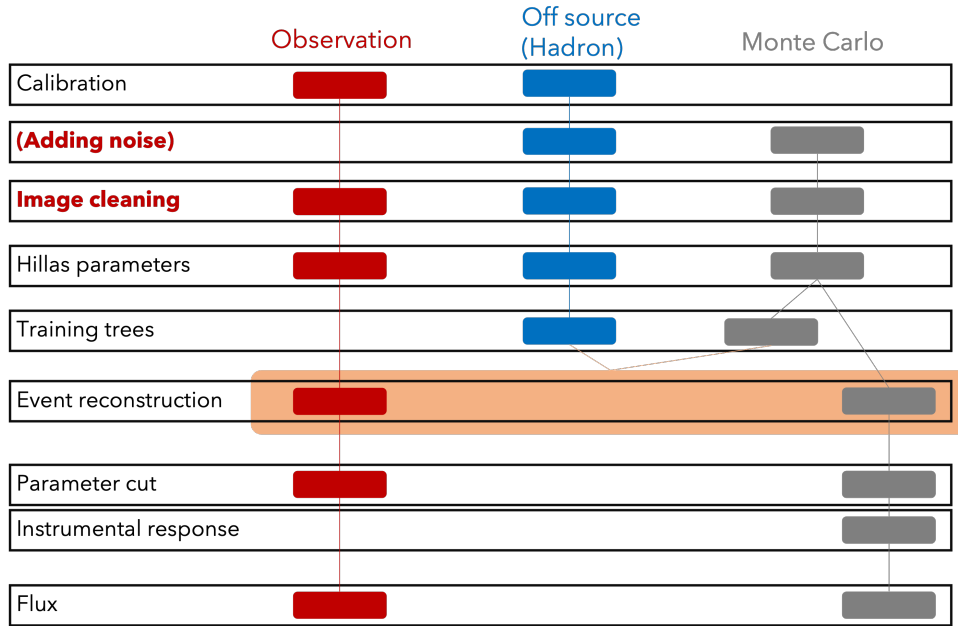


Figure 7.7: MAGIC data analysis structure. Each step was conducted with one or two programs of MAGIC Analysis and Reconstruction Software (MARS).

### 7.2.2. Signal calibration

The observed MAGIC raw data are stored in the form of digital counts of the PMTs, and those digital counts still include characteristics of the electronic circuitry. Thus we have to calibrate them. The goal of signal calibration is to convert the digital counts into the number of photons arriving at the camera. Since the intensity of the Cherenkov light correlates with the energy of the primary gamma ray, the precision of the number of incident photons is intensely related to the energy estimation.

The conversion factor between the digital counts and the number of incident photons is estimated using calibration events measured before and during the observation.

Since the calibration laser is continuously emitted during the observation, the conversion factor can be obtained even if the PMT response varies in time.

A calculation method of the conversion factor is called the F-factor method.

In the F-factor method, the coefficients are obtained based on Poisson statistics, assuming that the ratio of the mean value of the signal to the magnitude of fluctuations is proportional to the amount of light, including the PMT gain fluctuation.

Furthermore, in MAGIC, the PMT waveform is integrated around the maximum amplitude of the waveform to prevent night-sky background noise as much as possible.

In the end, the characteristics of the electronic circuit are also subtracted, and the image becomes information on the number of photo-electron per pixel. Moreover, the arrival time of the light pulse is also calculated for the image cleaning.

### 7.2.3. Image Cleaning

The technique of extracting the shower component from a calibrated image is called image cleaning. This analysis uses two thresholds to distinguish between noise and shower components from the image. First, the larger one of the two threshold values is used to search for the "core pixel.", which searches the brightest part of the shower image. Then, pixels neighboring the core with photons greater than another threshold value are extracted and considered to be shower-derived pixels.

In the MAGIC experiment, SUM cleaning, which includes timing information, is used. It is known that more pixels can be reconstructed by restricting the pulse arrival time based on the arrival time information of the core. This increases the detection efficiency of low-energy gamma-ray events, which is the goal of MAGIC.

In particular environments, such as under moonlight, the amount of background noise increases, so the threshold must be chosen appropriately as summarized in table 7.1. This choice is determined based on the survival rate of noise-only events (pedestal) and is usually optimized to keep noise events below 10

Table 7.1: cleaning levels for the moon analysis

NSB Level	M1 DC	Cleaning levels	MC Noise	min SIZE
–	[uA]	[p.e.]	[p.e.]	[p.e.]
DARK	< 2.2	6, 3.5	–	60
NSB2-3	< 3.3	7, 4.5	3.0, 1.3	80
NSB3-5	< 5.5	8, 5.0	3.5, 1.4	110
NSB5-8	< 8.8	9, 5.5	4.1, 1.7	150
NSB8-12	< 13.2	10, 5.5	4.8, 2.0	200

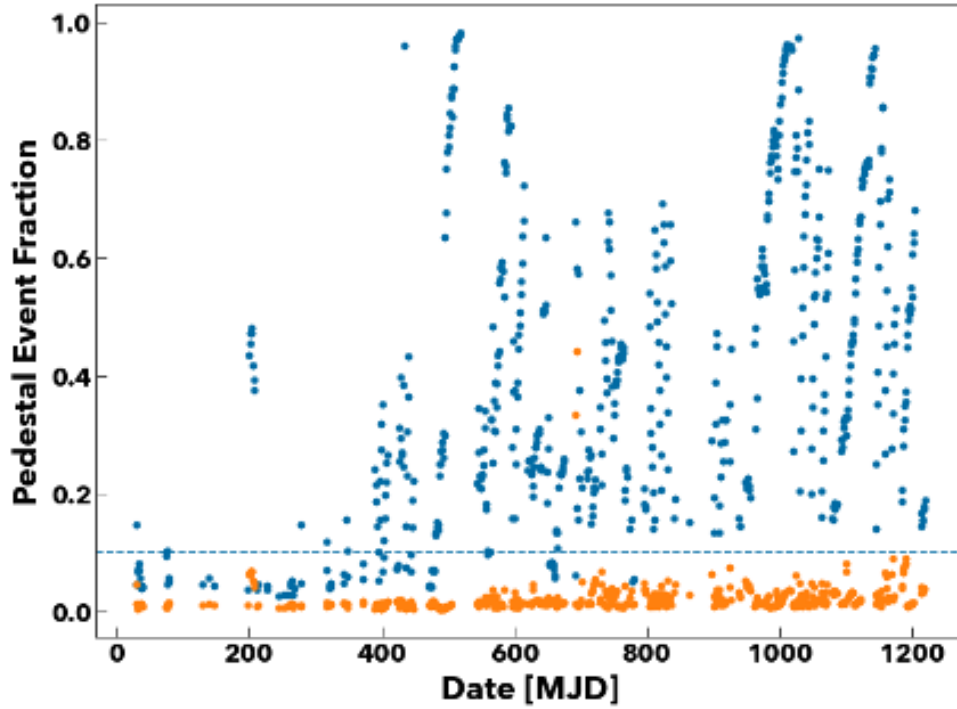


Figure 7.8: Results of applying Image cleaning for Moon analysis.

Figure 7.8 shows the horizontal axis for the date and time and the vertical axis for the percentage of background noise data after image cleaning. For normal data, it is confirmed that keeping this percentage below 10% does not affect the higher level analysis. The blue dots in the figure show the percentage of noise data remaining without the threshold adjusted for the moon analysis, and the orange dots are after applying image cleaning with the investigated threshold to the respective data. It was confirmed that the noise rate can be reduced to less than 10% for almost all data.

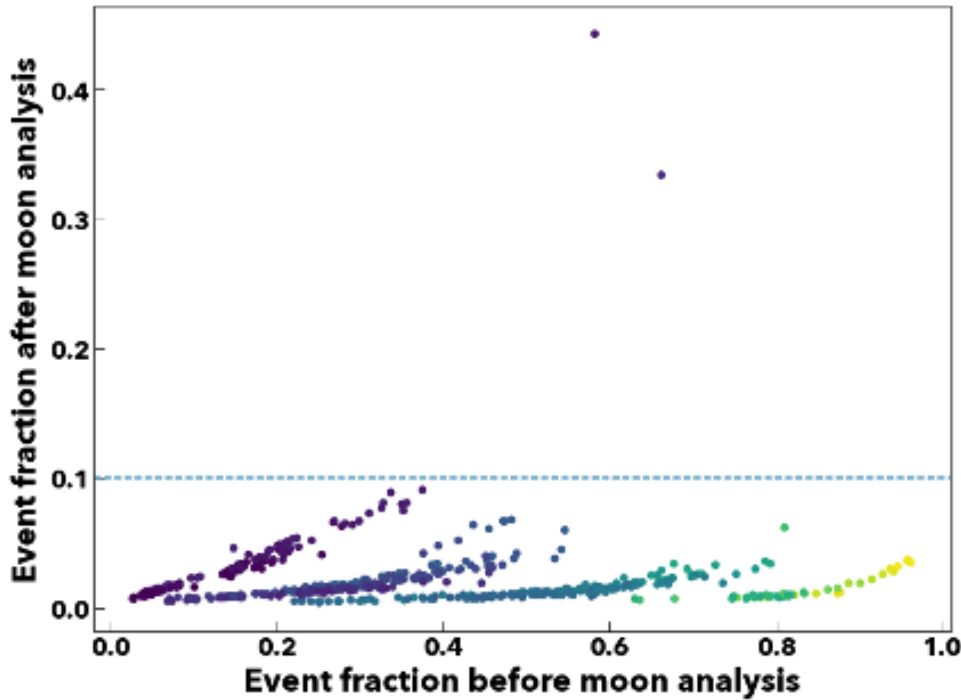


Figure 7.9: Results of applying Image cleaning for Moon analysis. Color represents relative difference of average current. Brighter point corresponds to large current.

Direct comparison of background noise event percentages, where the x-axis is the residual before MOON analysis. It can be seen that the rate is reduced to less than 10% over a wide region of luminosity.

**star** in MARS is in charge of the image cleaning. In order to make moon data available, I performed the dedicated image cleaning to the data. The data taken at the moon condition are affected by the strong NSB noise. So the threshold to obtain the shower image has to be increased depend on the strength of the NSB. The previous study using MAGIC telescope showed the complete study of the moon analysis using Crab (Ahn et al., 2017). I followed the study and applied the same cleaning levels.

Not only performing the image cleaning to the objective data, I also prepared the hadronic component with high-level noise. It is difficult to find the real observation with strong NSB noise, thus I mimic the noisy data by adding noise to the real observation.

The later step is completely same until I get the fundamental parameters of each events.

#### 7.2.4. Hillas parametrization

Image cleaning extracts only those pixels derived from Cherenkov light emitted from the atmospheric shower. The Hillas parameter is a quantitative measure of the amount of light (hereafter Cherenkov image) that these pixels possess and is used to estimate the cosmic-ray like nature of the event and the direction of arrival of gamma rays using machine learning techniques, which will be discussed later. Hillas parameters include *SIZE*, the

total amount of light in the image, and *WIDTH* and *LENGTH*, which describe the image's geometrical size. *WIDTH* and *LENGTH* are generally taken to be approximations of the image by ellipses, but in reality, they are quadratic moments of the light intensity on a camera plane.

Combining the Hillas parameters of several telescopes, it is possible to estimate the *IMPACT*, which is the distance between the atmospheric shower axis and the telescope, and  $X_{\max}$ , the maximum developed height of the atmospheric shower. These quantities effectively estimate energy and discriminate between gamma-ray and cosmic-ray events.

### 7.2.5. Event reconstruction

Using the Hillas parameters, one can estimate the fundamental parameter of gamma-rays. Those are energy and arrival direction. Adding that, we know the hadronic background far frequently than gamma-rays. Thus to discriminate gamma-ray and hadronic background, MAGIC adopt "Hadroness" parameter expressing the how signal looks like a gamma-ray. For those computation, we use observed cosmic-ray events and simulated gamma-ray events.

Recent days, the multi-variate analysis is used to discriminate the particle types. MAGIC analysis is using a random forest method as particle type classifier.

For the energy reconstruction, one use a look-up table prepared from the simulated gamma-ray in the MAGIC analysis. Validation test of each random forest trees was partially done using appropriate CrabNebula data. Using above Random forest trees, the energy, arrival direction, and hadroness are determined.

### 7.2.6. Signal detection

The following LiMa equation is commonly used when discussing the detection of gamma rays in IACT(Li & Ma, 1983),

$$S = \sqrt{-2} \left\{ N_{\text{ON}} \ln \left[ \frac{1 + \alpha}{\alpha} \left( \frac{N_{\text{ON}}}{N_{\text{ON}} + N_{\text{OFF}}} \right) \right] + N_{\text{OFF}} \ln \left[ (1 + \alpha) \left( \frac{N_{\text{OFF}}}{N_{\text{ON}} + N_{\text{OFF}}} \right) \right] \right\}^{1/2} \quad (7.1)$$

where  $N_{\text{ON}}$  and  $N_{\text{OFF}}$  are the number of events in the region where the celestial object is considered present and the region where it is not, respectively. Their regions are called ON region and OFF region, respectively. Moreover, the number of excess is defined as  $N_{\text{excess}} = N_{\text{ON}} - \alpha N_{\text{OFF}}$ .  $\alpha$  is the ratio of ON to OFF exposures, which is expected to correspond to the ratio of remaining gamma-like hadron events. If the area of each region is taken to be equal, alpha corresponds to the ratio of exposure times. These areas are necessary because background events due to cosmic ray contributions cannot be eliminated. In this study, the flux is calculated assuming that excess is the number of gamma rays from the celestial object. There are many different ways to choose between ON and OFF.



### 7.2.7. Flux derivation

The flux calculation requires, by definition, the time spent observing gamma rays and the area used in detecting them. These quantities are called the effective time  $t_{\text{eff}}$  and the effective area  $A_{\text{eff}}$ , respectively. Dividing the number of gamma rays detected by these two quantities yields the estimated photon flux  $\phi$ . This section will discuss the derivation of  $t_{\text{eff}}$  and  $A_{\text{eff}}$ .

**Effective time  $t_{\text{eff}}$**  The effective time  $t_{\text{eff}}$  roughly corresponds to the observed time  $t_{\text{obs}}$ . However, detectors with trigger systems such as MAGIC have a dead time  $\tau_{\text{dead}}$ , the inoperable time spent processing an event. Therefore, the effective time  $t_{\text{eff}}$  is precisely obtained by subtracting this contribution. From this, we see

$$t_{\text{eff}} = t_{\text{obs}} - N_{\text{trig}}\tau_{\text{dead}}, \quad (7.2)$$

where  $N_{\text{trig}}$  is the number of events triggered by the telescope.

**Effecttime area  $A_{\text{eff}}$**  The effective area  $A_{\text{eff}}$  is the area used by the detector to detect gamma rays. On the other hand, the effective area is defined as a quantity that includes the detection efficiency because, from the principle of IACT, the detection efficiency of gamma rays strongly depends on their energy and observation conditions. The definition is

$$A_{\text{eff}} = A_{\text{sim}} \times \frac{N_{\text{sur}}}{N_{\text{sim}}}, \quad (7.3)$$

where  $N_{\text{sur}}$  and  $N_{\text{sim}}$  are the number of gamma-ray events after the analysis and ones simulated, respectively. In the spectrum analysis, this calculation is performed for each energy bin. The energies used here are the true energies from the Monte Carlo simulations, not the reconstructed energies. On the other hand, the gamma rays detected are treated in terms of the reconstructed energies, so appropriate corrections are needed for accurate discussions. This correction is called unfolding.

To determine the light curve and spectra, I needed to define the energy threshold for the analysis. However, the analysis threshold defined by the peak energy of the survived gamma-ray events strongly depends on the NSB level. Figure 7.10 shows the distribution of the survived gamma-ray events for various NSB levels. I adopted 300 GeV as an energy threshold for the latter analysis, but it might be critical value for highest noise levels.

### 7.2.8. Combining the different analysis levels

To evaluate the instrumental responses properly for data having different noise levels, I performed NSB-wise analysis thus far. Combining them to get a final product was performed by following method. Consider each analysis has each fundamental parameters,

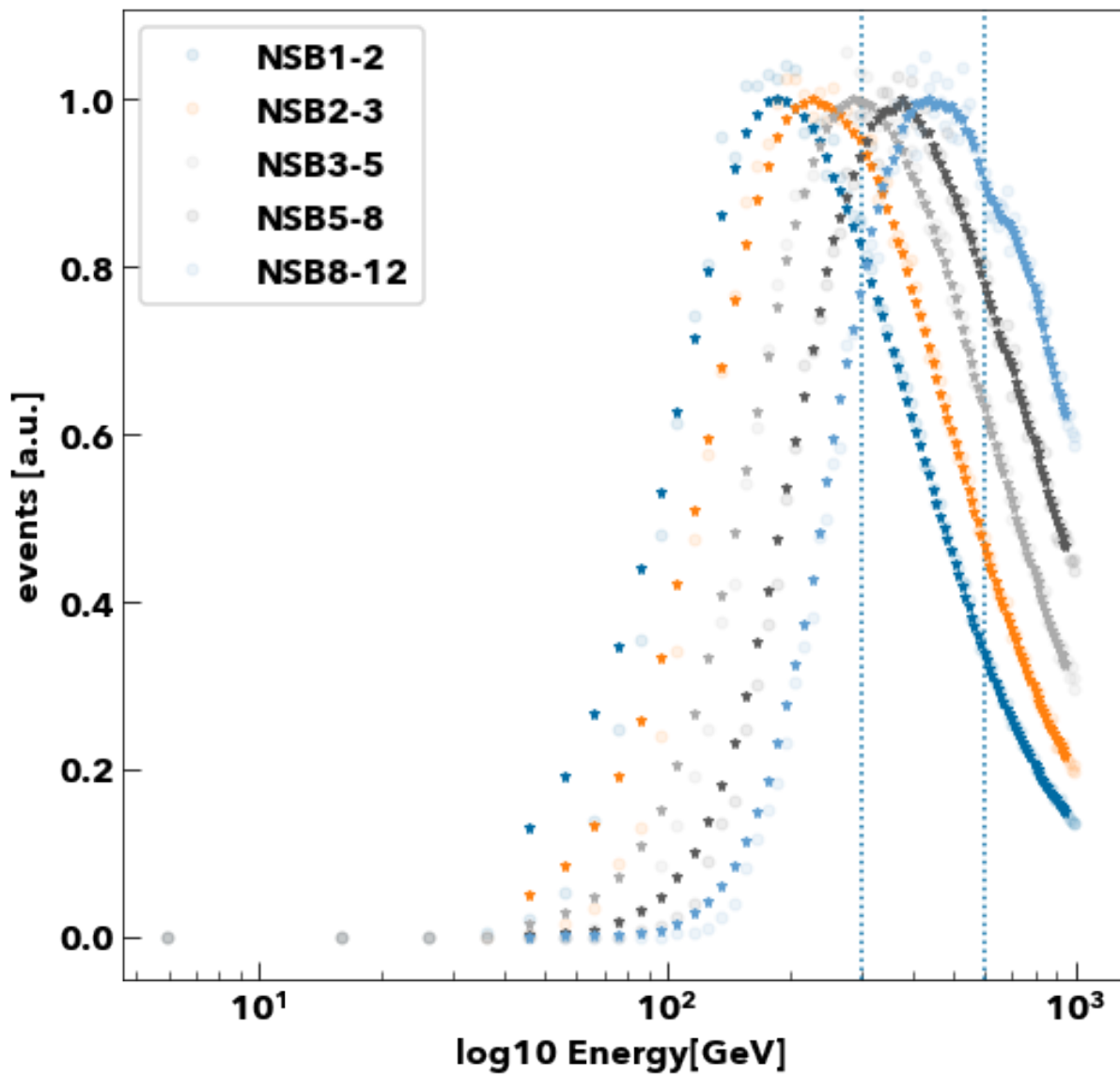


Figure 7.10: Analysis threshold comparison for the various NSB levels. Vertical axis is survived gamma-ray events after rough hadroness cut ( $\text{hadroness} < 0.3$ ). Each distribution is smoothed by taking average in neighboring bins. The number of events are normalized by the maximum value of the normalized event. Vertical lines show 300 GeV and 600 GeV. The former one is the threshold used in this study and the latter one is a threshold for comparison.

excess  $N$ , effective area  $A$ , livetime  $T$ . Here, total excess count will

$$N_{\text{tot}} = \sum_i N_i. \quad (7.4)$$

and, the average effective area is

$$A_{\text{eff,tot}} = \sum_i A_{\text{eff},i} \times t_{\text{eff},i} / \sum_i t_{\text{eff},i} \quad (7.5)$$

$$t_{\text{eff,tot}} = \sum_i t_{\text{eff},i} \quad (7.6)$$

Then, combined flux is,

$$F_{\text{combined}} = \frac{N_{\text{tot}}}{A_{\text{eff,tot}} \times t_{\text{eff,tot}}}. \quad (7.7)$$

Uncertainties in the excess and effective area can be propagated via usual error calculation.

### 7.2.9. Unfolding and forward-unfolding

Unfolding is correcting the difference between the spectra in true and estimated energies that depend on the accuracy of the energy reconstruction. For example, let the number of gamma rays per true energy be the vector  $\vec{x}$ , and the detector response is  $\check{R}$ . Here,  $\check{R}$  can be regarded as a matrix. Since what is obtained by the analysis is the estimated number of gamma rays per reconstructed energy  $\vec{y}$ , thus  $\vec{y} = \check{R}\vec{x}$  is satisfied. Mathematically, this can be solved by obtaining the inverse matrix of  $\check{R}$ . However, since the inverse matrix is rarely obtained in actual situations, thus it is necessary to estimate  $\vec{x}$  numerically. This correction allows us to estimate the spectrum in the true energy, which is essential for comparing results with other detectors, such as MWL modeling. There are several types of unfolding method named Bertero, Tikhonov, and Schelming. I tested every method to evaluate the systematic difference of them and selected the reasonable one for the MWL analysis.

A very similar but different means is forward-folding. In this method,  $\vec{x}$  is modeled, and a parameter of the model which reproduce  $\vec{y}$  is searched, taking into account the instrumental response  $\check{R}$ . This method is often sufficient if one only wants to model and discuss radiation.

.

## 8. Analysis Results

### 8.1. Analysis Results

This section shows analysis results of MAGIC observations. First, I introduce temporal analysis results, that are used to estimate the temporal evolution of the source. Then next, I will show the spectral analysis along the temporal analysis results.

#### 8.1.1. Light curve

Figure 8.1 shows the MAGIC light curve over a five-year period for the energy range is above 300 GeV.

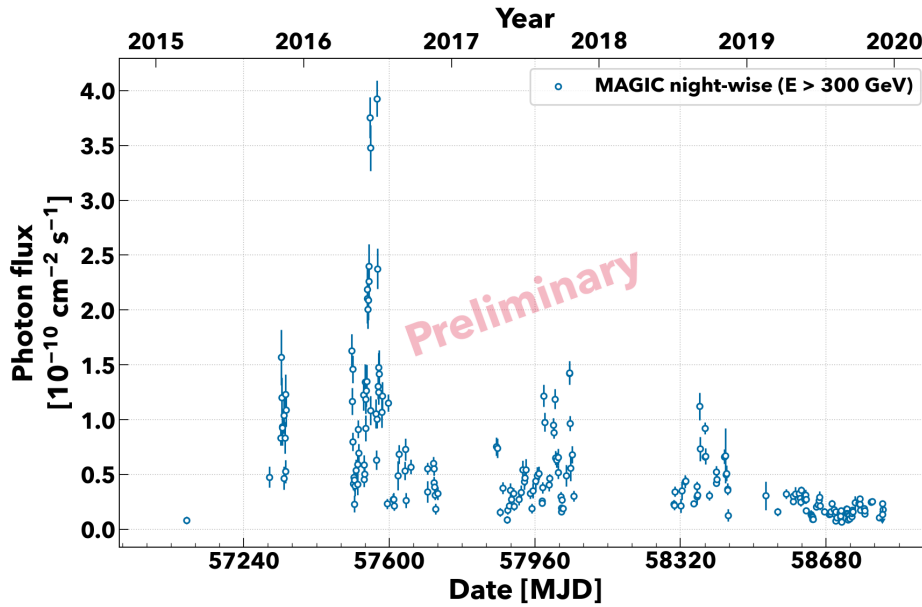


Figure 8.1: MAGIC light curve. Each point corresponds to a nightly flux above 300 GeV. Error bars are statistical uncertainty corresponding to one-sigma and arrows are flux upper limits with 95 % confidence level.

The light curve was made in nightly bins and clearly show an flaring episodes which equals to the Crab Nebula flux ( $\sim 1.2 \times 10^{-10} \text{ cm}^{-2} \text{ s}^{-1}$ ) or more in the same energy range. The nightly emission is on average higher in 2015 and 2016, but appears to be declining from 2017 onwards. Furthermore, despite the densest observations in 2019, no intensification was observed and the emission was at most as large as a 30 % Crab Nebula flux.

#### 8.1.2. Bayesian block analysis

To evaluate temporal evolution of the spectrum, I estimated constant-flux periods by the Bayesian block method proposed in [Scargle \(1998\)](#). The essential calculation is maxi-

mizing a likelihood by changing the durations where the measured flux is statistically constant. The likelihood in a certain duration  $k$  is defined as

$$L^{(k)} = \frac{-1}{2} \sum_{i=0}^N \left( \frac{x_i - \bar{x}}{\sigma_i} \right)^2. \quad (8.1)$$

Where  $N$  denotes the number of flux measurements in the duration,  $x_i$  and  $\bar{x}$  are a flux measurement and averaged flux in the duration.  $\sigma_i$  is a uncertainty of a flux point. Summing the likelihood through possible segments gives total likelihood of a certain data division. I used implemented program in astropy python package<sup>9</sup>. Figure 8.2 shows the comparison of the Bayesian block analysis with different dataset.

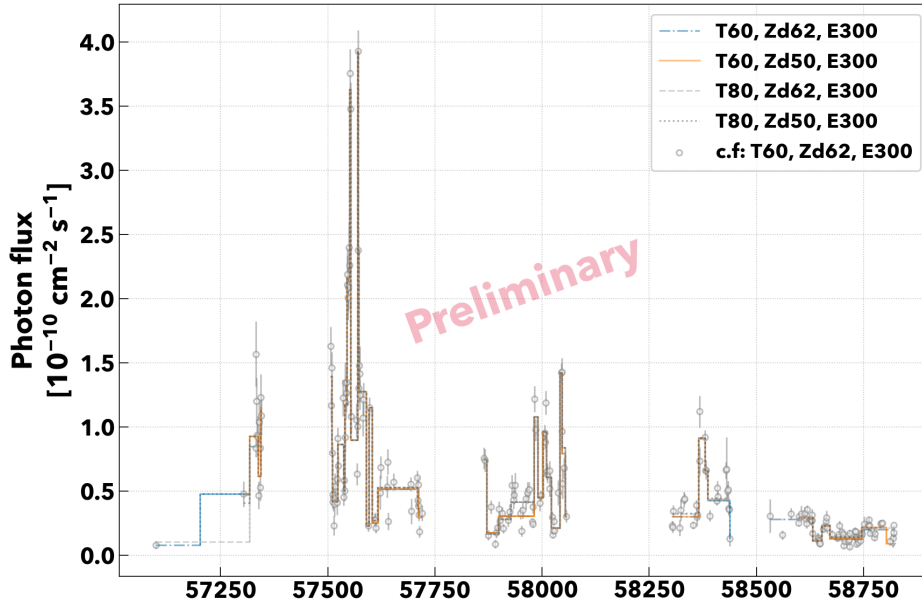


Figure 8.2: Temporal blocks obtained by the bayesian block algorithm. Gray points are light curve for a comparison. Each lines shows the result obtained from the different dataset. The red squares are averaged flux inside bayesian temporal bins.

The figure shows the Bayesian blocks and night-wise light curve as same as figure 8.1. Different data selections showed different bayesian binning. One can understand that it is the systematic difference originating from the data selection. The purpose of this study is characterizing the temporal evolution with better statistics. Therefore, I adopted the shorter period if there is a contradiction. Taking a shorter time should be more conservative for the integration of the data. The conclusive values are summarized in table 8.1 and 8.2. Daggers in tables are the edges which they fluctuate in the datasets. But no significant effect in the integration of the MAGIC data. Each temporal duration

<sup>9</sup>[https://docs.astropy.org/en/stable/api/astropy.stats.bayesian\\_blocks.html](https://docs.astropy.org/en/stable/api/astropy.stats.bayesian_blocks.html)

estimated by the bayesian block method was named as year and alphabets. For example, Bayesian block (BB) label 15C is third temporal bin in 2015.

Table 8.1: Bayesian block analysis result in 2015 and 2016

BBLabel	Period in MJD	Period in UTC
15A	57099.2 - 57201.6	2015-03-18 - 2015-06-28
15B	57201.6 - 57317.9	2015-06-28 - 2015-10-22
15C	57317.9 - 57337.4	2015-10-22 - 2015-11-11
15D	57337.4 - 57343.3	2015-11-11 - 2015-11-17
15E	57343.3 - 57344.9	2015-11-17 - 2015-11-18
16A	57507.2 - 57509.7	2016-04-29 - 2016-05-01
16B	57509.7 - 57510.7	2016-05-01 - 2016-05-02
16C	57510.7 - 57522.6	2016-05-02 - 2016-05-14
16D	57522.6 - 57536.6	2016-05-14 - 2016-05-28
16E	57536.6 - 57539.7	2016-05-28 - 2016-05-31
16F	57539.7 - 57544.7	2016-05-31 - 2016-06-05
16G	57544.7 - 57551.1	2016-06-05 - 2016-06-12
16H	57551.1 - 57553.6	2016-06-12 - 2016-06-14
16I	57553.6 - 57569.6	2016-06-14 - 2016-06-30
16J	57569.6 - 57570.6	2016-06-30 - 2016-07-01
16K	57570.6 - 57571.5	2016-07-01 - 2016-07-02
16L	57571.5 - 57589.0	2016-07-02 - 2016-07-20
16M	57589.0 - 57596.1	2016-07-20 - 2016-07-27
16N	57596.1 - 57603.6	2016-07-27 - 2016-08-03
16O	57603.6 - 57616.0†	2016-08-03 - 2016-08-16
16P	57616.0 - 57709.3	2016-08-16 - 2016-11-17
16Q	57709.3 - 57711.3	2016-11-17 - 2016-11-19
16R	57711.3 - 57719.8	2016-11-19 - 2016-11-27

Table 8.2: Bayesian block analysis result between 2017 and 2019

BBLabel	Period in MJD	Period in UTC
17A	57864.2 - 57870.7	2017-04-21 - 2017-04-27
17B	57870.7 - 57897.6	2017-04-27 - 2017-05-24
17C	57897.6 - 57927.6	2017-05-24 - 2017-06-23
17D	57927.6 - 57980.5	2017-06-23 - 2017-08-15
17E	57980.5 - 57989.9	2017-08-15 - 2017-08-24
17F	57989.9 - 58002.0†	2017-08-24 - 2017-09-05
17G	58002.0 - 58010.0	2017-09-05 - 2017-09-14
17H	58010.0 - 58020.9	2017-09-14 - 2017-09-24
17I	58020.9 - 58040.9	2017-09-24 - 2017-10-14
17J	58040.9 - 58046.4	2017-10-14 - 2017-10-20
17K	58046.4 - 58053.8	2017-10-20 - 2017-10-27
17L	58053.8 - 58055.8	2017-10-27 - 2017-10-29
18A	58303.1 - 58364.5	2018-07-04 - 2018-09-03
18B	58364.5 - 58380.5	2018-09-03 - 2018-09-19
18C	58380.5 - 58386.5	2018-09-19 - 2018-09-25
18D	58386.5 - 58437.9†	2018-09-25 - 2018-11-15
19A	58531.2 - 58598.2	2019-02-17 - 2019-04-25
19B	58598.2 - 58630.7	2019-04-25 - 2019-05-27
19C	58630.7 - 58652.1	2019-05-27 - 2019-06-18
19D	58652.1 - 58670.6	2019-06-18 - 2019-07-06
19E	58670.6 - 58744.5†	2019-07-06 - 2019-09-18
19F	58744.5 - 58748.5†	2019-09-18 - 2019-09-22
19G	58748.5 - 58802.9†	2019-09-22 - 2019-11-15
19H	58802.9 - 58820.9	2019-11-15 - 2019-12-03



### 8.1.3. Spectral energy distribution

Along the bayesian temporal bins, I performed spectral analyses. To obtain the averaged spectra, observations inside each bayesian bins were combined into a single spectrum. Fitting parameters were obtained via forward folding method by `fold` program. I assumed the EBL absorption with the dominguez model in the calculation. The normalization energy was fixed at 300 GeV to easy compare the flux at fixed energy. To assess the spectrum is curved or not, a simple power-law function and a log-parabola model were used. Fitting results are summarized in table 8.3, 8.5, 8.6, and 8.4.

If the p-value estimated from the  $\chi^2$  and the degree of freedom is less than the 5 %, the model is not appropriate to describe the data. The power-law function showed a small p-values in most of cases. Although the power law model is not explain data well, seeing the temporal variation in the index is good. According to the fitting result, the spectral index is close to 2.3 to 2.5 when the flux is low.

Log-parabola fitting results show more acceptable result except some cases. Among the exceptions, the p-values are not far from the five-percent limit. The fitting result shows harder index ( $\sim 1.8$ ) at the flaring state in 2016, and 2.1 in 2017. The difference can be seen clearly in the reconstructed spectrum shown in figure 8.3 to 8.7. Figures shows reconstructed spectra with various unfolding methods. Some unfolding procedures fails for some spectra, but no every cases. Thus I took one of the succeeded data points for the latter analysis.

Table 8.3: Spectral fitting result of MAGIC spectra with power-law function in 2015-2016

BBLabel	$K$	$\alpha$	P-value
–	[ $\text{cm}^{-2} \text{s}^{-1} \text{TeV}^{-1}$ ]	–	–
15A	$0.8 \pm 0.4 \times 10^{-10}$	$2.7 \pm 0.5$	1.5e-01
15B	$2.3 \pm 0.5 \times 10^{-10}$	$2.2 \pm 0.3$	7.2e-01
15C	$5.7 \pm 0.2 \times 10^{-10}$	$2.42 \pm 0.04$	5.1e-05
15D	$4.3 \pm 0.3 \times 10^{-10}$	$2.37 \pm 0.08$	7.7e-01
15E	$5.9 \pm 0.5 \times 10^{-10}$	$2.20 \pm 0.08$	8.7e-01
16A	$6.6 \pm 0.2 \times 10^{-10}$	$2.10 \pm 0.03$	5.3e-03
16B	$3.8 \pm 0.3 \times 10^{-10}$	$2.12 \pm 0.06$	6.3e-02
16C	$2.4 \pm 0.1 \times 10^{-10}$	$2.36 \pm 0.05$	8.2e-03
16D	$5.0 \pm 0.2 \times 10^{-10}$	$2.36 \pm 0.04$	1.6e-06
16E	$2.9 \pm 0.2 \times 10^{-10}$	$2.32 \pm 0.06$	1.7e-01
16F	$6.4 \pm 0.3 \times 10^{-10}$	$2.31 \pm 0.05$	1.3e-03
16G	$11.3 \pm 0.6 \times 10^{-10}$	$2.23 \pm 0.05$	7.2e-07
16H	$15.9 \pm 0.5 \times 10^{-10}$	$2.07 \pm 0.02$	9.9e-11
16I	$5.1 \pm 0.2 \times 10^{-10}$	$2.31 \pm 0.04$	1.5e-07
16J	$18.2 \pm 0.5 \times 10^{-10}$	$2.12 \pm 0.02$	6.9e-16
16K	$12.2 \pm 0.5 \times 10^{-10}$	$2.16 \pm 0.04$	5.4e-02
16L	$7.0 \pm 0.2 \times 10^{-10}$	$2.29 \pm 0.03$	4.8e-10
16M	$1.9 \pm 0.2 \times 10^{-10}$	$2.8 \pm 0.2$	6.5e-01
16N	$6.4 \pm 0.3 \times 10^{-10}$	$2.30 \pm 0.04$	6.6e-04
16O	$2.0 \pm 0.2 \times 10^{-10}$	$2.5 \pm 0.1$	5.6e-01
16P	$3.4 \pm 0.1 \times 10^{-10}$	$2.42 \pm 0.03$	7.2e-05
16Q	$3.1 \pm 0.2 \times 10^{-10}$	$2.62 \pm 0.10$	3.2e-01
16R	$2.7 \pm 0.2 \times 10^{-10}$	$2.69 \pm 0.07$	1.6e-01

Table 8.4: Spectral fitting result of MAGIC spectra with power-law function in 2017-2019

BBLabel	$K$	$\alpha$	P-value
–	[ $\text{cm}^{-2} \text{s}^{-1} \text{TeV}^{-1}$ ]	–	–
17A	$4.1 \pm 0.2 \times 10^{-10}$	$2.28 \pm 0.05$	9.2e-02
17B	$1.41 \pm 0.10 \times 10^{-10}$	$2.64 \pm 0.08$	4.2e-01
17C	$1.73 \pm 0.09 \times 10^{-10}$	$2.48 \pm 0.05$	9.3e-06
17D	$2.5 \pm 0.1 \times 10^{-10}$	$2.39 \pm 0.05$	1.4e-02
17E	$5.5 \pm 0.2 \times 10^{-10}$	$2.16 \pm 0.04$	2.1e-02
17F	$2.5 \pm 0.1 \times 10^{-10}$	$2.32 \pm 0.06$	3.7e-01
17G	$5.1 \pm 0.2 \times 10^{-10}$	$2.13 \pm 0.03$	6.5e-03
17H	$3.6 \pm 0.2 \times 10^{-10}$	$2.25 \pm 0.04$	1.1e-01
17I	$1.47 \pm 0.08 \times 10^{-10}$	$2.50 \pm 0.05$	3.0e-01
17J	$7.8 \pm 0.2 \times 10^{-10}$	$2.20 \pm 0.03$	4.0e-04
17K	$4.6 \pm 0.2 \times 10^{-10}$	$2.18 \pm 0.04$	1.4e-01
17L	$1.7 \pm 0.3 \times 10^{-10}$	$2.2 \pm 0.2$	9.0e-01
18A	$1.94 \pm 0.08 \times 10^{-10}$	$2.33 \pm 0.04$	1.9e-03
18B	$4.9 \pm 0.2 \times 10^{-10}$	$2.26 \pm 0.04$	3.5e-04
18C	$3.6 \pm 0.2 \times 10^{-10}$	$2.26 \pm 0.04$	4.2e-03
18D	$2.66 \pm 0.08 \times 10^{-10}$	$2.37 \pm 0.03$	1.0e-02
19A	$1.8 \pm 0.3 \times 10^{-10}$	$2.5 \pm 0.1$	8.1e-01
19B	$1.63 \pm 0.06 \times 10^{-10}$	$2.37 \pm 0.03$	2.8e-06
19C	$0.70 \pm 0.06 \times 10^{-10}$	$2.34 \pm 0.07$	3.3e-02
19D	$1.37 \pm 0.08 \times 10^{-10}$	$2.37 \pm 0.06$	3.1e-01
19E	$0.94 \pm 0.03 \times 10^{-10}$	$2.49 \pm 0.03$	1.7e-02
19F	$0.96 \pm 0.09 \times 10^{-10}$	$2.36 \pm 0.08$	1.1e-02
19G	$1.18 \pm 0.04 \times 10^{-10}$	$2.29 \pm 0.03$	3.5e-05
19H	$0.4 \pm 0.3 \times 10^{-10}$	$2.1 \pm 0.3$	3.2e-01

Table 8.5: Spectral fitting result of MAGIC spectra with Log-parabola function in 2015-2016

BLabel	$K$	$\alpha$	$\beta$	P-value
–	[ $\text{cm}^{-2} \text{s}^{-1} \text{TeV}^{-1}$ ]	–	–	–
15A	$0.8 \pm 0.3 \times 10^{-10}$	$2.7 \pm 1.6$	$0 \pm 3$	9.3e-02
15B	$2.3 \pm 0.5 \times 10^{-10}$	$2.2 \pm 0.5$	$0 \pm 2$	6.0e-01
15C	$6.0 \pm 0.2 \times 10^{-10}$	$2.14 \pm 0.08$	$0.4 \pm 0.2$	3.2e-02
15D	$4.4 \pm 0.3 \times 10^{-10}$	$2.3 \pm 0.1$	$0.2 \pm 0.3$	8.3e-01
15E	$5.9 \pm 0.5 \times 10^{-10}$	$1.9 \pm 0.2$	$0.4 \pm 0.3$	9.9e-01
16A	$6.7 \pm 0.2 \times 10^{-10}$	$1.86 \pm 0.06$	$0.3 \pm 0.1$	5.3e-01
16B	$3.9 \pm 0.3 \times 10^{-10}$	$1.9 \pm 0.1$	$0.4 \pm 0.2$	2.2e-01
16C	$2.6 \pm 0.1 \times 10^{-10}$	$2.0 \pm 0.1$	$0.6 \pm 0.2$	5.8e-01
16D	$5.4 \pm 0.2 \times 10^{-10}$	$2.01 \pm 0.07$	$0.6 \pm 0.1$	1.8e-01
16E	$3.1 \pm 0.2 \times 10^{-10}$	$2.12 \pm 0.10$	$0.4 \pm 0.2$	7.1e-01
16F	$6.9 \pm 0.4 \times 10^{-10}$	$1.96 \pm 0.08$	$0.5 \pm 0.1$	8.7e-01
16G	$12.2 \pm 0.6 \times 10^{-10}$	$1.87 \pm 0.07$	$0.5 \pm 0.1$	1.5e-01
16H	$16.4 \pm 0.4 \times 10^{-10}$	$1.76 \pm 0.04$	$0.37 \pm 0.07$	9.5e-01
16I	$5.6 \pm 0.2 \times 10^{-10}$	$1.99 \pm 0.06$	$0.5 \pm 0.1$	2.7e-01
16J	$19.1 \pm 0.5 \times 10^{-10}$	$1.83 \pm 0.04$	$0.37 \pm 0.07$	1.6e-02
16K	$12.7 \pm 0.6 \times 10^{-10}$	$1.94 \pm 0.07$	$0.3 \pm 0.1$	7.4e-01
16L	$7.6 \pm 0.2 \times 10^{-10}$	$1.96 \pm 0.05$	$0.50 \pm 0.10$	2.2e-01
16M	$2.0 \pm 0.3 \times 10^{-10}$	$2.8 \pm 0.2$	$0.2 \pm 1.0$	5.5e-01
16N	$6.8 \pm 0.3 \times 10^{-10}$	$2.01 \pm 0.08$	$0.4 \pm 0.2$	2.0e-01
16O	$2.0 \pm 0.2 \times 10^{-10}$	$2.5 \pm 0.1$	$0.0 \pm 0.9$	4.6e-01
16P	$3.7 \pm 0.1 \times 10^{-10}$	$2.16 \pm 0.06$	$0.5 \pm 0.1$	6.5e-01
16Q	$3.2 \pm 0.3 \times 10^{-10}$	$2.5 \pm 0.2$	$0.3 \pm 0.4$	3.3e-01
16R	$2.7 \pm 0.2 \times 10^{-10}$	$2.69 \pm 0.08$	$0.0 \pm 0.6$	1.2e-01

Table 8.6: Spectral fitting result of MAGIC spectra with Log-parabola function in 2017-2019

BBLabel	$K$	$\alpha$	$\beta$	P-value
–	[ $\text{cm}^{-2} \text{s}^{-1} \text{TeV}^{-1}$ ]	–	–	–
17A	$4.3 \pm 0.2 \times 10^{-10}$	$2.1 \pm 0.1$	$0.4 \pm 0.2$	3.8e-01
17B	$1.5 \pm 0.1 \times 10^{-10}$	$2.5 \pm 0.1$	$0.2 \pm 0.4$	4.4e-01
17C	$2.0 \pm 0.1 \times 10^{-10}$	$2.1 \pm 0.1$	$0.7 \pm 0.2$	6.4e-02
17D	$2.7 \pm 0.2 \times 10^{-10}$	$2.14 \pm 0.08$	$0.4 \pm 0.2$	5.3e-01
17E	$5.8 \pm 0.3 \times 10^{-10}$	$1.98 \pm 0.08$	$0.3 \pm 0.2$	1.8e-01
17F	$2.5 \pm 0.1 \times 10^{-10}$	$2.2 \pm 0.1$	$0.2 \pm 0.3$	4.8e-01
17G	$5.1 \pm 0.2 \times 10^{-10}$	$1.94 \pm 0.07$	$0.2 \pm 0.2$	9.9e-02
17H	$3.6 \pm 0.2 \times 10^{-10}$	$2.18 \pm 0.07$	$0.1 \pm 0.2$	1.2e-01
17I	$1.48 \pm 0.08 \times 10^{-10}$	$2.2 \pm 0.1$	$0.4 \pm 0.2$	8.7e-01
17J	$8.0 \pm 0.2 \times 10^{-10}$	$2.06 \pm 0.05$	$0.2 \pm 0.1$	1.0e-02
17K	$4.7 \pm 0.2 \times 10^{-10}$	$2.10 \pm 0.08$	$0.1 \pm 0.2$	1.6e-01
17L	$1.7 \pm 0.2 \times 10^{-10}$	$1.9 \pm 0.5$	$0.5 \pm 0.8$	9.0e-01
18A	$1.89 \pm 0.09 \times 10^{-10}$	$1.9 \pm 0.1$	$0.5 \pm 0.2$	7.9e-01
18B	$5.0 \pm 0.2 \times 10^{-10}$	$2.00 \pm 0.08$	$0.4 \pm 0.2$	6.9e-02
18C	$3.4 \pm 0.2 \times 10^{-10}$	$1.8 \pm 0.1$	$0.5 \pm 0.2$	7.7e-01
18D	$2.66 \pm 0.08 \times 10^{-10}$	$2.12 \pm 0.07$	$0.3 \pm 0.1$	8.1e-01
19A	$1.6 \pm 0.3 \times 10^{-10}$	$2.0 \pm 0.5$	$0.5 \pm 0.6$	8.6e-01
19B	$1.57 \pm 0.06 \times 10^{-10}$	$1.90 \pm 0.10$	$0.6 \pm 0.1$	6.5e-01
19C	$0.65 \pm 0.06 \times 10^{-10}$	$2.0 \pm 0.2$	$0.4 \pm 0.3$	9.5e-02
19D	$1.40 \pm 0.08 \times 10^{-10}$	$2.1 \pm 0.1$	$0.3 \pm 0.3$	6.6e-01
19E	$0.96 \pm 0.03 \times 10^{-10}$	$2.32 \pm 0.07$	$0.3 \pm 0.2$	1.9e-01
19F	$0.93 \pm 0.10 \times 10^{-10}$	$1.9 \pm 0.2$	$0.6 \pm 0.3$	8.8e-02
19G	$1.13 \pm 0.05 \times 10^{-10}$	$1.90 \pm 0.09$	$0.4 \pm 0.1$	2.2e-01
19H	$0.4 \pm 0.2 \times 10^{-10}$	$2.1 \pm 1.1$	$0 \pm 2$	2.5e-01

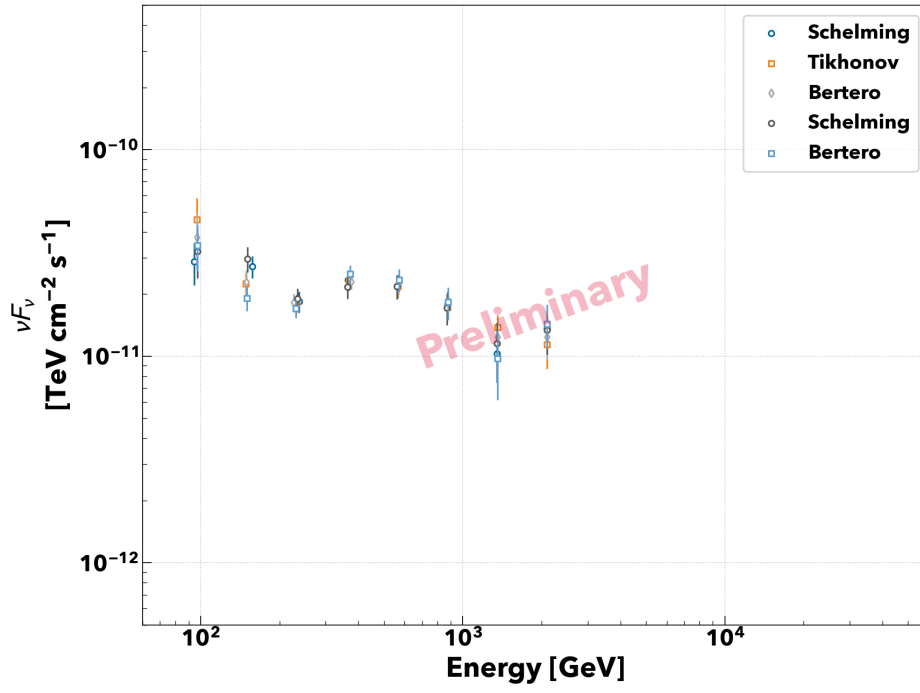


Figure 8.3: MAGIC SED in the bayesian block period of 16C

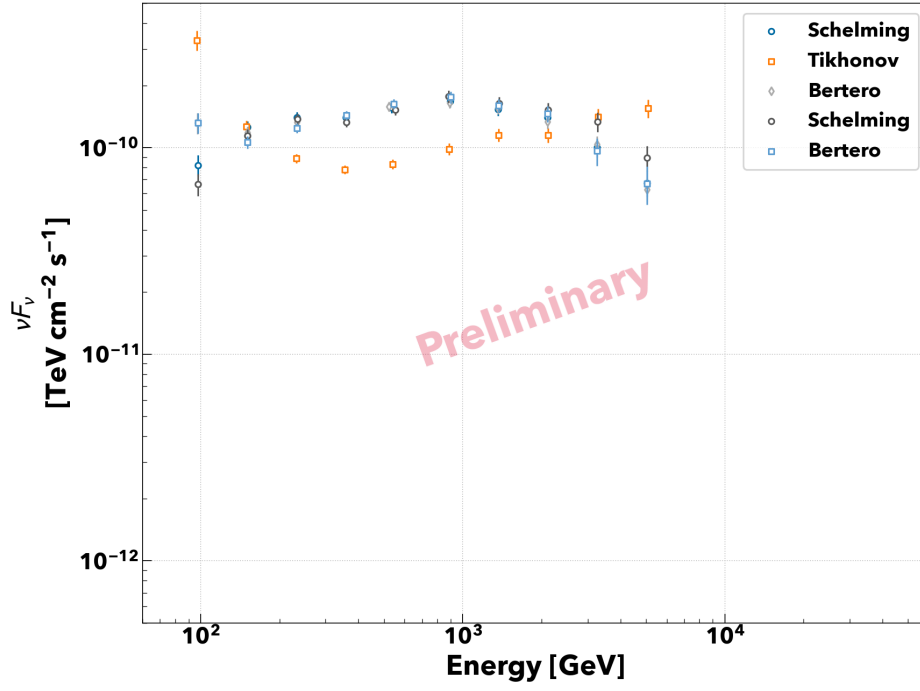


Figure 8.4: MAGIC SED in the bayesian block period of 16H. The result with Tikhonov regularization shows different spectral points with others. This is because estimated intrinsic

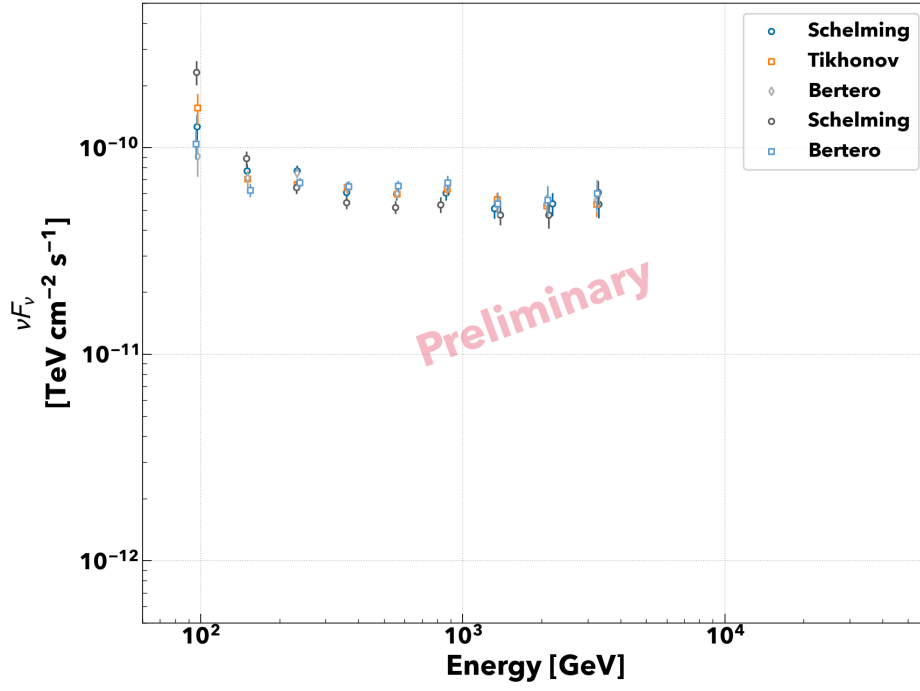


Figure 8.5: MAGIC SED in the bayesian block period of 17J

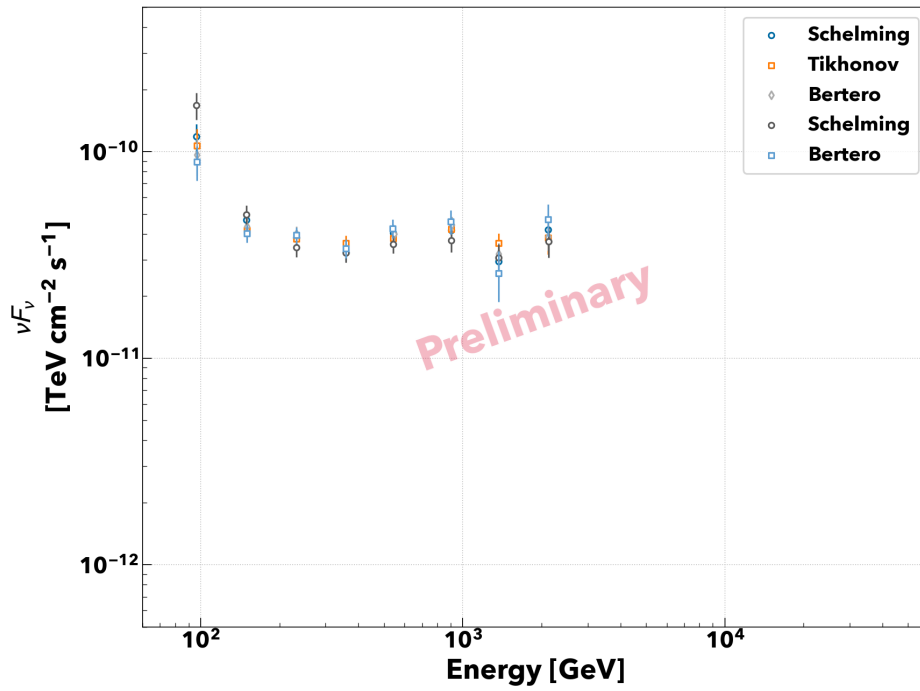


Figure 8.6: MAGIC SED in the bayesian block period of 17K



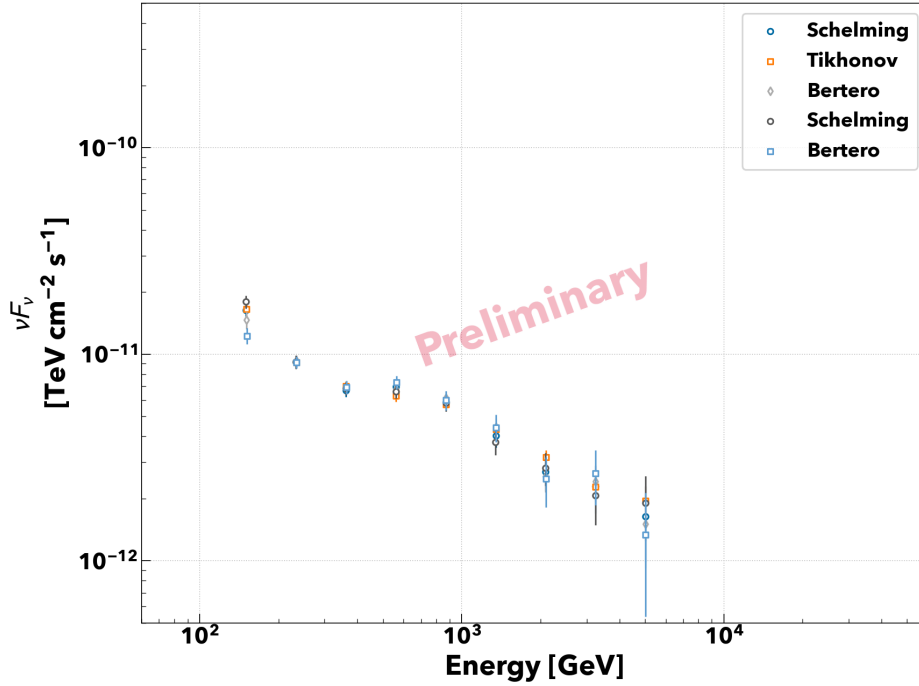


Figure 8.7: MAGIC SED in the bayesian block period of 19E

## 9. Summary of MAGIC analysis result

Very high-energy (VHE) gamma-ray observations by MAGIC telescope more than 300 hours were analyzed to investigate the variability of AGN 1ES 1959+650. Half of the observations were conducted under moonlight, which is normally discarded as worse quality. In this study, I performed the moon analysis and recovered those high noise level observations. Photon flux light curve above 300 GeV (fig. 8.1) showed historical maximum flux and decaying trend 2017 onwards. Bayesian block analysis enabled to perform spectral analysis along the variability. The reconstructed spectral shapes were clearly different in 2016 and 2017 flare (fig. 8.4 and 8.5). This suggests emission mechanism in gamma-ray band is changing in time. However, information obtained from VHE gamma-ray data is limited. To evaluate multiwavelength (MWL) property of 1ES 1959+650, MWL analysis and results are discussed in the following sections.

## **Part III.**

# **Study of Temporal Variabilities and Emission Models of 1ES 1959+650 with Multiwavelength data**

## 10. Multiwavelength Instruments

As discussed in part II, the MAGIC observation showed variable emissions over five years. But multiwavelength (MWL) data is required to deeply understand the emission mechanism of 1ES 1959+650 because information from VHE gamma rays is limited.

This section gives MWL instruments and MWL analysis details of the temporal and the spectral analysis. First, each instrument is introduced with their results and temporal analysis is explained later. Finally, spectral modeling with a one-zone SSC model is discussed to understand the variability of 1ES 1959+650 and estimate what was happening over the observation period.

### 10.1. Fermi Large Area Telescope

The Large Area Telescope (LAT or *Fermi*-LAT) is a pair-conversion gamma-ray detector on the *Fermi* gamma-ray satellite together with Gamma-ray Burst Monitor. *Fermi*-LAT is a successor of the EGRET telescope (Sreekumar et al., 1998), and it has detected more than 5000 gamma-ray sources since it launched in 2008 (Abdollahi et al., 2020).

LAT measures the energy and direction of gamma rays using silicon-strip detectors and calorimeters. Gamma rays are converted into electron-positron pairs at the tungsten layer in the middle of silicon trackers. Once electron pair is produced, they leave their trajectories on the trackers. The electron pair reaching the calorimeter makes electromagnetic showers as discussed 6.1.1. Finally, the electrons are absorbed in the calorimeters.

The charged particles, such as electrons and protons, are recognized using veto counters at the surface of the LAT detector (Anti Coincidence Detector, ACD). The veto plays an essential role in the background rejection. Thus LAT can observe gamma rays without huge background contamination. Figure 10.1 is a picture of *Fermi*-LAT, the upper part is the trackers and the bottom is the calorimeter. See Ackermann et al. (2012) for instrumental details.

LAT can observe the entire sky every three hours. Therefore LAT is the best gamma-ray instrument to monitor the gamma-ray object and sky. However, the effective area is limited compared with the ground-based telescopes. Thus the statistical error is always large when one analyzes the short-term data.

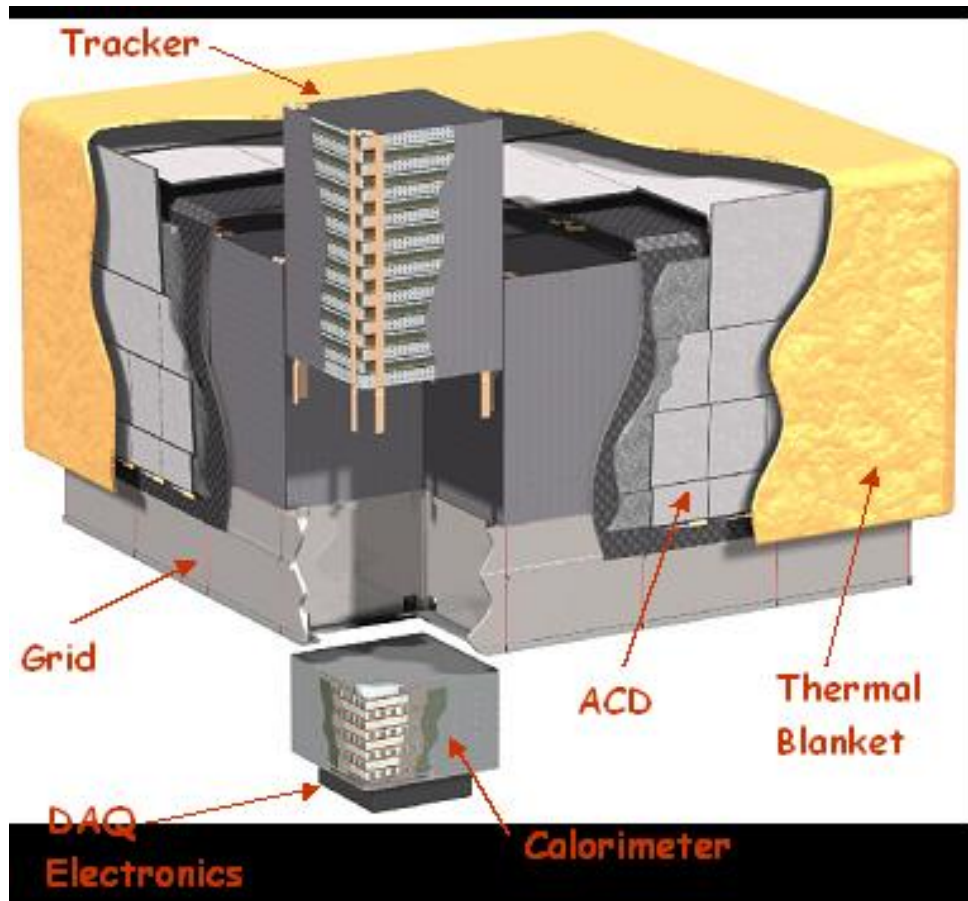


Figure 10.1: Schematic view of Fermi LAT telescope. ADC denotes anti-coincidence detector for charged particles. Gamma rays are converted into electron pairs and are absorbed by calorimeter. Credit: <https://fermi.gsfc.nasa.gov/>

### 10.1.1. Performance

Here, the latest performance of *Fermi*-LAT are introduced. The performance depends on the event selection, but I will show the one evaluated with the standard event selection (PASS8\_SOURCE\_V3). The energy resolution is 10 % at 1 GeV, and even better till 1 TeV as shown in figure 10.2.

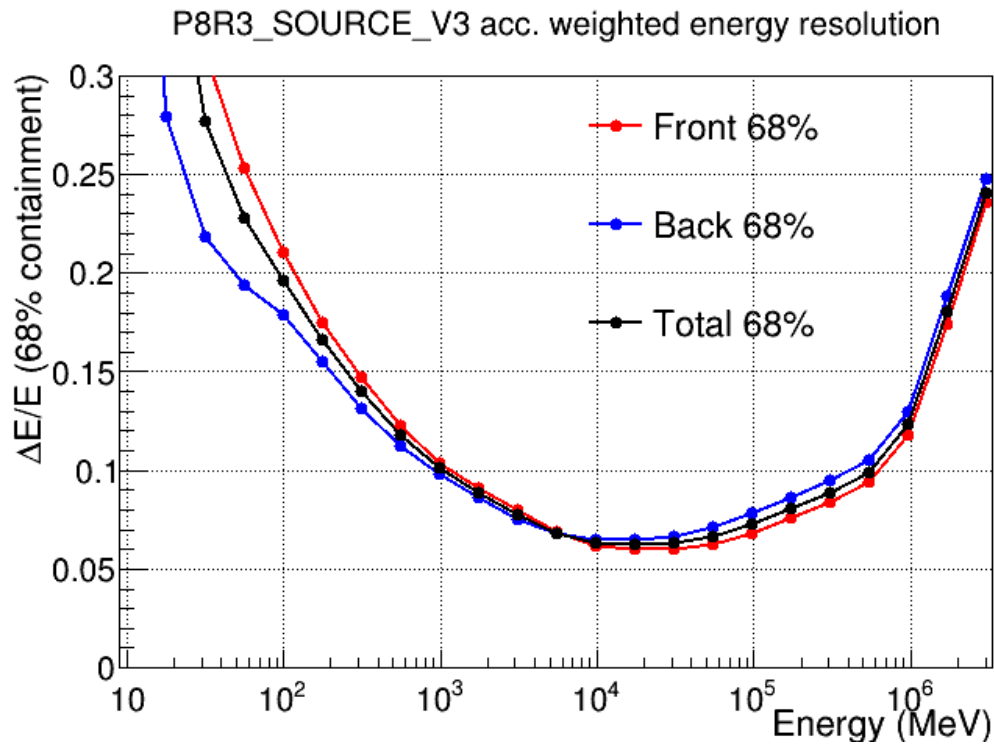
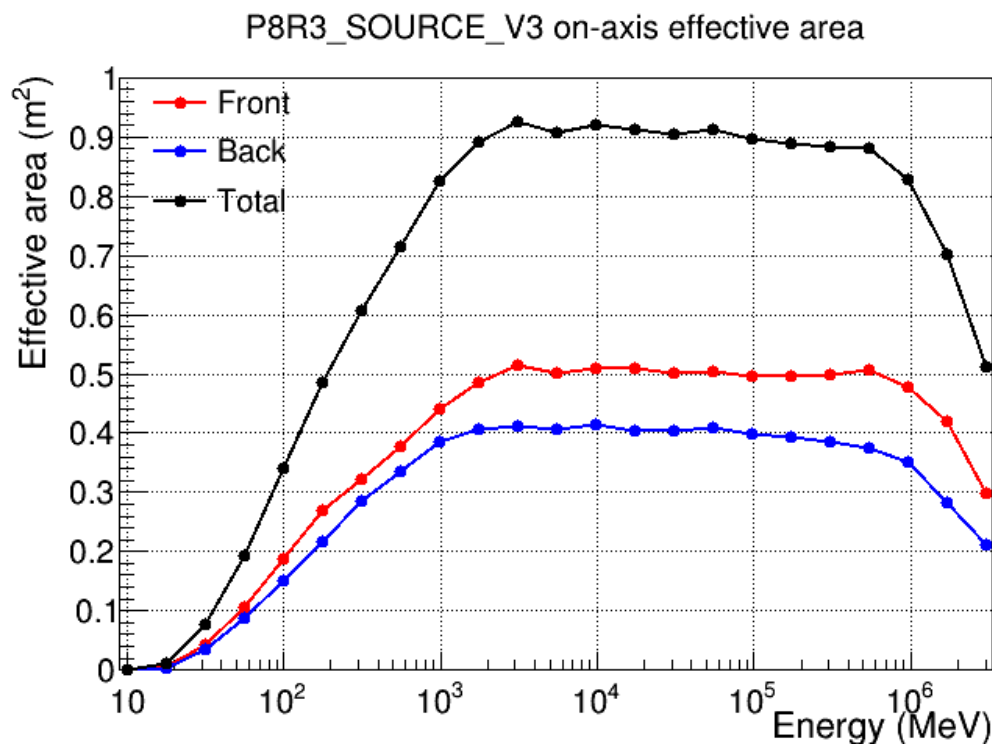


Figure 10.2: *Fermi*-LAT energy resolution<sup>10</sup>. the energy resolution is defined as the half width of 68% containment of reconstructed photon energy distribution. Front and Back denote the incoming direction of gamma rays with respect to LAT zenith direction.

<sup>10</sup>SLAC webpage: [https://www.slac.stanford.edu/exp/glast/groups/canda/lat\\_Performance.htm](https://www.slac.stanford.edu/exp/glast/groups/canda/lat_Performance.htm)

Figure 10.3: *Fermi*-LAT effective Area<sup>11</sup>

On-axis effective area is shown in figure 10.3. The typical value is about one square meter, which is quite small compared with ground-base telescope (about  $10^5 \text{ m}^2$ ).

Angular resolution is roughly 1 degree and even better at high energy as shown in figure 10.4. In this study I used only good PSF events to avoid contamination from galactic plane.

<sup>11</sup>SLAC webpage: [https://www.slac.stanford.edu/exp/glast/groups/canda/lat\\_Performance.htm](https://www.slac.stanford.edu/exp/glast/groups/canda/lat_Performance.htm)

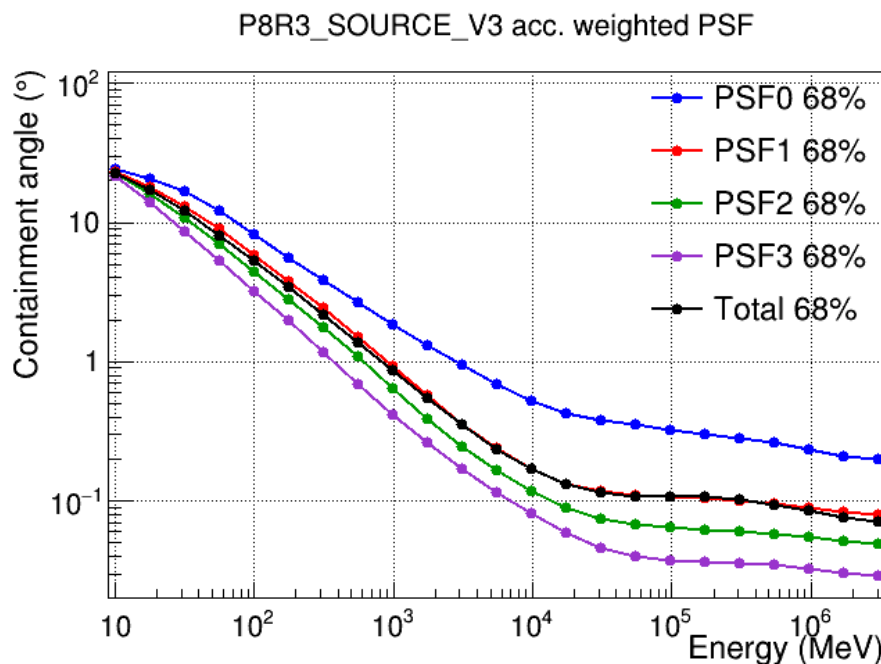


Figure 10.4: *Fermi*-LAT angular resolution<sup>12</sup>, 68% radii of the reconstructed photon direction are shown. PSF0 is worst angular precision events, and PSF3 is the best.

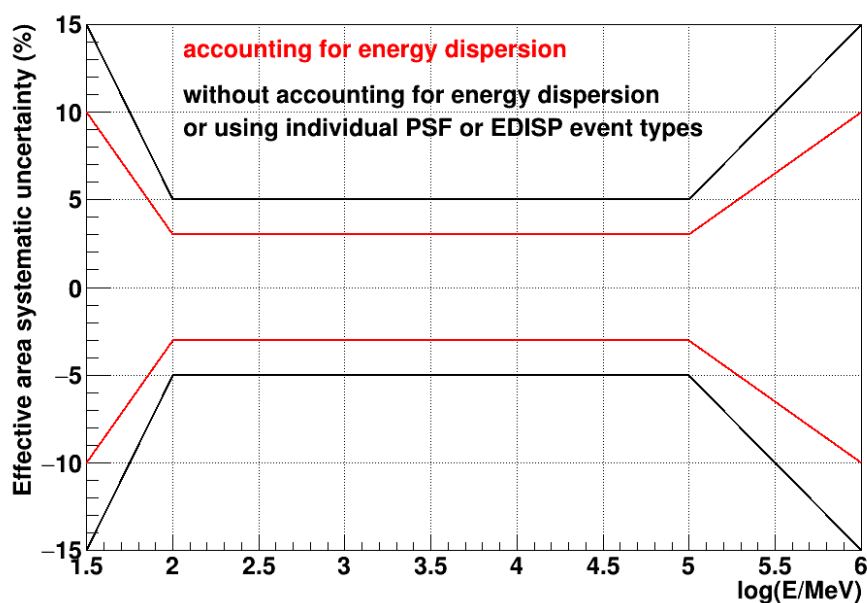


Figure 10.5: Systematic uncertainty in the effective area<sup>13</sup>.

<sup>12</sup>SLAC webpage: [https://www.slac.stanford.edu/exp/glast/groups/canda/lat\\_Performance.htm](https://www.slac.stanford.edu/exp/glast/groups/canda/lat_Performance.htm)

Table 10.1: Selected period for *Fermi*-LAT spectral analysis

MJD start	MJD end	days	Label
57510.75	57522.25	11.5	16-C
57551.75	57553.25	1.5	16-H
58046.75	58052.25	5.5	17-K
58675.75	58745.25	69.5	19-E

Figure 10.5 shows systematic uncertainties in the effective area of *Fermi*-LAT analysis. It is less than 5 % between 100 MeV to 100 GeV when energy dispersion is taking into account. I included 5 % in the MWL spectral modeling to improve huge  $\chi^2$  values.

Background-free gamma-ray observation enables a likelihood approach to estimate fluxes of individual objects. This section introduces binned likelihood method and analysis used in *Fermi*-lat data analysis.

### 10.1.2. Analysis Software

Standard software `fermitools` and python package `fermipy` were used to perform the binned likelihood analysis ([Fermi Science Support Development Team, 2019](#); [Wood et al., 2017](#)).

### 10.1.3. Data Selection

For the light curve, I downloaded the all available photon files and space-craft files from the NASA GodDard space center server. For the Spectral analysis, I selected the following period corresponding to the VHE analysis results.

### 10.1.4. Photon Reconstruction

Reconstruction of the energy and direction of incoming gamma rays was done automatically at the NASA server<sup>14</sup>. This event reconstruction program is called "Pass", the latest version is Pass 8 release 3 (P8R3, [Atwood et al. \(2013\)](#)). The events are classified by precision of the reconstructed parameters and divided into `eventclass` and `eventtype`. In this study I used `eventclass` = 128, P8R3.SOURCE which is recommended in standard analysis, appropriate for the point source. `eventtype` = 8,16,32 was used, the event type is defined as Point Spread Function (PSF) type. This is classified by the quality of reconstructed direction. I adopted this type because 1ES 1959+650 locates near the galactic plane to avoid the contamination from the plane.

<sup>13</sup>Caveats About Analyzing LAT Pass 8 (P8R3.V3) Data: [https://fermi.gsfc.nasa.gov/ssc/data/analysis/LAT\\_caveats.html](https://fermi.gsfc.nasa.gov/ssc/data/analysis/LAT_caveats.html)

<sup>14</sup><https://fermi.gsfc.nasa.gov/cgi-bin/ssc/LAT/LATDataQuery.cgi>



### 10.1.5. Binned Likelihood Analysis

Data analysis of *Fermi*-LAT have two options. One is an aperture photometry method. This method regards gamma rays coming from inside a specific radius as emission from a source. This method is simple but not precise because gamma-ray position accuracy is worse than the one of lower frequency like optical astronomy. Contaminations from the surrounding source or isotropic, or galactic background can not be subtracted. Aperture photometry is useful when it is important to check relative variability if the background contribution is constant.

Alternatively, one can choose of the likelihood analysis. In the likelihood analysis, gamma-ray sources are modeled its position and spectra. Once models are defined, the expected signal can be determined by convoluting instrument response performance. Assuming the poisson statistics, likelihood  $\mathcal{L}$  is defined as

$$\mathcal{L} = \prod_{i \in \text{source}} \frac{e^{-m_i} m_i^{n_i}}{n_i!} = e^{-N_{\text{obs}}} \prod_{i \in \text{source}} \frac{m_i^{n_i}}{n_i!}, \quad (10.1)$$

where  $N_{\text{obs}}$  is total observed gamma-rays,  $n_i$  is a count from  $i$ -th source, and  $m_i$  is an expected count from the source  $i$  and is defined by

$$m_i(E', \vec{\Omega}', t) = \int S(E, \vec{\Omega}, t) R(E', \vec{\Omega}'; E, \vec{\Omega}, t) dE d\vec{\Omega} \quad (10.2)$$

$$R(E', \vec{\Omega}'; E, \vec{\Omega}, t) = A(E, \vec{\Omega}, \vec{L}(t)) D(E'; E, \vec{\Omega}, \vec{L}(t)) P(\vec{\Omega}'; E, \vec{\Omega}, \vec{L}(t)) \quad (10.3)$$

$S$  and  $R$  is source model and instrument response respectively.  $R$  depends on the energy  $E$ , telescope direction  $\vec{\Omega}$  and time  $t$ .  $A$  is effective area,  $D$  is energy dispersion, and  $P$  is point spread function. One can regard the model providing the maximum likelihood as most plausible model. Once the best model is estimated, significance of the source is estimated through maximum likelihood ratio test as

$$\text{TS} = -2 \log \left( \frac{\mathcal{L}_{\text{max},0}}{\mathcal{L}_{\text{max},1}} \right) \sim \chi^2, \quad (10.4)$$

where  $\mathcal{L}_{\text{max},0}$  is the maximum likelihood without a target and  $\mathcal{L}_{\text{max},1}$  is that with the target. See this website for more details<sup>15</sup>. I used a power-law function and log-parabola function for the analysis of 1ES 1959+650. Because of less statistics in short time analysis data and log-parabola function well explain long-term spectra.

For the analysis setting, the 20 degree squared region centered at 1ES 1959+650 was used in the analysis and the spatial resolution was set to 0.1 degree. For the energy, I adopted 6 bins per energy decade, and combined them in the Spectral Energy Distribution (SED) calculation. The energy range in the analysis was 300 MeV to 300 GeV for the light curve analysis and 100 MeV to 300 GeV for the SED analysis. In order to

<sup>15</sup>NASA website: [https://fermi.gsfc.nasa.gov/ssc/data/analysis/scitools/source\\_models.html](https://fermi.gsfc.nasa.gov/ssc/data/analysis/scitools/source_models.html)

cut the earth-limb contribution, events have the incident zenith angle larger than 90 degrees are excluded from the analysis. The gamma-ray sources inside 30 degrees from the 1ES1959+650 are included in the likelihood model. After the likelihood maximization, the differential map between model and data were checked as shown in figure 10.6. If excess reaching five sigma was found, additional source was modeled with a power-law assumption. The additional sources were needed for the latter half of 2018, and 2019. But no critical effect in the spectral model of 1ES1959+650.

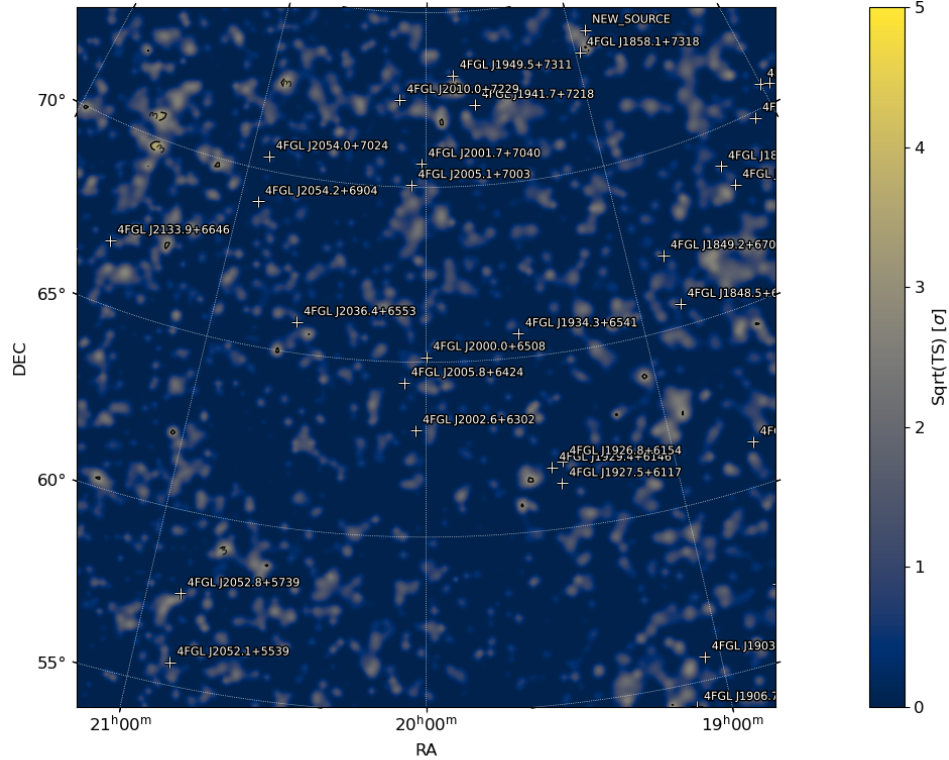


Figure 10.6: Validation plot after model optimization, no large significance indicates the model can explain the data well. 1ES 1959+650 are placed at the center of plot.

### 10.1.6. Light curves

Light curves was calculated by optimizing a normalization of the source flux. Figure 10.7 shows *Fermi*-LAT light curves with weekly and 21-day bins. The energy range is from 30 MeV to 300 GeV. When TS is less than nine, which corresponds to three sigma, 95 % confidence level upper limit is plotted instead of the flux point. Because of the statistical error largeness, one can difficult to judge the variability. However, the from mid 2015 to 2016 and middle 2016, flux bins are deviated from the zero flux level more than 3 sigma in

weekly bins. Some short increasing period roughly coincides with VHE gamma-ray light curve as discussed later. In the gap in 2018, *Fermi*-LAT stopped its operation because of the operation problem. It seems that the flux showed decaying trend in time, as similar as the MAGIC light curve.

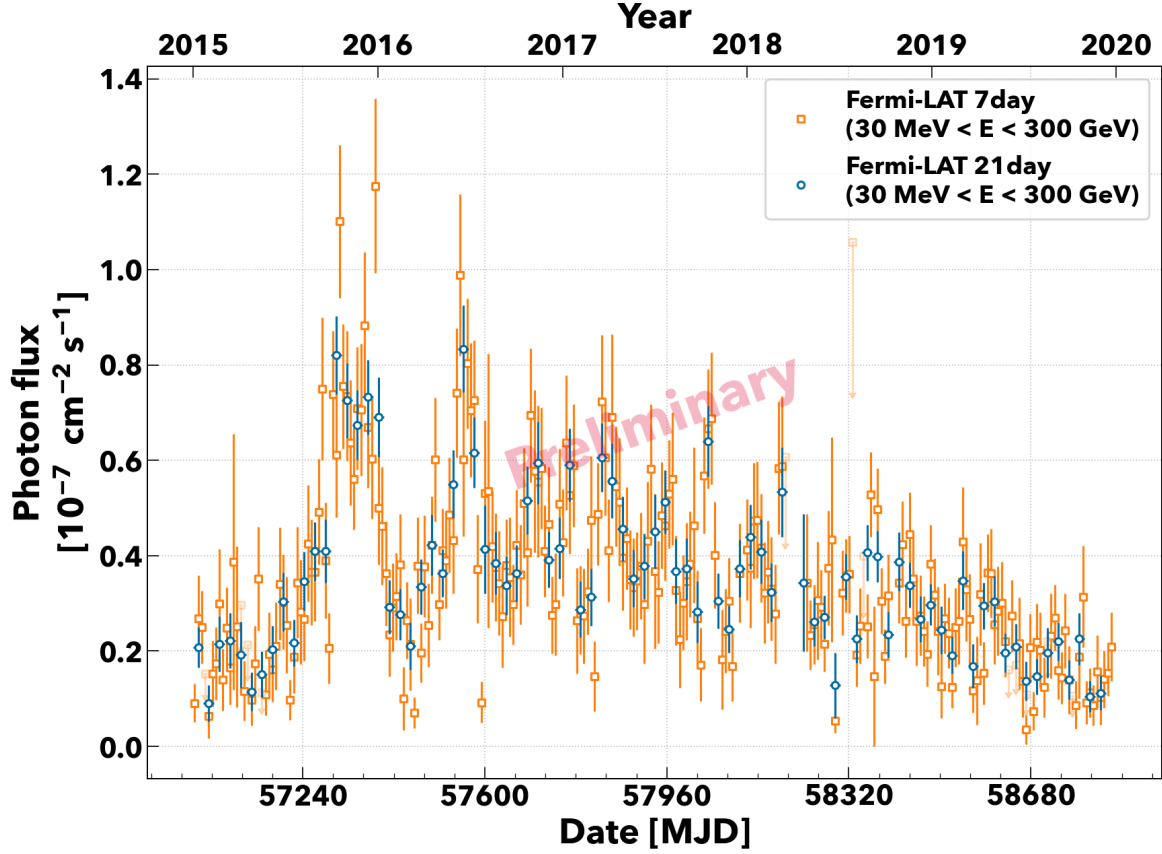


Figure 10.7: LAT light curve. Blues are 21-day flux and oranges are weekly flux, respectively. If TS is less than 9 (equals to three sigma confidence level), it is shown as 95 % confidence level upper limit.

x

### 10.1.1.7. Spectral Energy Distrubution

*Fermi*-LAT SEDs were calculated for the selected periods derived by the MAGIC analysis. Figures 10.8 to 10.11 show spectral energy distributions for the energy range 100 MeV to 300 GeV. Flux points are shown if the test statistic of each energy bin is larger equal four (two sigma level). Figures 10.9 and 10.10 are in the VHE gamma-ray active states, and others are in the low states. Comparing with MAGIC SEDs (e.g., Fig. 8.3), All the spectra smoothly connect to the MAGIC SEDs at the end of the analysis energy range.

Spectral index become a hard when the source is bright, and it is really flat ( $\alpha \sim 2$ ,  $dN/dE \propto E^{-\alpha}$ ) in the low state suggested by previous studies.

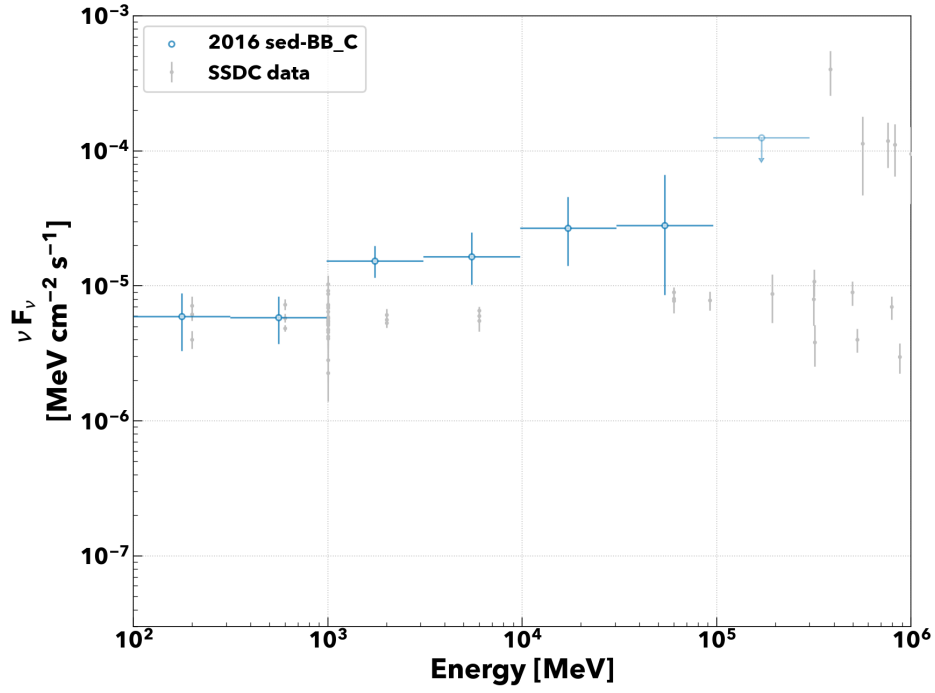


Figure 10.8: LAT SED for Bayesian block 16C

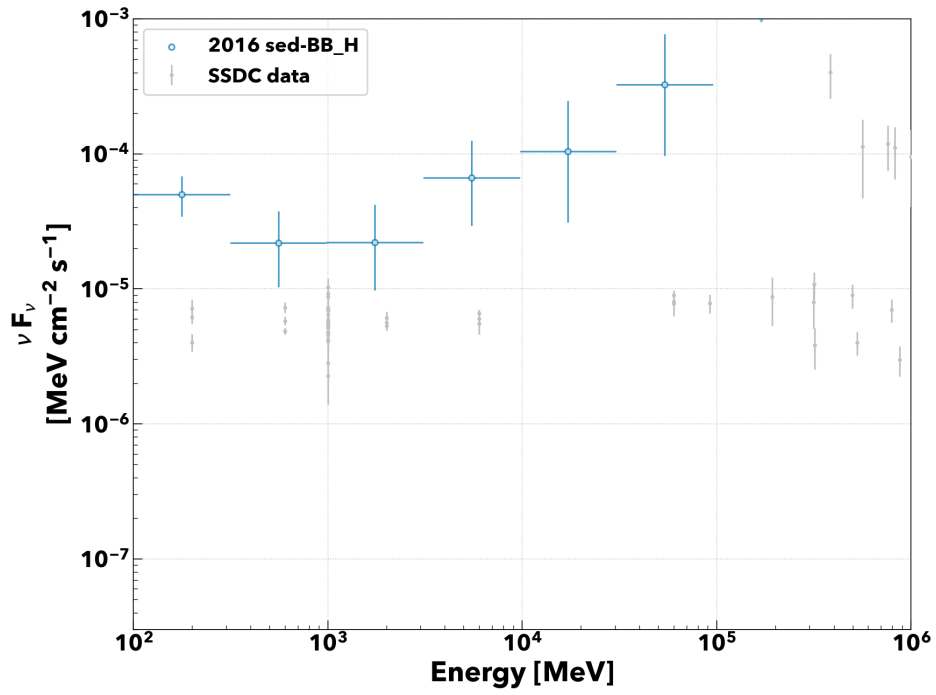


Figure 10.9: LAT SED for Bayesian block 16H

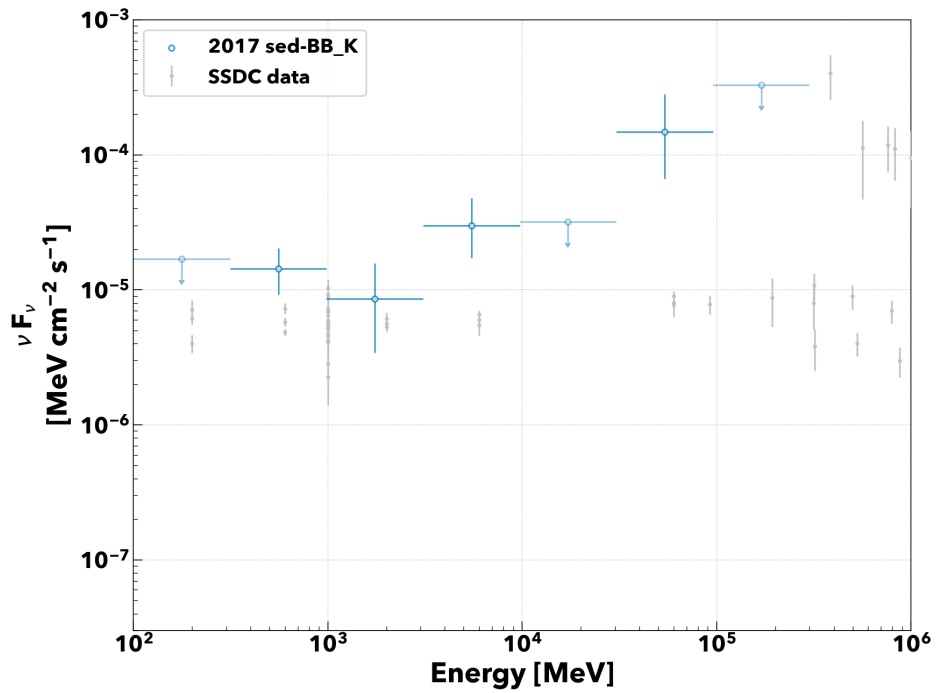


Figure 10.10: LAT SED for Bayesian block 17K

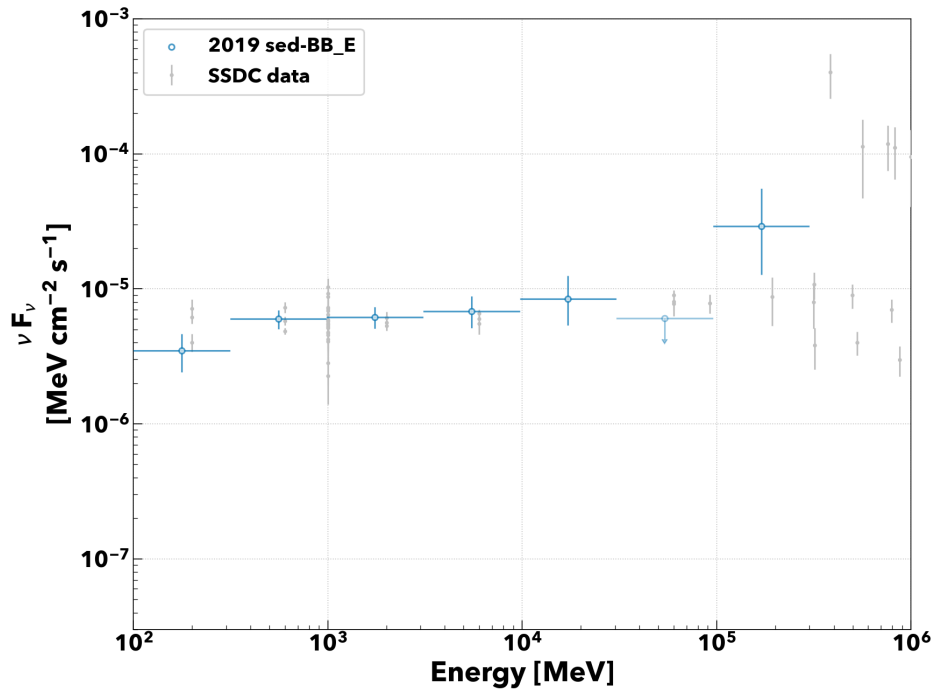


Figure 10.11: LAT SED for Bayesian block 19E

## 10.2. *Swift* X-Ray Telescope

*Swift* satellite was developed to study gamma ray bursts (GRB) and the early universe using GRBs (Gehrels et al., 2004). The satellite is equipped with several instruments to know the happenings of GRBs and to observe multi-wavelength properties.

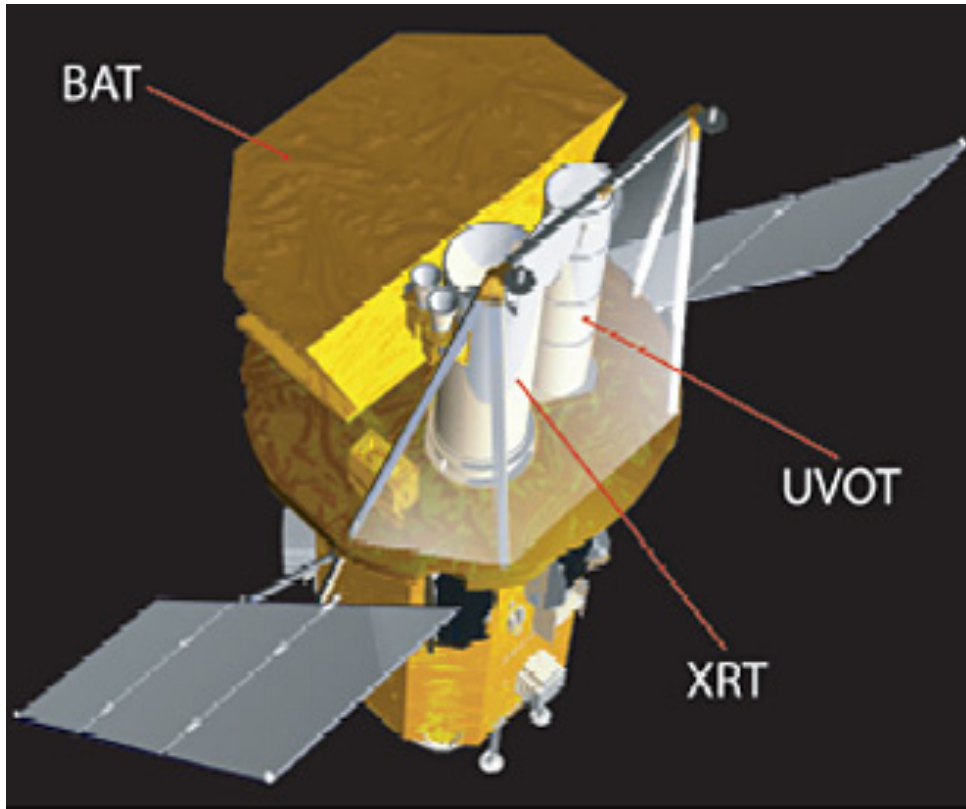


Figure 10.12: *Swift*satellite([https://www.nasa.gov/mission\\_pages/swift/spacecraft/](https://www.nasa.gov/mission_pages/swift/spacecraft/)). There are three instruments on board, Burst Alert Telescope detects x-ray transient events by wide field of view and slews the satellite. Co-aligned X-ray Telescope and Ultraviolet and Optical Telescope start observation as soon as possible.

The X-ray telescope (XRT) is a Wolter type-I telescope on the *Swift* satellite as shown in figure 10.12 (Burrows et al., 2005). The telescope has a dedicated mirrors to focus x rays onto the imaging detector. The available x-ray energy range is 0.2 to 10keV, and XRT has a good angular resolution 18 arc sec comparing with gamma-ray instruments. Focused x rays by grazing incident reflectors are recorded on the CCD with  $600 \times 600$  pixels. The field of view is 23 arcmins, and the effective area is about  $100 \text{ cm}^2$  at 1 keV. The energy resolution is less than 5 % at 6 keV. The high energy resolution enables measurement of iron emission line and the redshift with 10 % precision.

XRT instantaneously observes gamma-ray bursts once *Swift*-satellite slewed toward GRB. Moreover, XRT provides soft-xray ToOs activated by multiwavelength instrument.

XRT has several observation modes appropriating the source flux. There used to be Photo Diode (PD), Photon Counting (PC), and Window Timing (WT) mode, but currently WT, and PC modes are available in the observation. PC mode enable to resolve x-ray sky in two-dimensional image, although it will be saturate for bright source. WT mode can observe more luminous source than PC mode, although WT mode observe photons as integrated 1D image. In the WT mode, integrating CCD columns enable to increase dynamic range of incident photon intensity. In this study WT mode was used in the observation.

### 10.2.1. Software

The data analysis was performed with HEASoft provided by NASA<sup>16</sup>. The analysis was conducted from the level 1 which corresponds to the calibration.

### 10.2.2. Calibration

The conversion of CCD signal to the incident X-ray energy is done by the calibration table. Usual users do not touch in this process, and starts from the next level.

### 10.2.3. Data Selection

The data selection for the detail spectral analysis is based on the VHE gamma-ray analysis. To model the MWL spectra, I prepared SED points for the selected runs as described below in table 10.2. ObsID shows an individual observation, which contains continuous data with several hundred seconds. For the light curve, as much data as possible were used. The fundamental analysis steps are the same for the SED points.

---

<sup>16</sup><http://heasarc.gsfc.nasa.gov/ftools>



Table 10.2: Observation details of selected runs.

ObsID	Start time	Exposure [sec]
34532008	2016-05-03T03:42:44	1028
34532010	2016-05-04T03:48:23	988
35025224	2016-05-09T03:09:43	728.6
35025243-01	2016-06-13T02:46:45	505.1
35025243-02	–	489
35025245	2016-06-14T02:18:11	882.7
34588103	2017-10-21T19:51:03	768.5
34588104-01	2017-10-25T17:35:48	487
34588104-02	–	498.8
34588188-01	2019-07-29T22:07:24	1589
34588188-02	–	1097
34588190	2019-08-07T16:26:46	1023
95332016	2019-08-20T23:42:05	1068
95332020	2019-09-16T16:00:34	918.2

#### 10.2.4. Aperture photometry

The aperture photometry is a standard way to estimate the net brightness of the astronomical source on the background contribution. The method requires several regions to obtain the contribution from the source and background radiations. Broad astronomical regions commonly use this method to extract the source information. Figure 10.13 shows a sketch of the method, and it illustrates the source and background regions. When some uniform contribution component exists, subtracting the background region from the source region gives the net brightness of a specific object. How to define those regions are slightly different depending on the experiments. Thus We will introduce details in each instrumental section. In the XRT data analysis, the data taken with the WT mode makes the 1D image as similar as the figure.

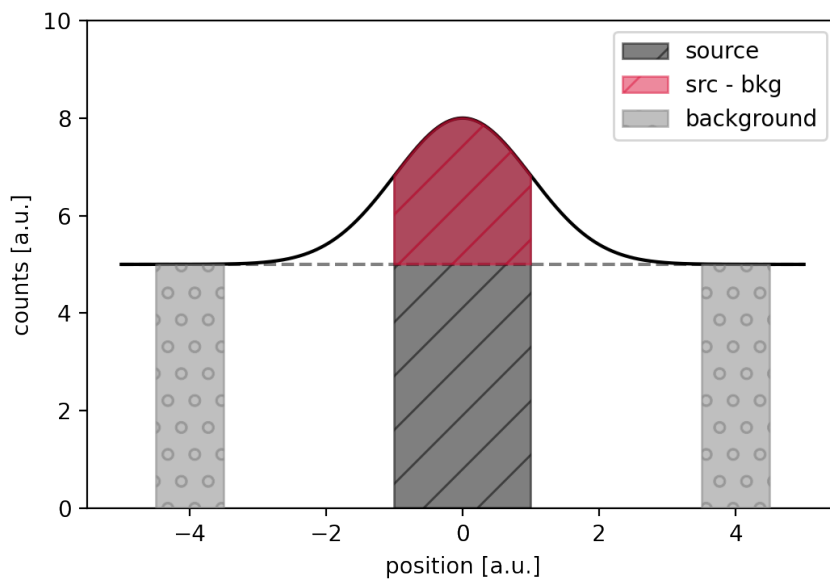


Figure 10.13: Schematic picture of aperture photometry method. Observed image contains a background component and a source component. Subtracting a background component from observation data gives a net source contribution.

### 10.2.5. Background Reduction

In order to subtract a background contribution, I defined the source and background region on the obtained image. The source region is 20 pixels at the center of 1ES 1959+650 and the background region is defined by an annulus with radius 80 pixels to 120 pixels as shown in figure [10.14](#).

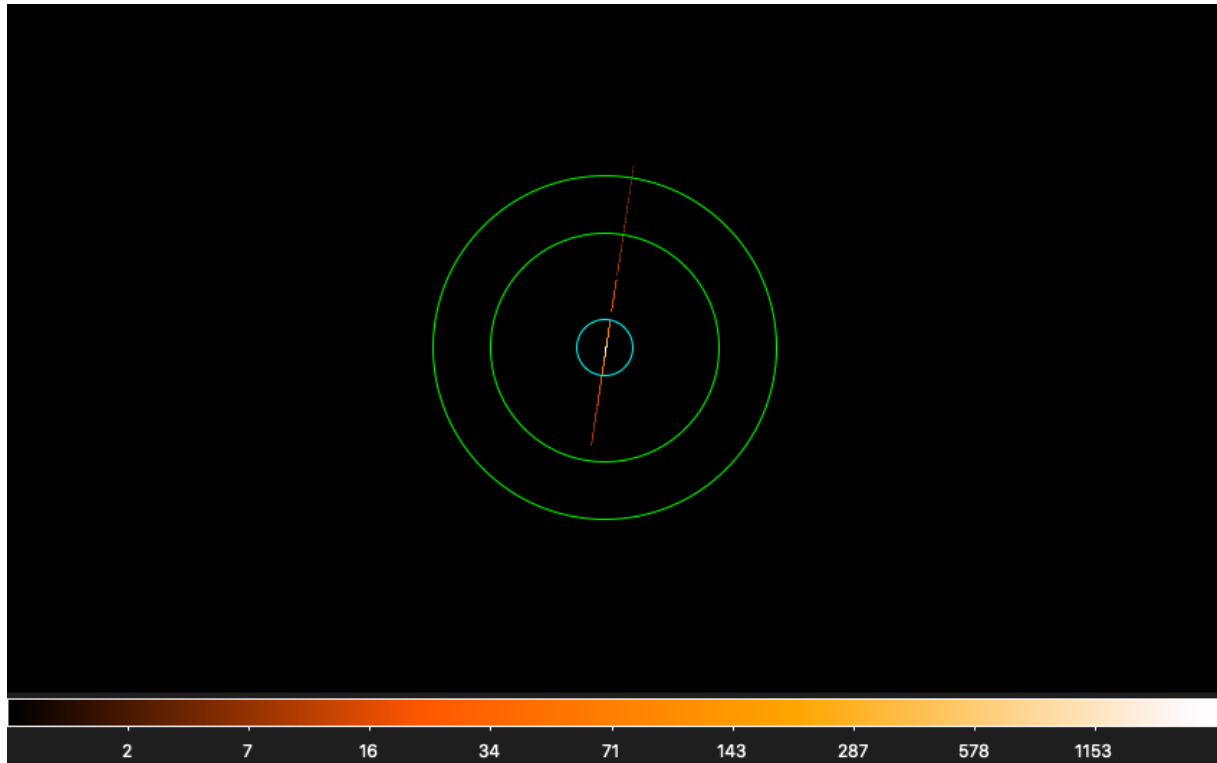


Figure 10.14: Selected regions for analysis of the WT image. Cyan circle is a source region and a green annulus is background region.

Those definition is based on the recommendation by the official XRT analysis document. Some observation contains more than one snapshot as shown in figure 10.15, where the snapshot corresponds to continuous data storing with several hundred seconds.

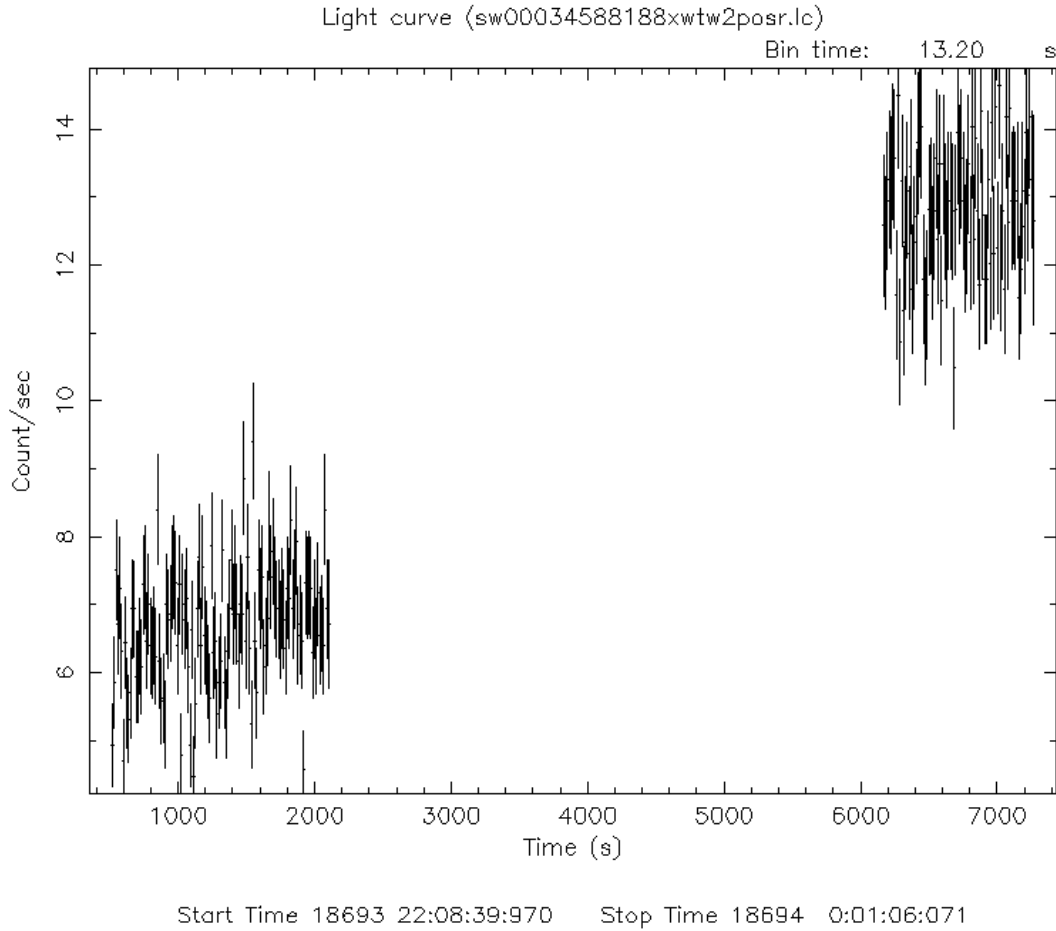


Figure 10.15: Example of the observation containing snapshots.

For such a observation, the data is divided in time and processed as same as other observation.

XRT has dead pixels on the detector, and correction for the dead pixels are taken into account. However, for some observations, the source was out of the window despite the observation was performed. In the case, I excluded the runs from the analysis.

### 10.2.6. Spectral analysis

Spectral analysis requires the spectral model and statistics. The statistics define how to perform the spectral fitting. In this study, I used chi-square statistics for the index of the goodness of fit. For the spectral model, I adopted the power-law function (eq. 10.5) and

log-parabola function (eq. ??) as same as VHE gamma-ray analysis.

$$\frac{dN}{dE} \propto \left( \frac{E}{1 \text{ keV}} \right)^{-\alpha} \quad (10.5)$$

$$\frac{dN}{dE} \propto \left( \frac{E}{1 \text{ keV}} \right)^{-\alpha - \beta \log_{10} \left( \frac{E}{1 \text{ keV}} \right)} \quad (10.6)$$

Moreover, Soft x-rays receive photo-electric absorption due to stellar gas (Morrison & McCammon, 1983). Thus I included the effect in the modeling.

I performed spectral analyses using a software `xspec` in HEASoft. When the parameter estimation is performed, I used two types of binning depending on the purpose. One is a fine binning, at least 25 photons are required in each energy bin to guarantee Gaussian approximation in the fitting procedure. For the fine binning, the energy range is fixed above 0.3 keV. The fitting parameters showing the result section are taken from this binning result.

For the multiwavelength spectral study, I adopted the course binning, which has 8 and 16 bins per decade. The energy range of SED points is 0.3 to 10 keV.

The fixed column density  $n_H$  of  $1.07 \times 10^{21} \text{ cm}^{-2}$  was used for photo-electric absorption

### 10.2.7. Light curve

The long-term light curve of *Swift*-XRT is shown in Figure 10.16.

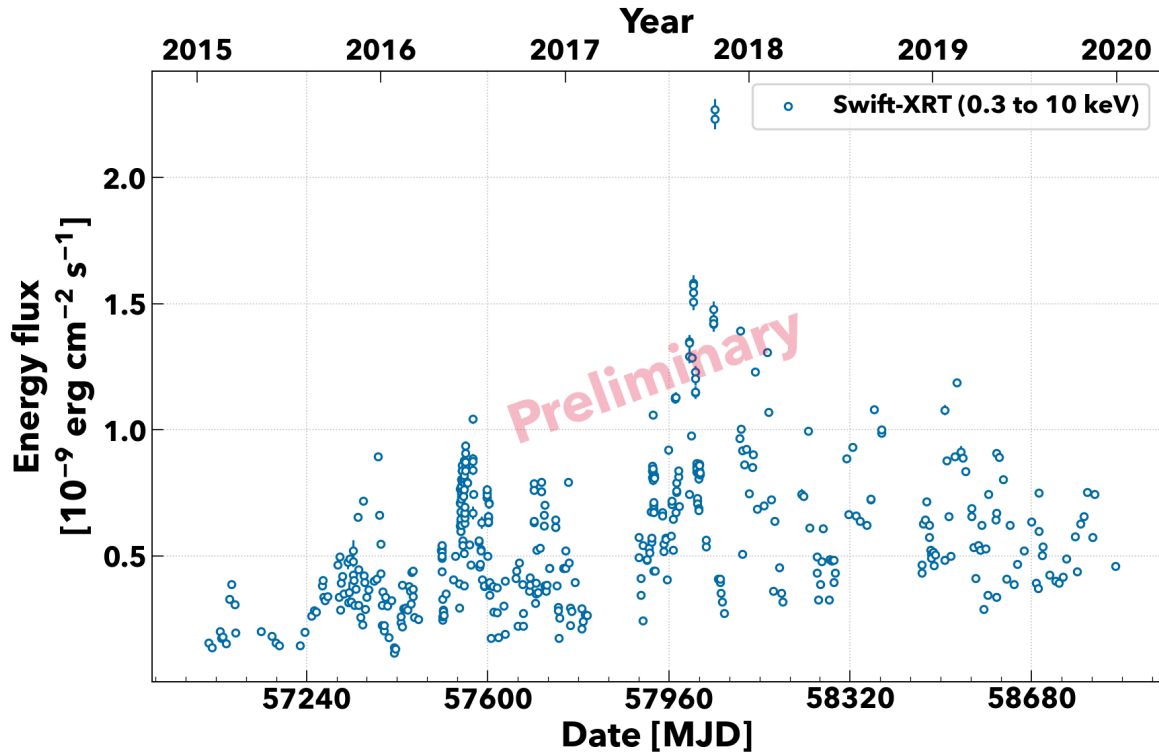


Figure 10.16: X-ray energy-flux light curve. One sigma uncertainties are shown but they are negligibly small.

Energy flux shows variable state through the five-year campaign. As already reported in [MAGIC Collaboration et al. \(2020b\)](#), the X-ray flux showed the historical maximum in 2016 at that time. However, the source became more active in 2017, then showed the new maximum state in 2017 October. This is also reported in [Chandra et al. \(2021\)](#).

To investigate the spectral evolution, the log-parabola index  $\alpha$  and curvature  $\beta$  also plotted with energy flux in Figure 10.17. Correlation plots between two of each parameters are presented in figures 10.18, 10.19, and 10.20. Figure 10.17 implies harder spectra when the energy flux increase, it can be confirmed in figure 10.18. But figure 10.18 suggests more complex behavior of the flux; The average index increased slowly then the values reached about 2.1 despite the average flux was high with respect to 2015. The peak of the log-parabola model can be calculated via:

$$E_{\text{peak}} = 10^{\frac{2-\alpha}{2\beta}} E_{\text{pivot}}, \quad (10.7)$$

where  $E_{\text{pivot}}$  is fixed at 1 keV.

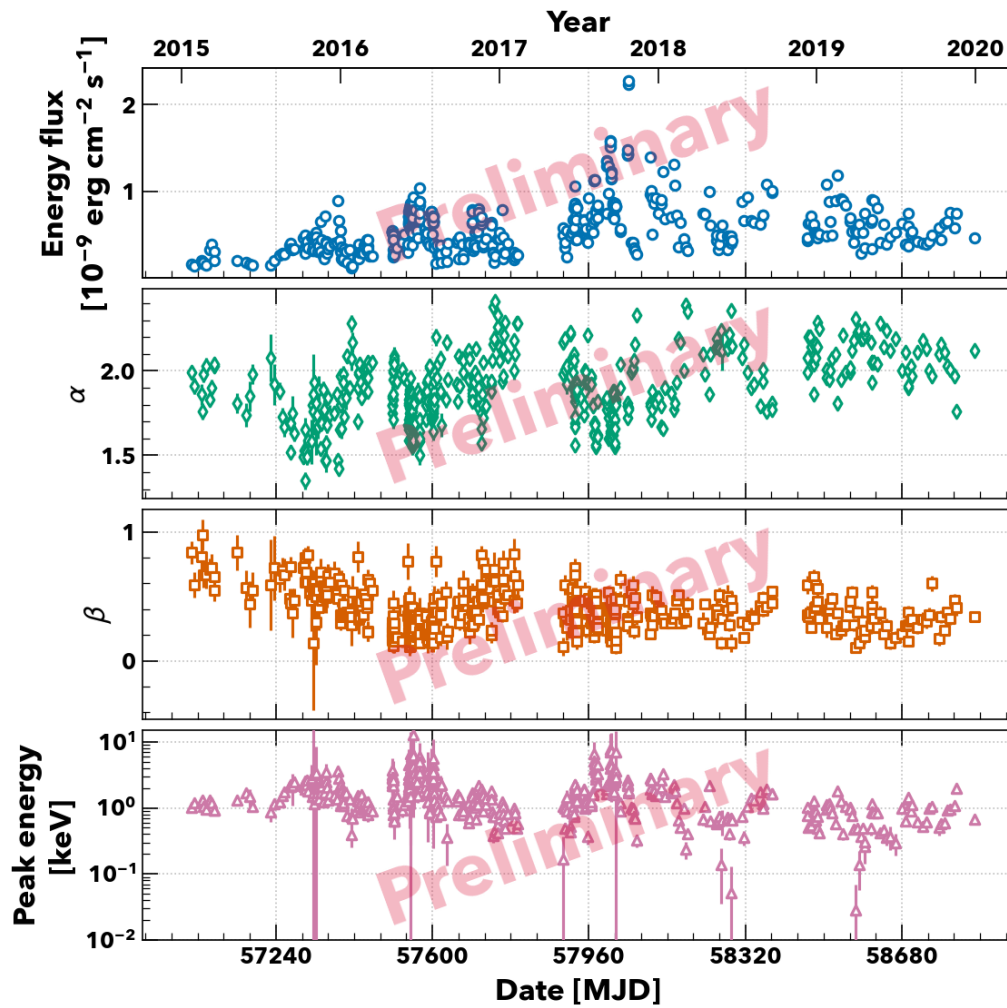


Figure 10.17: XRT spectral evolution with log-parabola model. **Top panel:** Energy flux as same as figure 10.16, **Upper middle panel:** the log-parabola index  $\alpha$ , **lower middle panel:** the log-parabola beta  $\beta$ , and **Bottom panel:** Peak energy obtained from eq 10.7.

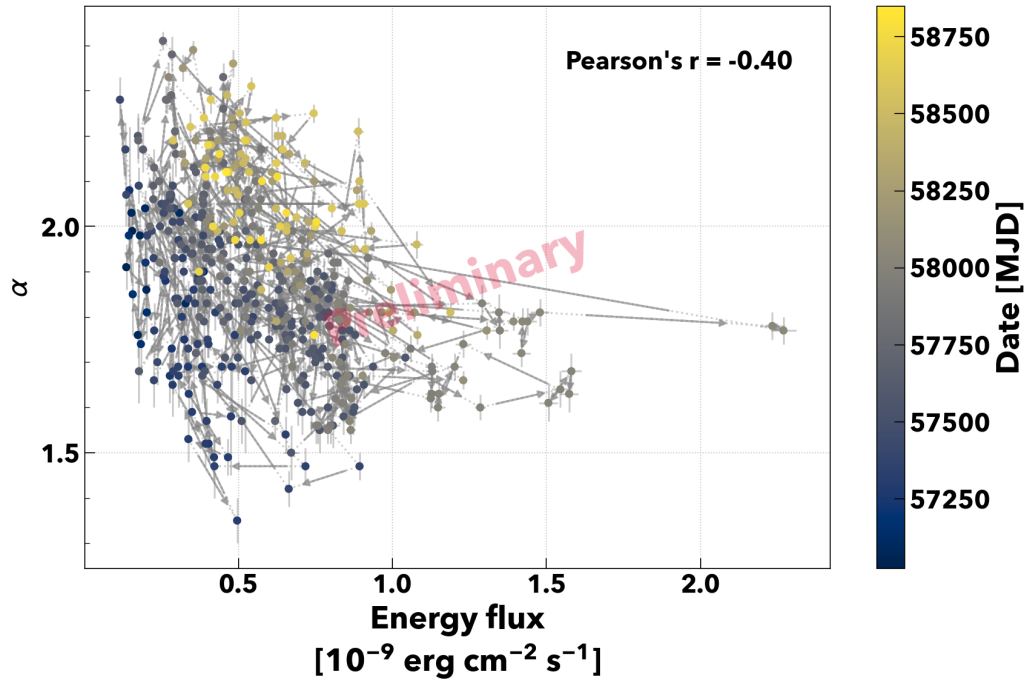


Figure 10.18: Fitting parameter correlation, index v.s. flux

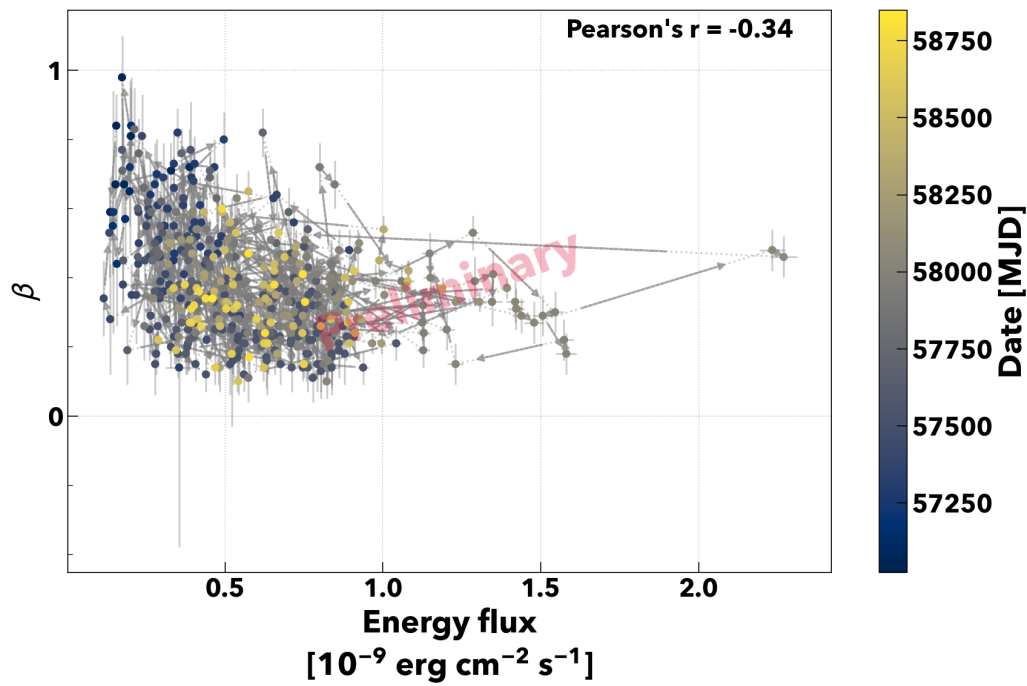


Figure 10.19: Fitting parameter correlation, beta v.s. flux



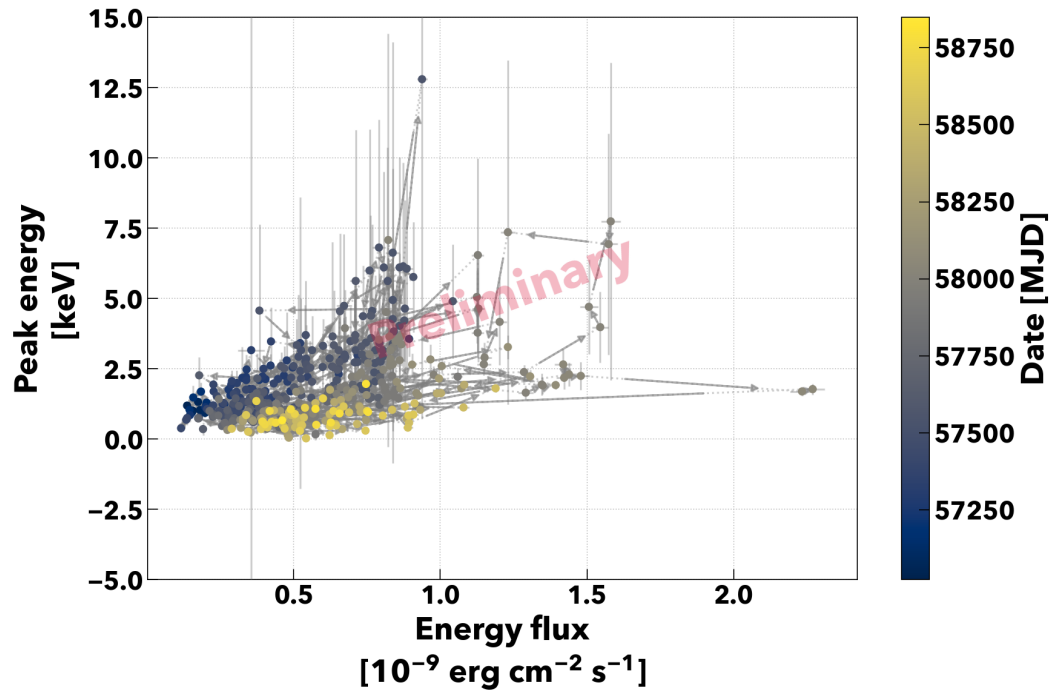


Figure 10.20: Fitting parameter correlation, beta v.s. index

### 10.2.8. Spectral analysis

Tables 10.4 and 10.3 summarize fitting parameters of soft X-ray spectrum measured by *Swift*-XRT. The selection of the observation is based on the MAGIC Bayesian block result and the MWL flux correlation discussed later sections. To characterize the curved spectra, which is expected from the synchrotron peak, I adopted the log-parabola function and the simplest model: power-law. Both models show a trend that a spectral index become hard (small) when the flux increase. The interesting result is that most of the fitting probabilities are less than 5 % for 2017 and later. Thus curved model, log-parabola implies more reasonable result in recent period. There are two low states (34532008,34532010,and 35025224 for 2016 and 34588188,34588190,95332016,and 95332020) selected as a low states, but spectra can be explained with pure power-law in 2016, but not in 2019. This requires power-law populated electron making the soft x-ray emissions.

Table 10.3: Fitting parameters of XRT spectrum with the power-law model

ObsID	$\alpha$	$K [\text{cm}^{-2} \text{s}^{-1} \text{keV}^{-1}]$	P-value
00034532008	$2.13 \pm 0.02$	$0.0580 \pm 0.0008$	4.1e-01
00034532010	$2.11 \pm 0.02$	$0.0573 \pm 0.0008$	5.2e-01
00035025224	$1.96 \pm 0.02$	$0.0666 \pm 0.0010$	4.7e-01
00035025243-01	$1.74 \pm 0.02$	$0.123 \pm 0.002$	1.6e-01
00035025243-02	$1.77 \pm 0.02$	$0.125 \pm 0.002$	6.0e-01
00035025245	$1.78 \pm 0.01$	$0.145 \pm 0.001$	4.4e-02
00034588103	$1.827 \pm 0.009$	$0.258 \pm 0.002$	9.3e-14
00034588104-01	$1.77 \pm 0.06$	$0.139 \pm 0.006$	1.2e-01
00034588104-02	$1.86 \pm 0.01$	$0.428 \pm 0.004$	1.7e-13
00034588188-01	$1.91 \pm 0.01$	$0.102 \pm 0.001$	2.3e-07
00034588188-02	$1.92 \pm 0.01$	$0.151 \pm 0.001$	5.8e-08
00034588190	$1.98 \pm 0.01$	$0.107 \pm 0.001$	2.6e-06
00095332016	$2.05 \pm 0.01$	$0.0862 \pm 0.0009$	8.1e-08
00095332020	$2.00 \pm 0.01$	$0.0852 \pm 0.0010$	7.8e-06

Table 10.4: Fitting parameters of XRT spectrum with the log-parabola model

ObsID	$\alpha$	$\beta$	$K [\text{cm}^{-2} \text{s}^{-1} \text{keV}^{-1}]$	p-value
34532008	$2.10 \pm 0.03$	$0.09 \pm 0.06$	$0.0587 \pm 0.0009$	4.4e-01
34532010	$2.06 \pm 0.03$	$0.13 \pm 0.06$	$0.0583 \pm 0.0009$	6.2e-01
35025224	$1.89 \pm 0.03$	$0.20 \pm 0.06$	$0.068 \pm 0.001$	7.0e-01
35025243-01	$1.62 \pm 0.03$	$0.26 \pm 0.05$	$0.126 \pm 0.002$	5.7e-01
35025243-02	$1.76 \pm 0.03$	$0.03 \pm 0.05$	$0.126 \pm 0.002$	5.9e-01
35025245	$1.72 \pm 0.02$	$0.12 \pm 0.03$	$0.146 \pm 0.001$	1.1e-01
34588103	$1.65 \pm 0.02$	$0.41 \pm 0.03$	$0.269 \pm 0.002$	2.5e-01
34588104-01	$1.62 \pm 0.11\ddagger$	$0.4 \pm 0.2$	$0.144 \pm 0.007$	2.2e-01
34588104-02	$1.66 \pm 0.02$	$0.49 \pm 0.04$	$0.451 \pm 0.005$	3.2e-02
34588188-01	$1.70 \pm 0.03$	$0.52 \pm 0.05$	$0.108 \pm 0.001$	5.9e-01
34588188-02	$1.80 \pm 0.02$	$0.30 \pm 0.04$	$0.156 \pm 0.002$	4.7e-04
34588190	$1.82 \pm 0.02$	$0.42 \pm 0.04$	$0.113 \pm 0.001$	3.6e-01
95332016	$1.92 \pm 0.02$	$0.37 \pm 0.05$	$0.090 \pm 0.001$	2.8e-03
95332020	$1.85 \pm 0.03\ddagger$	$0.42 \pm 0.05$	$0.090 \pm 0.001$	1.3e-01

Figures 10.21 to 10.33 present reconstructed spectra of the selected observations. One can confirm the relatively flat spectrum in 2016. Contrary, the spectra in 2017, especially in the bright state, shows curved shape as shown in the fitting result. It is interesting that the curved spectra is often reproduce the x-ray spectra for the blazar emission. In case the spectra can be explained by a power-law model, it indicates that electrons contributing into the emission follows the power-law distribution too. Moreover, they are not the end of electron distribution, otherwise the curved shape originating from the synchrotron spectrum is expected. Those spectra are used in the MWL SED modeling after averaging them properly.

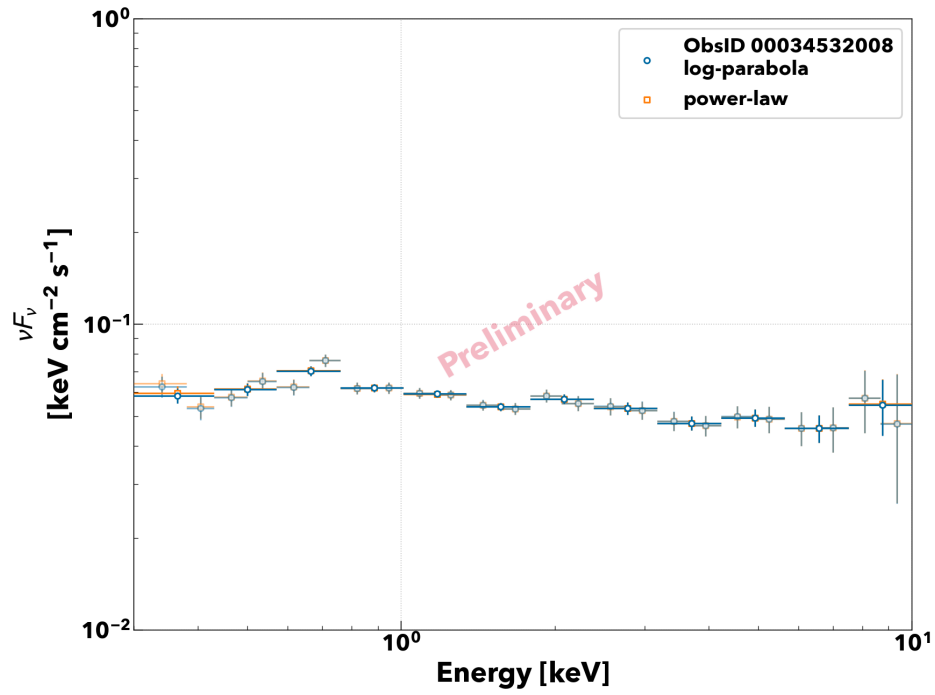


Figure 10.21: XRT SED for the low state in 2016. obsid:34532008

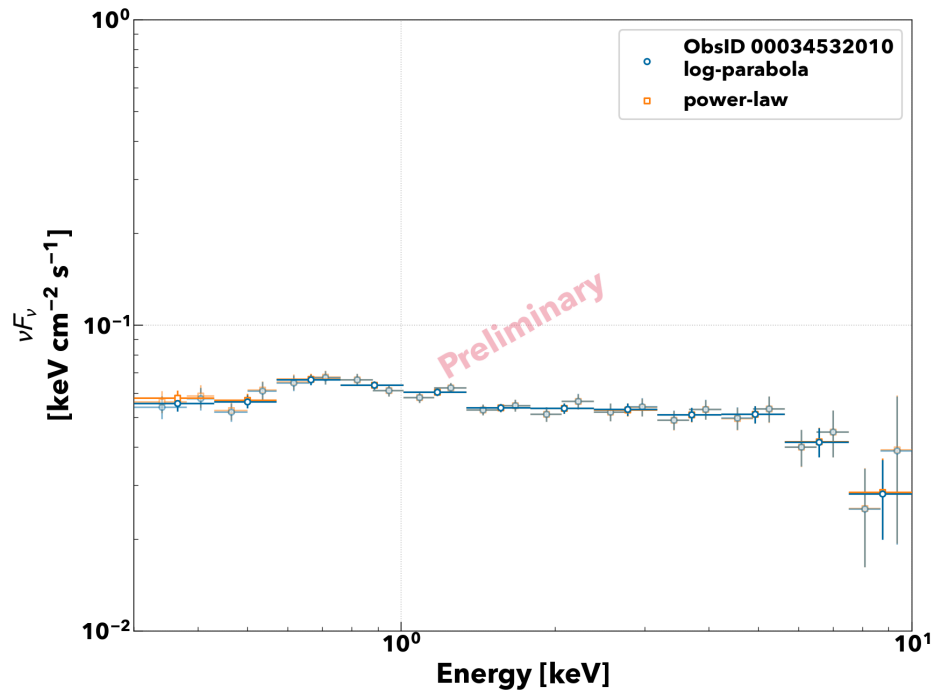


Figure 10.22: XRT SED for the low state in 2016. obsid:34532010

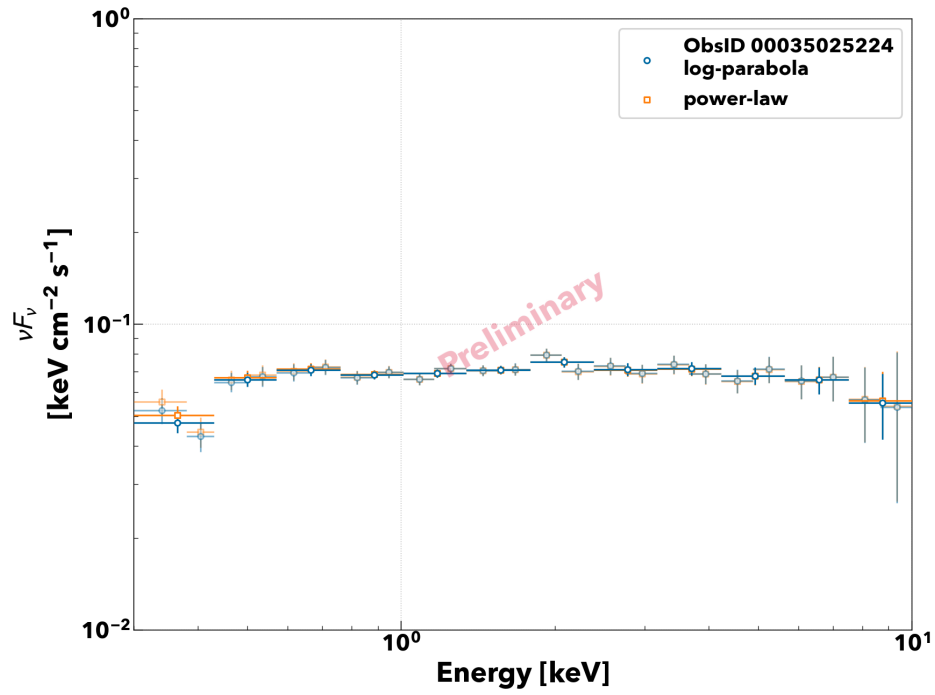


Figure 10.23: XRT SED for the low state in 2016. obsid:35025224

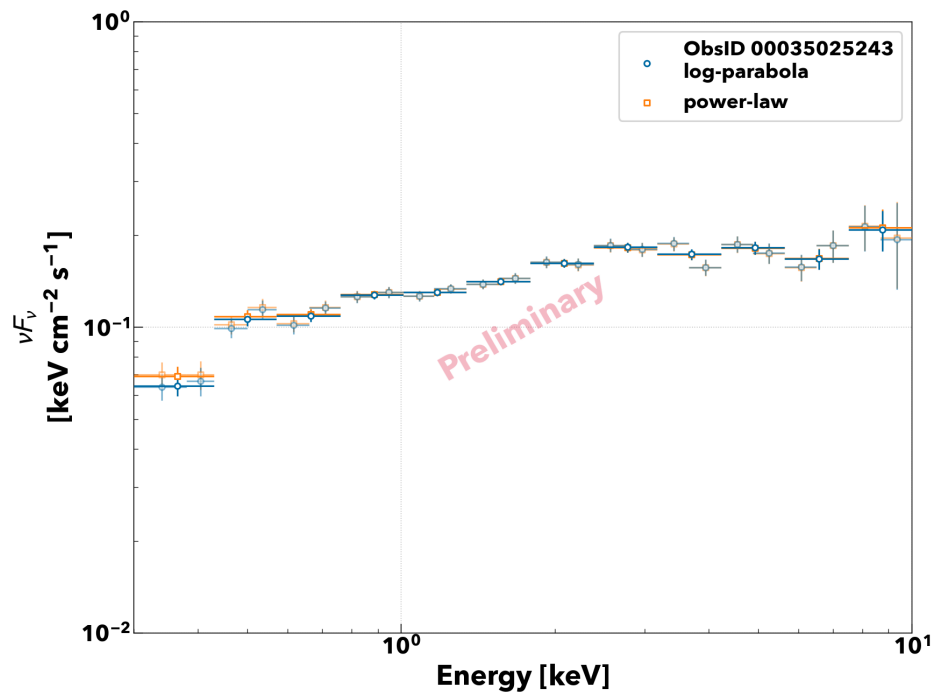


Figure 10.24: XRT SED for the high state in 2016. obsid:35025243, snap shot 1

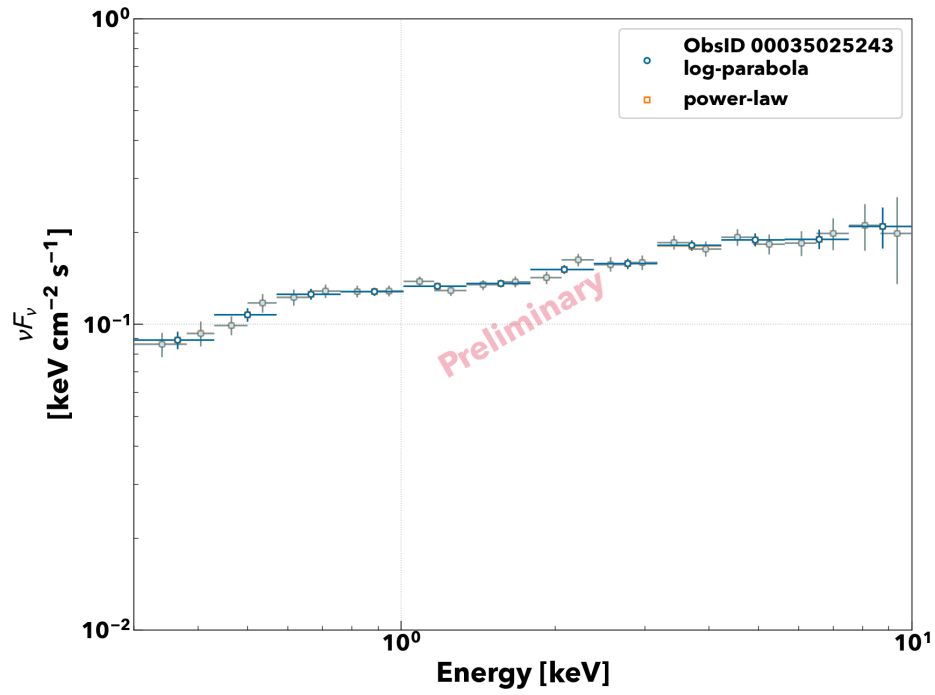


Figure 10.25: XRT SED for the high state in 2016. obsid:35025243, snap shot 2

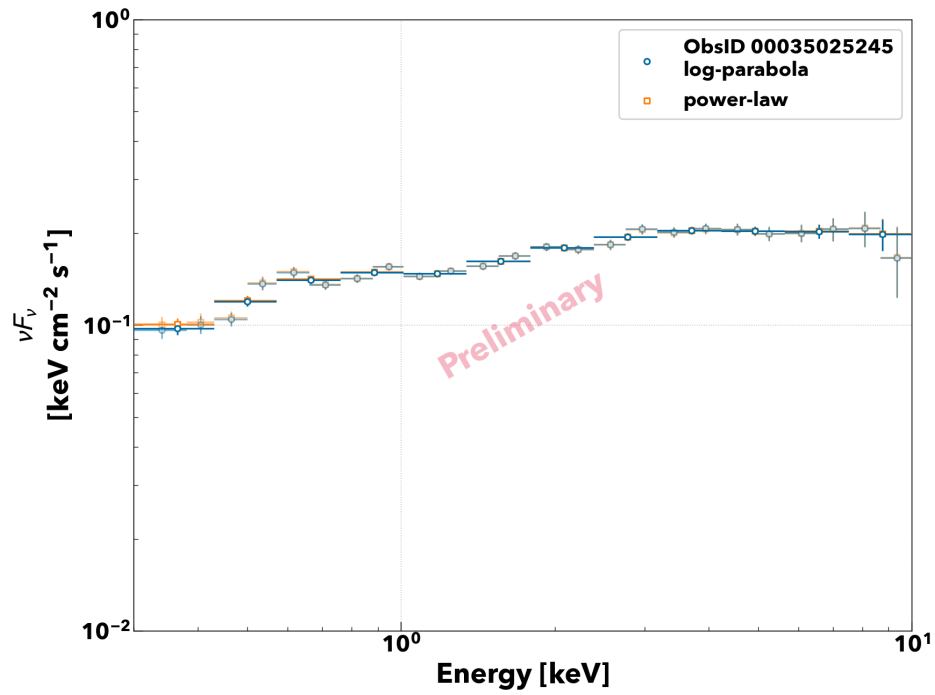


Figure 10.26: XRT SED for the high state in 2016. obsid:35025245, snap shot 2

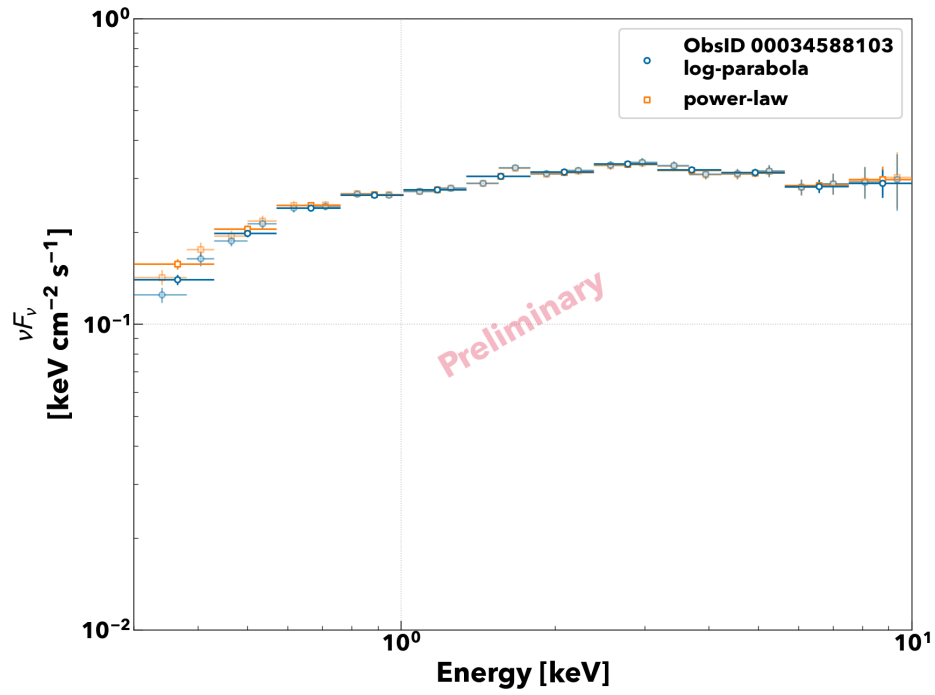


Figure 10.27: XRT SED for the high state in 2017. obsid:34588103

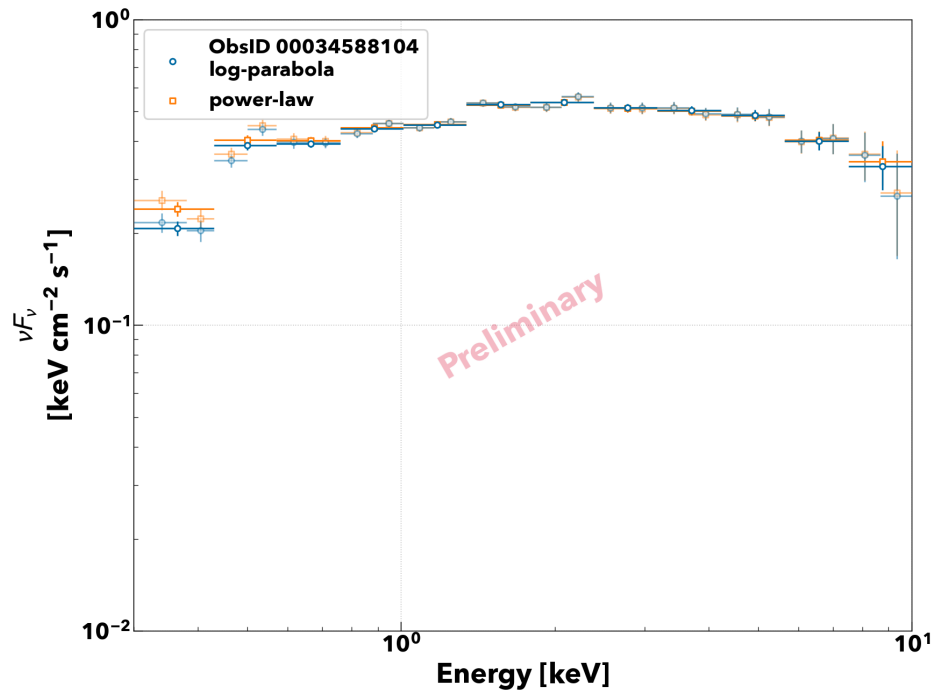


Figure 10.28: XRT SED for the high state in 2017. obsid:34588103, snapshot 2

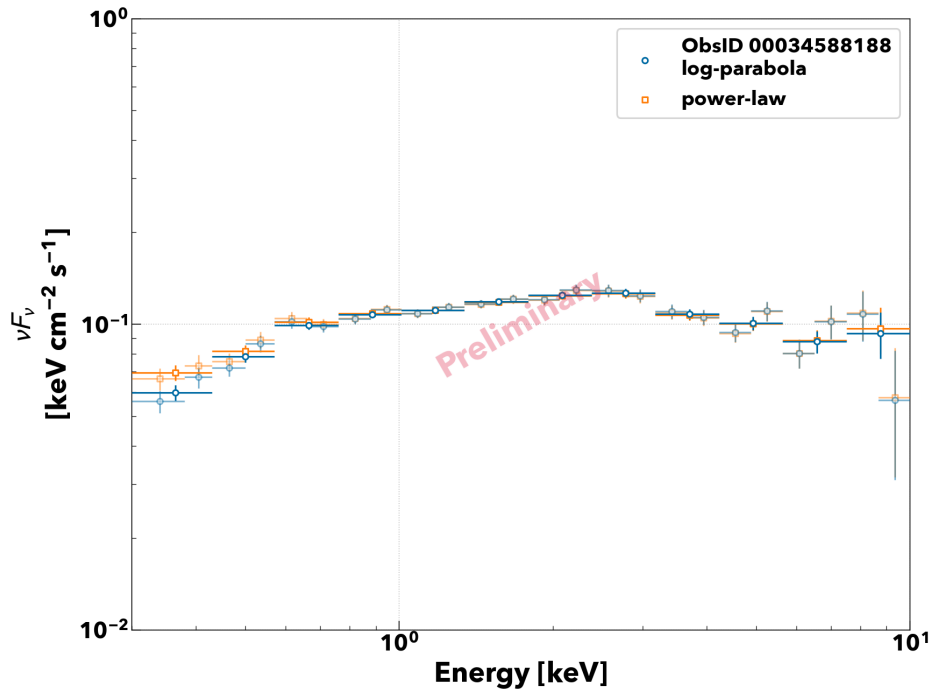


Figure 10.29: XRT SED for the low state in 2019. obsid:34588188, snap shot 1

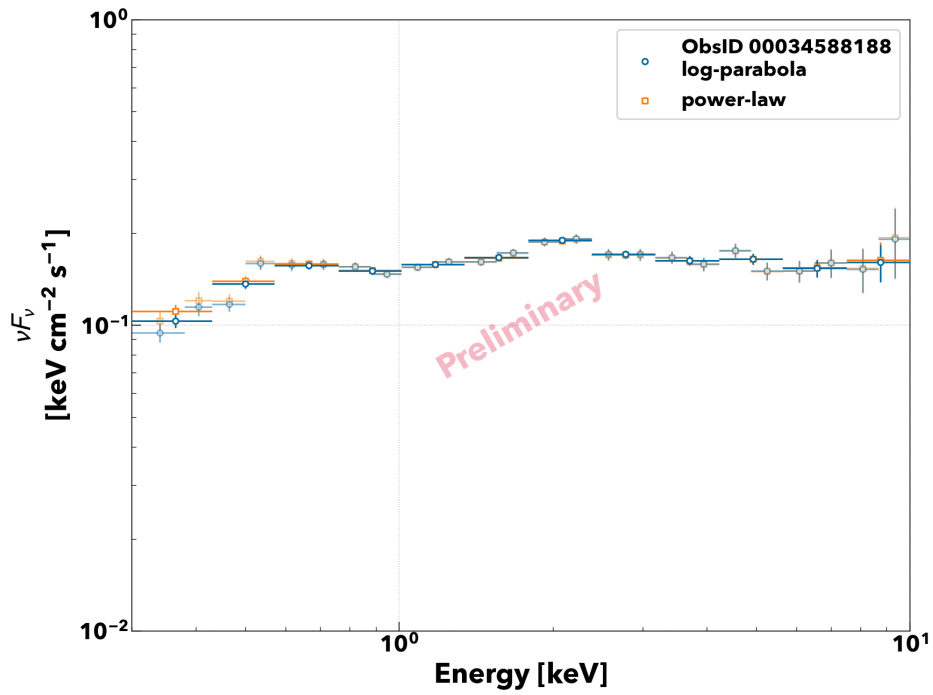


Figure 10.30: XRT SED for the low state in 2019. obsid:34588188, snap shot 2



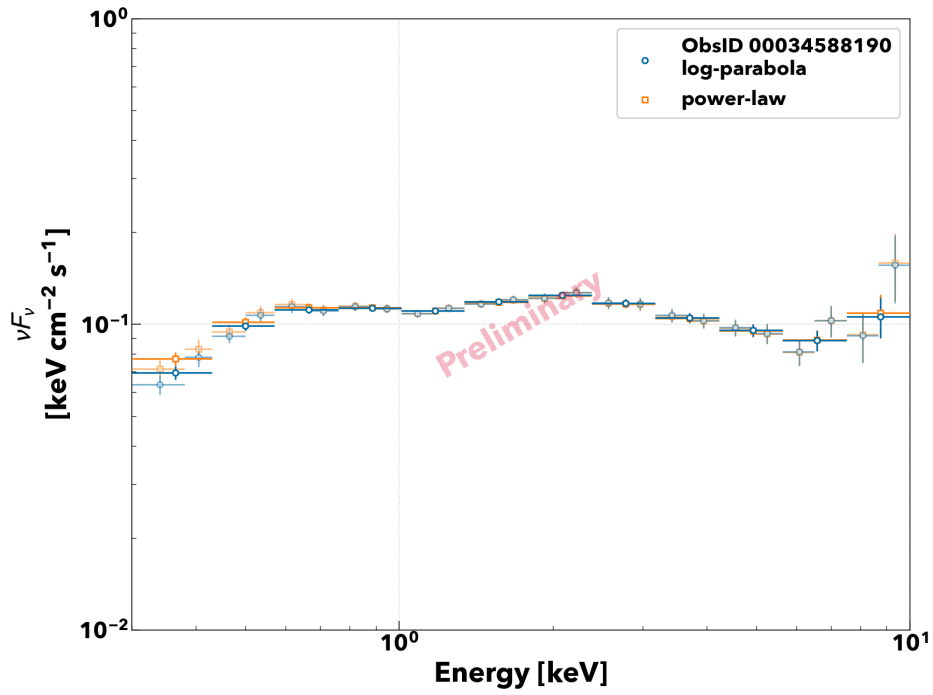


Figure 10.31: XRT SED for the low state in 2019. obsid:34588190

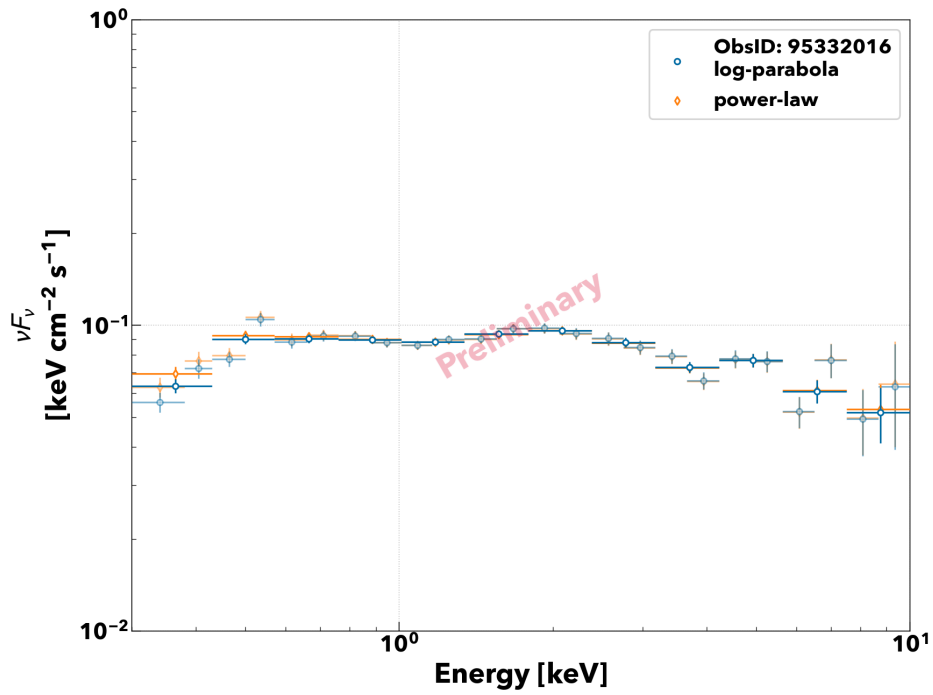


Figure 10.32: XRT SED for the low state in 2019. obsid:395332016

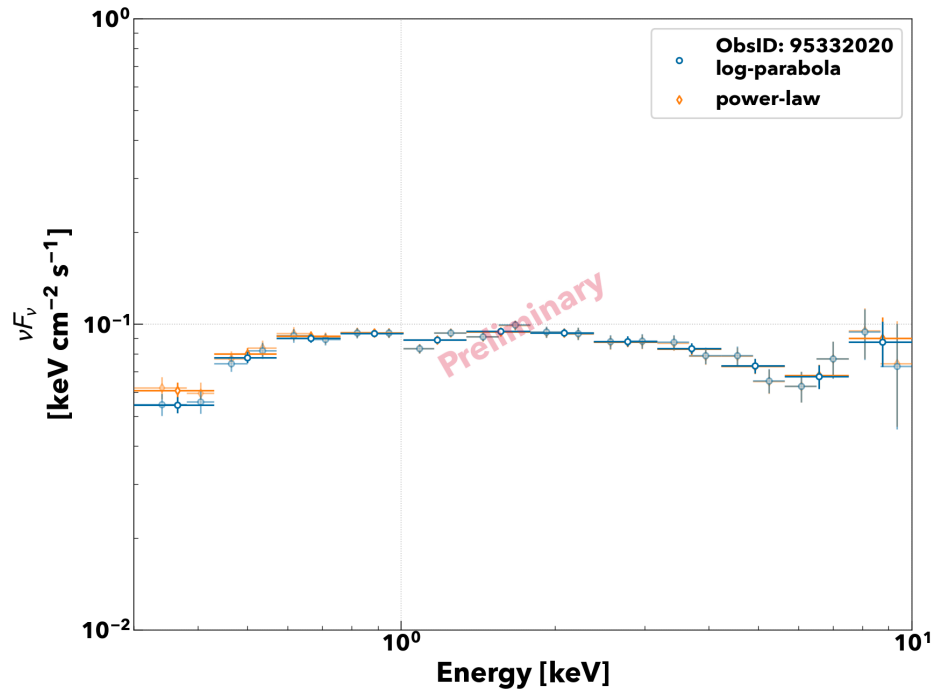


Figure 10.33: XRT SED for the low state in 2019. obsid:395332020

### 10.3. Swift Burst Alert Telescope

BAT is one of the detectors onboard the Swift satellite and is primarily responsible for detecting GRBs and identifying their location; when BAT identifies a GRB, the satellite automatically slews the satellite to the direction of the GRB and begins detailed observations with the telescopes also onboard. The field of view is wide, making it suitable for detecting sudden celestial objects. The energy band is from 10 keV to 50 KeV. Since BAT monitors a broad region, its data are publicly available for celestial objects in prominence. In this study, we used public data to limit the energy spectrum at the hard x-ray band.

*Swift*-BAT has a large field of view, thus can provide whole sky monitoring observation in hard x-ray. The analyzed data are published at the website of NASA. I took the data from there and used in the latter analysis. Detailed description about the analysis can be found in ??.

I used public monitoring data in the MWL modeling, not in the temporal analysis. This is because most of the measurements are consistent with zero flux.

Observed photon flux  $\phi_{\text{BAT}}$  can calculate as follows:

$$\phi_{\text{BAT}} = \int_{E_{\text{min}}}^{E_{\text{max}}} \frac{d\phi}{dE} dE, \quad (10.8)$$

where  $d\phi/dE$  is differential photon flux. If we assume  $d\phi/dE$  follows the power-law distribution approximately:  $d\phi/dE = \phi_0(E/E_0)^{-\Gamma}$ , where  $E_0$  is the normalization energy and  $\phi_0$  is differential flux at the normalization energy, and  $\Gamma$  is photon index. One can conduct integration, thus:

$$\phi_{\text{BAT}} = \phi_0 E_0 I_\phi(\Gamma) \quad (10.9)$$

$$I_\phi(\Gamma) = \begin{cases} \ln \frac{E_{\text{max}}}{E_{\text{min}}} & \text{for } \Gamma = 1 \\ \frac{(E_{\text{max}}/E_0)^{1-\Gamma} - (E_{\text{min}}/E_0)^{1-\Gamma}}{1-\Gamma} & \text{for } \Gamma \neq 1 \end{cases} \quad (10.10)$$

In the equations,  $E_0$  and  $\Gamma$  are given. Thus one can convert  $\phi_{\text{BAT}}$  to  $\phi_0$  for given condition. Once  $\phi_0$  is specified, one can compute SED by  $E^2 d\phi/dE$ . One caution is the ignoring the instrument response in the above calculation.

### 10.3.1. Light curve

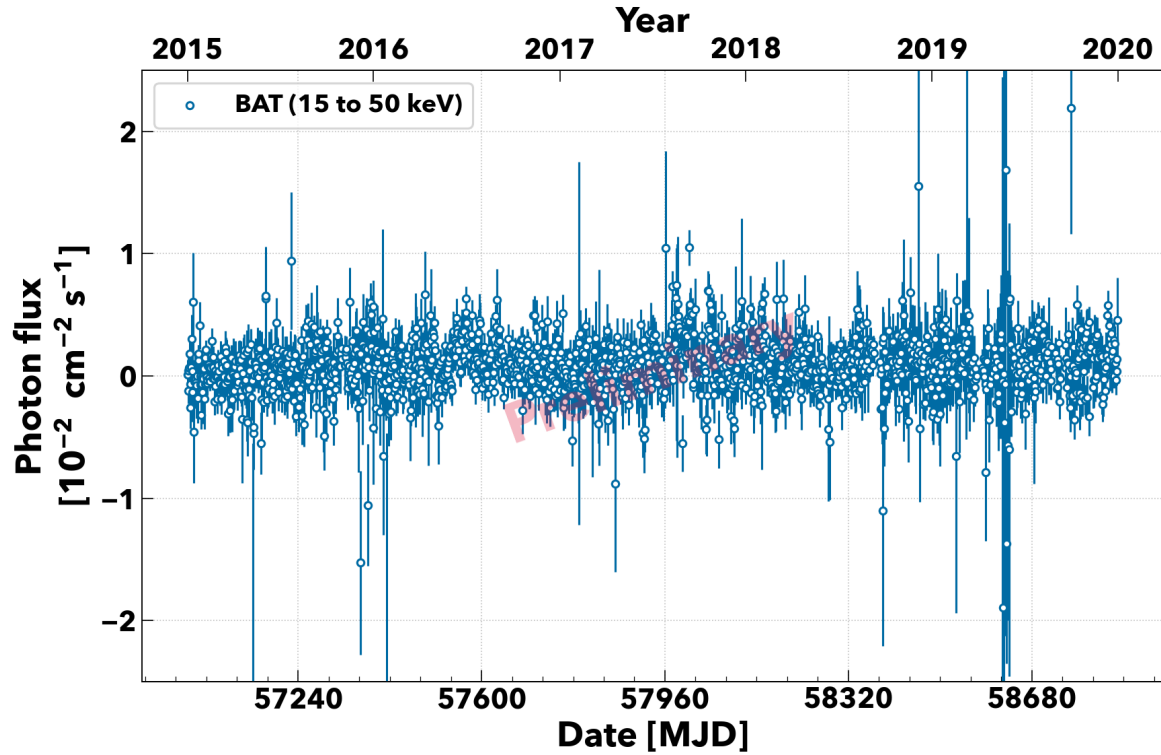


Figure 10.34: BAT five-year light curve. The errors correspond to one sigma including a statistical and systematic uncertainty.

The *Swift*-BAT light curve between 15 keV to 50 keV is shown in figure 10.34. Because of its large uncertainty, the data is excluded from the MWL temporal analysis. However, estimating the energy flux with the assumption of the spectral index, it was used in the MWL SED modeling. For the purpose I assumed the spectral index 2.2, and normalization energy 27 keV.

## 10.4. *Swift* Ultra Violet and Optical Telescope

The Ultraviolet and optical telescope (UVOT) is a multi-band instrument on the *Swift* satellite.

The UVOT telescope is co-aligned to XRT to conduct multiwavelength observation for gamma-ray bursts.

The UVOT detector can perform multi-band photo counting observations via multi-channel plate-intensified devices. and amplified photon signals are stored by CCD, which has available pixels  $256 \times 256$ . The pixels correspond to a field of view of  $17 \times 17$  arcmin<sup>2</sup>.

The UVOT telescope has seven available color filters to characterize the spectral features of the source. The filter information is summarized in table 10.5. Precisely speaking, the effective wavelength depends on the spectral shape of the observed source, but the dependency seems to be not significant.

Table 10.5: UVOT filters

Band	Central wavelength	FWHM
–	[nm]	[nm]
V	546.8	76.9
B	439.2	97.5
U	346.5	78.5
UV-W1	260.0	69.3
UV-M2	224.6	49.8
UV-W2	192.8	65.7

The representative wavelength is slightly different depending on the estimations. Thus I used the values from [Poole et al. \(2007\)](#) for the conversion from flux density into energy flux.

The telescope's optics is based on the Ritchey-Chretien (RC) telescope. The Ritchey Chretien telescope can provide a sharp image at the edge of the field of view. Moreover, the RC telescope can be more compact than other designs of telescopes. Thus, RC-type optics are adopted in also large optical telescopes such as the Hubble telescope and Gran telescope Canarias. The f-number is 12.7 of 30 cm aperture. The minimum sensitivity is 24-th magnitude for B-star in 1000 sec.

As same as *Swift*-XRT analysis, an aperture photometry is used to extract the source contribution. Furthermore, the contribution from the host galaxy will be problematic for the AGN study. The contribution from the galaxy is subtracted by modeling the host galaxy profile. After that, the observed photon counts are converted into the magnitude and flux.

The data analysis was conducted by Dr. Bidzina Kapanadze. The contamination and absorption by the host galaxy was taken into account. The energy flux  $F_\nu$  was provided for the available wavelength bands.

The data taken from the beginning of 2016 to the end of 2019 was used as much as possible. To obtain the spectral energy distribution point at specific frequency, I convert

Table 10.6: Conversion factors of UVOT flux densities

Band	Wavelength[nm]	factor
V	546.8	5.483e-12
B	439.2	6.826e-12
U	346.5	8.652e-12
W1	260.0	1.153e-11
M2	224.6	1.335e-11
W2	192.8	1.555e-11

each wavelength to the frequency. Table 10.6 provides conversion factors to convert  $F_\nu$  to  $\nu F_\nu$  at each color band.

#### 10.4.1. Light curve

The multi-band optical flux density measurement are shown in Figure 10.35. Currently the analysis for the data in 2015 is ongoing.

The flux changes in time over its statistical errors, thus the source is literally variable. The light curve showed two large peak at the end of 2016 and 2017. The one in 2017 seems to be correlated in the X-ray maximum state. Adding that, the broader bump is also found in 2019. It looks similar the peak appeared in OVRO light curve (Fig. 10.40)

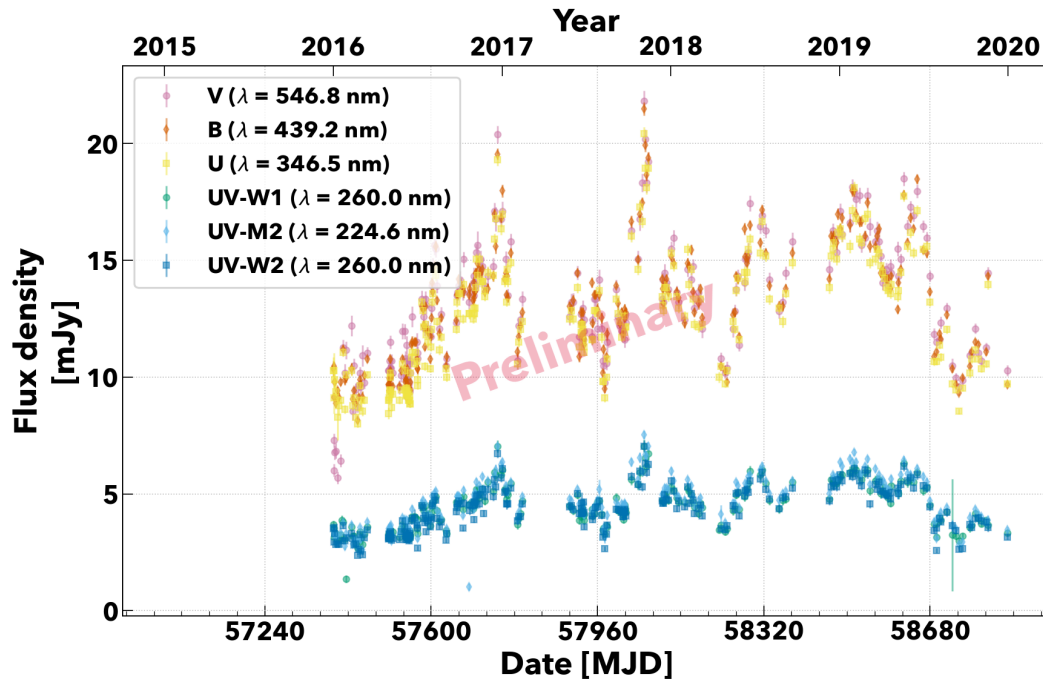


Figure 10.35: UVOT five-year light curve. The errors correspond to one sigma.

## 10.5. Tuorla observatory

The tuorla observatory consists of several telescopes in several places, where is mainly Finland. Especially two telescopes among the observatory are used in the optical Blazar monitoring campaign since 2000 for the selected sources (Nilsson, K. et al., 2018). Both telescopes monitored blazars in the optical R band continuously.

One is Tuorla 1.03 m Dall-Kirkham telescope, and it is located at 56 m above sea level. The telescope has focal length of 8.45 m and field of view of  $10 \times 10$  arcmin<sup>2</sup> with commercial CCD. During the observation, the images of night sky, dark, and dome flats are taken for the image calibration.

Another telescope is the KVA telescope located at the Observatorio del Roque de Los Muchachos in La Palma, Spain. The KVA telescope composed from the two telescopes. a 60 cm telescope and 35 cm telescope sold by Celestron. The monitoring was performed by the latter smaller telescope and the telescope is located at 2396 m above sea level, it is slightly higher place than MAGIC telescopes. The focal length is 3.91 m and  $12 \times 8$  arcmin<sup>2</sup> filed of views. The exposure for one observation is 10 to 30 mins for the KVA telescope.

The R-band observed data was analyzed by the aperture photometry method. The raw image is calibrated by subtracting bias, dark, and flat-fielded using the simultaneously observed data. The number of photons are extracted from the region around the source corresponds to approximately the PSF.

The flux analysis is as similar as the UVOT analysis. The measured count is converted to the flux and magnitude by comparing the ones of reference stars..

The data analysis for KVA telescopes was performed by an expert in the Tuorla collaboration. The flux density  $F_\nu$ , its error, and observation time were provided from them. The conversion to the spectral distribution, I multiplied  $\nu = c_0/\lambda$  at  $\lambda = 658$  nm. Which corresponds to  $4.556 \times 10^{14}$  Hz. Thus conversion factor is  $4.556 \times 10^{-12}$  erg cm<sup>2</sup> s<sup>-1</sup> mJy<sup>-1</sup>.

### 10.5.1. Light curve

The differential energy flux light curve is shown in figure 10.36.

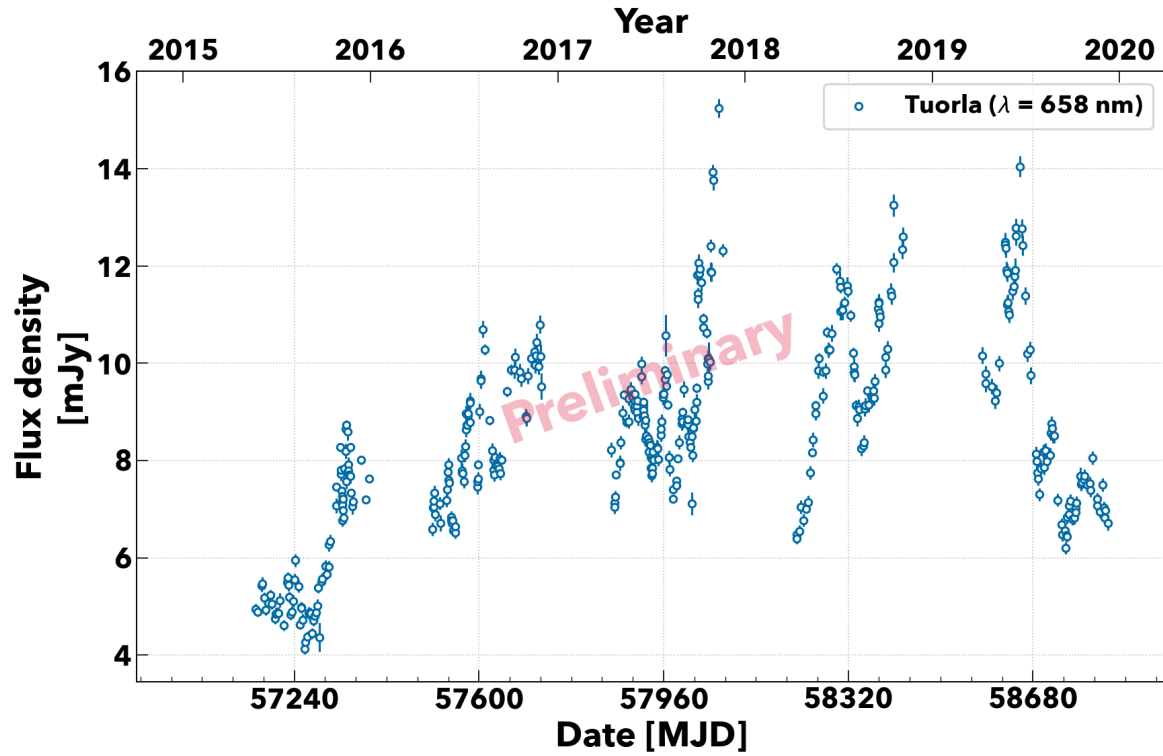


Figure 10.36: Tuorla light curve

The overall trend looks similar with the radio light curve as shown in figure 10.40. However, the optical light curve shows more fast variability than radio as often observed in blazars. There is a broad peak observed in 2019, it is also found in the radio light curve.

### 10.5.2. SED

I calculated the spectral energy distribution from the light curve and compared with archived data from SSDC. Figure 10.37 shows this comparison, and one can confirm that the flux level agrees with previous UVOT observations. The red lines are power-law functions with spectral index  $a = 0.25, 0.5, 0.75$ . Except for the excess in the UVOT optical bands,  $a = 0.75$  is more preferable. It suggests that the electron distribution changes its index by whatever reason at the optical band. Comparing with previous studies, the observed fluxes are relatively higher.



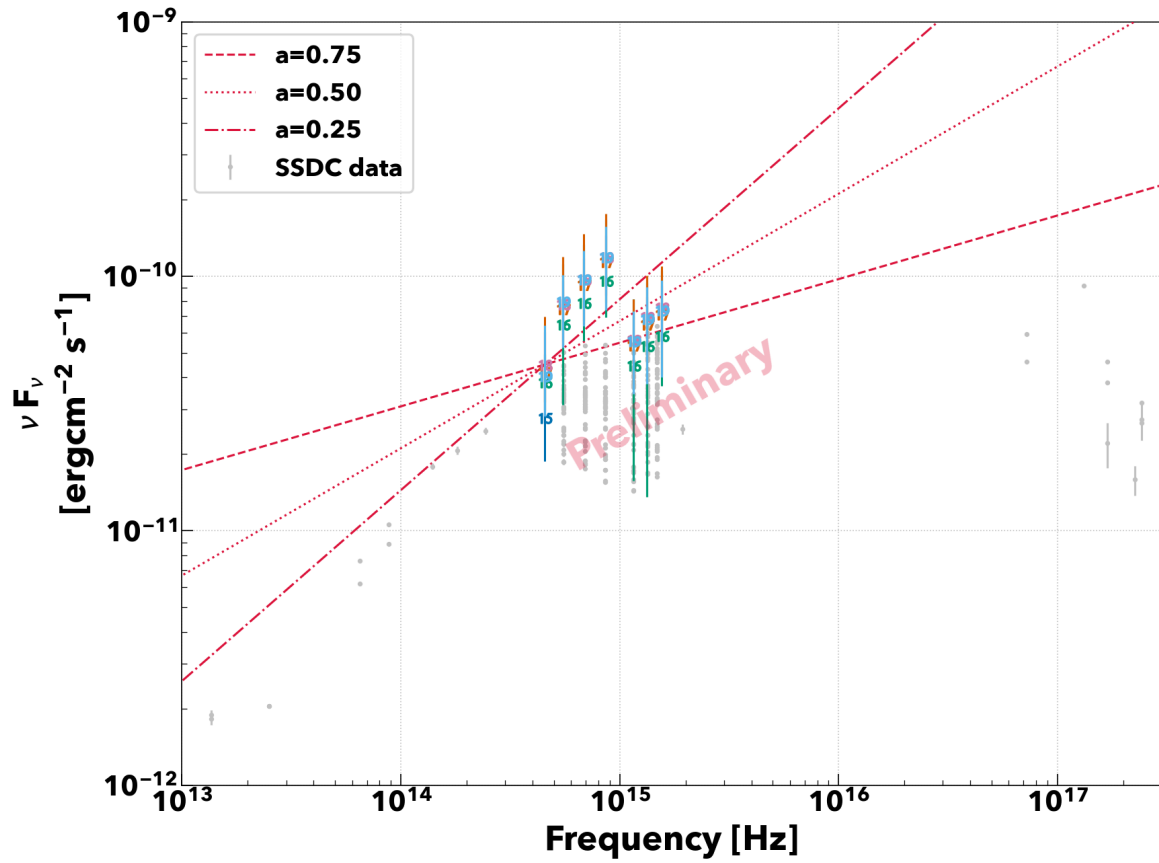


Figure 10.37: Optical-UV SED. To compare with the previous measurements, archived data from SSDC are shown as gray points. The red lines indicate synchrotron power-law models, dashed, dotted, and dash-dotted lines are models index of  $p = 1.5, 2.0, 2.5$  respectively. Their indices in SED  $\sim \nu^\alpha$  are  $\alpha = 0.75, 0.5, 0.25$ . The numbers shows years and mean flux. The error bars corresponds minimum-maximum range of  $\nu F_\nu$ .

## 10.6. Owens Valley Radio Observatory

Owens Valley Radio Observatory (OVRO) is a radio observatory in the state of California in the United States of America and is located at 1222 meters above sea level<sup>17</sup>. OVRO consists of several radio projects<sup>18</sup> and one 40-m dish radio telescope, named OVRO 40-m telescope (hereafter OVRO telescope), as shown in Figure 10.38.



Figure 10.38: OVRO 40-m radio telescope. The biggest one is OVRO telescope. Image credit: James Wilson, (Flickr: <https://www.flickr.com/photos/135665552@N04/48040892991/in/photostream/>)

The OVRO telescope was built in 1968 and is currently used to study supermassive black holes and relativistic jets. In 2008, a radio monitoring program was initiated for over 1000 gamma-ray blazars(Richards et al., 2011). This program was discontinued in 2020, but a new monitoring program covering more than 5000 objects was started in 2021 to search for the origin of high-energy neutrinos. The relationship between radio and neutrinos has been investigated using observation data until 2020, but no significant correlation has been found(Hovatta, T. et al., 2021).

OVRO's optical system is a 40-m diameter parabolic reflector with a focal ratio of  $f/0.4$ . Two cooled signal receivers are installed at the focal point, and the observation is

<sup>17</sup>Wikipedia: [https://en.wikipedia.org/wiki/Owens\\_Valley\\_Radio\\_Observatory](https://en.wikipedia.org/wiki/Owens_Valley_Radio_Observatory)

<sup>18</sup>Project webpage: <https://www.ovro.caltech.edu/projects>

performed by taking the difference between them. The beam size is  $157''$  with a Gaussian FWHM and a center frequency is 15 GHz with a frequency bandwidth of 3 GHz. The receiver can be positioned to optimize performance, which varies due to the gravitational deformation of the reflector and is corrected accordingly. The signal strength measured at the receiver is converted to flux density after being calibrated. The flux density limit is approximately 4 mJy, and typical uncertainty is 3 %. See [Richards et al. \(2011\)](#) for more detailed descriptions of the telescope.

The flux density is observed by the power difference between the two receivers on the telescope. In order to eliminate systematic errors in the observation, four 8-second integrations are made in a single 32-second observation. The radio signal strength is directly converted to flux density by averaging them appropriately. This conversion factor is calibrated from time to time. The uncertainty of the flux density measurement is evaluated along with the absolute value of the flux density. Figure 10.39 shows the results of the flux measurement uncertainty evaluation. According to the figure, the relative uncertainty does not exceed 5 %.

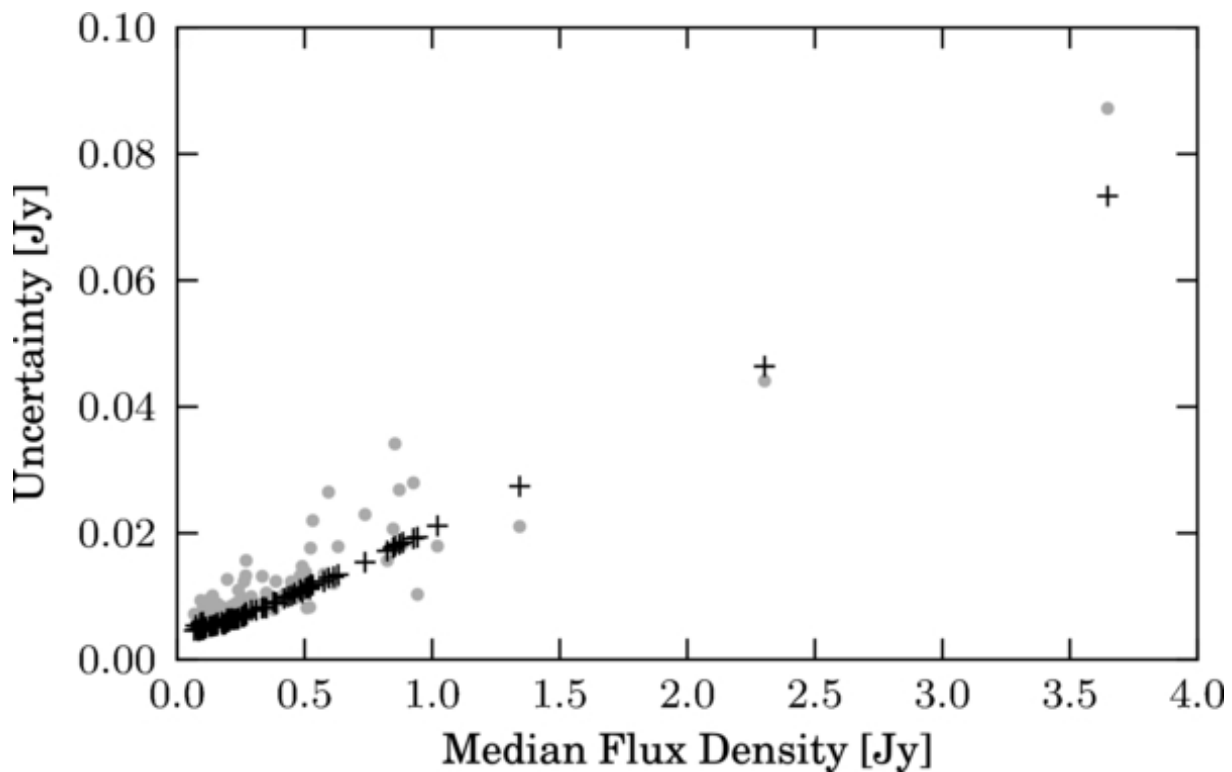


Figure 10.39: Uncertainty evaluation of OVRO flux density measurement [Richards et al. \(2011\)](#). Black points shows the modeled errors assuming the term proportional to the median flux density. The gray points are uncertainties from the real data.

The OVRO collaborators provided the blazar monitoring data from the OVRO 40m telescope. They provided the flux density, its uncertainty, and the observation time.

Based on Figure 10.39, I also applied additional data reduction if the relative uncertainty  $\sigma_{F_\nu}/F_\nu$  is greater than 10%, and it is discarded. This was discussed with the OVRO collaborator<sup>19</sup>. To obtain the Spectral Energy Distribution at 15 GHz, we multiplied  $\nu=15$  GHz by  $F$  and calculated  $\nu F_\nu$ .

### 10.6.1. Light curve

Five-year 15 GHz radio light curve is shown in figure 10.40.

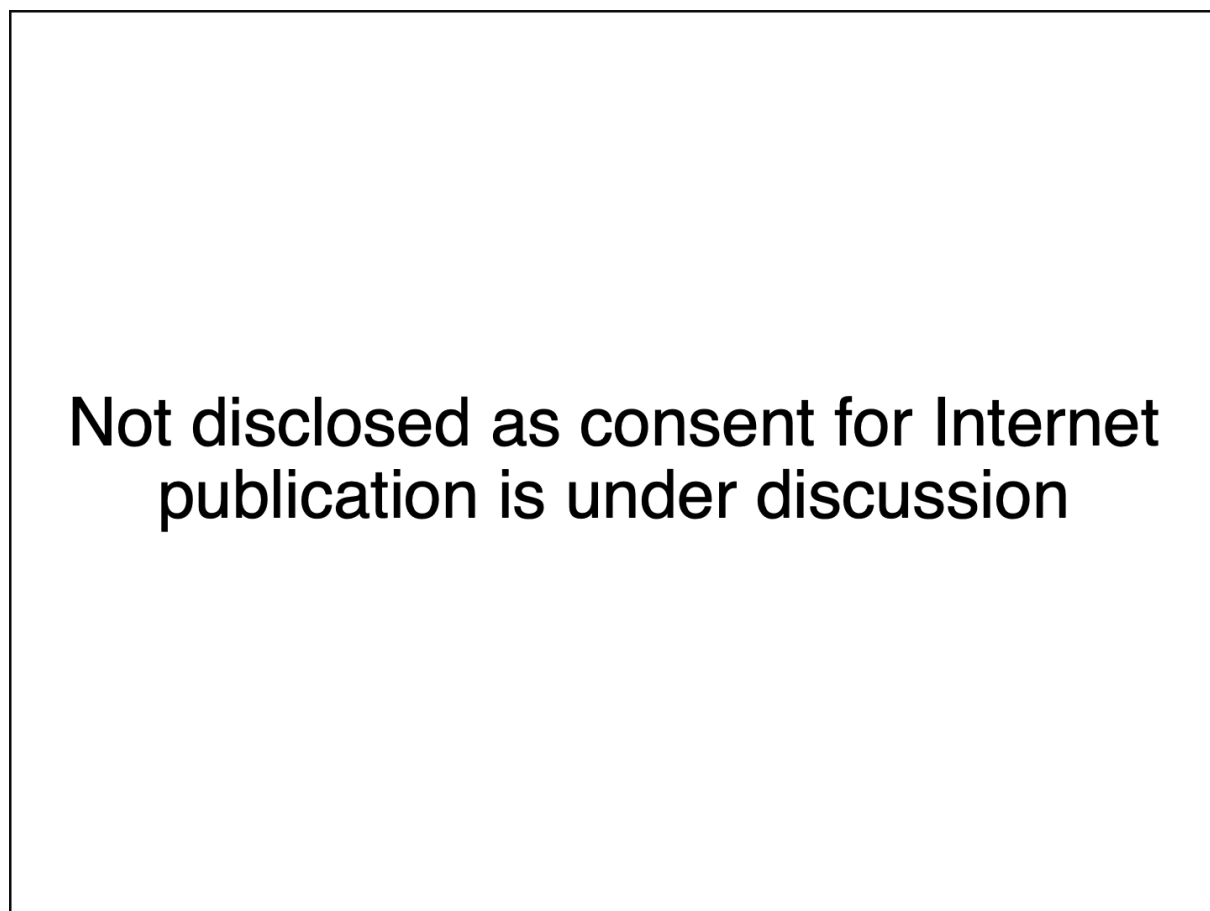


Figure 10.40: OVRO five-year light curve measured at 15 GHz. Error bars correspond to one sigma errors. Some data points having the relative error more than 10 % are excluded as discussed in section ??.

The light curve shows significant variability beyond its statistical uncertainty of each measurement and the large amplitude peak is common with Tuorla light curve (Fig. 10.36)

To obtain the temporal scale of the broad component, I modeled the broad peak with

---

<sup>19</sup>Private communication

an exponential decay component with a following flaring component:

$$F(t) = F_{\text{const}} + \frac{2F_{\text{flare}}}{e^{(t-t_{\text{rf}})/\tau_{\text{rise}}} + e^{(t_{\text{rf}}-t)/\tau_{\text{fall}}}} + F_{\text{decay}}e^{(t_{\text{rd}}-t)/\tau_{\text{decay}}}, \quad (10.11)$$

where  $F$  denotes flux density of each component, and  $\tau$  is temporal scale of the flare and decay components. Fitting results are summarized in table 10.7. The sum of rising time  $\tau_{\text{rise}}$  and falling time  $\tau_{\text{fall}}$ , is  $\sim 50$ days, it is significantly longer than the variability time scale usually observed in the higher energy bands.

Table 10.7: Fitting results of the exponential flare model for 2019.

$F_{\text{const}}$ [Jy]	$F_{\text{decay}}$ [Jy]	$\tau_{\text{decay}}$ [day]	$F_{\text{flare}}$ [Jy]	$t_{\text{rf}}$ [MJD]	$\tau_{\text{rise}}$ [day]	$\tau_{\text{fall}}$ [day]	$t_{\text{peak}}$ [MJD]	$\chi^2/\text{DoF}$ –	Prob –4
$0.253 \pm 0.002$	$0.12 \pm 0.03$	$80 \pm 20$	$0.092 \pm 0.005$	$58\,636.9 \pm 1.0$	$5.1 \pm 0.7$	$34 \pm 3$	$58\,645 \pm 1$	127.43/69	<b>2.39e-05</b>

### 10.6.2. SED

I calculated flux density from the flux density values in the light curves. Figure 10.41 displays OVRO sed and SSDC archived SED data with some power-law functions. The OVRO data seems to follow the same trend as archive data.

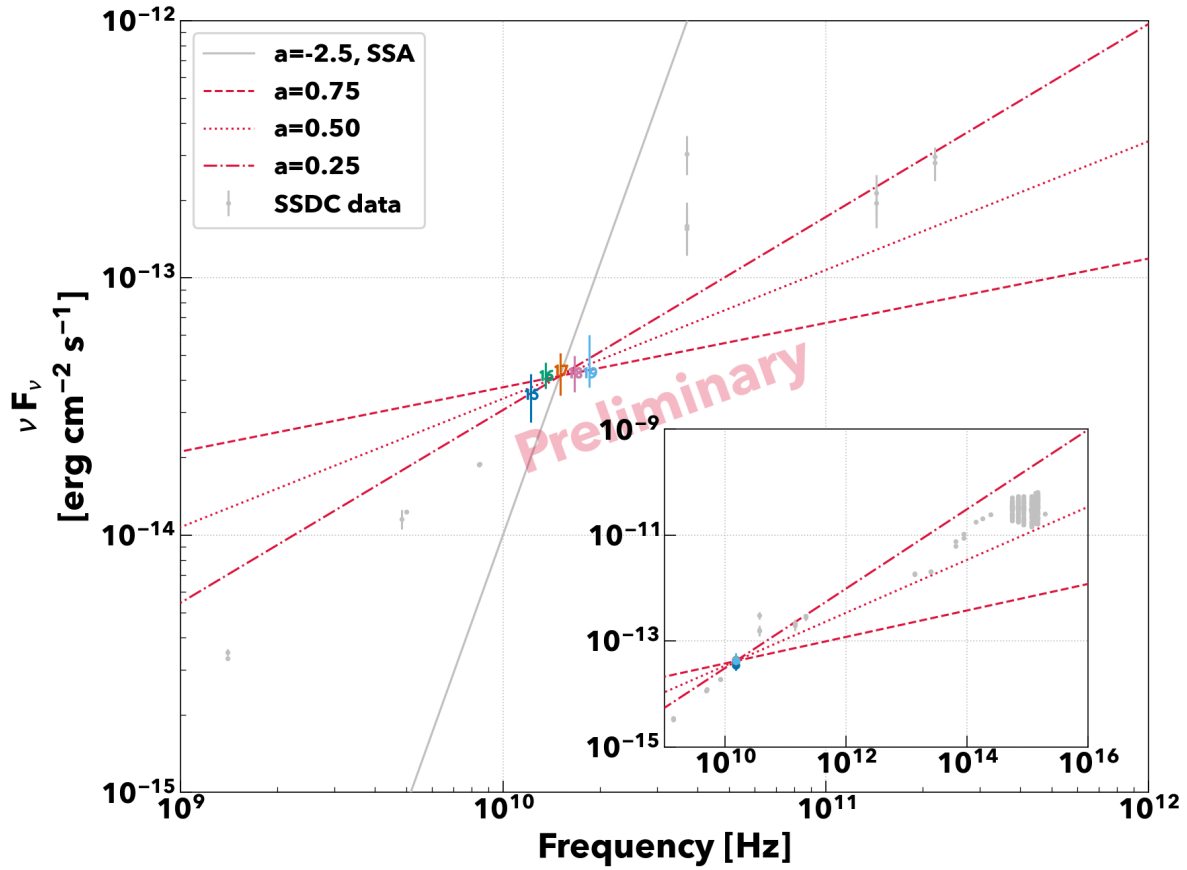


Figure 10.41: OVRO SED. To compare with the previous measurements, archived data from SSDC are shown as gray points. The red lines indicate synchrotron power-law models, dashed, dotted, and dash-dotted lines are models with electron index of  $p = 1.5, 2.0, 2.5$  respectively. Their indices in SED  $\sim \nu^\alpha$  are  $\alpha = 0.75, 0.5, 0.25$ . Moreover, the black dark gray solid line shows a cutoff due to SSA. **Outer plot:** SED in radio frequency, the numbers shows years and mean flux. The error bars corresponds minimum-maximum range of  $\nu F_\nu$ . The values are slightly shifted for plotting. **Inner plot:** SED comparison for the wider energy range. One can confirm that OVRO measurements roughly follow the single power-law index  $p$  of  $1.5 \sim 2$

The dashed lines are power-law functions with an index  $a$  of 0.25, 0.5, and 0.75, respectively, and a solid line is a function when SSA affects. The archive data and OVRO sed have an index of roughly 1.5 to 2.0. Although I plotted the predicted SSA absorption, but no clear cut off found. Thus, the long-term variability is might not be due to the change of the minimum energy of electrons. However no clear evidence exist from the observation.

## 11. Temporal Analysis with Multiwavelength light curves

This chapter reports the results of a multi-wavelength analysis of 1ES 1959+650 based on the very-high energy gamma-ray data. First, I discuss the time variation of the flux identified from the correlation analysis using time series data as shown in figure 11.1. Then I discuss whether the time variation can be reasonably explained using a simple spectral model. The analysis results for each wavelength are discussed in previous sections.

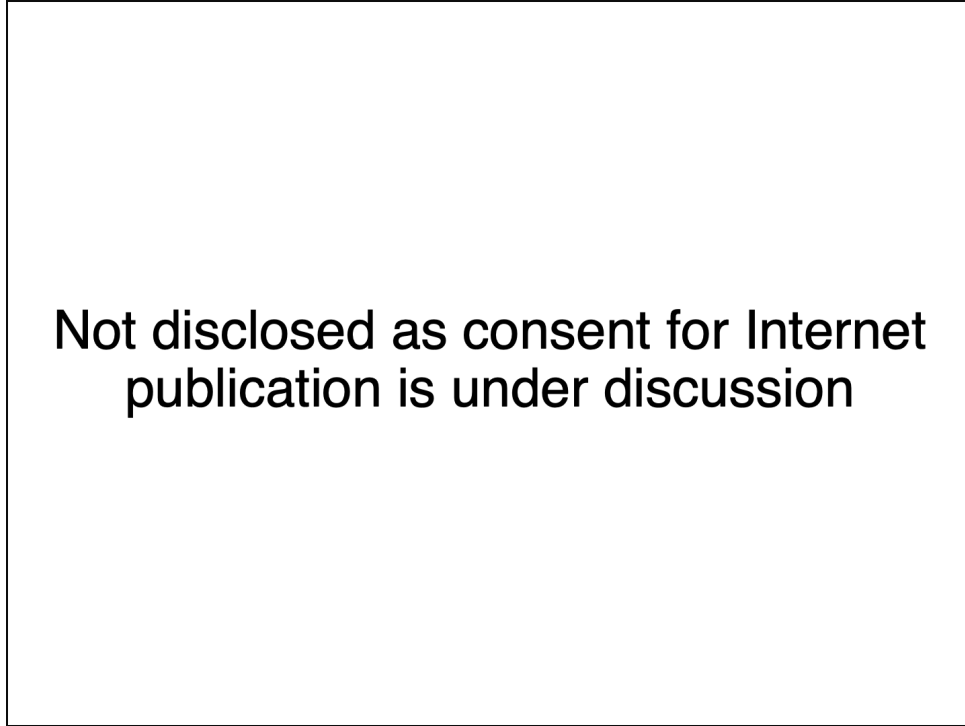


Figure 11.1: Multiwavelength light curves. From the top, MAGIC, *Fermi*-LAT, *Swift*-BAT, *Swift*-XRT, *Swift*-UVOT B & UV-M2, Tuorla, and OVRO. Vertical color bands indicate periods used in the spectral modeling. Light red band corresponds to 16C, and dark red one shows 16H in the bayesian block result of MAGIC light curve. Dark blue bands represent gamma-ray flares in 2017, and the right one is used in spectral modeling. Light blue bands indicate bayesian bins of low states in 2019. The period after the radio flare was used in the modeling.

Light curves from each instruments showed a unique temporal and spectral characteristics in each energy band.

MAGIC, the most energetic photon in the data set presented a intense flares and quiescent flux despite the frequent observations. The reconstructed spectra along the bayesian blocks were totally different even the value of the photon flux is similar. Especially, the spectrum in the 2016 flare was clearly curved, but not in the 2017 flare. I think this suggesting a change in the emission mechanism or environment.



*Fermi*-LAT, which is continuously observing the gamma-ray sky, showed an interesting light curve. The photon flux increasing has been stated since the end of 2015, it was more apparent the one in 2016. Unfortunately, MAGIC did not observe the source at the period, but I could confirm the similarity between MAGIC and *Fermi*-LAT. Spectra for short-term period are not so precise, but it would be helpful for the MWL modeling. The flat spectra, it is not expected from the SSC emission model, were reproduced in the 2019 SED.

*Swift*-XRT showed a rich light curve and spectral parameters. Light curve presented a historical maximum flux in 2017 and a temporal behavior which is completely different with the MAGIC curve. Those data enable us to see the temporal evolution of the X-ray spectrum. According to the correlation of the spectral parameters, correlations looks changing in time. Spectral fitting showed a tendency which spectra are seem to be curved in 2017 and later, but straight in 2016. Those difference would play a key role to model a synchrotron peak in the emission model.

*Swift*-UVOT, optical and ultraviolet data were really interesting. The light curves showed temporal behaviors as similar as the one of *Swift*-XRT, and also similar to the Tuorla and OVRO. It indicates that optical and UV emissions are superposition from several origins, expected as multi-component models. However, unexpected excess in U,V, and B bands are still remains and further investigations are required.

Tuorla and OVRO showed a similar light curves, especially the peak in 2019. That feature can not be seen in the higher frequency, thus it suggests that radio and infrared band originates from unique emission component. SED of OVRO indicates that optical and radio spectrum will be smoothly connected with single power-law distribution.

In the next sections, I performed multiwavelength analyses to evaluate the complex behaviors among the wavelength. The discussion point raised here will be discussed with the mwl result again.

## 11.1. Variability in Blazar emission

As shown in figure 3.5, Blazar emission shows various type of spectral variability. One example, if Doppler factor  $\delta_D$  changes, the spectrum shift in energy and normalization with same scale (solid line and dotted line). In case electrons get energy, in other words, they are accelerated, the peak of electromagnetic emission only increase. Such a variability is drawn as transition from solid line to red dotted-dashed line. Moreover, if the density of electron increase, inverse compton component (or, possibly hadronic component) independently vary. This variability is drawn as blue dashed line.

Those possible variability depends on the emission model, but is clear that different variability shows different energy dependence. We have several approach to evaluate the variabilities. Thus I adopted some of them and discuss the result in the following sections.



## 11.2. Multiwavelength Temporal Analysis

### 11.2.1. Fractional variability

The fractional variability (or excess variance) is a quantitative method to evaluate the intrinsic variability of the astronomical source excluding statistical uncertainty of measurement (Vaughan et al., 2003). The value is defined as:

$$F_{\text{var}} = \sqrt{\frac{S^2 - \sigma_{\text{err}}^2}{\bar{F}^2}}, \quad (11.1)$$

$$S^2 = \frac{\sum_{i=1}^N (F_i - \bar{F})^2}{N - 1}, \quad (11.2)$$

$$\sigma_{\text{err}}^2 = \frac{\sum_{i=1}^N \sigma_i^2}{N}. \quad (11.3)$$

Where  $F_i$ ,  $\sigma_i$ ,  $\bar{F}$  are a flux measurement, its error, and its average, respectively. Error of  $F_{\text{var}}$  is,

$$\sqrt{F_{\text{var}}^2 \sqrt{\frac{2}{N} \left( \frac{\sigma_{\text{err}}^2}{F_{\text{var}}^2} \right)^2 + \frac{\sigma_{\text{err}}^2}{N} \left( \frac{2F_{\text{var}}}{\bar{F}} \right)^2}} - F_{\text{var}}. \quad (11.4)$$

I used  $F_{\text{var}}$  to estimate an excess variance of each wavelength data.

Table 11.1 and 11.2 summarize analysis result of the MWL fractional variabilities. Concerning *Swift*-BAT, I did not use in the analysis because of its huge uncertainties. As a result, High energy bands showed higher  $F_{\text{var}}$  except *Fermi*-LAT. The trend is similar with a previous study(e.g.,(Patel et al., 2018)). Figure 11.2 demonstrates the values in one plot. For the annual result, OVRO and Tuorla presented their maximum in 2019 on one hand. On the other hand,*Swift*-UVOT and *Swift*-XRT showed its maximum in 2016 and 2017, respectively. *Fermi*-LAT showed the maximum in 2015, and MAGIC presented the highest in 2016.

$F_{\text{var}}$  of MAGIC in 2015 is not larger than one of *Fermi*-LAT as other years are. I think it is due to the observation bias. As shown in equation 11.1,  $F_{\text{var}}$  is defined as an excess variance divided by an average flux. Thus if the observation is not well sampled, the value would be small. Except 2015, the trend in HE nad VHE gamma-rays are similar.

Table 11.1: Fractional variabilities amplitude for *Swift*-XRT,*Fermi*-LAT, and MAGIC

Period	$F_{\text{var,XRT}}$	$F_{\text{var,LAT}}$	$F_{\text{var,MAGIC}}$
2015	$0.425 \pm 0.005$	$0.63 \pm 0.04$	$0.43 \pm 0.05$
2016	$0.398 \pm 0.002$	$0.32 \pm 0.04$	$0.80 \pm 0.01$
2017	$0.485 \pm 0.002$	$0.22 \pm 0.05$	$0.63 \pm 0.02$
2018	$0.363 \pm 0.002$	$0.16 \pm 0.07$	$0.47 \pm 0.03$
2019	$0.325 \pm 0.002$	$0.22 \pm 0.07$	$0.34 \pm 0.02$
5year	$0.493 \pm 0.001$	$0.44 \pm 0.02$	$1.02 \pm 0.01$

Table 11.2: Fractional variabilities amplitude for the radio and optical bands

Period	$F_{\text{var,OVRO}}$	$F_{\text{var,Tuorla}}$	$F_{\text{var,UVOTB}}$	$F_{\text{var,UVOTUV-M2}}$
2015	$0.079 \pm 0.009$	$0.217 \pm 0.002$	—	—
2016	$0.063 \pm 0.002$	$0.141 \pm 0.002$	$0.191 \pm 0.002$	$0.231 \pm 0.003$
2017	$0.075 \pm 0.003$	$0.159 \pm 0.002$	$0.172 \pm 0.002$	$0.180 \pm 0.005$
2018	$0.079 \pm 0.002$	$0.160 \pm 0.002$	$0.124 \pm 0.002$	$0.105 \pm 0.005$
2019	$0.124 \pm 0.003$	$0.234 \pm 0.002$	$0.184 \pm 0.002$	$0.214 \pm 0.005$
5year	$0.111 \pm 0.002$	$0.2351 \pm 0.0009$	$0.198 \pm 0.001$	$0.226 \pm 0.002$

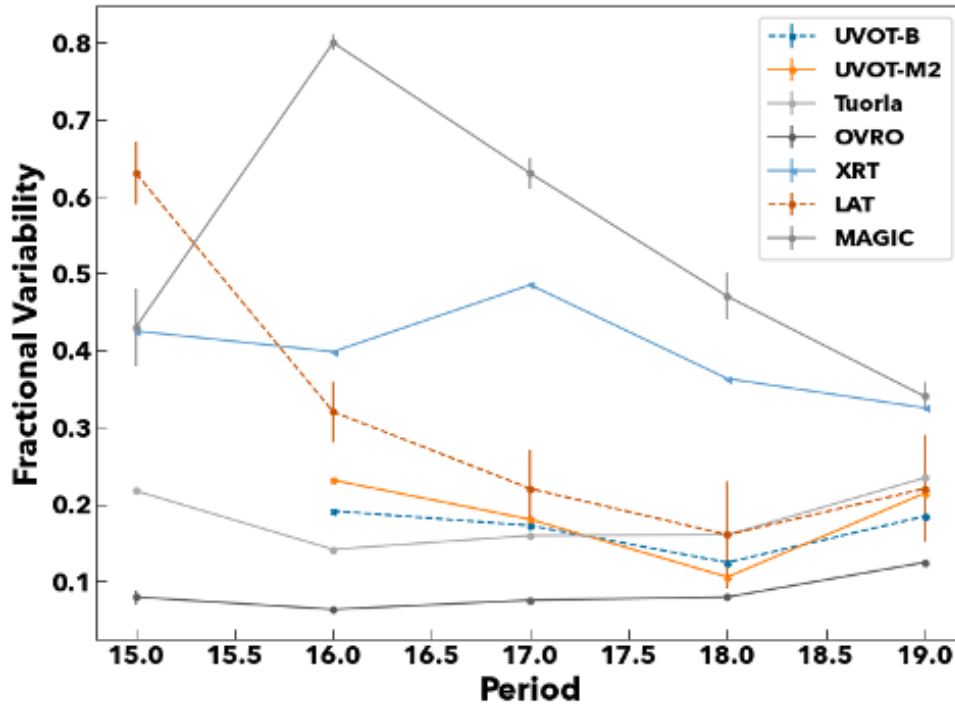


Figure 11.2: Fractional variability with MWL light curves. Results from 2015 to 2019 are shown for each instruments.

### 11.2.2. Simultaneous flux correlation

The flux correlation is an analysis method to evaluate how the source flux change through multiwavelength data. To find simultaneous observations I defined a reference and compared samples for the two light curves as shown in figure 11.3. Among the two light curves, I adopted more frequently sampled data as compared, and another is as reference. In the calculation, I set a coincidence window from the one of reference measurement, and find a most closest measurement in the window. By doing so, one can avoid duplicate counting for a specific flux measurement as a coincident pair. The method is historically used and predicts show different slopes in the correlation plot (Katarzynski et al., 2005).

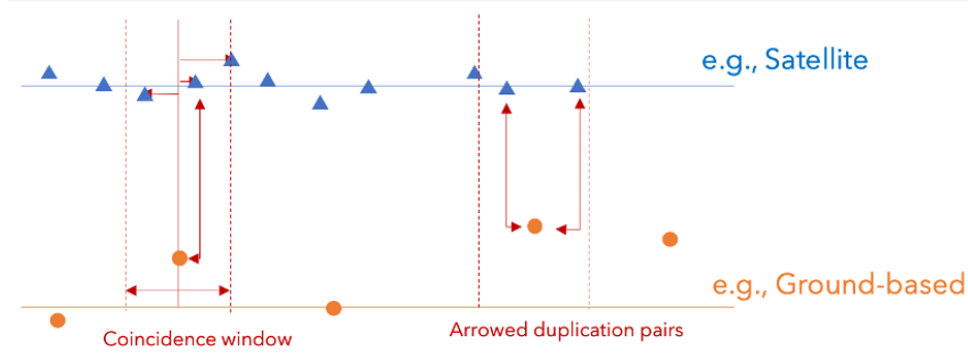


Figure 11.3: Calculation method of the flux calculation. Find a observation within the coincidence window with respect to certain observation. To avoid duplicate counting, I adopted left case in this study.

For the coincident flux pairs, I calculated Pearson coefficient to see the strength of the linear correlation. Pearson coefficient is defined as,

$$\rho = \frac{S_{xy}}{\sqrt{S_x S_y}} \quad (11.5)$$

$$= \frac{\sum_i (x_i - \bar{x})(y_i - \bar{y})}{\sqrt{\sum_i (x_i - \bar{x})^2 \sum_i (y_i - \bar{y})^2}}. \quad (11.6)$$

If  $\rho$  is close to unity, it indicates a linear correlation exists.

I adopted the coincidence window  $\pm 24$  hours. This is because there is time difference between ground-based telescopes. Figures 11.4 to 11.9 show the results with respect to the MAGIC data. While the correlation coefficient between *Fermi*-LAT and MAGIC was positive, around 0.6, the correlation coefficients for other wavelengths ranged from 0.17 to -0.5, indicating an inverse correlation. However, the correlation diagram reveals something interesting feature. The correlation that changes with time is particularly remarkable in the correlation between *Swift*-XRT and MAGIC as shown in figure 11.5. The correlation coefficient for this wavelength is 0.17 for the five years, but for 2016 and 2017 only, the correlation is relatively strong at 0.77 and 0.59. The results for gamma rays with radio and optical bands are shown in figures 11.6 to 11.9, with the negative correlation coefficients (-0.11 to -0.44).

The correlation coefficients of *Fermi*-LAT with other wavelengths are small, and the plots did not show a clear structures as seen in the MAGIC results. It was also same for X-rays, low correlation coefficients of about 0.3.

Concerning the correlations between optical wavelengths and radio bands showed strong correlations with the coefficients ranging from 0.56 to 0.93. Figures 11.10 to 11.14 show the clear correlations in the flux densities.

I tested the systematic effect in the flux correlation structure by changing coincidence windows. The overall structure in VHE gamma-ray and X-ray correlation does not change significantly with the window. See section C for details.

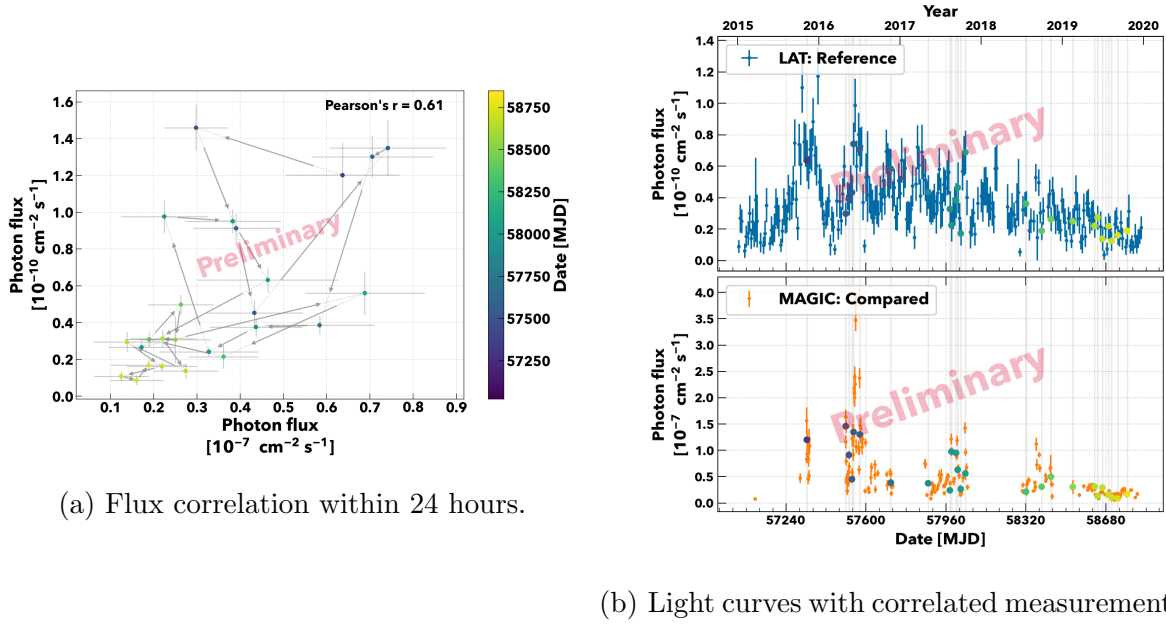


Figure 11.4: Flux correlation between MAGIC and LAT. Left panel: flux correlation. x-axis is low-energy and y-axis is high-energy data. The color shows the date in MJD. Pearson coefficient is also shown. Right panel: Light curves with correlated points. The color of filled circle is same for the left panel.

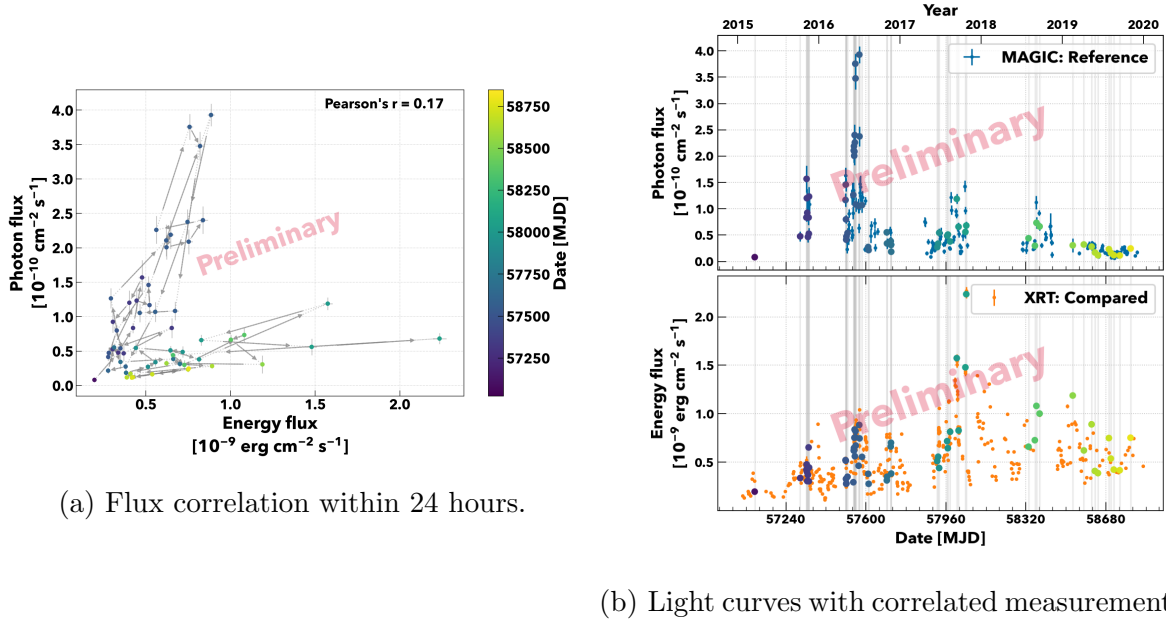
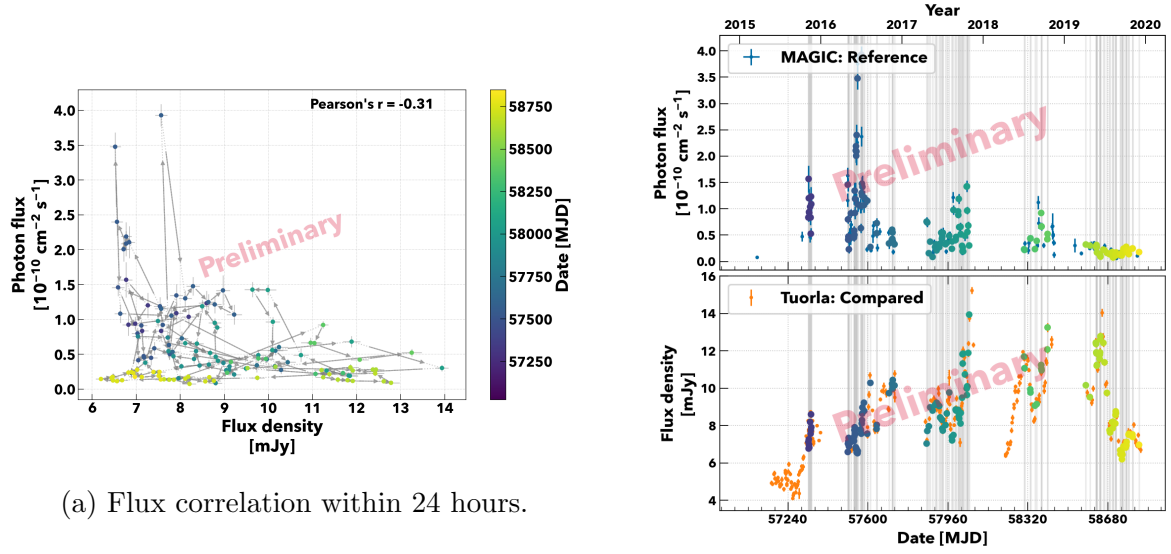


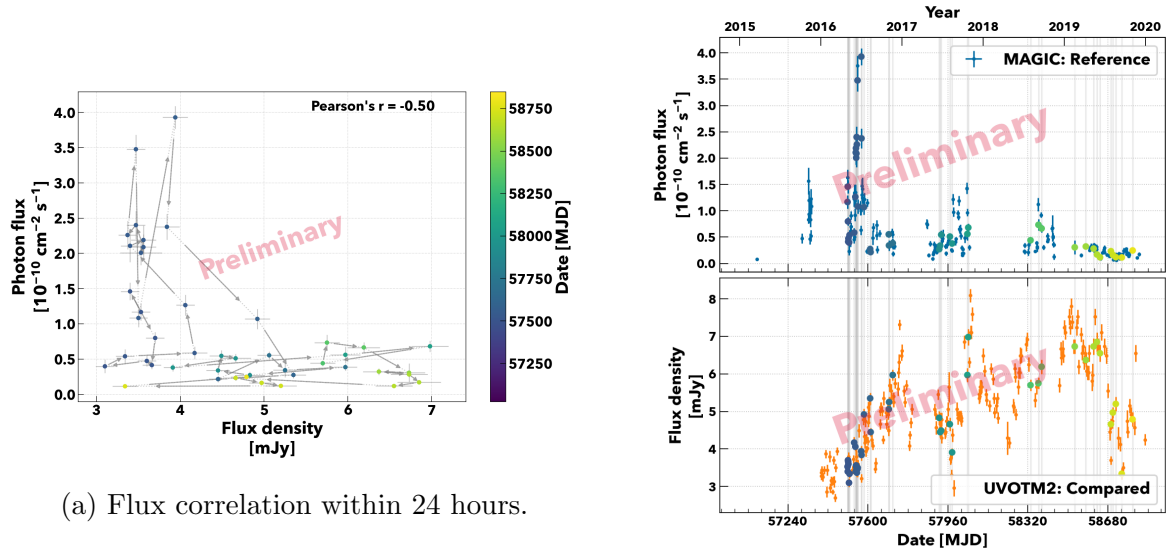
Figure 11.5: Flux correlation between MAGIC and XRT



(a) Flux correlation within 24 hours.

(b) Light curves with correlated measurements.

Figure 11.6: Flux correlation between MAGIC and Tuorla



(a) Flux correlation within 24 hours.

(b) Light curves with correlated measurements.

Figure 11.7: Flux correlation between MAGIC and UVOT-M2

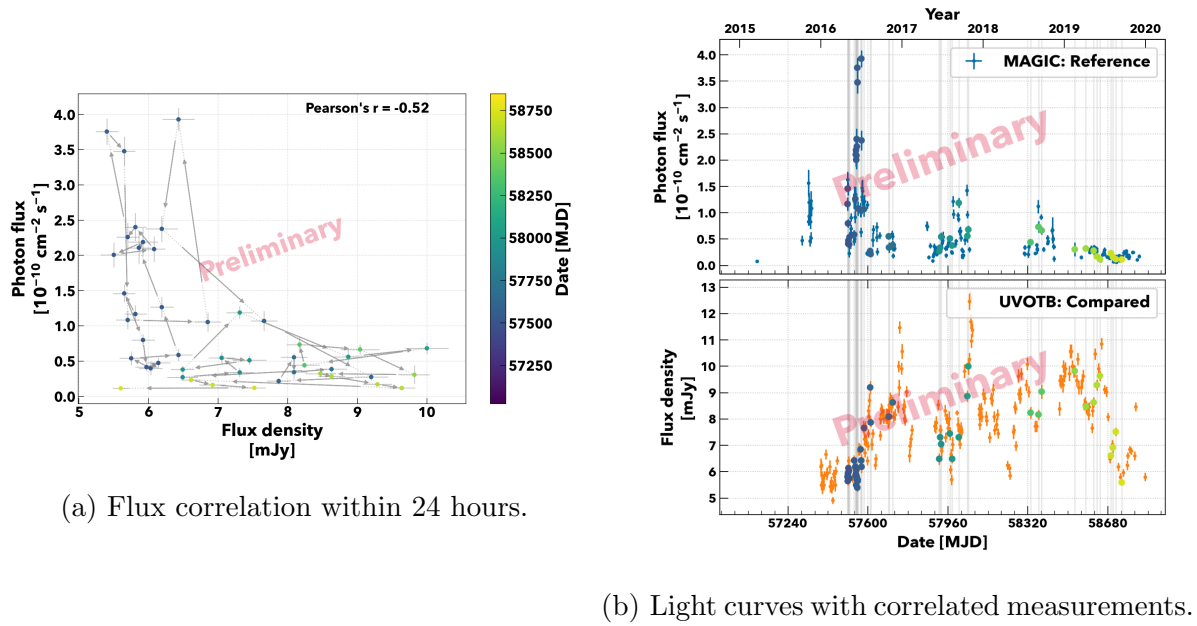


Figure 11.8: Flux correlation between MAGIC and UVOT-B

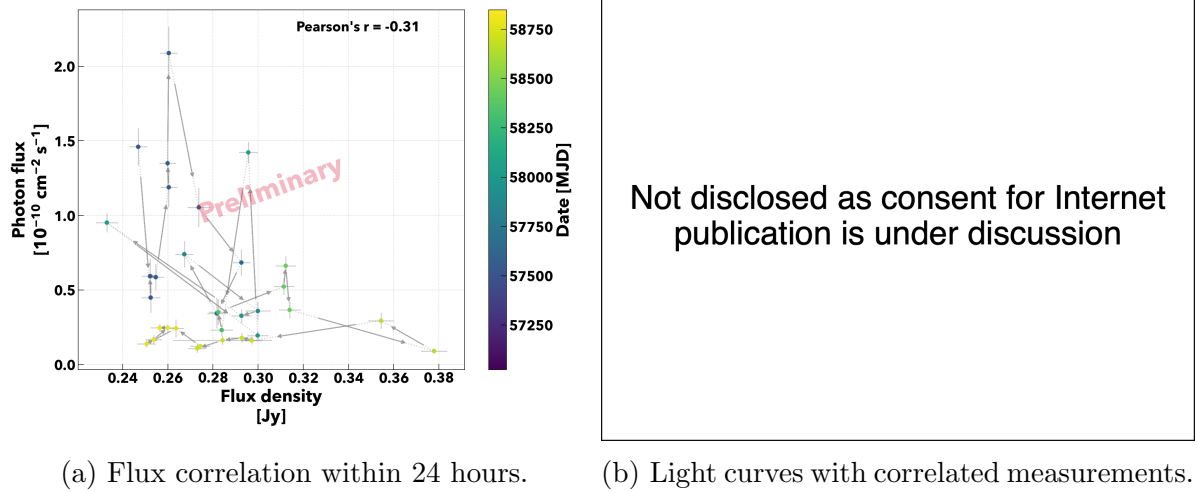
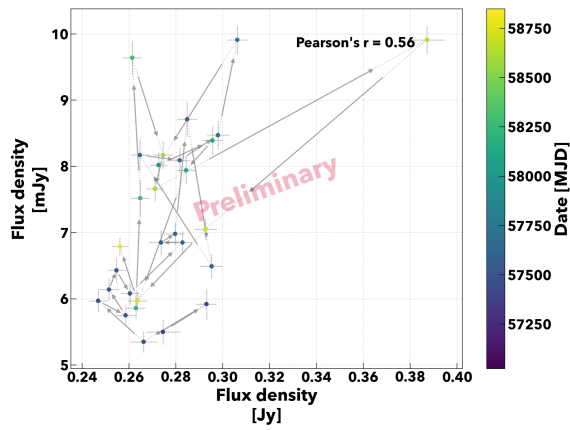


Figure 11.9: Flux correlation between MAGIC and OVRO

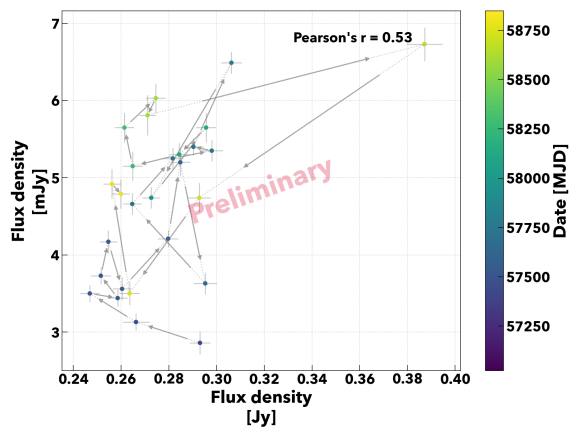


(a) Flux correlation within 24 hours.

Not disclosed as consent for Internet publication is under discussion

(b) Light curves with correlated measurements.

Figure 11.10: Flux correlation between UVOT-B and OVRO

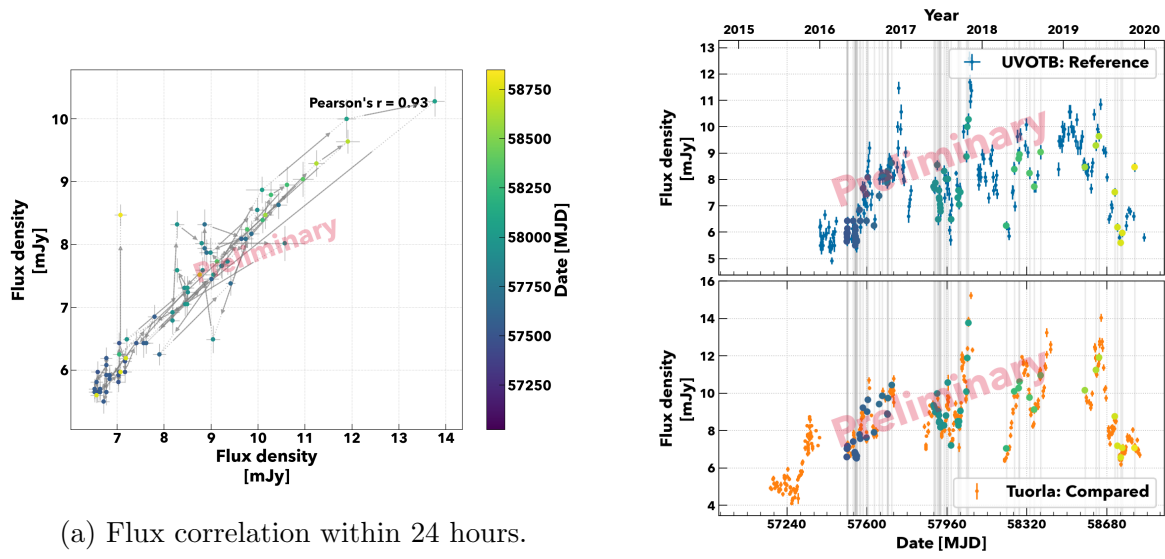


(a) Flux correlation within 24 hours.

Not disclosed as consent for Internet publication is under discussion

(b) Light curves with correlated measurements.

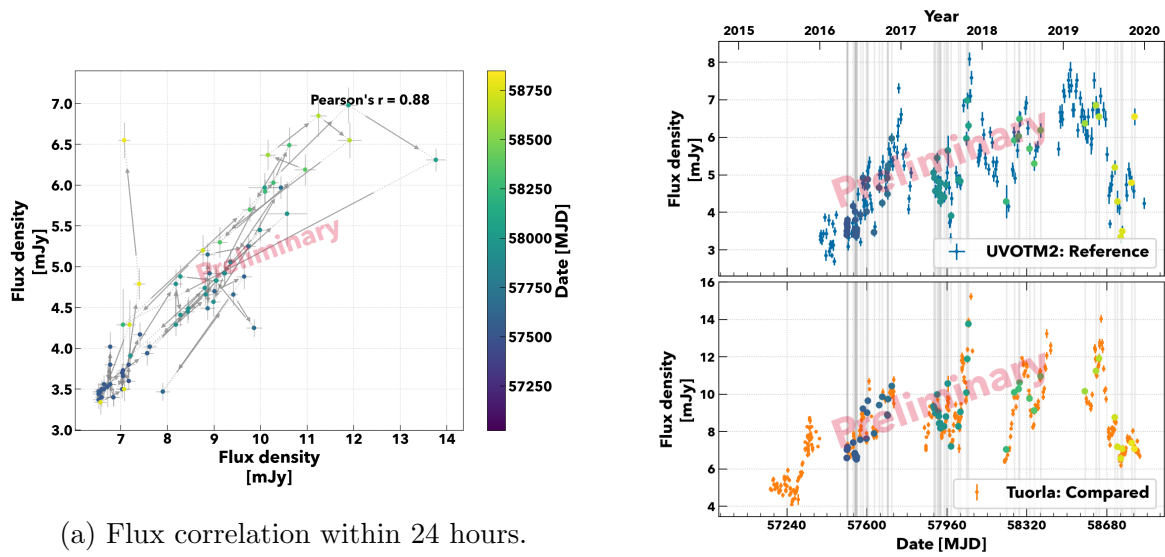
Figure 11.11: Flux correlation between UVOT-M2 and OVRO



(a) Flux correlation within 24 hours.

(b) Light curves with correlated measurements.

Figure 11.12: Flux correlation between UVOT-B and Tuorla

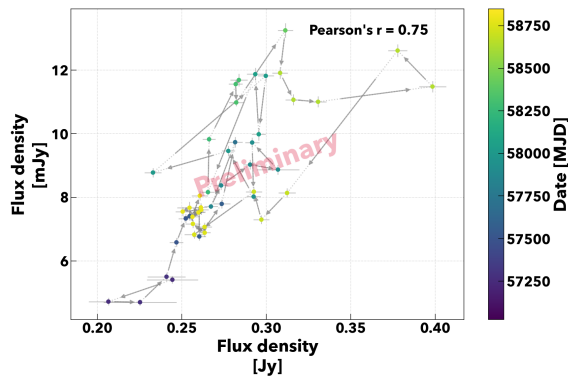


(a) Flux correlation within 24 hours.

(b) Light curves with correlated measurements.

Figure 11.13: Flux correlation between UVOT-M2 and Tuorla





(a) Flux correlation within 24 hours.

Not disclosed as consent for Internet publication is under discussion

(b) Light curves with correlated measurements.

Figure 11.14: Flux correlation between Tuorla and OVRO

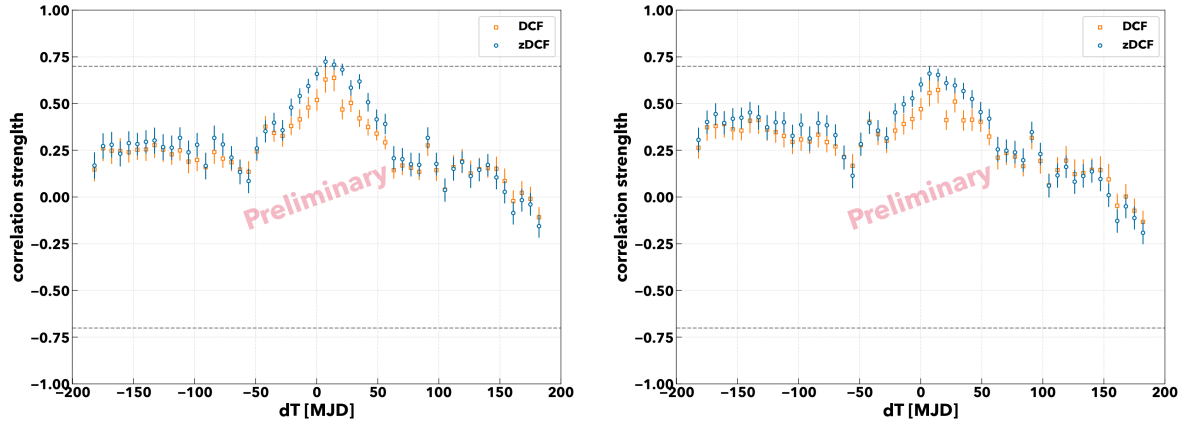
### 11.2.3. Discrete Correlation Function (DCF)

The discrete correlation function (DCF) is a method to evaluate whether there are similar structures between data at different wavelengths. If the luminosity curves of two wavelengths have similar variations with time difference, DCF will show a value close to 1 at time difference  $A$ . In the case of anti-correlation, it is -1. The flux correlation described in the previous section cannot evaluate variations with time difference. If the two light curves used in the DCF are identical, it is possible to check for periodicity in a given light curve. In this study, DCF and a modified zDCF were used to examine the similarity between wavelengths (Edelson & Krolik, 1988; Alexander, 2014).

Figure 11.15 shows an example of a DCF calculated using radio and optical light curves. The vertical axis represents the strength of the correlation, and the horizontal axis represents the time difference. Here the time difference is the time of the lower energy data minus the time of the higher energy data. Suppose a strong correlation is suggested for a given time difference  $dt$ . In that case, it indicates that the lower energy data has a similar structure to the higher energy data with a delay of  $dt$ . DCF calculations were performed for all pairs among gamma-ray to radio frequency light curves.

First, the correlation between radio and optical light curves in figure 11.15 as an example. This result shows a delay of about 20 days for radio light curve. The two data are similar when looking at the light curves for each wavelength (fig. 11.14). The broad peak structure, especially in 2019, and the overall trend probably produce the delayed correlation.

The result can be interpreted as the two radiations produced from the common emission region. A similar DCF results were also obtained in the data up to the ultraviolet as shown in figure 11.16, thus it might be they are also from the same emission region responsible for radio to ultraviolet band. On the other hand, the analysis results with higher energy bands did not show a strong correlation ( $\rho > 0.7$ ), leading to the conclusion that there is no similarity.



(a) DCF of OVRO-UVOT-B

(b) DCF of OVRO-UVOT-M2

Figure 11.16: Discrete correlation functions of UVOT bands with respect to OVRO

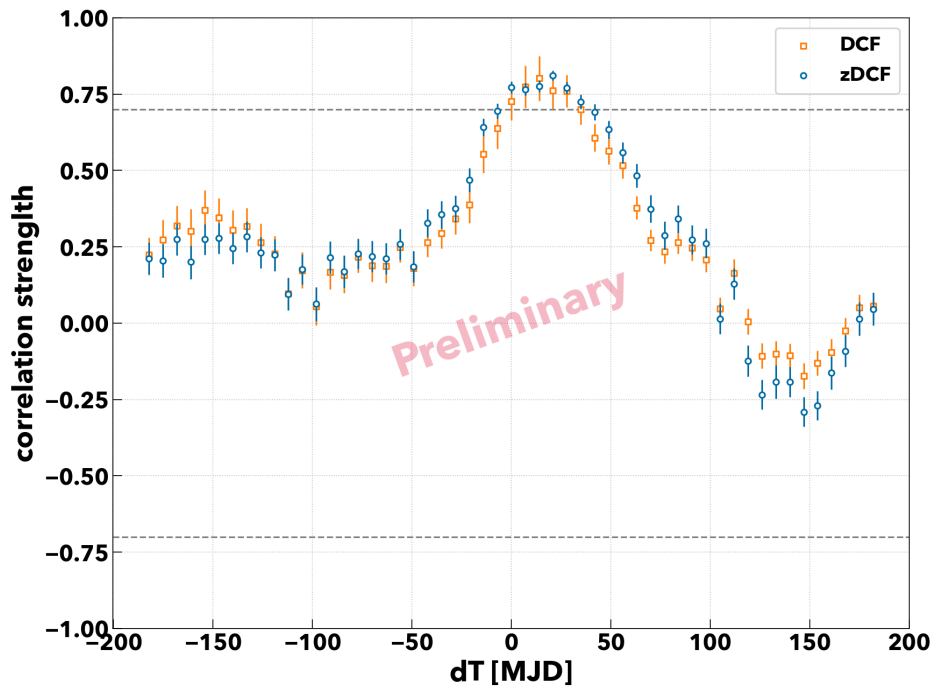


Figure 11.15: Discrete correlation of OVRO-Tuorla

DCF between *Fermi*-LAT and MAGIC showed zero time-lag correlation. This is consistent with the expectation from the simplest model of blazar emission, which consists of two peaks, considering HE and VHE gamma rays as the same origin. Moreover, the correlation between optical wavelengths strongly suggests coincidence correlations as shown in figure 11.17.

DCF results with other combinations are summarized in the Appendix. See section B

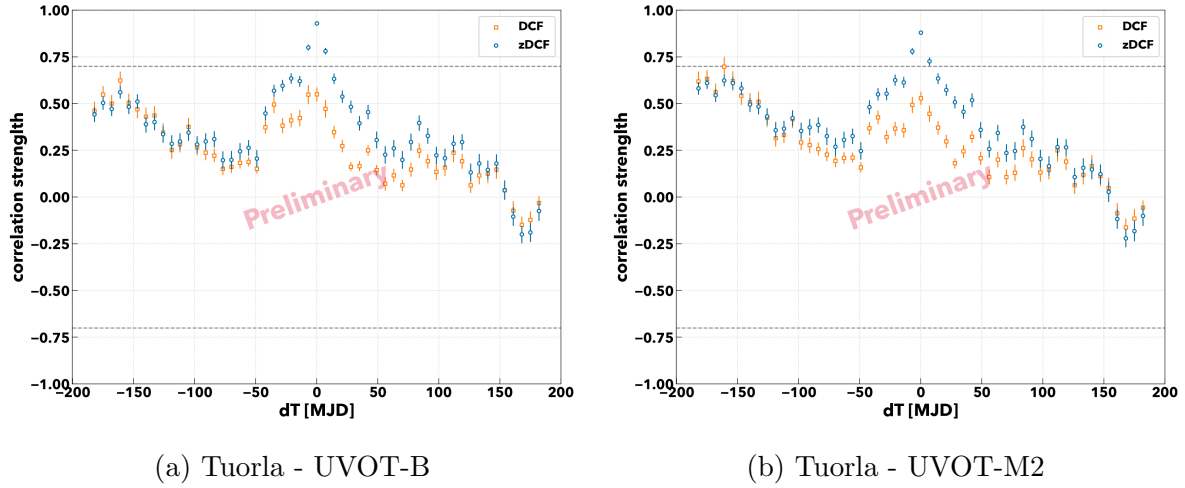


Figure 11.17: Discrete correlation functions of UVOT bands with respect to Tuorla

for other combinations.

### 11.3. Summary and Discussion of the Temporal Analysis

Thus far, several temporal analysis with MWL light curves were shown. First, the trends of fractional variability amplitudes through five years are similar in optical to radio bands, and HE to VHE gamma-ray bands. Larger amplitudes in X-ray and VHE gamma-ray are expected if spectrum has peaks around those energies. This supports the spectral distribution has a two-bump shape as usually considered.

Adding that, flux correlations between MAGIC and others are really interesting. The X-ray correlation plot showed clear V-shape, each branch has a strong correlation in 2016 and 2017 (Fig. 11.5a). The flux correlation clearly varies in time, it indicates the environment of the emission region also changed. One can consider two scenarios for the explanation of the flux correlation. One is emission evolves in time and the environment was changed at the end of 2016. If this scenario is true, spectral modeling parameters might be continuously changed in time.

Another scenario is different blobs are in charge of the emission in 2016 and later, respectively. This scenario is more straightforward and simple. One need to consider different emission regions in time, and they are not required to have the same environment.

As shown in section 10.2.7, spectral parameters of *Swift*-XRT also showed the trend varying in time. This might be also due to the difference of the blob.

To evaluate those scenarios, I performed the spectral modeling with the one-zone SSC model for the selected periods.

## 12. Evaluation of temporal variability with one-zone SSC model

### 12.1. Multiwavelength Spectral Energy Distribution modeling

A one-zone SSC model was used to model the MWL SED. As discussed in section 3.3, The model considers a spherical region (blob) inside a jet of radius  $R_{\text{blob}}$  and assumes that its interior is filled with a uniform magnetic field  $B$  and electrons. In the observer's system, the celestial object is assumed to be located at distance  $z$  and the radiating region is moving with relativistic velocity  $\beta_r$  and is observed at an apparent angle  $\theta_{\text{obs}}$ . The Doppler factor is  $\delta_D$ . By considering the specific electron density  $k_e$ , power  $p$ , and energy range  $\gamma_{e,\text{min}}$  to  $\gamma_{e,\text{max}}$ , the expected radiation can be calculated (See [Dermer et al. \(2009\)](#) for details). In this study, I assumed that the electron distribution has a spectral break at  $\gamma_{\text{break}}$  to radiative cooling, in reference to previous studies.

The results of the time series analysis suggested that something changed in the emission region after the end of 2016. I tried to unravel what environmental changes in the emission region are responsible for the changing flux correlation through other wavelength spectral modeling.

First, I selected four periods for the spectral modeling as shown in figure 12.1. These four periods are based on the periods indicated by the Bayesian analysis of MAGIC (fig. 8.2) and also correspond to the root and tip of each "branch" structure in the flux correlation plot (fig 11.4a).

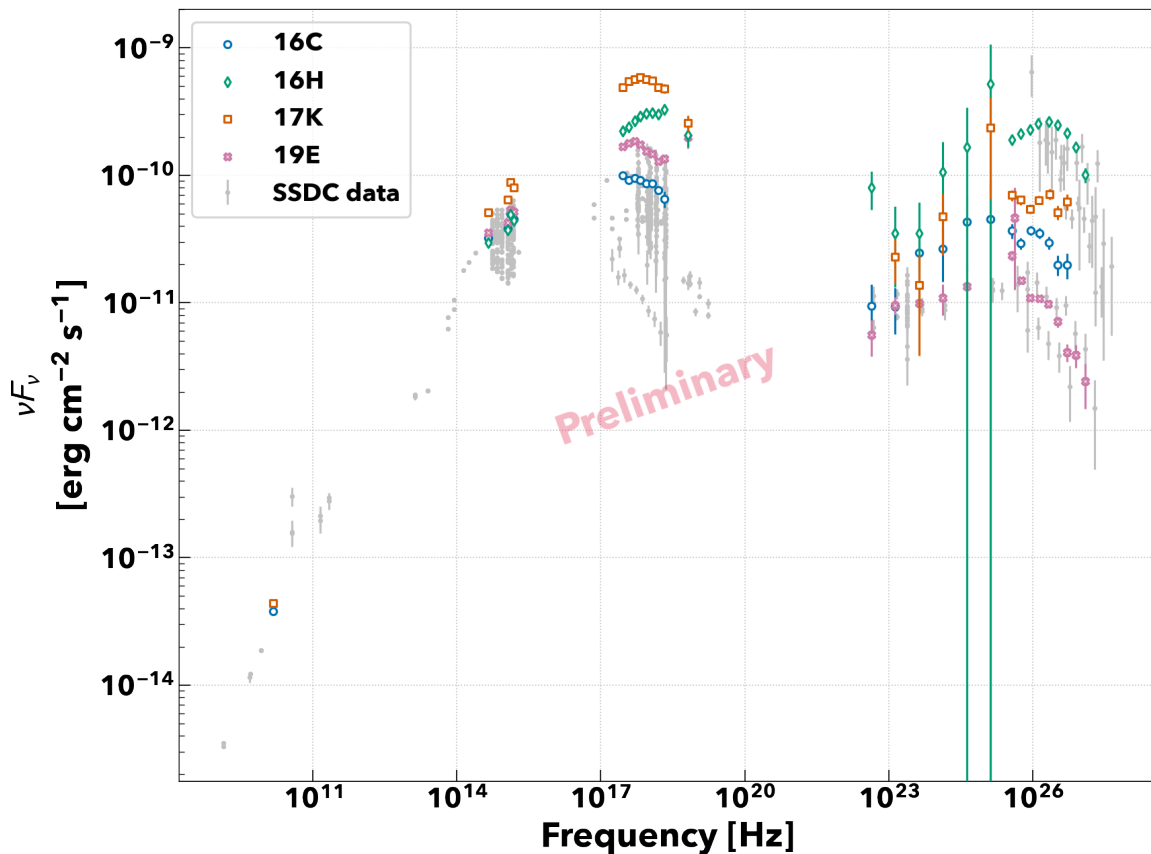


Figure 12.1: MWL SED data. 16C is the lower state before the 2016 flare, 16H is the 2016 flare, 17K corresponds to the X-ray maximum state, and 19E equals to the lower state in 2019. Flaring states locates at the tip of each branch and the low states are on the root in figure 11.4a.

Figure 12.1 shows spectral energy distribution (SED) of selected four periods. As expected from the flux correlation plot, the ratio of X-ray to gamma-ray luminosities changed during the 2016 and 2017 flares. Not only that, but it can be seen that in 2017, there is a peak around 2 keV, the peak shifts to higher energies during the 2016 flare. The trend is also true for HE and, VHE gamma rays: in the respective low states of 2016 and 2019, the peak is located at lower energies than during the flares in X-rays and gamma rays. However, again, the ratio of X-rays to gamma rays is different, with the ratio of X-rays to gamma rays appearing closer in 2016.

In particular, since 1ES1959+650 is a BLLac-type celestial object, self-Compton scattering is expected. Therefore, I assumed the one-zone SSC model for each multiwavelength spectrum and estimated the parameters defining the environment of the emitting region from the best fit model.

The  $\chi^2$  statistic was used to optimize the model. Historically, mathematical optimization methods have not been used in multiwavelength modeling of blazars. There are two

main reasons for this. The first is that the data obtained are mostly not simultaneous. This is due to not only observational condition such as the weather, but also due to a timezone difference. e.g., ground-based optical telescopes can not observe during day, but *Swift* satellite or radio telescope can.

In this point, the following improvements were made in this study. For MAGIC, I used spectra averaged within time bins estimated by the Bayesian block method. Since the Bayesian block method estimates a period during which the flux can be considered statistically constant, thus I assumed that the spectra are also statistically identical during this period. For *Fermi*-LAT, I used data integrated within the same Bayesian period of MAGIC. Since *Fermi*-LAT data has a larger statistical error than other wavelengths, thus this assumption seems to be acceptable.

Next, for the *Swift*-XRT spectra, only the data observed within the period estimated by the Bayesian block method, and data which were measured within 12 hours before and after the MAGIC observations, were analyzed. Those data were averaged and used for the fitting. By this operation, data as close as possible to the time of the MAGIC data. For the optical data, that existed inside the Bayesian block of MAGIC were averaged. Finally, radio data were ignored in the modeling, as is done in the modeling of blazar studies (MAGIC Collaboration et al., 2020d). This is because the radio emission from the blazar is considered to be a superposition of the emission from the entire jet.

The one-zone SSC model has at least 10 parameters and they are degenerated as discussed in 12.1. To avoid instabilities in the fitting procedure, I assumed some relations among parameters and fixed. First, the electron spectral index  $p$  was fixed at 2.3, and has synchrotron cooling break at  $\gamma_{e,\text{break}}$ . The spectral index for the energy larger than  $\gamma_{e,\text{break}}$  is expected to be  $p + 1 = 3.3$  if synchrotron cooling is assumed. The values was estimated from the MWL SED (fig 12.1) especially for the flaring states. Adding that, electron minimum Lorentz factor  $\gamma_{e,\text{min}}$  is fixed at  $1 \times 10^3$ . There is no concrete reason, but similar values used for the previous studies (section 5.4).

It is assumed that the bulk Lorentz factor  $\Gamma$  equals Doppler factor  $\delta_D$ . This corresponds to  $\cos \theta_{\text{obs}} = \beta_F$ . There is no information concerning  $\theta_{\text{obs}}$ , thus this is an assumption for simplicity.

Futhermore, the magnetic field  $B$ , Doppler factor  $\delta_D$ , and the maximum Lorentz factor  $\gamma_{e,\text{max}}$  are given when the model fit performs. This is because  $B$  and  $\delta$  are degenerated each other, and also with the electron density  $k_e$ . Thus both parameters are given for a specific fit with reasonable values ( $\delta_D = 10, 30$  and  $B = 0.01, 0.03, 0.1, 0.3\text{G}$ ). The range of the given values are based on previous studies. Finally,  $\gamma_{e,\text{max}} = 6, 6.5, 7$  are given to find a reasonable fit,  $\gamma_{e,\text{max}}$  is obtained from the X-ray data, but the uncertainty of the value is often zero. As a result, I performed fitting with free parameters of the emission region's radius  $R_{\text{blob}}$ ,  $\gamma_{e,\text{break}}$ , and the electron density  $k_e$ .

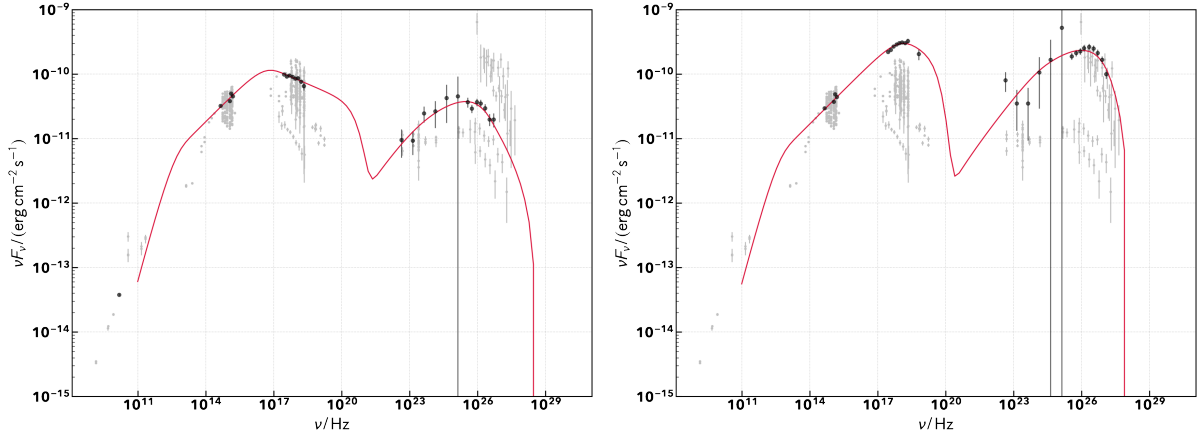
In addition, since statistical uncertainties in the X-ray and optical data are very small, still the optimization fails. To improve the procedure, I introduced systematic uncertainties in quadratic term. A systematic error of 10 % was introduced for MAGIC, 5 % for *Fermi*-LAT, and 3 % for *Swift*-XRT, UVOT, and Tuorla.

Tables 12.1 and 12.2 summarizes the fitting results for the 2016 and 2017 and 2019 spectra. I summarized the resultant parameters if  $\chi^2$  is less than 100. This selection

criterion is an artificial, but fitted curves with large  $\chi^2$  looks not well converged.

Table 12.1: MWL SED fitting result for 2016 spectrum with One-zone SSC model

Period	$\delta_D$	$B$	$\log R_{\text{blob}}$	$\log \gamma_{e,\text{max}}$	$\log \gamma_{e,\text{break}}$	$\log k_e$	$\chi^2/\text{DoF}$
–	–	[G]	[cm]	–	–	[cm <sup>-3</sup> ]	–
16C	10	0.01	17.74 $\pm$ 0.01	6.5	5.587 $\pm$ 0.010	-1.57 $\pm$ 0.04	59.0/22
16C	10	0.01	17.74 $\pm$ 0.01	7.0	5.557 $\pm$ 0.010	-1.59 $\pm$ 0.04	38.4/22
16C	10	0.03	17.26 $\pm$ 0.01	6.5	5.315 $\pm$ 0.010	-0.95 $\pm$ 0.04	55.5/22
16C	10	0.03	17.26 $\pm$ 0.01	7.0	5.309 $\pm$ 0.010	-0.96 $\pm$ 0.04	49.4/22
16C	10	0.10	16.77 $\pm$ 0.01	6.5	5.063 $\pm$ 0.010	-0.33 $\pm$ 0.04	78.8/22
16C	10	0.10	16.77 $\pm$ 0.01	7.0	5.061 $\pm$ 0.010	-0.33 $\pm$ 0.04	73.1/22
16C	30	0.01	16.88 $\pm$ 0.01	6.5	5.311 $\pm$ 0.010	-0.81 $\pm$ 0.04	38.6/22
16C	30	0.01	16.88 $\pm$ 0.01	7.0	5.304 $\pm$ 0.010	-0.83 $\pm$ 0.04	37.6/22
16C	30	0.03	16.39 $\pm$ 0.01	6.0	5.084 $\pm$ 0.010	-0.17 $\pm$ 0.04	55.1/22
16C	30	0.03	16.39 $\pm$ 0.01	6.5	5.057 $\pm$ 0.010	-0.19 $\pm$ 0.04	37.8/22
16C	30	0.03	16.40 $\pm$ 0.01	7.0	5.055 $\pm$ 0.010	-0.19 $\pm$ 0.04	37.2/22
16C	30	0.10	15.90 $\pm$ 0.01	6.0	4.814 $\pm$ 0.010	0.48 $\pm$ 0.04	52.4/22
16C	30	0.10	15.90 $\pm$ 0.01	6.5	4.808 $\pm$ 0.010	0.46 $\pm$ 0.04	46.6/22
16C	30	0.10	15.90 $\pm$ 0.01	7.0	4.808 $\pm$ 0.010	0.46 $\pm$ 0.04	45.7/22
16C	30	0.30	15.40 $\pm$ 0.01	6.0	4.562 $\pm$ 0.010	1.13 $\pm$ 0.04	71.5/22
16C	30	0.30	15.41 $\pm$ 0.01	6.5	4.561 $\pm$ 0.010	1.12 $\pm$ 0.04	65.7/22
16C	30	0.30	15.41 $\pm$ 0.01	7.0	4.560 $\pm$ 0.010	1.12 $\pm$ 0.04	65.1/22
16H	10	0.01	17.400 $\pm$ 0.010	6.5	6.5	-0.60 $\pm$ 0.03	79.1/25
16H	10	0.01	17.43 $\pm$ 0.01	7.0	6.21 $\pm$ 0.02	-0.67 $\pm$ 0.03	58.7/25
16H	10	0.03	16.94 $\pm$ 0.01	6.5	6.01 $\pm$ 0.02	-0.05 $\pm$ 0.03	93.4/25
16H	10	0.03	16.96 $\pm$ 0.01	7.0	5.97 $\pm$ 0.02	-0.10 $\pm$ 0.03	71.7/25
16H	30	0.01	16.110 $\pm$ 0.010	7.0	5.70 $\pm$ 0.02	0.63 $\pm$ 0.03	58.8/25
16H	30	0.01	16.56 $\pm$ 0.01	6.5	5.98 $\pm$ 0.02	0.10 $\pm$ 0.03	63.1/25
16H	30	0.01	16.58 $\pm$ 0.01	7.0	5.94 $\pm$ 0.02	0.05 $\pm$ 0.03	68.4/25
16H	30	0.03	15.630 $\pm$ 0.010	7.0	5.47 $\pm$ 0.02	1.23 $\pm$ 0.03	65.5/25
16H	30	0.03	16.070 $\pm$ 0.010	6.0	6.5	0.73 $\pm$ 0.03	72.4/25
16H	30	0.03	16.100 $\pm$ 0.010	6.5	5.71 $\pm$ 0.02	0.66 $\pm$ 0.03	57.6/25
16H	30	0.10	15.610 $\pm$ 0.010	6.0	5.52	1.27 $\pm$ 0.03	95.6/25
16H	30	0.10	15.630 $\pm$ 0.010	6.5	5.47 $\pm$ 0.02	1.24 $\pm$ 0.03	69.0/25
16H	30	0.30	15.16 $\pm$ 0.01	7.0	5.23 $\pm$ 0.02	1.82 $\pm$ 0.03	95.7/25



(a) Fitting model and data of 16C.

(b) Fitting model and data of 16H

Figure 12.2: Examples of the fitted models

Table 12.2: MWL SED fitting result with One-zone SSC model

Period	$\delta_D$	$B$	$\log R_{\text{blob}}$	$\log \gamma_{e,\text{max}}$	$\log \gamma_{e,\text{break}}$	$\log k_e$	$\chi^2/\text{DoF}$
—	—	[G]	[cm]	—	—	[cm <sup>-3</sup> ]	—
17K	10	0.01	17.97 $\pm$ 0.01	6.5	6.5	-2.02 $\pm$ 0.04	63.9/21
17K	10	0.03	17.51 $\pm$ 0.01	6.5	5.97 $\pm$ 0.02	-1.47 $\pm$ 0.04	86.1/21
17K	10	0.10	17.03 $\pm$ 0.01	6.0	6.01	-0.84 $\pm$ 0.04	89.6/21
17K	30	0.01	17.11 $\pm$ 0.01	6.5	5.96 $\pm$ 0.02	-1.27 $\pm$ 0.04	80.7/21
17K	30	0.03	16.64 $\pm$ 0.01	6.0	6.00	-0.69 $\pm$ 0.04	65.0/21
17K	30	0.10	16.18 $\pm$ 0.01	6.0	5.46 $\pm$ 0.02	-0.13 $\pm$ 0.04	87.2/21
19E	10	0.01	18.08 $\pm$ 0.01	7.0	5.775 $\pm$ 0.009	-2.55 $\pm$ 0.03	96.2/25
19E	10	0.03	17.56 $\pm$ 0.01	6.5	5.537 $\pm$ 0.009	-1.82 $\pm$ 0.03	67.9/25
19E	10	0.03	17.58 $\pm$ 0.01	7.0	5.526 $\pm$ 0.009	-1.87 $\pm$ 0.03	70.6/25
19E	10	0.10	17.06 $\pm$ 0.01	6.5	5.282 $\pm$ 0.009	-1.16 $\pm$ 0.03	63.6/25
19E	10	0.10	17.07 $\pm$ 0.01	7.0	5.279 $\pm$ 0.009	-1.19 $\pm$ 0.03	59.6/25
19E	10	0.30	16.56 $\pm$ 0.01	6.5	5.035 $\pm$ 0.009	-0.49 $\pm$ 0.03	79.1/25
19E	10	0.30	16.57 $\pm$ 0.01	7.0	5.034 $\pm$ 0.009	-0.50 $\pm$ 0.03	71.4/25
19E	30	0.10	16.22 $\pm$ 0.01	6.0	5.035 $\pm$ 0.010	-0.46 $\pm$ 0.03	72.4/25
19E	30	0.10	16.24 $\pm$ 0.01	6.5	5.026 $\pm$ 0.009	-0.51 $\pm$ 0.03	76.2/25
19E	30	0.10	16.25 $\pm$ 0.01	7.0	5.025 $\pm$ 0.009	-0.52 $\pm$ 0.03	78.7/25
19E	30	0.30	15.73 $\pm$ 0.01	6.5	4.777 $\pm$ 0.009	0.19 $\pm$ 0.03	62.6/25
19E	30	0.30	15.73 $\pm$ 0.01	7.0	4.777 $\pm$ 0.009	0.19 $\pm$ 0.03	62.9/25

The best fit models are shown in figures 12.2 and 12.3. As seen from the figures, the best fit models well reproduce the observed spectra. Some of the fittings has been converged without the uncertainty in  $\gamma_{e,\text{break}}$ . For those trial, I excluded them from items for the discussion.



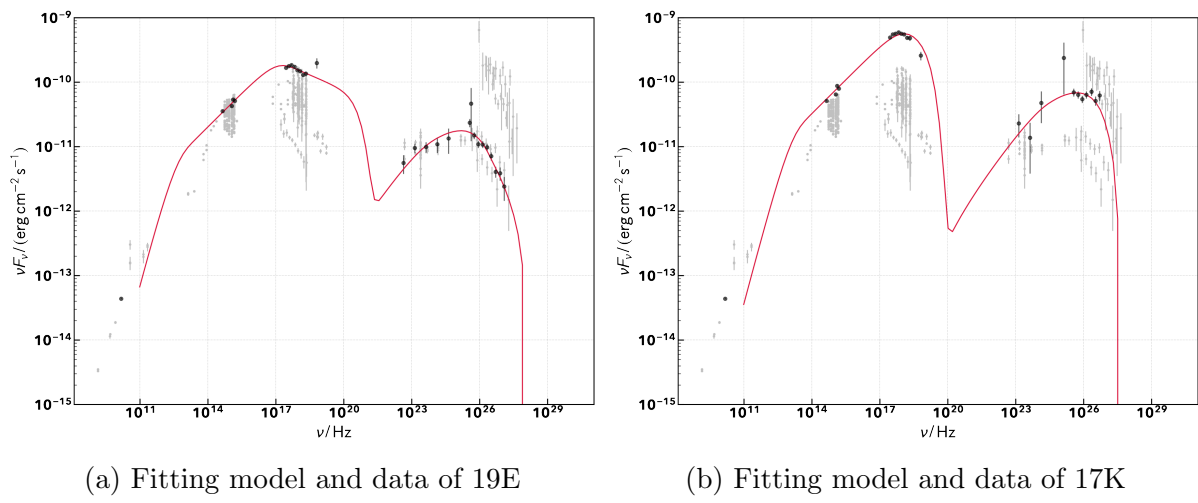


Figure 12.3: Examples of the fitted models

## 12.2. Discussion and Summary

In this section, I will discuss the interpretation of the fitting results and possible scenarios.

Looking first at 2016, the one-zone SSC model with  $\delta_D$  of 30 and  $B$  of 0.03 G explains the observed data best during the 2016 flare with  $\chi^2/\text{DoF}$  of 57.6/25. During the quiescent period in 2016, the model with  $\delta_D$  of 30 and  $B$  of 0.03 G shows the smallest  $\chi^2$  of 37.2/22. The size of the emission region  $R_{\text{blob}}$  become also smaller (16.40 to 16.10) by a factor of 2, without changing  $B$ . The change is not expected from the standard magnetic field dependence with respect to  $R_{\text{blob}}$ . It is often assumed that the magnetic field has a dependence with respect to  $R_{\text{blob}}$  as;

$$B \propto R^{-m}, \quad (12.1)$$

where  $m$  is 1 and 2 for the toroidal and poloidal case. If it is true, the transition between the two models is not realized. Instead, let's consider the second best fit model in comparison. The second best fit model has a  $B$  of 0.01 G with a statistic 37.6/22. For the case, magnetic field  $B$  increase by a factor of three with the decreasing radius of (16.88 to 16.10). It is more reasonable rather than no change in  $B$ . According to the dependency, the change of  $B$  by a factor of 3 with respect to the change of the radius by a factor of 6 is less than expected. However, the relation between  $B$  and  $R_{\text{blob}}$  is an ideal case. Thus, I think slight difference from the precision is acceptable. Furthermore, the density of electron  $k_e$  is also increased by a factor of about 30 ( $-0.83$  to  $0.66$ ), and this causes increasing the ratio of VHE gamma rays to X-ray.

Next, I will discuss for the models in 2017 and 2019. The one with  $\delta_D$  of 30 and  $B$  of 0.01 G showed the smallest  $\chi^2/\text{DoF}$  of 80.7/21. In 2019, the model with  $\delta_D$  of 10 and  $B$  of 0.1 G is the best (59.6/25). Comparing these two results, one can consider that  $\delta_D$  decelerate but  $B$  become stronger since the flare in 2017, contrary. In this scenario, the blob radius must decrease toward the quiescent period (17.11 to 17.07), while the density increases at the same time ( $-1.27$  to  $-1.19$ ). However, this scenario does not fulfill equation 12.1. Thus there is no explanation for the intensification of  $B$  by a factor of ten.

An alternative model would be to consider the model of 2017 flare where  $\delta_D$  is 30 while  $B$  remains at 0.1 G with a statistic of 87.2/21. In this case, as in 2016, the density is reduced and the blob radius become larger. However no change in the magnetic field while the radius change by a factor of eight (16.18 to 17.07). Thus, no clear picture with reasonable parameter connection between the flaring state in 2017 and the low state in 2019.

Summarizing the above discussions, I could not find a complete parameter set to explain a transition between the flaring and quiescent states. However, ignoring the dependency of the magnetic field allow to compare the two sets of the models. It is indeed the purpose of this modeling to explain the flux correlation. Consider the case the some electrons are injected into a small part of the emission region. In the case, electron density rises without a magnetic field amplification. Under the hypothesis, spectral evolution without changing the magnetic field might be realized. Then, the difference of the two branch of the flux

correlation might be caused by the difference of  $B$ . In 2016, the expected magnetic field is 0.03 G and 0.1 G later. Synchrotron energy loss is proportional to the square of the magnetic field, thus the difference will be a factor of ten. Adding that, electron densities also differ by a factor of ten (-0.19 and -1.19). Flux correlation indicated something happened at the end of 2016. Although I proposed a scenario which the emission blob evolve in time, the difference by a factor of ten would not happen. Therefore I conclude that the blobs produce the branches in the flux correlation are physically different.

Modeling parameters obtained from fitting on tables 12.1 and 12.2 are plotted in figures 12.4 to 12.5. Figure 12.4 shows the relation between the blob radius and the electron density at  $E_e = 5.11 \times 10^9$  eV.

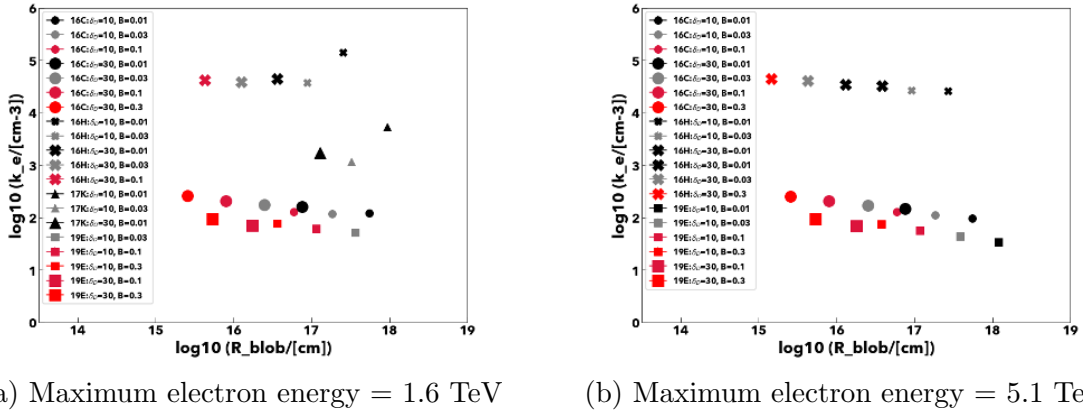


Figure 12.4: Modeling parameter correlation: the electron density and the blob radius

The electron density on the table are the value at the energy  $E_e = \gamma_{\text{break}} m_e c_0^2$ . Thus the density was scaled by

$$k_e = k_e^{\text{fit}} \left( \frac{10^4}{\gamma_{\text{break}}} \right)^{-2.3}. \quad (12.2)$$

Where  $k_e^{\text{fit}}$  is the electron density at  $E_{e,\text{break}} = \gamma_{\text{break}} m_e c_0^2$  and  $k_e$  is the density at  $\gamma = 10^4$ . The figure indicate there is a fix density not depending on the magnetic field  $B$  and Doppler factor  $\delta_D$ . Thus synchrotron flux at the observer frame satisfies:

$$\frac{h\nu d^3 N}{dA dt d\nu} \propto \delta_D^{3+\alpha} B^{1+\alpha} k_e R_{\text{blob}}^3. \quad (12.3)$$

Precisely speaking, the electron density has to be integrated through energy which contributes in the photon emission at the frequency  $\nu$ . In this study, the spectral index is fixed by  $p = 2.3$ , thus one can ignore the dependency in the energy.  $a$  is the photon's index of energy flux and has relation with  $p$  as  $a = (p - 1)/2$ .

Equation 12.3 predicts that a spectral model try to explain data by varying  $R_{\text{blob}}$  or  $k_e$  for given  $B$  and  $\delta_D$ . Moreover, the emissivity of x-ray and gamma-ray bands are expected

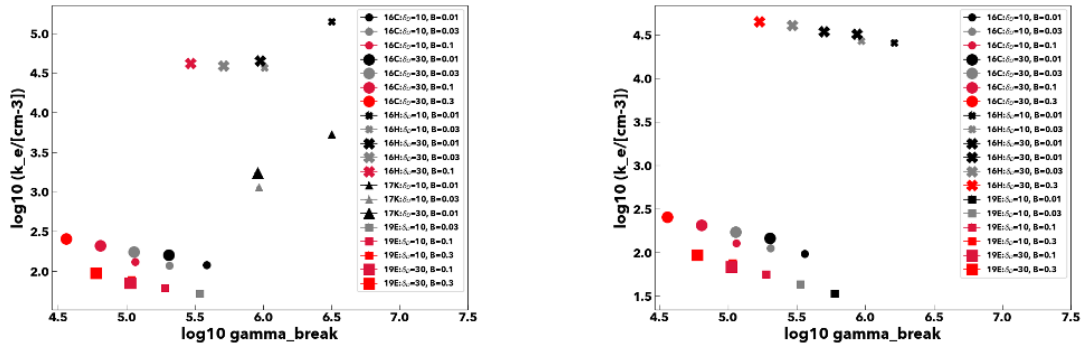
to follow synchrotron and SSC emissivity, respectively:

$$j_{\nu}^{\text{Sync}} = \frac{1}{4\pi} \int P(\gamma, \nu) N(\gamma) d\gamma \quad (12.4)$$

$$j_{\nu}^{\text{SSC}} = \frac{3}{4} \frac{h\nu\sigma_{\text{T}}}{4\pi} \int \frac{j_{\nu'}^{\text{Sync}}}{h\nu'} d\nu' \int F_{\text{C}}(\nu, \nu', \gamma) \frac{N(\gamma)}{\gamma^2} d\gamma. \quad (12.5)$$

Where  $N(\gamma) \propto k_e(\gamma/\gamma_{\text{break}})^{-p}$  is the electron density distribution. Thus, simply thinking, the synchrotron emissivity  $j_{\nu}^{\text{Sync}}$  is proportional to the density and the SSC emissivity  $j_{\nu}^{\text{SSC}}$  follows a square of the density. In order to keep the ratio between x-ray and gamma-ray flux, certain electron density is required despite the values of  $B$ ,  $\delta_D$ , and  $R_{\text{blob}}$ . The observed flux in the optical band is almost constant compared with x-ray and gamma-ray domains. Thus when larger  $B$  or  $\delta_D$  are given,  $R_{\text{blob}}$  is required to be small to suppress the apparent flux according to equation 12.3. The relation is clearly shown in figure 12.4. The electron density in 2016 flare and 2017 flare are clearly differ roughly by a factor of ten to 30.

Figure 12.5 shows a relation between the electron density  $k_e$  and the break Lorentz factor  $\gamma_{\text{break}}$ . The figure also shows weak correlation between two parameters.



(a) Maximum electron energy = 1.6 TeV

(b) Maximum electron energy = 5.1 TeV

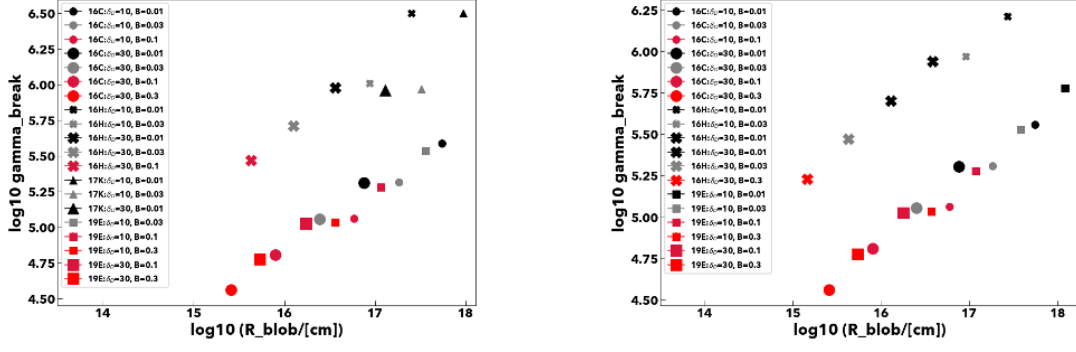
Figure 12.5: Modeling parameter correlation: the electron density and the break energy

This can be understood by the fact that  $k_e$  only contributes on the flux normalization and  $\gamma_{\text{break}}$  only works to change the spectral shape. Moreover, the peak of spectral energy distribution  $\nu_{\text{ph,peak}}^{\text{Sync}}$  roughly satisfy:

$$\nu_{\text{ph,peak}}^{\text{Sync}} \propto \delta_D B \gamma_{e,\text{peak}}^2. \quad (12.6)$$

Where  $\gamma_{e,\text{peak}}$  is the Lorentz factor of the electron contributing to the peak, it depends on the spectral index  $p$ . In this study,  $\gamma_{e,\text{peak}} = \gamma_{e,\text{break}}$ . Thus, as similar as figure 12.4, larger  $B$  and  $\delta_D$  give smaller  $\gamma_{e,\text{break}}$ .

At last, figure 12.5 shows the electron density and the break Lorentz factor.



(a) Maximum electron energy = 1.6 TeV

(b) Maximum electron energy = 5.1 TeV

Figure 12.6: Modeling parameter correlation: the break energy and the blob radius

The figure demonstrates the correlation between parameters, but I think it is an apparent correlation. In other words, the blob radius do not have direct correlation with the break Lorentz factor. This is because the above two plots (fig. 12.4 and fig. 12.5) indicate the clear relations theoretically expected. Based on the plots bigger  $B$  or  $\delta_D$  require smaller  $R_{\text{blob}}$ , and smaller  $\gamma_{\text{break}}$ , it is shown in the figure. No significant difference between 2016 flare and 2017 flare.

Some of points do not follow the relations discussed so far. They are (e.g., 17K: $\delta_D = 10$  and  $B = 0.01\text{G}$ , 16H: $\delta_D = 10$  and  $B = 0.01\text{G}$ ) not converged well. One can check it in tables 12.1 and 12.2 by the fact that uncertainties of the break Lorentz factor was not well estimated.

Summarizing the above discussion, I performed spectral modeling of few periods by SSC model with some physical assumptions and given  $B$  and  $\delta_D$ . According to the investigation between the fitting results, the electron density was clearly increased when flares happen. But the amplitude of the density change is not common. The density increased roughly by a factor of 100 in 2016 case, it is about a factor of ten in 2017. If the emission mechanism is SSC, the difference of density can easily changes the flux ratio between x rays and gamma rays.

However, it is not answer to the structure on the flux correlation between x rays and VHE gamma rays (Fig. 11.5a). This is because the difference in the electron density can not explain the V-shape correlation. If the electron density simply increase, the flux correlation draws a single line on the plot.

So what is the difference in the correlation brunches? One possible difference is the difference in the magnetic field  $B$ . For example, if the radius of the emission region is common for the flaring states (2016 and 2017), the magnetic field has to be different as shown in Fig. 12.4. The difference is approximately a factor of three. The variability amplitude of x-ray flux in 2017 onward is a factor of three to four (Fig. 11.5a) and the one of optical flux is a factor of two. Those amplitude are similar, thus it is naturally expected that both variabilities originate on the change in whole synchrotron spectra. Larger variability amplitude can be explained by varying the spectral shape. Moreover, similarity of the difference in magnetic field and thee synchrotron flux also support the change in the magnetic field.

One can consider possible scenario that how the magnetic field difference is realized. One possibility is simply different blobs contribute in observed flux in different periods. A blob became active in the beginning of 2015 and the activity continued until the end of 2016. Then alternative blobs having stronger  $B$  started activity showed x-ray historical flare in 2017 and became quiet.

Another possible case is the evolution of a emission region. One blob continuously contributed in the observed emission and gained its magnetic field at some point. However, is case the emission region radius are similar, magnetic field density should be amplified by a factor of ten. It is not naturally explained if the blob moves along the jet.

Anyway the spectral modeling performed in this study will be improved later. To improve the modeling, for example, observed variability time scale  $\Delta t_{\text{obs}}$  can be used to constrain the model as:

$$\frac{R_{\text{blob}}}{c} < \frac{\delta_D \Delta t_{\text{obs}}}{1+z}. \quad (12.7)$$

### 12.3. Comparison with the previous study

Temporal analysis and spectral modeling were performed to understand the nature of variability in this study. The remarkable result was the complex structure in x-ray and gamma-ray flux correlation (Fig. 11.5a). There are several previous studies can be compared with this study for Markarian 501 and 421. In this section, I will refer them and discuss the uniqueness of the complex structure.

First for Markarian 421, [Acciari et al. \(2014\)](#) showed the long-term correlation study using the 14-year dataset. The TeV observation was conducted by Whipple telescope and figure 12.7 shows the analysis result.

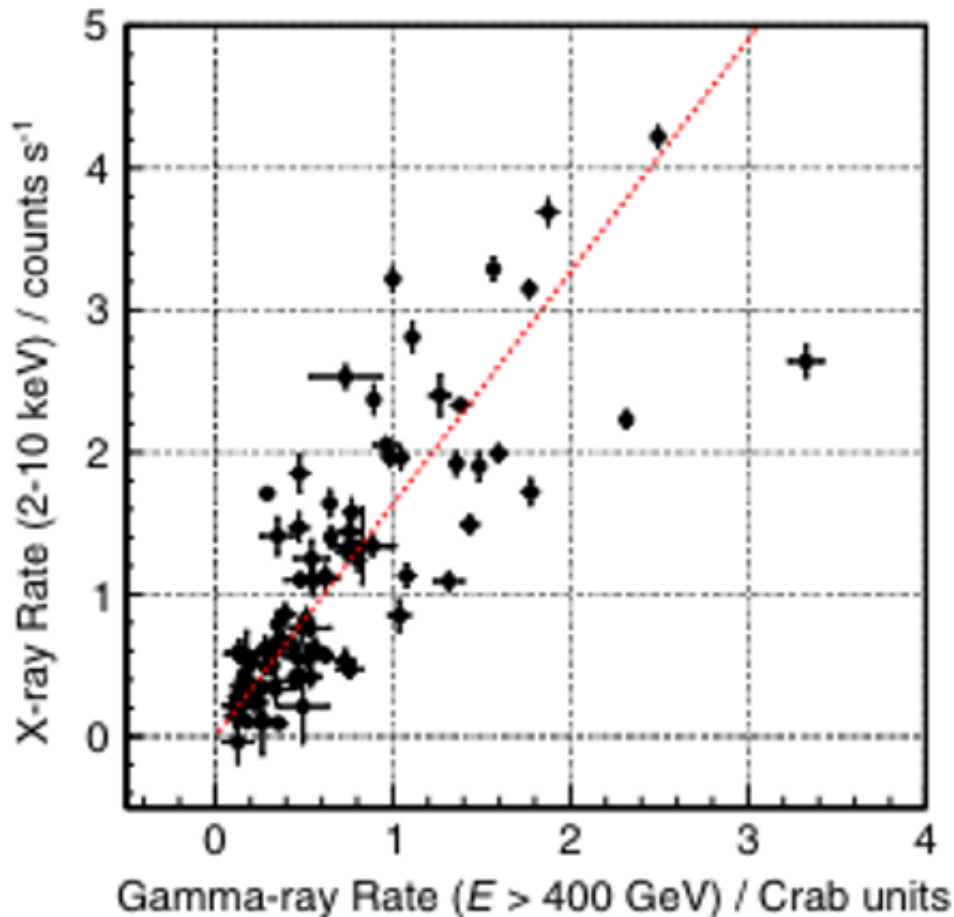


Figure 12.7: TeV and X-ray flux correlation of Markarian 421 with the 14-year dataset (Acciari et al., 2014).

The axes are opposite with this study, and VHE gamma-ray flux are the energy above 400 GeV and x ray is shown in the count rate for 2 to 10keV. The definition is slightly different but it's not crucial for the comparison with 1ES 1959+650. Another difference is light curve binning, it is monthly in Acciari et al. (2014). Considering the these difference, correlation coefficient = 0.75 imply strong correlation along the 14-years period. Similar structure as figure 11.5a also exists, but correlation coefficient of this study is 0.17.

One possibility of the difference in the correlation coefficient might be due to the bias of x-ray observation. If observations were performed unevenly in time, the calculated coefficient would be affected. Anyway, authors concluded x-ray and gamma-ray flux were linearly correlated.

For the case of Markarian 501, Arbet-Engels, Axel et al. (2021) showed the six-years correlation. Figure 12.8 shows the flux correlation in log axis. The result also linear correlation except a bright gamma-ray point. According to the multiwavelength light curves in Arbet-Engels, Axel et al. (2021), the point is the period both x-ray and gamma-ray flux increased. The correlation was calculated with 24-hour coincidence window which is common to this study. Although it was similar analysis with a longer period, no complex

correlation was reported.

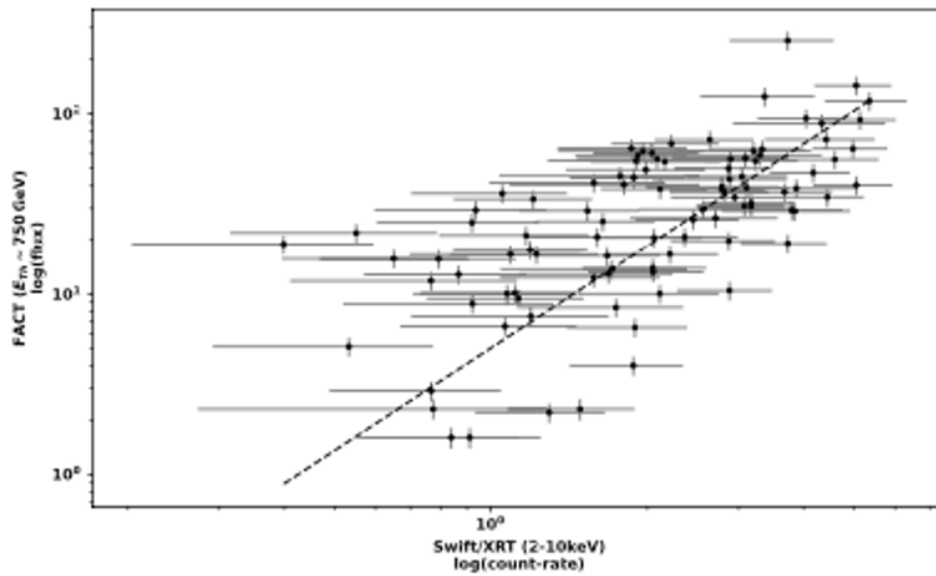


Figure 12.8: TeV and X-ray flux correlation of Markarian 501 with the six-year dataset (Arbet-Engels, Axel et al., 2021).

At last, I compared with the result of 1ES1959+650 in 2002. Krawczynski et al. (2004) was reported an orphan gamma-ray flare in the past. Figure 12.9 shows the flux correlation observed by Whipple and RXTE.



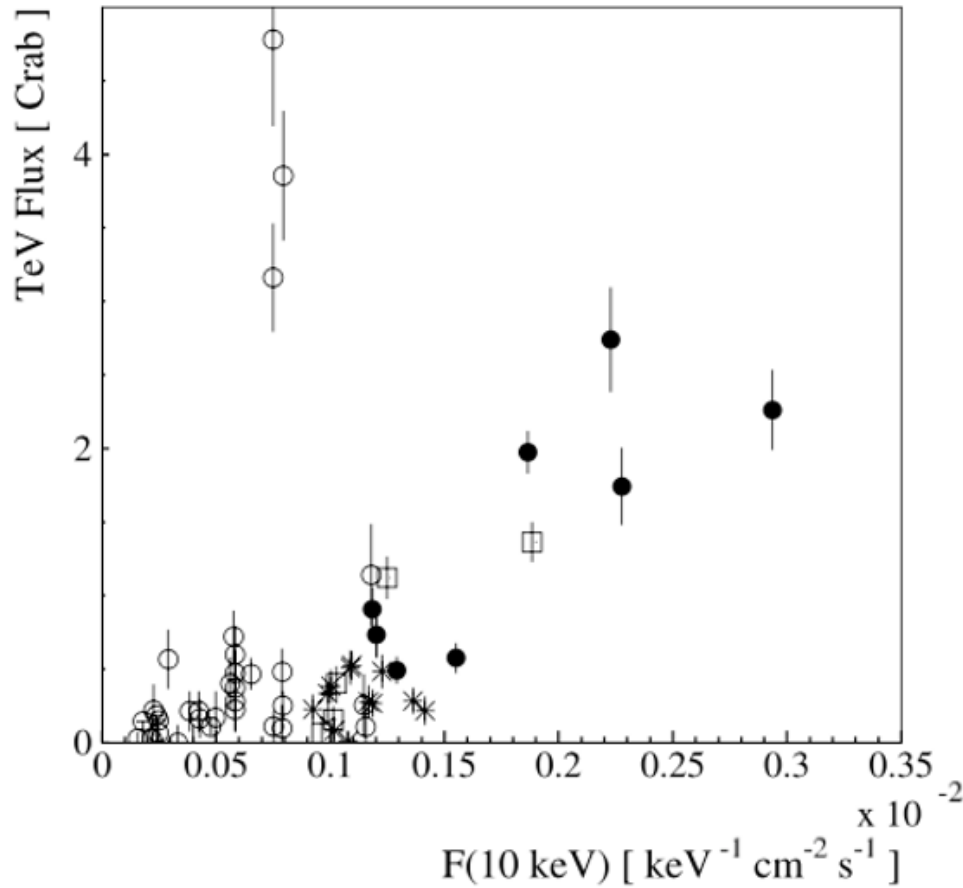


Figure 12.9: TeV and X-ray flux correlation of 1ES1959+650 in 2002 (Krawczynski et al., 2004).

In the study, gamma-ray band showed an independent flaring state without x-ray increase. The whole structure looks similar with this study, but simple conversion from differential flux to integrated flux (multiplying 10 keV) gives rough estimate as  $0.2 \text{ keV}^{-1} \text{ cm}^{-2} \text{ s}^{-1}$  equals  $2.0 \text{ erg cm}^{-2} \text{ s}^{-1}$ . Comparing this study, the 2016 branch corresponds to the four black filled markers around 2 Crab Unit. In the 2016 flare, the variability about 30-min time scale was found from VHE gamma-ray light curve, and no intra-night variability was found in 2017 flares. As mentioned in equation 12.7, faster time scale indicates smaller emission region. Combining with larger electron density suggested by the model fitting, the orphan flare was happened quite dense and small region compared with flares explored in this study.

The proposed emission model in Krawczynski et al. (2004), requires the blob radius smaller than  $10^{15} \text{ cm}$ , it agrees with the tendency of this study. As a result, as shown in fig. 11.5a, no complex flux correlation has been found in classical TeV blazars. The V-shaped flux correlation is unique, it should contain the information of the temporal change in the emission region. In this study, only SSC model was evaluated. Thus, more detailed emission model assessment is needed to understand what makes the complex shape in the flux correlation.

### 13. Conclusion and Future prospect

In this study, I studied the temporal variability of 1ES1959+650, a BLLac-type blazer, by performing multiwavelength analyses based on very high-energy gamma rays observed by the MAGIC telescopes. Many MAGIC observations have been conducted under the moonlight, thus dedicated analysis procedure was required. Using the method proposed in Ahnen et al. (2017), I succeeded to recover more than 150 hours data containing the higher moonlight noise. MAGIC light curve (Fig. 8.1) showed several flaring episode with a decaying trend through five years.

On top of that, I performed temporal analysis using MWL light curves in section 11. Among the results, the correlation between X-ray and gamma-ray fluxes showed the strong correlation varying in time. Since the time-varying correlations were also confirmed in the analysis of MAGIC and other wavelengths, I tried to determine which parameters in the emission region were responsible for this complex correlations by modeling with the synchrotron self-Compton (SSC) model. The optimized model suggested the presence of emission regions with different magnetic fields in 2016 and 2017 later and higher electron density was realized in 2016 flare. The modeling parameters are not special compared to previous studies, but the V-shape structure in the X-ray and Gamma-ray flux correlation is new comparing with other BL Lac blazars (Arbet-Engels, Axel et al., 2021; Acciari et al., 2014). Furthermore, this interpretation is based on analyzing multiwavelength light curves over five years, so the temporal analysis played a critical role.

On the other hand, the optimization of the model required many assumptions, and the chi-square values are not statistically meaningful. This point needs to be improved in the future when conducting multiwavelength analyses.

Currently, the Cherenkov Telescope Array is underway as the next generation project in the GeV-TeV region, and AMEGO and e-ASTROGAM are ongoing as the MeV-GeV gamma-ray facilities. Once those instruments start the operations, more precise studies will become possible. If precise spectra is obtained more frequently in the GeV-TeV gamma-ray band, it enable us to study spectral parameter's changes over time in gamma rays, as seen in X-ray analysis. This would allow the temporal evolution of the emission models to be more tightly constrained. Since the MeV gamma rays correspond to the switching point between the synchrotron and Compton components in BLLac type objects, it will be easier to give limits on the maximum energy of the electrons, etc.

Radio and optical light curve showed strong correlations in flux, suggesting that a common origin contributes to them. If we consider this additional component, the expected peak of SSC at about MeV could explain the flat spectrum in *Fermi*-LAT catalogue. On the other hand, adding such a component is equivalent to adding degree of freedom to the model and requires further validation.

The application of the temporal evolution of the spectrum energy distribution is still the state-of-art. I hope future development of the multiwavelength instruments and analysis method allow us to reveal out the concrete picture of the relativistic jet and the environment around the supermassive black holes.

# Appendix

## A. Spectral function

In order to characterize the observed spectral shape, I used several functions usually used in the research field. See appendix ?? for detail explanations about the flux.

### A.1. Power law

It is expected that accelerated charged particles follow a power-law function.

$$\phi_E(E) \propto E^{-p}$$

In parameter estimation, a more concrete function shape is used.

$$\phi_E(E) = \phi_0 \left( \frac{E}{E_0} \right)^{-p} \quad (\text{A.1})$$

Where  $\phi_0$  is a normalization constant and  $E_0$  is normalization energy, and  $p$  is an index. Thanks to the normalization energy,  $\phi_0$  always has the same unit as  $\phi_E$ . As discussed in appendix ??, when a differential photon flux follows a power-law function, SED naturally follows too. Thus, we distinguish the indices depending on the quantify, e.g., a photon index for a differential photon flux and a spectral index for a differential energy flux.

### A.2. Log Parabola

Log-parabola function was introduced in a blazar study by ((Massaro, E. et al., 2004, see section 3 and 6)). The advantage of the function is expressing the curved shape only with one additional parameter from the power-law function.

$$\phi_E(E) = \phi_0 \left( \frac{E}{E_0} \right)^{-\alpha - \beta \log_{10} \left( \frac{E}{E_0} \right)} \quad (\text{A.2})$$

The log-parabola function can be derived when allowing the energy-dependent escape through the particle acceleration. The function is suitable to test whether the observed spectra have a curvature because the log-parabola includes the power-law function. By taking a log-derivative, one can calculate a peak energy of SED  $\nu F_\nu$  as  $E_{\text{peak}} = E_0 \times 10^{(2-\alpha)/(2\beta)}$ . Then one can rewrite a function as

$$\nu F_\nu(E) = \phi_0 \times 10^{-\beta \left[ \log_{10} \left( \frac{E}{E_{\text{peak}}} \right) \right]^2} \times 10^{\frac{(2-\alpha)^2}{4\beta}} \quad (\text{A.3})$$

Equation A.3 clearly represents a quadratic function in a log-energy axis.

### A.3. Power-law with exponential cutoff

As already discussed in section ref, to be filled, a differential photon flux of synchrotron emission originating from mono-energetic particles is proportional to  $\nu^{1/2} \exp(-\nu/\nu_c)$  at

the high-frequency limit. Thus, the power-law function with exponential cut-off is naturally introduced. The concrete function is

$$\phi_E(E) = \phi_0 \left( \frac{E}{E_0} \right)^{-p} \exp \left\{ \left( -\frac{E}{E_{\text{cutoff}}} \right) \right\}. \quad (\text{A.4})$$

However, this function is

## B. Discrete Correlation Functions

This section provides results of DCF analysis. Figures B.1 to B.20 are all the results calculated in this study. X-axis is the time difference defined as:

$$\Delta t = T_{\text{lowene}} - T_{\text{highene}}. \quad (\text{B.1})$$

Thus if  $\Delta t$  has a peak at positive delay, it means lower-energy light curve has delayed temporal variability and the variability is similar in the compared bands. To discuss the significance of the correlation, further statistical evaluations using monte-carlo simulation are needed.

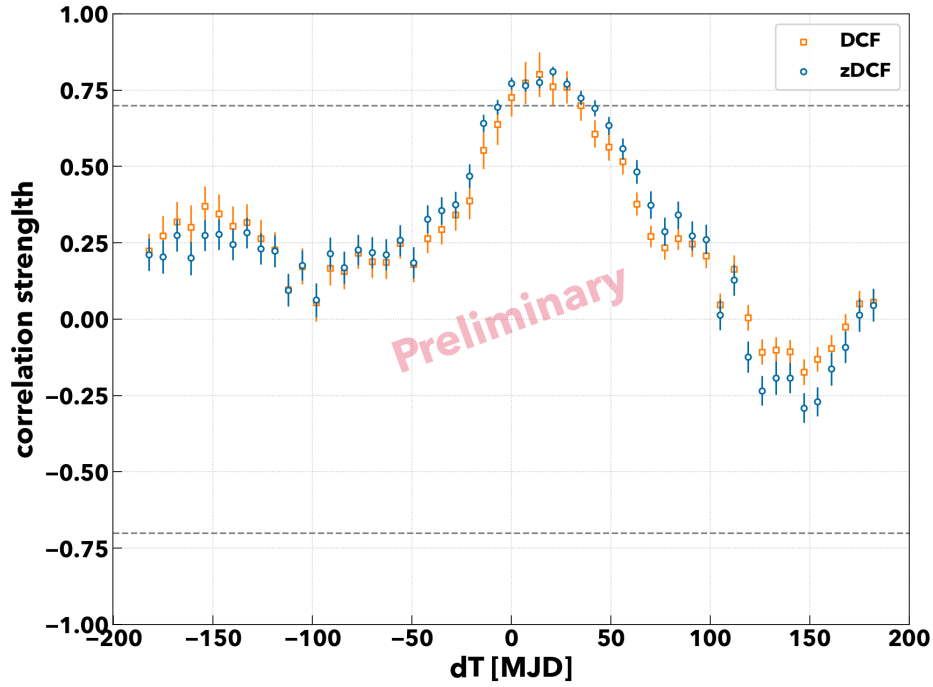


Figure B.1: discrete correlation OVRO-Tuorla. Orange shows original DCF method and blue represents modified DCF (zeta DCF) method.

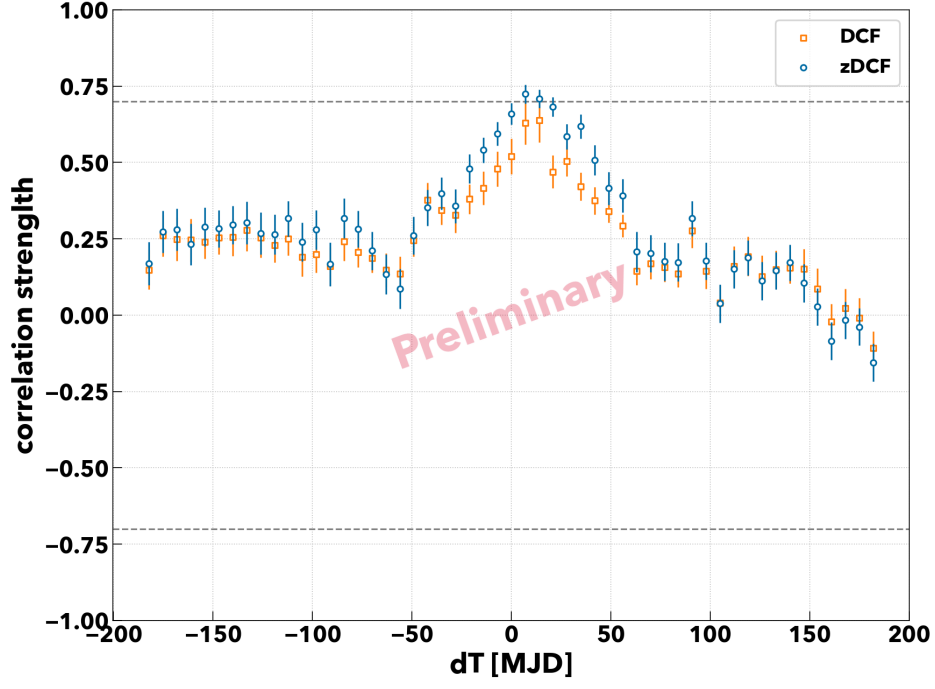


Figure B.2: Discrete correlation function: OVRO - UVOT B band. See figure B.1 details.

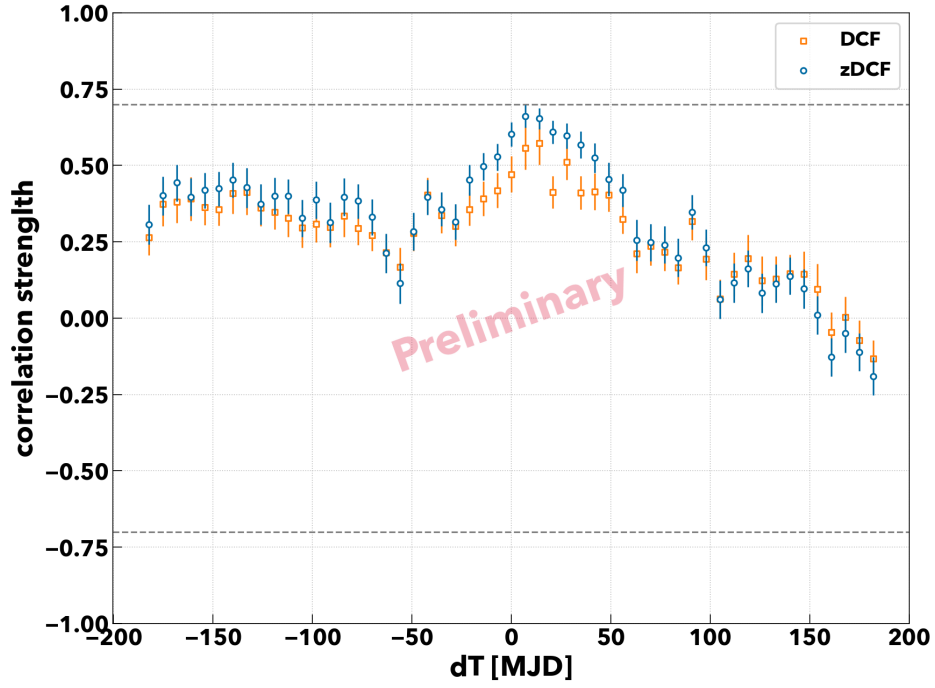


Figure B.3: Discrete correlation function: OVRO - UVOT UV M2 band. See figure B.1 details.

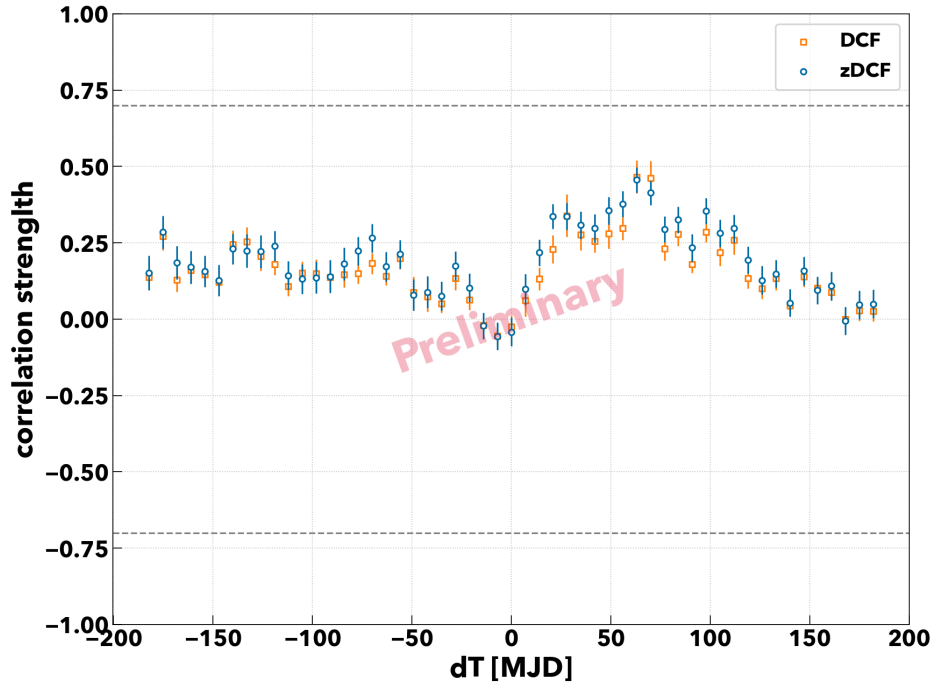


Figure B.4: Discrete correlation function: OVRO - XRT. See figure B.1 details.

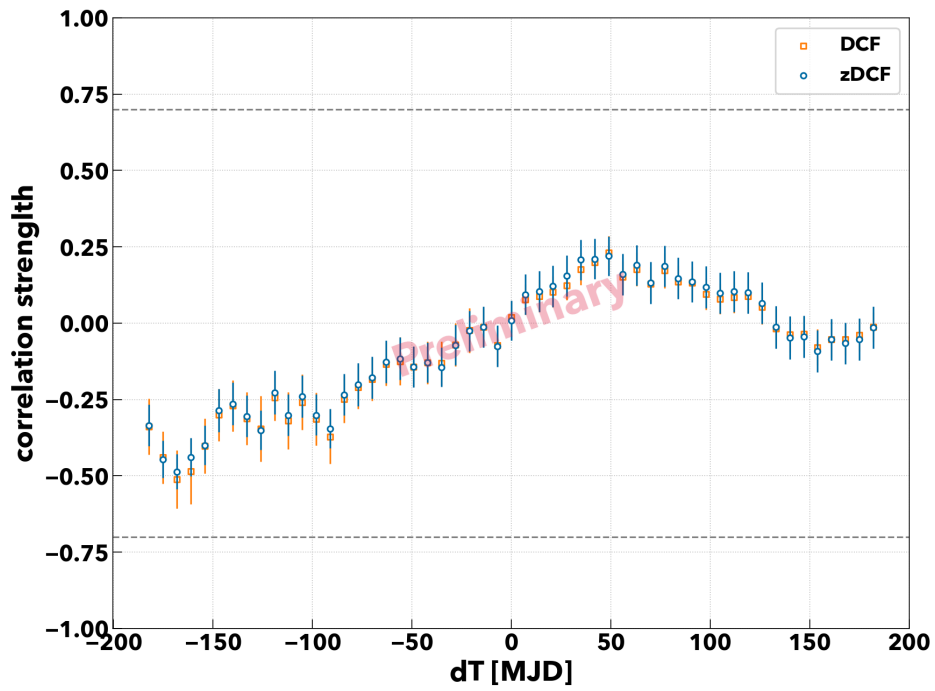


Figure B.5: Discrete correlation function: OVRO - LAT. See figure B.1 details.



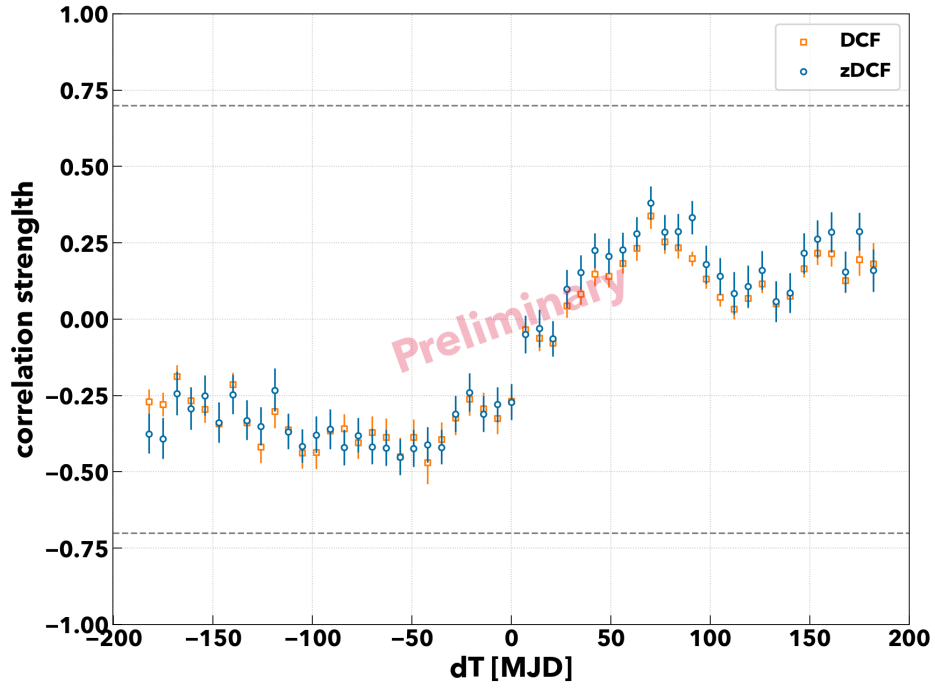


Figure B.6: Discrete correlation function: OVRO - MAGIC. See figure B.1 details.

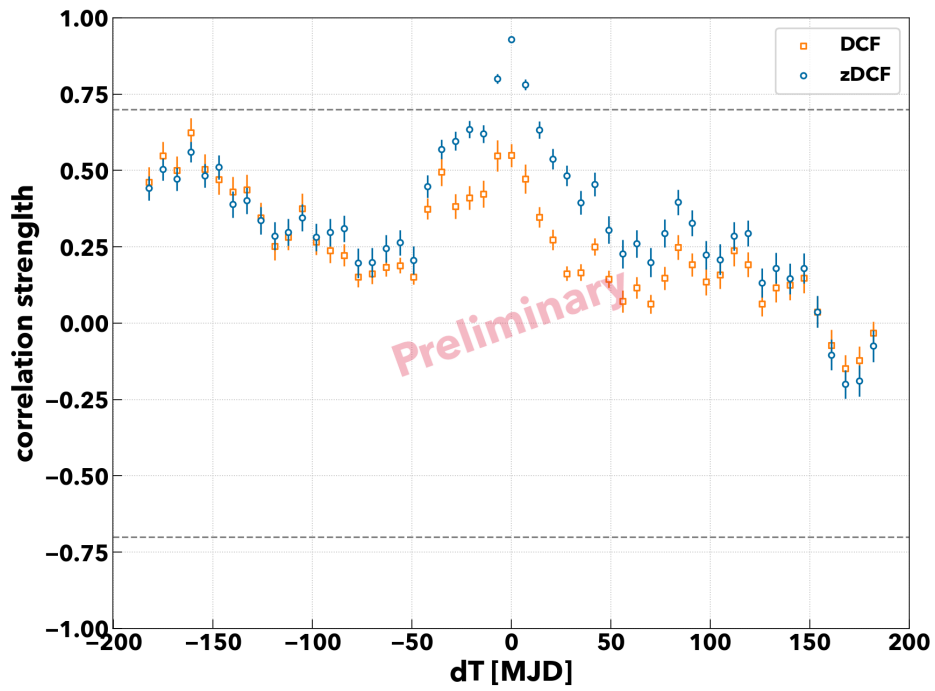


Figure B.7: Discrete correlation function: Tuorla - UVOT B band. See figure B.1 details.

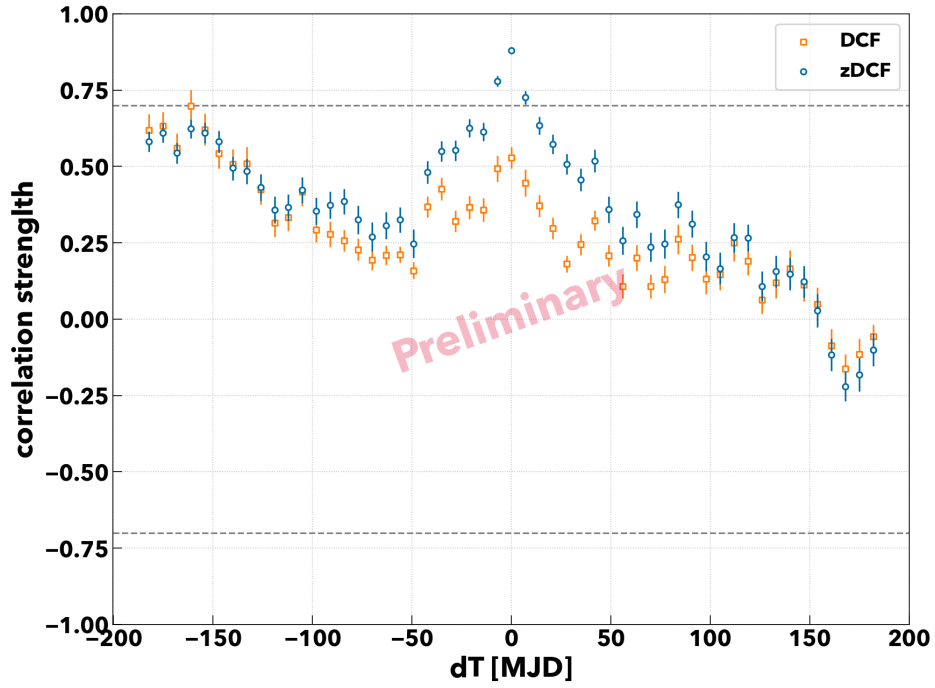


Figure B.8: Discrete correlation function: Tuorla - UVOT UV M2 band. See figure B.1 details.

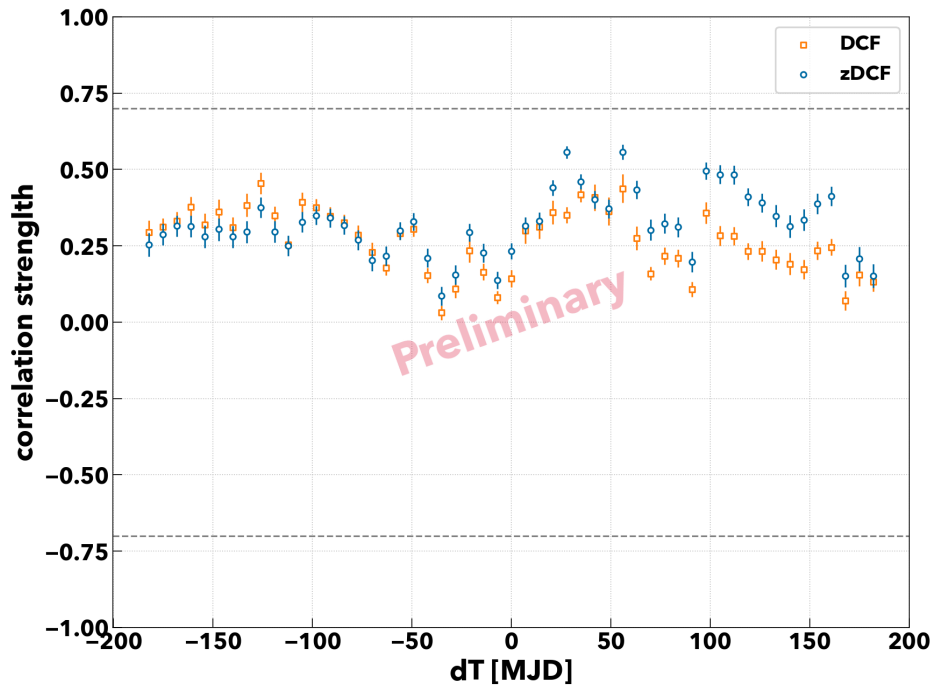


Figure B.9: Discrete correlation function: Tuorla - XRT. See figure B.1 details.

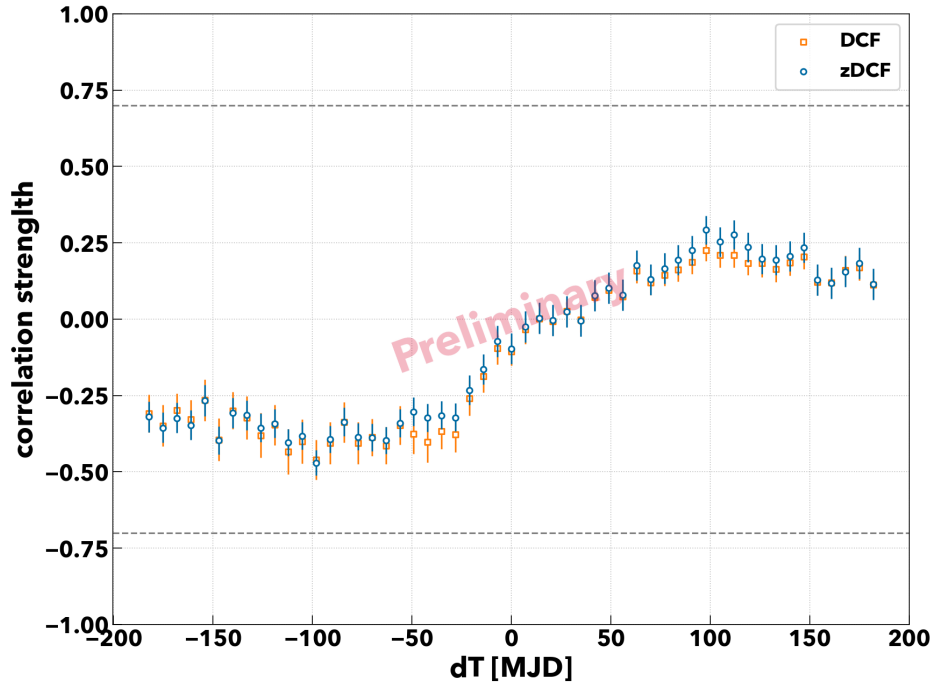


Figure B.10: Discrete correlation function: Tuorla - LAT. See figure B.1 details.

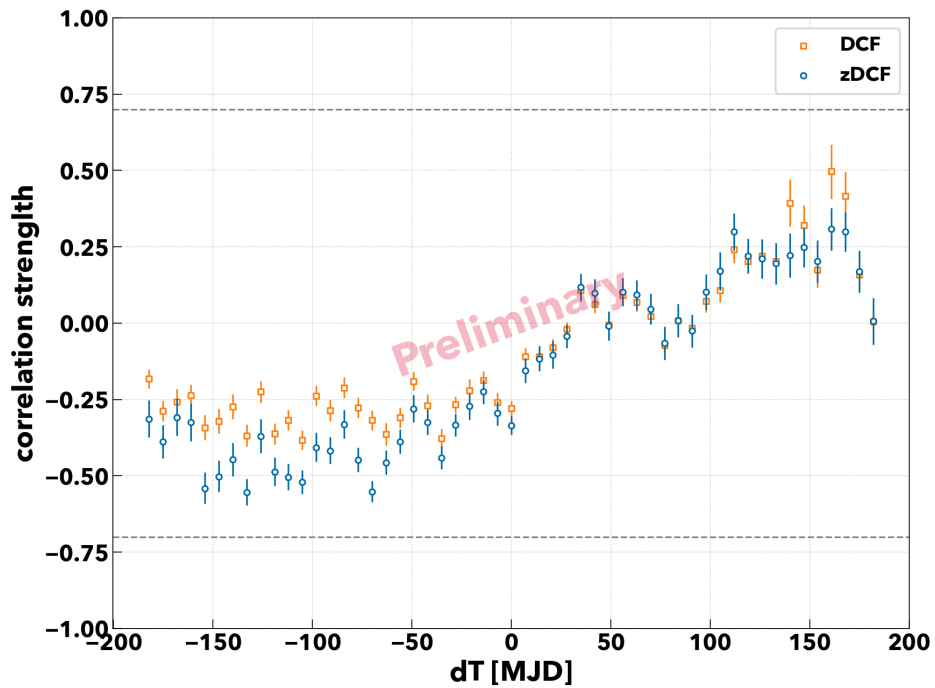


Figure B.11: Discrete correlation function: Tuorla - MAGIC. See figure B.1 details.

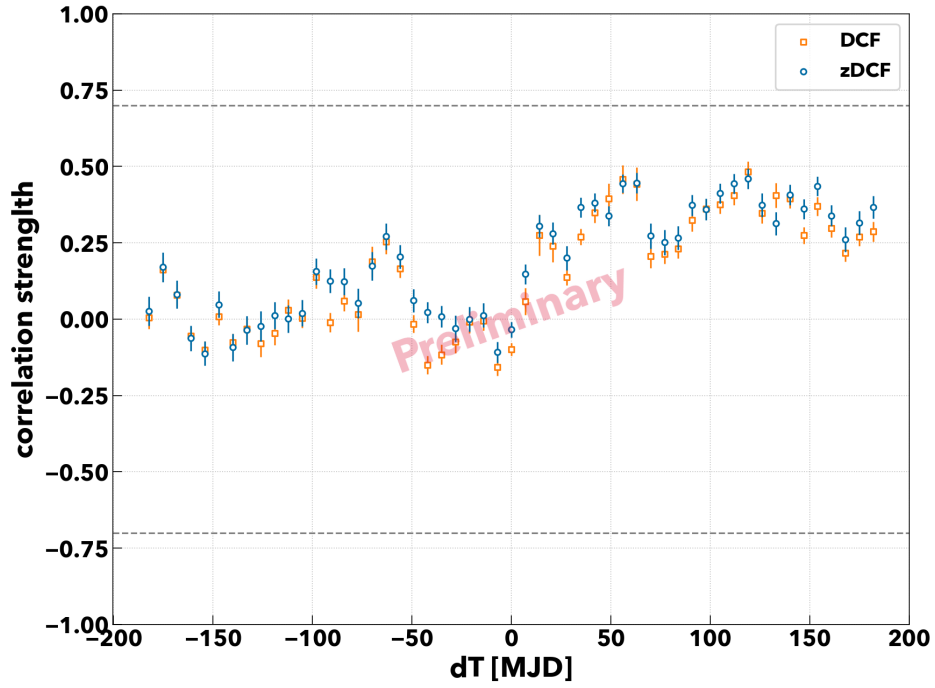


Figure B.12: Discrete correlation function: UVOT B band - XRT. See figure B.1 details.

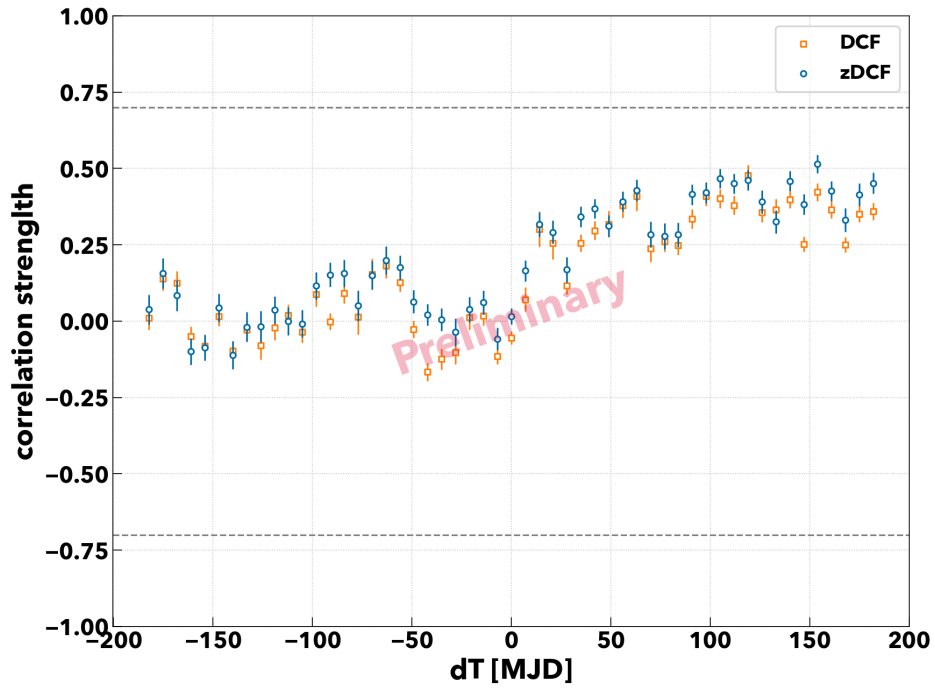


Figure B.13: Discrete correlation function: UVOT UV M2 band - XRT. See figure B.1 details.

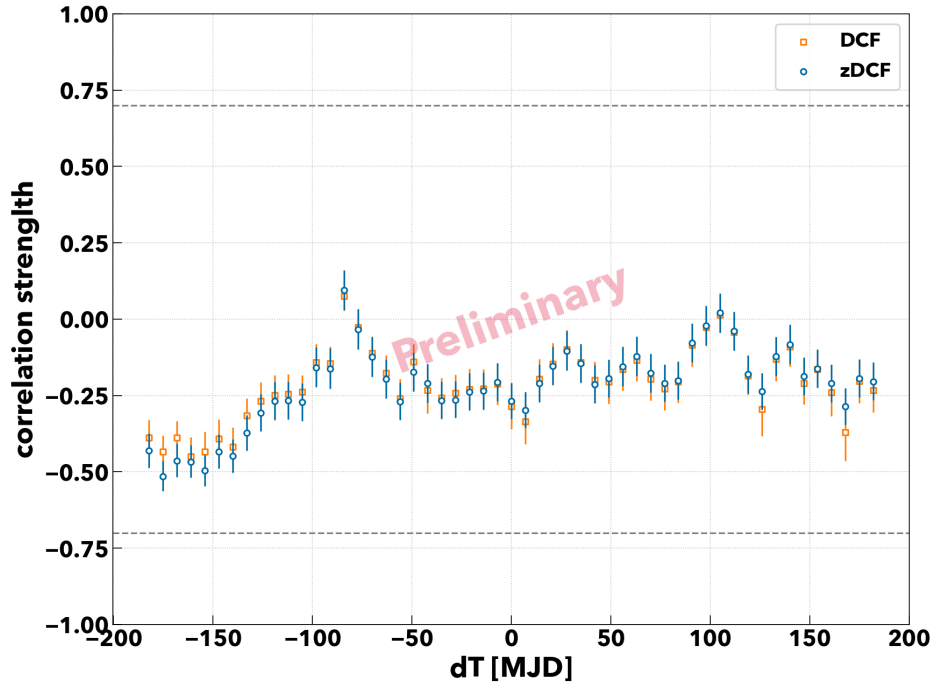


Figure B.14: Discrete correlation function: UVOT B band - LAT. See figure B.1 details.

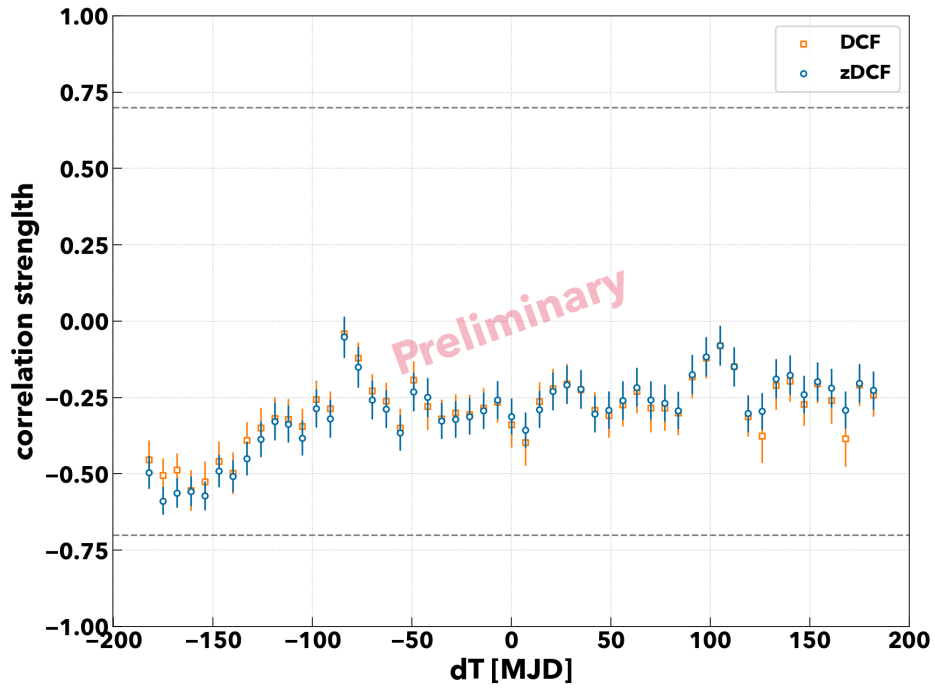


Figure B.15: Discrete correlation function: UVOT UV M2 band - LAT. See figure B.1 details.

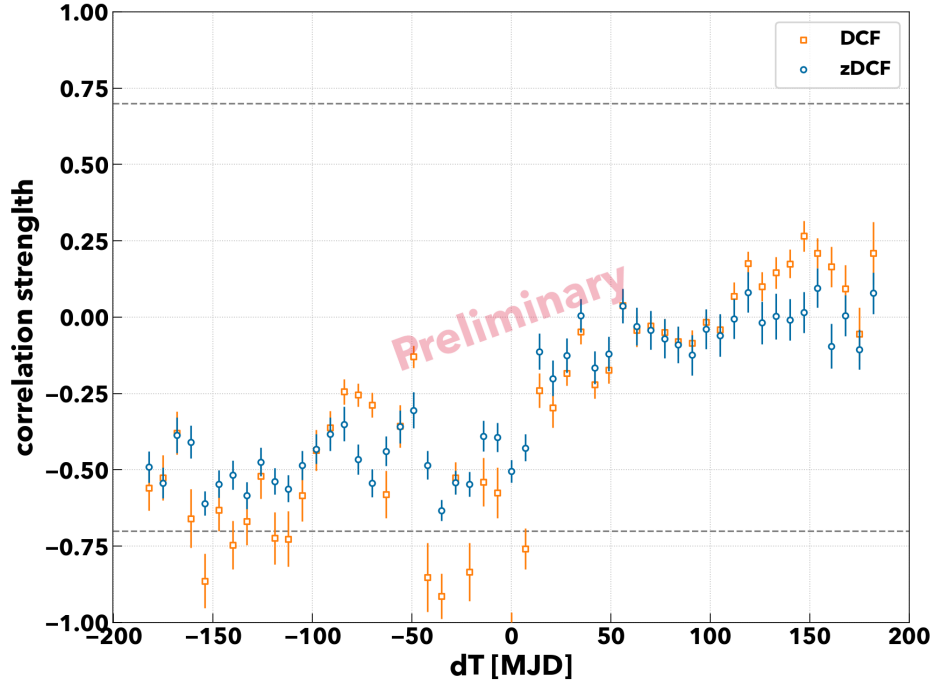


Figure B.16: Discrete correlation function: UVOT B band - MAGIC. See figure B.1 details.

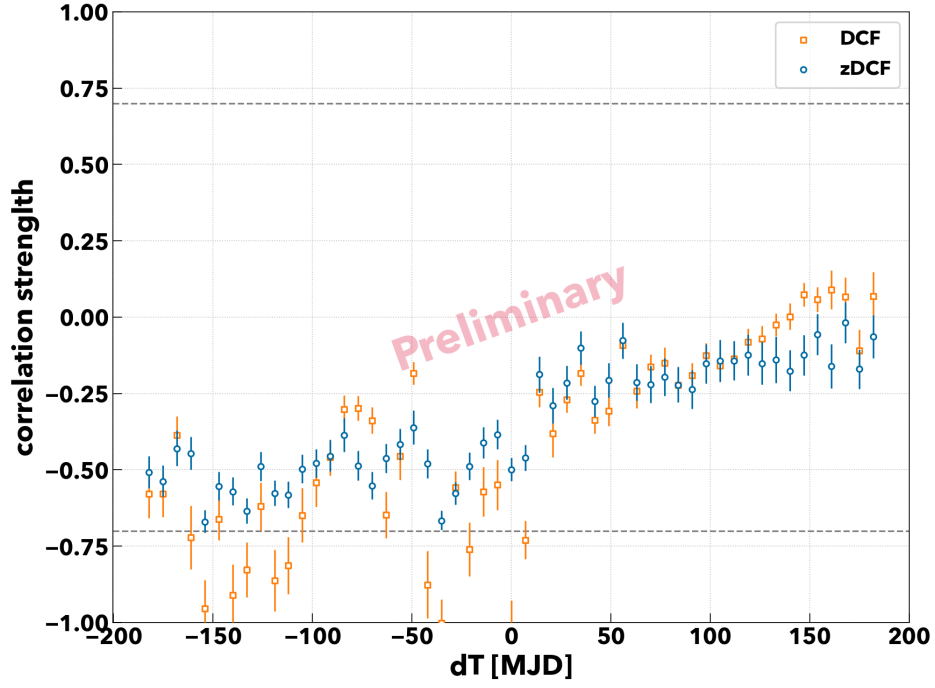


Figure B.17: Discrete correlation function: UVOT UV M2 band - MAGIC. See figure B.1 details.

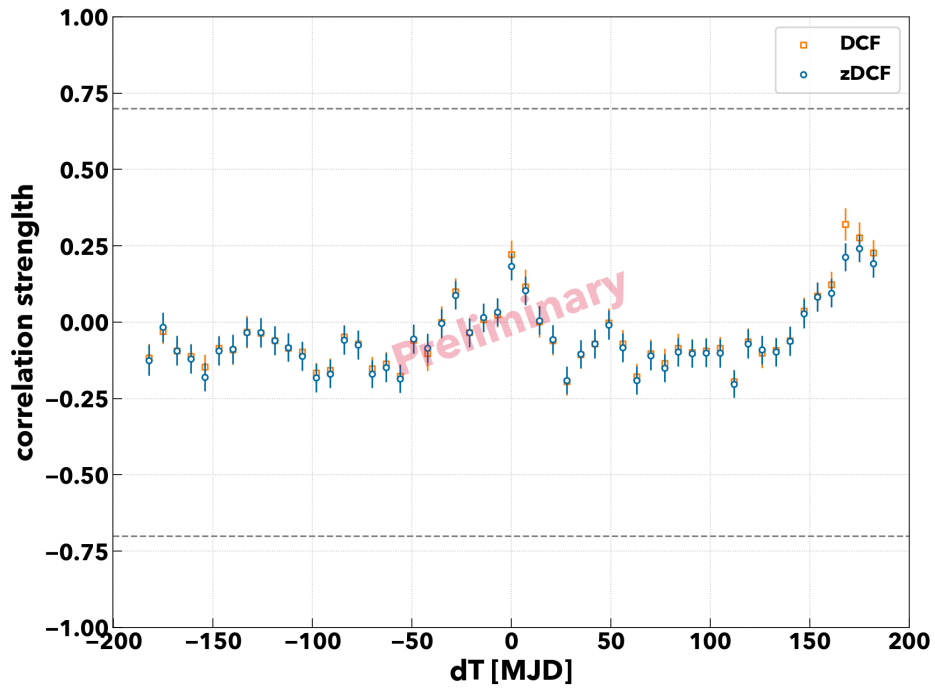


Figure B.18: Discrete correlation function: XRT - LAT. See figure B.1 details.

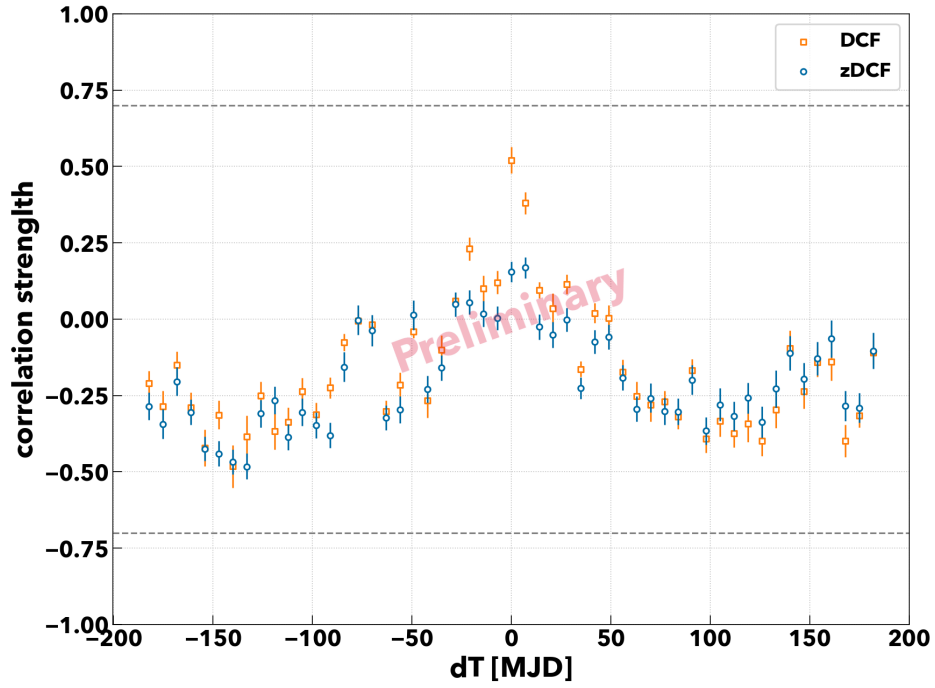


Figure B.19: Discrete correlation function: XRT - MAGIC. See figure B.1 details.

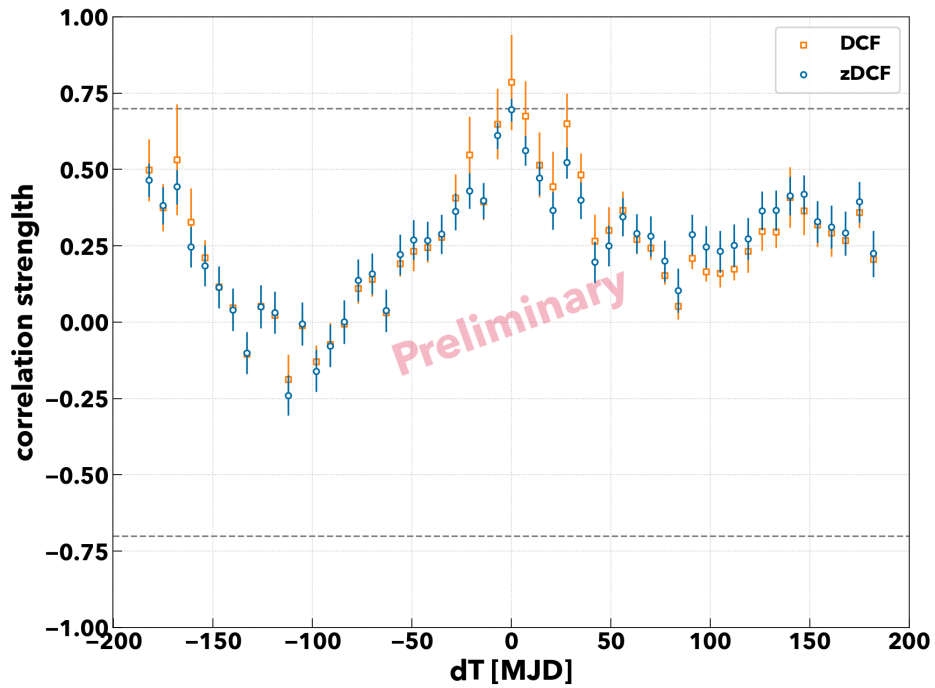


Figure B.20: Discrete correlation function: LAT - MAGIC. See figure B.1 details.



## C. Systematic effect of coincidence windows in the flux correlation

In this section, I report results of systematic check using various coincidence windows in the flux correlation. Figures C.1 and C.2 show the flux correlation of VHE gamma-ray and X-ray flux. To check the robustness of the structure of the flux correlation, I tested the coincidence window from six hours to 48 hours. As figures shown, the correlation structure does not depend on the width of the window. Thus the observed structure between VHE gamma ray and X ray seems to be robust.

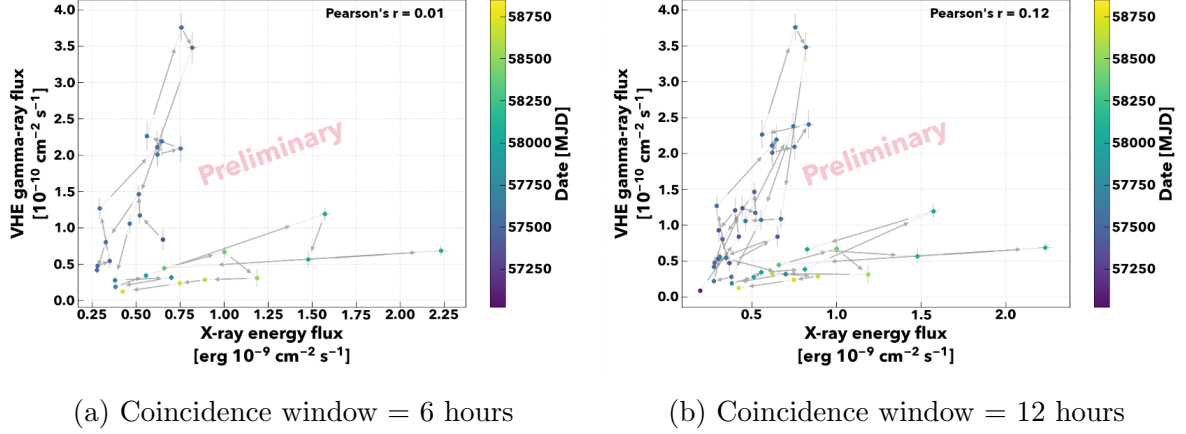


Figure C.1: Flux correlation between VHE gamma ray and X ray with various coincidence windows (1)

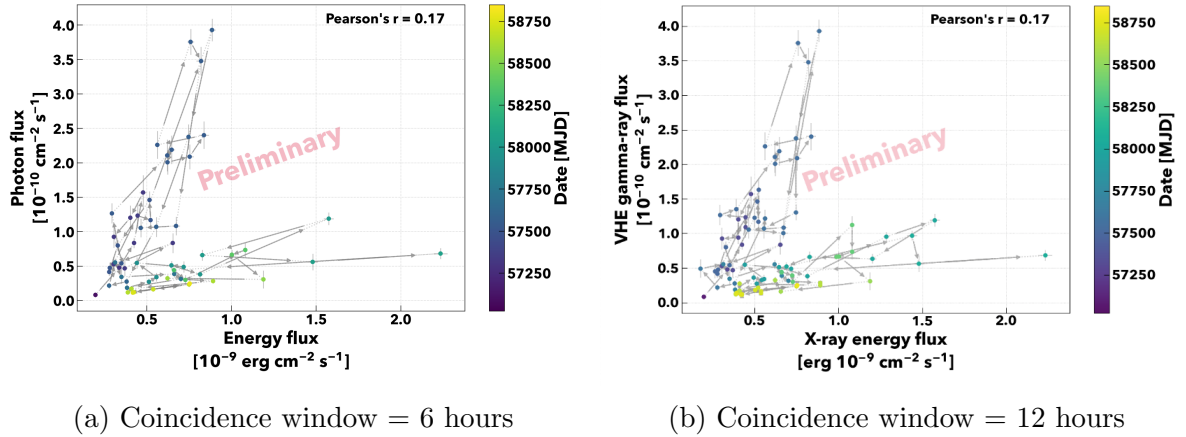


Figure C.2: Flux correlation between VHE gamma ray and X ray with various coincidence windows (2)

## D. Flux correlations

This section provides all the calculated flux correlations. See captions and section 11.2.1 for the details.

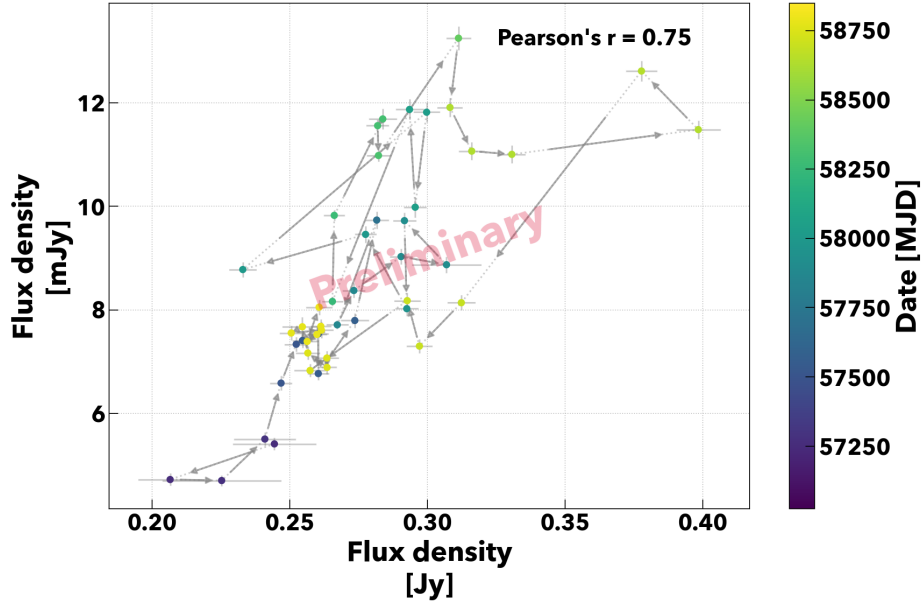


Figure D.1: Flux correlation with Tuorla and OVRO light curves. X-axis shows the lower energy band, here it is OVRO and Y-axis represents Tuorla flux. Y-X notation gives you Y-axis instrument and X-axis instrument in the following figures. The coincidence window is 24 hours.

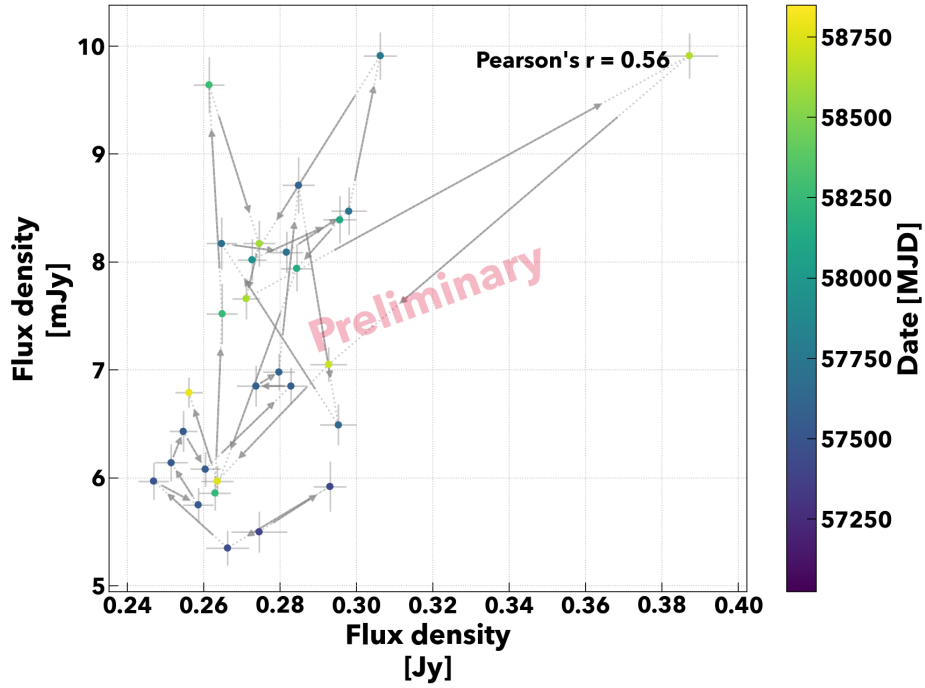


Figure D.2: Flux correlation with UVOT B band and OVRO. See figure D.1 details.

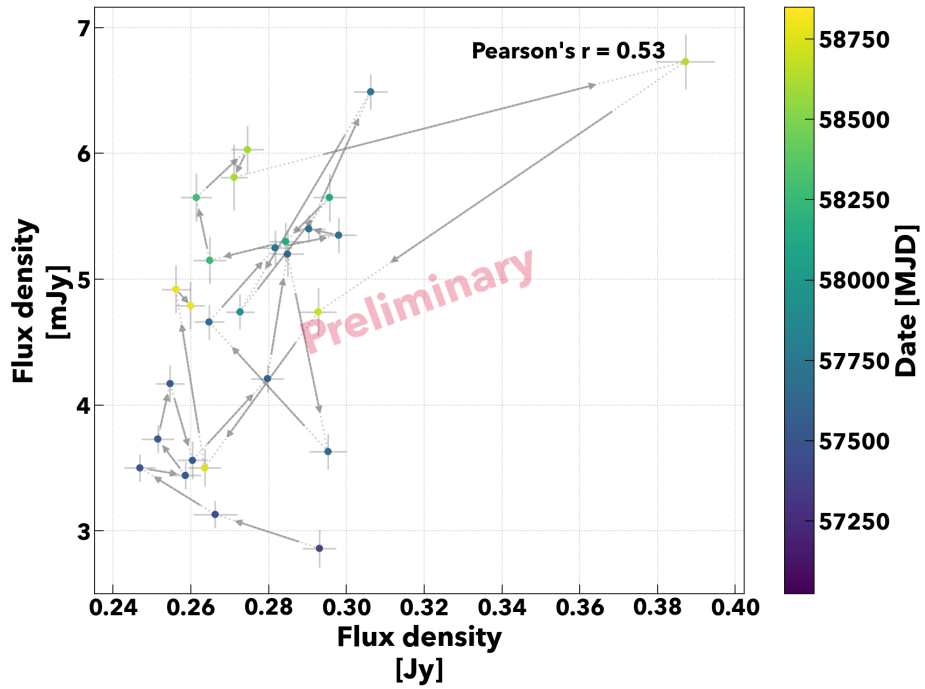


Figure D.3: Flux correlation with UVOT UV M2 band and OVRO. See figure D.1 details.

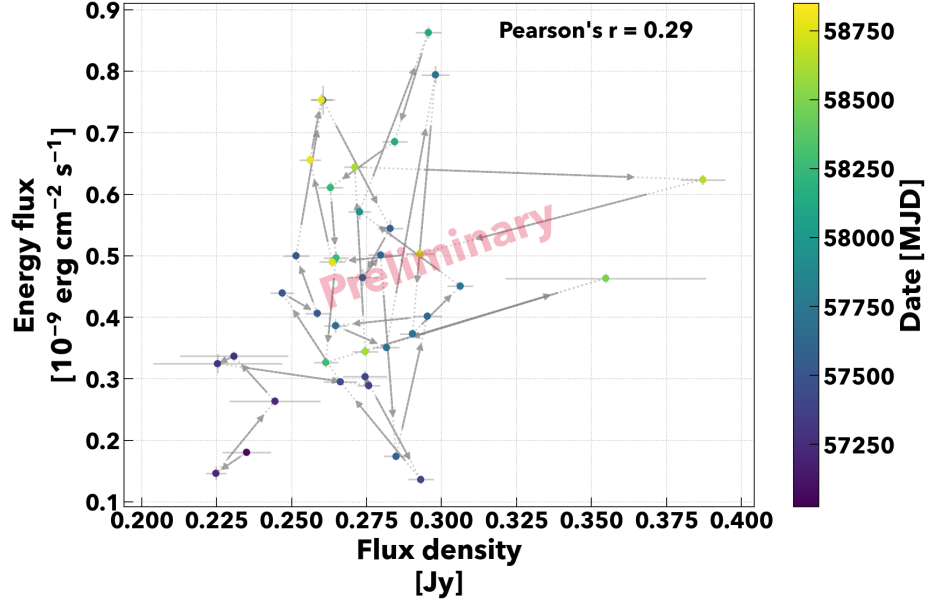


Figure D.4: Flux correlation with XRT and OVRO. See figure D.1 details.

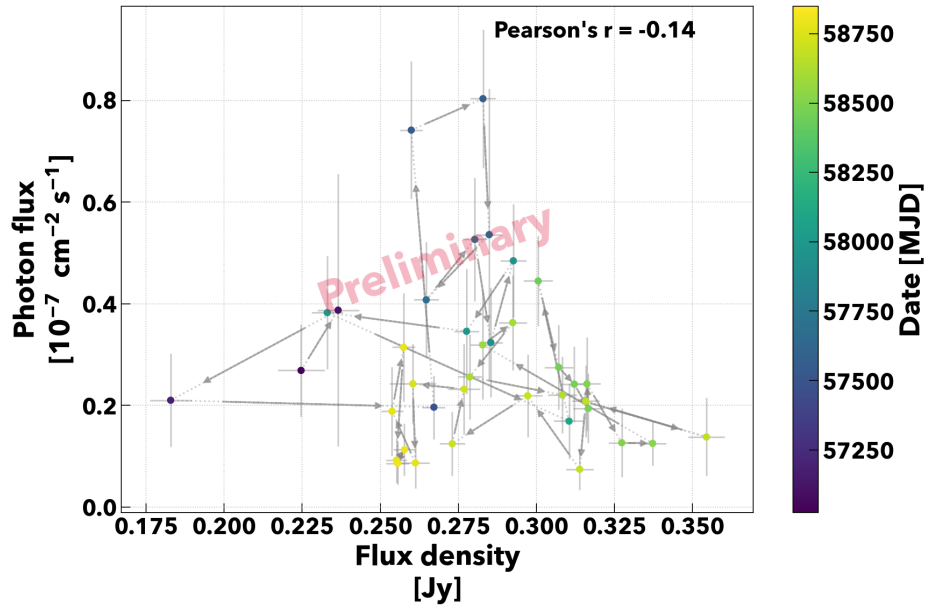


Figure D.5: Flux correlation with LAT and OVRO. See figure D.1 details.

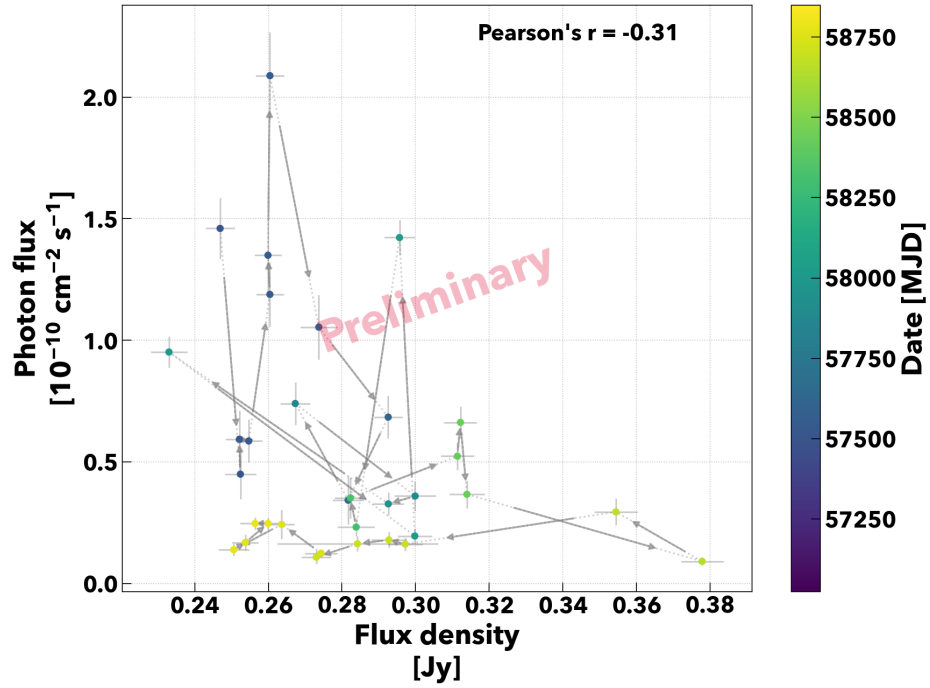


Figure D.6: Flux correlation with MAGIC and OVRO. See figure D.1 details.

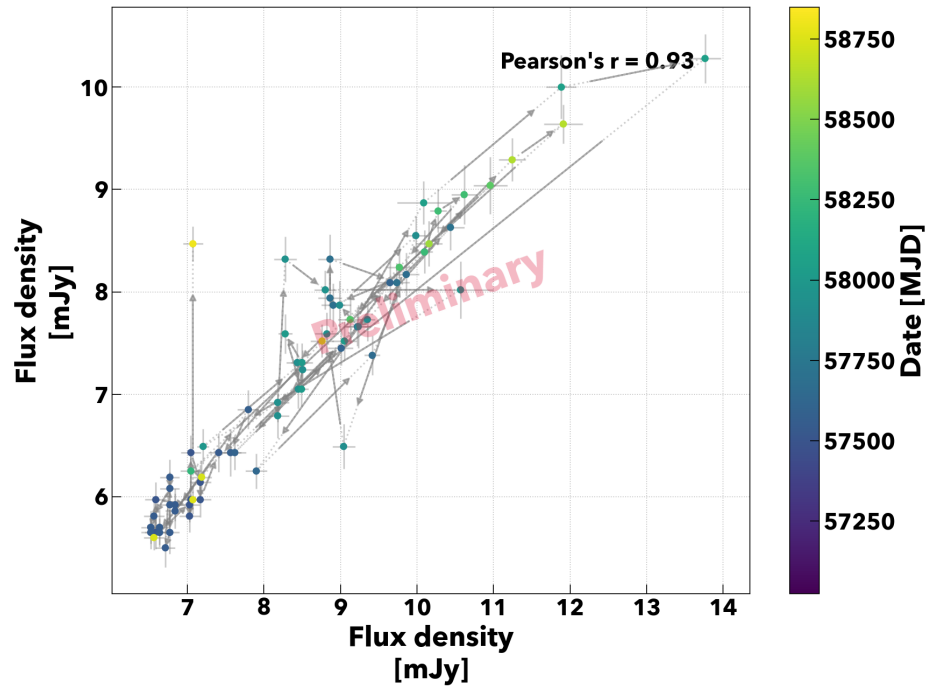


Figure D.7: Flux correlation with UVOT B band and Tuorla. See figure D.1 details.

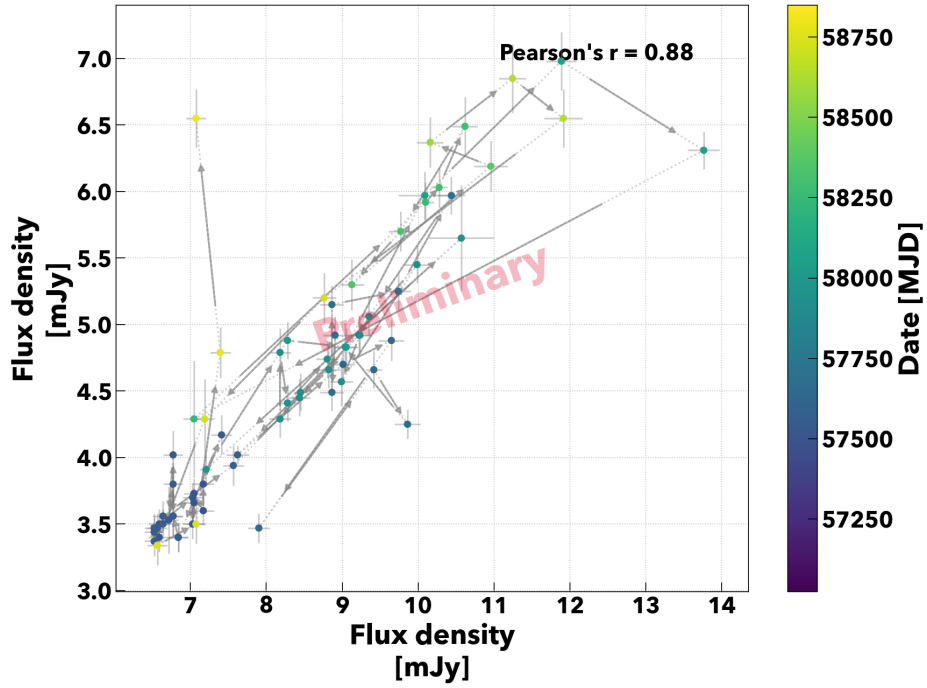


Figure D.8: Flux correlation with UVOT UV M2 band and Tuorla. See figure D.1 details.

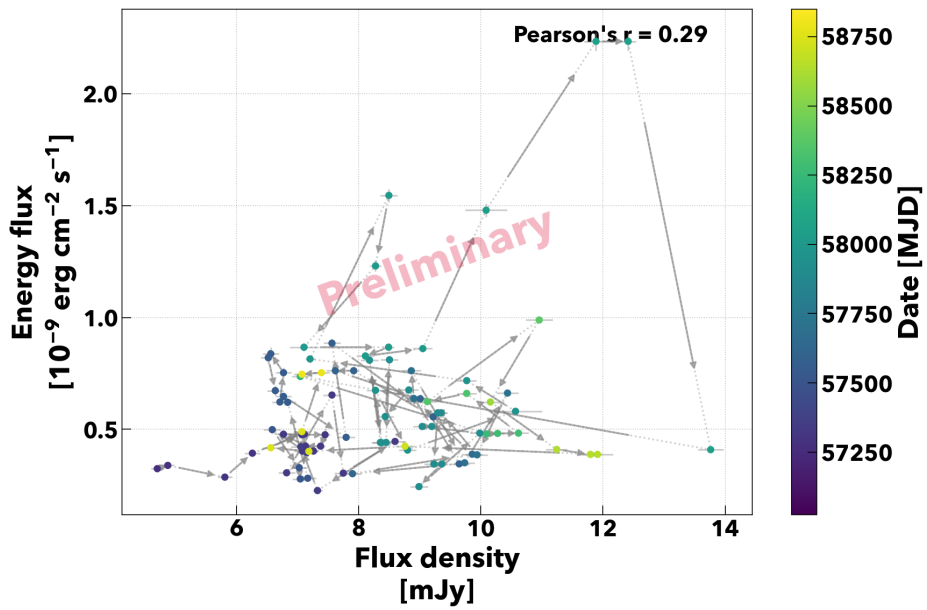


Figure D.9: Flux correlation with XRT and Tuorla. See figure D.1 details.

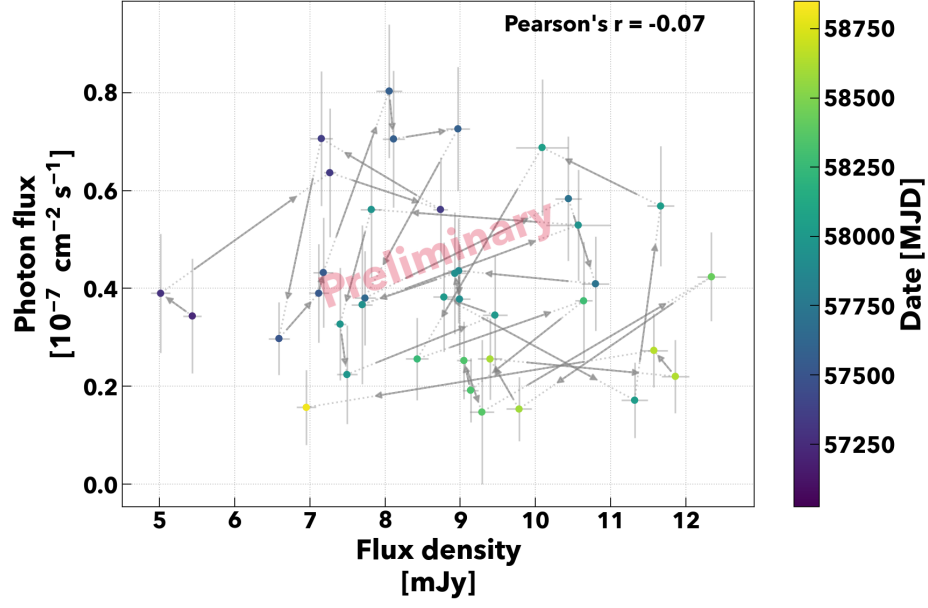


Figure D.10: Flux correlation with LAT and Tuorla. See figure D.1 details.

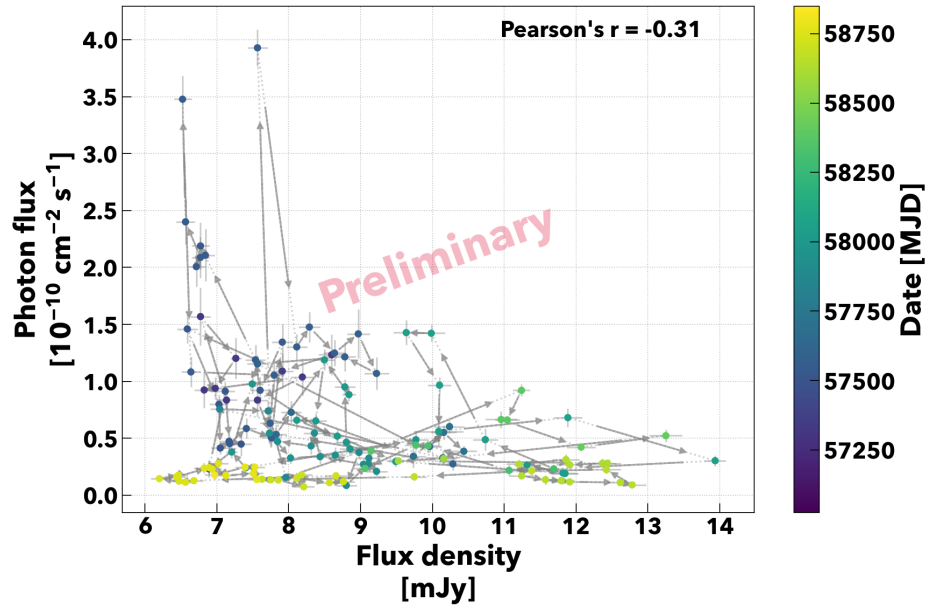


Figure D.11: Flux correlation with MAGIC and Tuorla. See figure D.1 details.

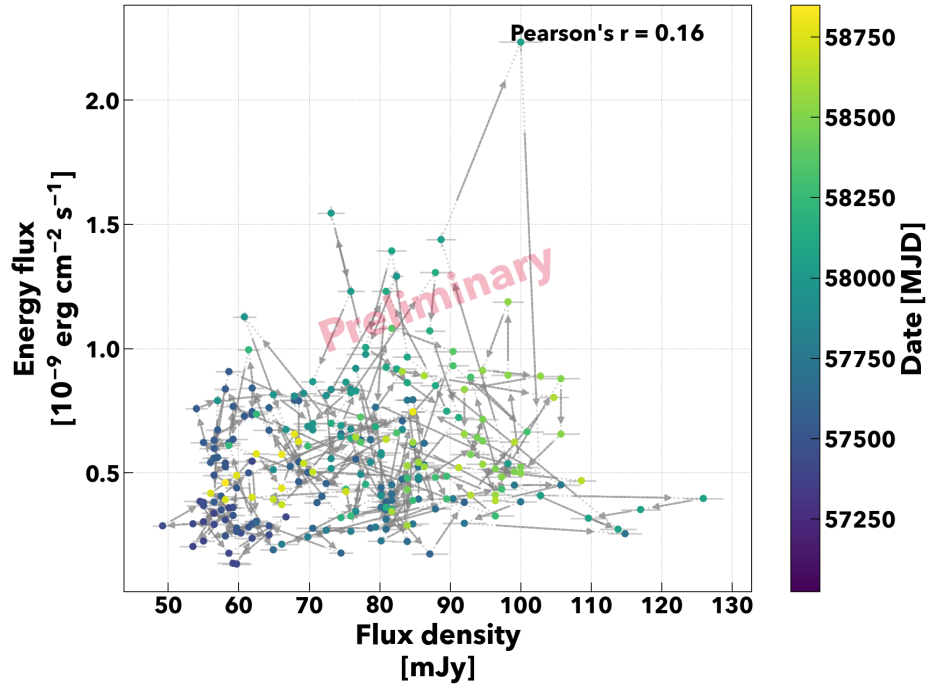


Figure D.12: Flux correlation with XRT and UVOT B band. See figure D.1 details.

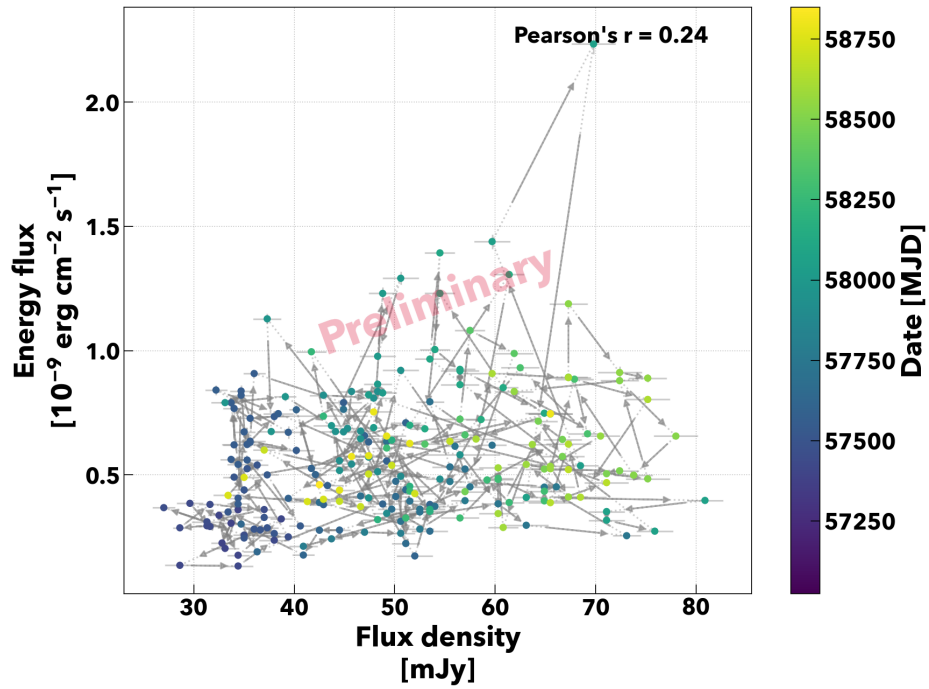


Figure D.13: Flux correlation with XRT and UVOT UV M2 band. See figure D.1 details.



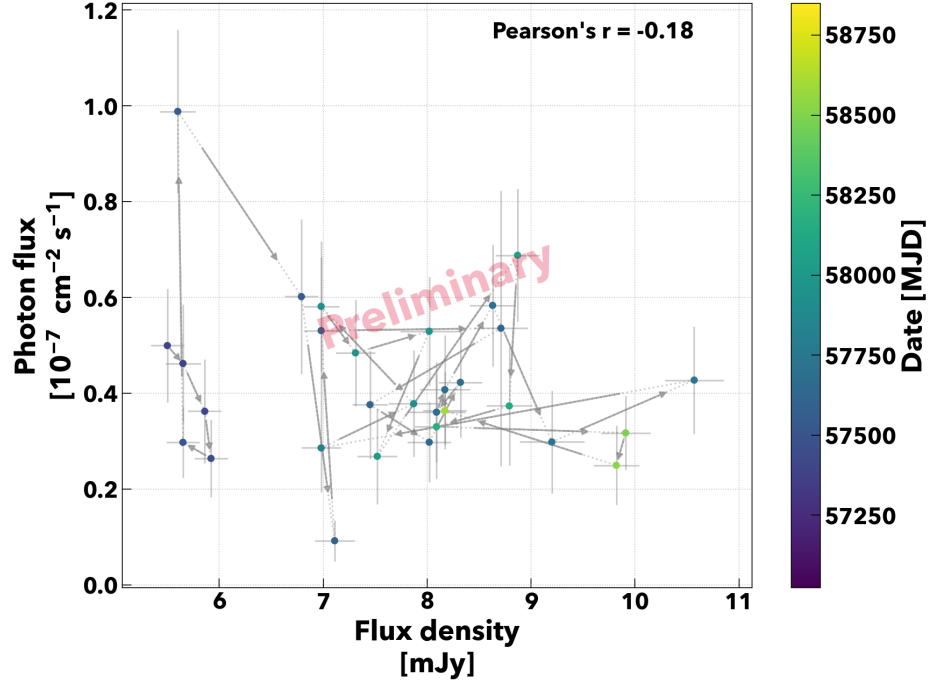


Figure D.14: Flux correlation with LAT and UVOT B band. See figure D.1 details.

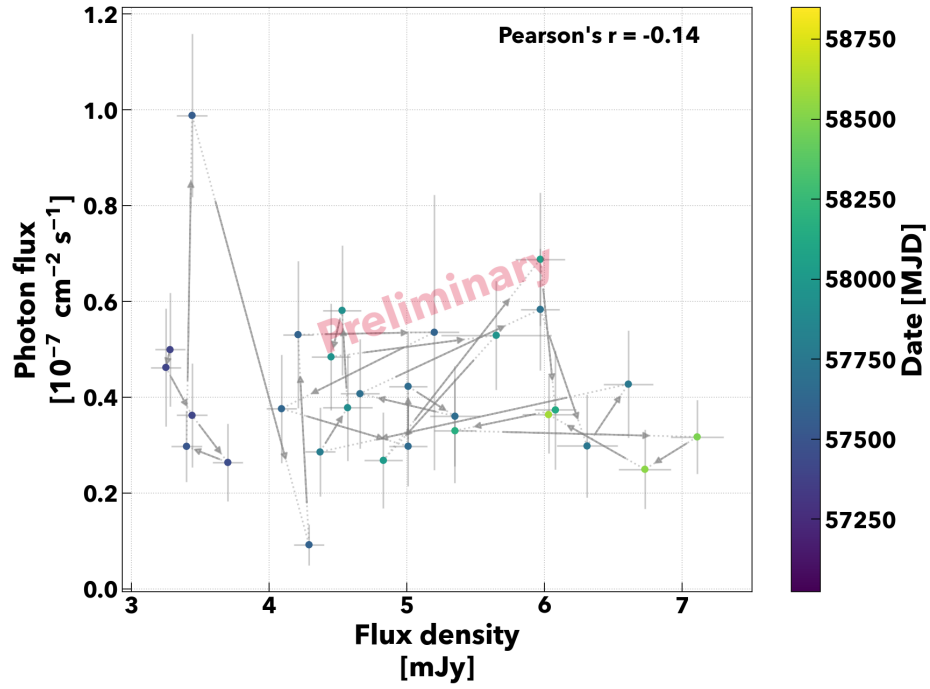


Figure D.15: Flux correlation with LAT and UVOT UV M2 band. See figure D.1 details.

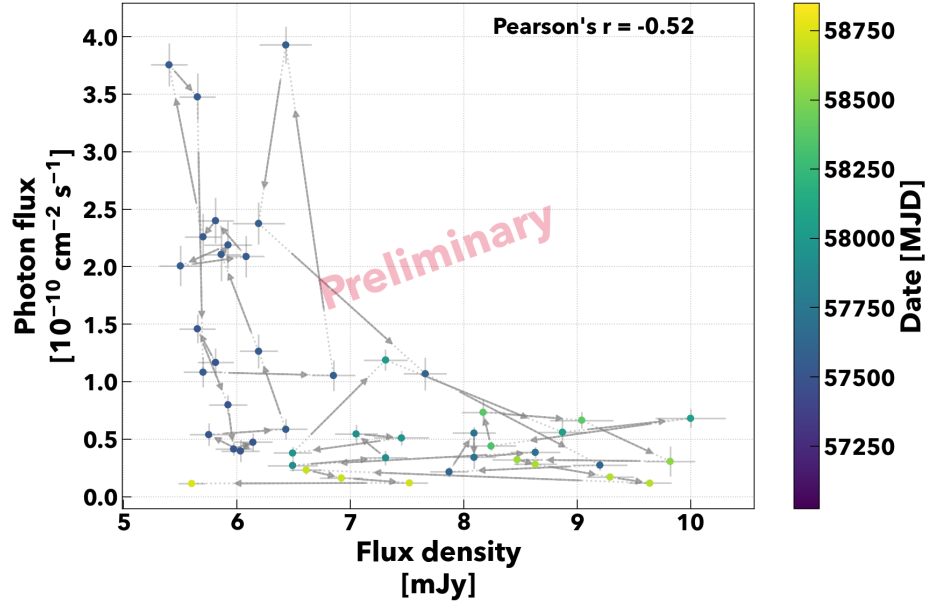


Figure D.16: Flux correlation with MAGIC and UVOT B band. See figure D.1 details.

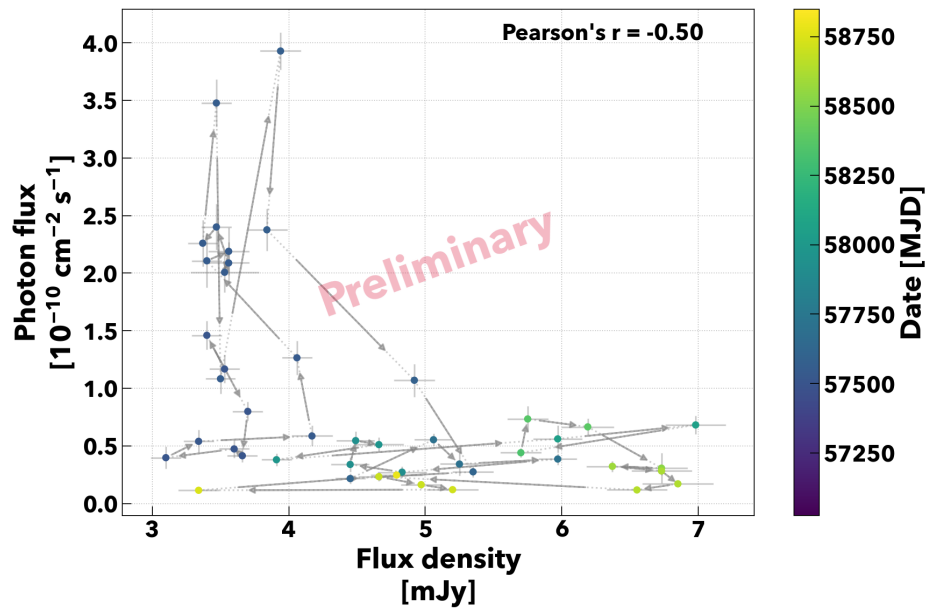


Figure D.17: Flux correlation with MAGIC and UVOT UV M2 band. See figure D.1 details.

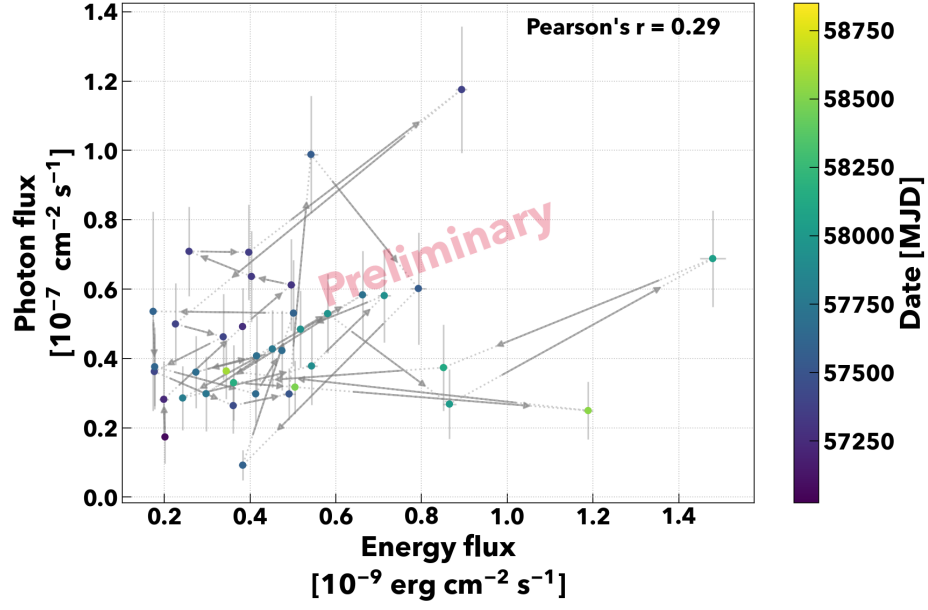


Figure D.18: Flux correlation with LAT and XRT. See figure D.1 details.

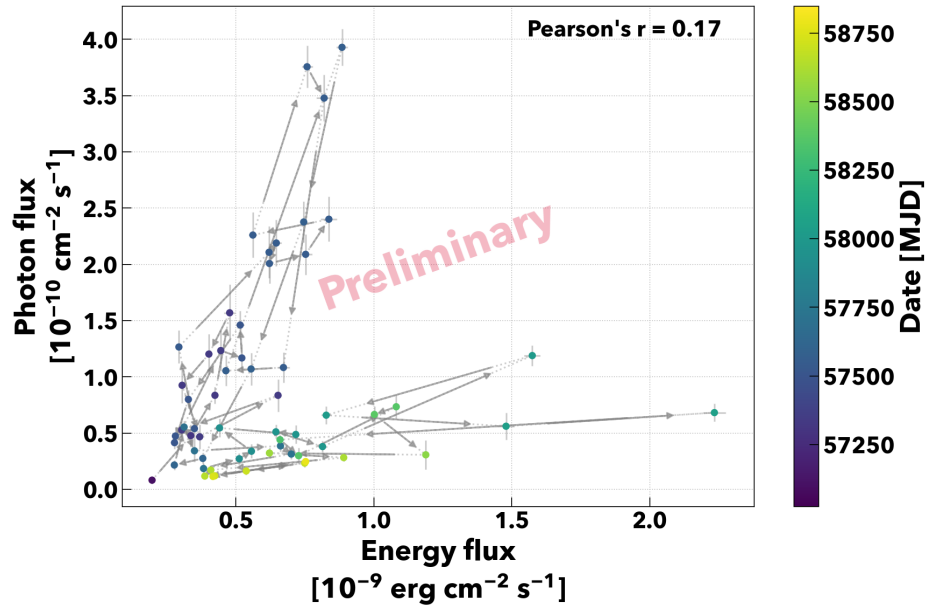


Figure D.19: Flux correlation with MAGIC and XRT. See figure D.1 details.

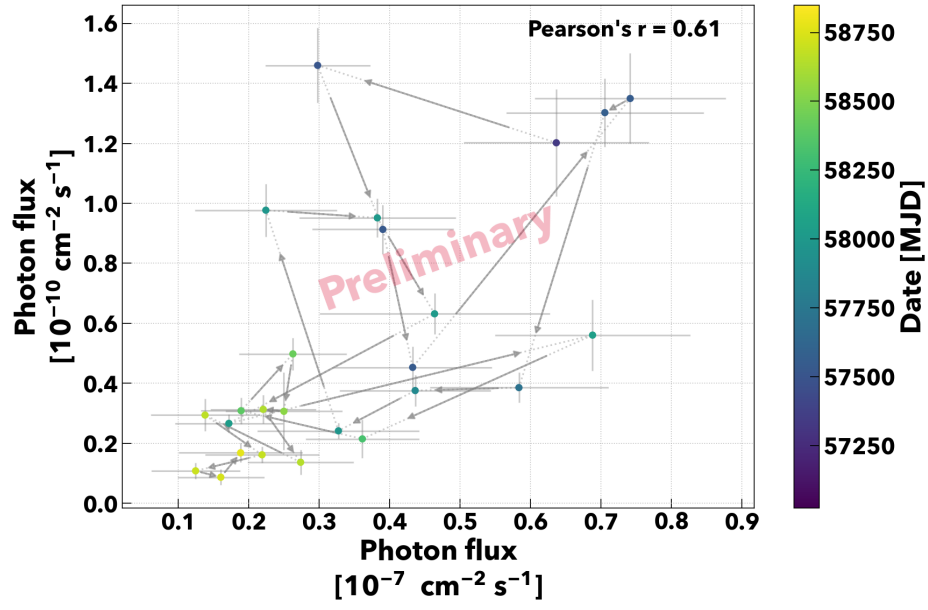


Figure D.20: Flux correlation with MAGIC and LAT. See figure D.1 details.

## References

- Abdo, A. A., Ackermann, M., Ajello, M., et al. 2011a, *The Astrophysical Journal*, 736, 131, doi: [10.1088/0004-637X/736/2/131](https://doi.org/10.1088/0004-637X/736/2/131)
- . 2011b, *The Astrophysical Journal*, 736, 131, doi: [10.1088/0004-637X/736/2/131](https://doi.org/10.1088/0004-637X/736/2/131)
- Abdollahi, S., Acero, F., Ackermann, M., et al. 2020, *The Astrophysical Journal Supplement Series*, 247, 33, doi: [10.3847/1538-4365/ab6bcb](https://doi.org/10.3847/1538-4365/ab6bcb)
- Acciari, V., Arlen, T., Aune, T., et al. 2014, *Astroparticle Physics*, 54, 1, doi: <https://doi.org/10.1016/j.astropartphys.2013.10.004>
- Acciari, V. A., Aliu, E., Arlen, T., et al. 2011, *The Astrophysical Journal*, 738, 25, doi: [10.1088/0004-637X/738/1/25](https://doi.org/10.1088/0004-637X/738/1/25)
- Ackermann, M., Ajello, M., Albert, A., et al. 2012, *The Astrophysical Journal Supplement Series*, 203, 4, doi: [10.1088/0067-0049/203/1/4](https://doi.org/10.1088/0067-0049/203/1/4)
- Ahnen, M., Ansoldi, S., Antonelli, L., et al. 2017, *Astroparticle Physics*, 94, 29, doi: [10.1016/j.astropartphys.2017.08.001](https://doi.org/10.1016/j.astropartphys.2017.08.001)
- Aleksić, J., Ansoldi, S., Antonelli, L., et al. 2016a, *Astroparticle Physics*, 72, 61, doi: <https://doi.org/10.1016/j.astropartphys.2015.04.004>
- . 2016b, *Astroparticle Physics*, 72, 76, doi: <https://doi.org/10.1016/j.astropartphys.2015.02.005>
- Alexander, T. 2014, ZDCF: Z-Transformed Discrete Correlation Function, *Astrophysics Source Code Library*, record ascl:1404.002. <http://ascl.net/1404.002>
- Amenomori, M., Cao, Z., Ding, L. K., et al. 1992, *PRL*, 69, 2468, doi: [10.1103/PhysRevLett.69.2468](https://doi.org/10.1103/PhysRevLett.69.2468)
- Amenomori, M., Bao, Y. W., Bi, X. J., et al. 2021, *Phys. Rev. Lett.*, 126, 141101, doi: [10.1103/PhysRevLett.126.141101](https://doi.org/10.1103/PhysRevLett.126.141101)
- Arbet-Engels, Axel, Baack, Dominik, Balbo, Matteo, et al. 2021, *A&A*, 655, A93, doi: [10.1051/0004-6361/202141886](https://doi.org/10.1051/0004-6361/202141886)
- Asano, K., & Hayashida, M. 2018, *The Astrophysical Journal*, 861, 31, doi: [10.3847/1538-4357/aac82a](https://doi.org/10.3847/1538-4357/aac82a)
- Atwood, W., Albert, A., Baldini, L., et al. 2013, Pass 8: Toward the Full Realization of the Fermi-LAT Scientific Potential, *arXiv*, doi: [10.48550/ARXIV.1303.3514](https://doi.org/10.48550/ARXIV.1303.3514)
- Backes, M. 2012, doi: [10.17877/DE290R-4809](https://doi.org/10.17877/DE290R-4809)

- Bernardini, E. 2005, Multi-Messenger Studies with AMANDA/IceCube: Observations and Strategies, arXiv, doi: [10.48550/ARXIV.ASTRO-PH/0509396](https://doi.org/10.48550/ARXIV.ASTRO-PH/0509396)
- Britto, R. J., Bottacini, E., Böttcher, M., et al. 2016, in SF2A-2016: Proceedings of the Annual meeting of the French Society of Astronomy and Astrophysics, ed. C. Reyl  , J. Richard, L. Cambr  sy, M. Deleuil, E. P  contal, L. Tresse, & I. Vauglin, 93–101
- Burrows, D. N., Hill, J. E., Nousek, J. A., et al. 2005, SSR, 120, 165, doi: [10.1007/s11214-005-5097-2](https://doi.org/10.1007/s11214-005-5097-2)
- Cao, Z., della Volpe, D., Liu, S., et al. 2019, arXiv e-prints, arXiv:1905.02773, doi: [10.48550/arXiv.1905.02773](https://doi.org/10.48550/arXiv.1905.02773)
- Cerruti, M., Zech, A., Boisson, C., et al. 2018, Monthly Notices of the Royal Astronomical Society: Letters, 483, L12, doi: [10.1093/mnrasl/sly210](https://doi.org/10.1093/mnrasl/sly210)
- Chandra, S., Boettcher, M., Goswami, P., et al. 2021, The Astrophysical Journal, 918, 67, doi: [10.3847/1538-4357/ac01d1](https://doi.org/10.3847/1538-4357/ac01d1)
- Cortina, J., Goebel, F., & Schweizer, T. 2009, Technical Performance of the MAGIC Telescopes, arXiv, doi: [10.48550/ARXIV.0907.1211](https://doi.org/10.48550/ARXIV.0907.1211)
- Dermer, C., Dermer, C., & Menon, G. 2009, High Energy Radiation from Black Holes: Gamma Rays, Cosmic Rays, and Neutrinos, Princeton Series in Astrophysics (Princeton University Press). <https://books.google.co.jp/books?id=XtXLlgVlMEcC>
- Dom  nguez, A., Primack, J. R., Rosario, D. J., et al. 2011, Monthly Notices of the Royal Astronomical Society, 410, 2556, doi: [10.1111/j.1365-2966.2010.17631.x](https://doi.org/10.1111/j.1365-2966.2010.17631.x)
- Dova, M. 2015, doi: [10.5170/CERN-2015-001.169](https://doi.org/10.5170/CERN-2015-001.169)
- Edelson, R. A., & Krolik, J. H. 1988, apj, 333, 646, doi: [10.1086/166773](https://doi.org/10.1086/166773)
- Elvis, M., Plummer, D., Schachter, J., & Fabbiano, G. 1992, ApJs, 80, 257, doi: [10.1086/191665](https://doi.org/10.1086/191665)
- Evoli, C. 2020, The Cosmic-Ray Energy Spectrum, Zenodo, doi: [10.5281/zenodo.4396125](https://doi.org/10.5281/zenodo.4396125)
- Fermi Science Support Development Team. 2019, Fermitools: Fermi Science Tools, Astrophysics Source Code Library, record ascl:1905.011. <http://ascl.net/1905.011>
- Franceschini, A., Rodighiero, G., & Vaccari, M. 2008, A&A, 487, 837, doi: [10.1051/0004-6361:200809691](https://doi.org/10.1051/0004-6361:200809691)
- Fruck, C., Gaug, M., Zanin, R., et al. 2014, A novel LIDAR-based Atmospheric Calibration Method for Improving the Data Analysis of MAGIC, arXiv, doi: [10.48550/ARXIV.1403.3591](https://doi.org/10.48550/ARXIV.1403.3591)

- Gehrels, N., Chincarini, G., Giommi, P., et al. 2004, *ApJ*, 611, 1005, doi: [10.1086/422091](https://doi.org/10.1086/422091)
- Gilmore, R. C., Somerville, R. S., Primack, J. R., & Domínguez, A. 2012, *Monthly Notices of the Royal Astronomical Society*, 422, 3189, doi: [10.1111/j.1365-2966.2012.20841.x](https://doi.org/10.1111/j.1365-2966.2012.20841.x)
- Gruppen, C. 2020, *Astroparticle Physics, Undergraduate Texts in Physics* (Springer International Publishing). <https://books.google.co.jp/books?id=gKbMDwAAQBAJ>
- Hada, K. 2017, *Galaxies*, 5, doi: [10.3390/galaxies5010002](https://doi.org/10.3390/galaxies5010002)
- Hayashida, M., Madejski, G. M., Nalewajko, K., et al. 2012, *The Astrophysical Journal*, 754, 114, doi: [10.1088/0004-637X/754/2/114](https://doi.org/10.1088/0004-637X/754/2/114)
- Hess, V. 2018, *On the Observations of the Penetrating Radiation during Seven Balloon Flights*, arXiv, doi: [10.48550/ARXIV.1808.02927](https://doi.org/10.48550/ARXIV.1808.02927)
- Hinton, J. 2004, *New Astronomy Reviews*, 48, 331, doi: <https://doi.org/10.1016/j.newar.2003.12.004>
- Horns, D. 2003, in *Astronomical Society of the Pacific Conference Series*, Vol. 299, *High Energy Blazar Astronomy*, ed. L. O. Takalo & E. Valtaoja, 13. <https://arxiv.org/abs/astro-ph/0209454>
- Hovatta, T., Lindfors, E., Kiehlmann, S., et al. 2021, *A&A*, 650, A83, doi: [10.1051/0004-6361/202039481](https://doi.org/10.1051/0004-6361/202039481)
- Katarzyński, K., Ghisellini, G., Tavecchio, F., et al. 2005, *A&A*, 433, 479, doi: [10.1051/0004-6361:20041556](https://doi.org/10.1051/0004-6361:20041556)
- Kildea, J., Atkins, R. W., Badran, H. M., et al. 2007, *Astroparticle Physics*, 28, 182, doi: [10.1016/j.astropartphys.2007.05.004](https://doi.org/10.1016/j.astropartphys.2007.05.004)
- Kintscher, T., Icecube Collaboration, FACT Collaboration, et al. 2017, in *International Cosmic Ray Conference*, Vol. 301, 35th International Cosmic Ray Conference (ICRC2017), 969
- Krawczynski, H., Hughes, S. B., Horan, D., et al. 2004, *The Astrophysical Journal*, 601, 151, doi: [10.1086/380393](https://doi.org/10.1086/380393)
- Krennrich, F., Bond, I., Boyle, P., et al. 2004, *New Astronomy Reviews*, 48, 345, doi: <https://doi.org/10.1016/j.newar.2003.12.050>
- Krolik, J. 2021, *Active Galactic Nuclei: From the Central Black Hole to the Galactic Environment*, Princeton Series in Astrophysics (Princeton University Press). <https://books.google.co.jp/books?id=vucSEAAAQBAJ>
- Li, T. P., & Ma, Y. Q. 1983, *apj*, 272, 317, doi: [10.1086/161295](https://doi.org/10.1086/161295)

- Liodakis, I., Hovatta, T., Huppenkothen, D., et al. 2018, *The Astrophysical Journal*, 866, 137, doi: [10.3847/1538-4357/aae2b7](https://doi.org/10.3847/1538-4357/aae2b7)
- Longair, M. S. 2011, *High Energy Astrophysics*, 3rd edn. (Cambridge University Press), doi: [10.1017/CB09780511778346](https://doi.org/10.1017/CB09780511778346)
- MAGIC Collaboration:, Acciari, V. A., Ansoldi, S., et al. 2020, *A&A*, 637, A86, doi: [10.1051/0004-6361/201834603](https://doi.org/10.1051/0004-6361/201834603)
- MAGIC Collaboration, Acciari, V. A., Ansoldi, S., et al. 2020a, *A&A*, 640, A132, doi: [10.1051/0004-6361/202037811](https://doi.org/10.1051/0004-6361/202037811)
- . 2020b, *A&A*, 638, A14, doi: [10.1051/0004-6361/201935450](https://doi.org/10.1051/0004-6361/201935450)
- . 2020c, *A&A*, 635, A158, doi: [10.1051/0004-6361/201936899](https://doi.org/10.1051/0004-6361/201936899)
- MAGIC Collaboration, Acciari, V. A., Ansoldi, S., et al. 2020d, *aap*, 638, A14, doi: [10.1051/0004-6361/201935450](https://doi.org/10.1051/0004-6361/201935450)
- Massaro, E., Perri, M., Giommi, P., & Nesci, R. 2004, *A&A*, 413, 489, doi: [10.1051/0004-6361:20031558](https://doi.org/10.1051/0004-6361:20031558)
- Matthews, J. 2005, *Astroparticle Physics*, 22, 387, doi: <https://doi.org/10.1016/j.astropartphys.2004.09.003>
- Moralejo, A., Gaug, M., Carmona, E., et al. 2009, *MARS, the MAGIC Analysis and Reconstruction Software*, arXiv, doi: [10.48550/ARXIV.0907.0943](https://doi.org/10.48550/ARXIV.0907.0943)
- Morrison, R., & McCammon, D. 1983, *ApJ*, 270, 119, doi: [10.1086/161102](https://doi.org/10.1086/161102)
- Nakajima, D., Fink, D., Hose, J., et al. 2013, in *International Cosmic Ray Conference*, Vol. 33, *International Cosmic Ray Conference*, 3044
- Nilsson, K., Lindfors, E., Takalo, L. O., et al. 2018, *A&A*, 620, A185, doi: [10.1051/0004-6361/201833621](https://doi.org/10.1051/0004-6361/201833621)
- Nishiyama, T. 1999, in *International Cosmic Ray Conference*, Vol. 3, *26th International Cosmic Ray Conference (ICRC26)*, Volume 3, 370
- Patel, S. R., Shukla, A., Chitnis, V. R., et al. 2018, *aap*, 611, A44, doi: [10.1051/0004-6361/201731987](https://doi.org/10.1051/0004-6361/201731987)
- PDG, Workman, R. L., Burkert, V. D., et al. 2022, *Progress of Theoretical and Experimental Physics*, 2022, doi: [10.1093/ptep/ptac097](https://doi.org/10.1093/ptep/ptac097)
- Perlman, E. S., Stocke, J. T., Schachter, J. F., et al. 1996, *apjs*, 104, 251, doi: [10.1086/192300](https://doi.org/10.1086/192300)
- Piner, B. G., & Edwards, P. G. 2004, *The Astrophysical Journal*, 600, 115, doi: [10.1086/379769](https://doi.org/10.1086/379769)



- Piner, B. G., Pant, N., & Edwards, P. G. 2008, 678, 64, doi: [10.1086/533521](https://doi.org/10.1086/533521)
- Piner, B. G., Pant, N., & Edwards, P. G. 2010, *The Astrophysical Journal*, 723, 1150, doi: [10.1088/0004-637x/723/2/1150](https://doi.org/10.1088/0004-637x/723/2/1150)
- Poole, T. S., Breeveld, A. A., Page, M. J., et al. 2007, *Monthly Notices of the Royal Astronomical Society*, 383, 627, doi: [10.1111/j.1365-2966.2007.12563.x](https://doi.org/10.1111/j.1365-2966.2007.12563.x)
- Richards, J. L., Max-Moerbeck, W., Pavlidou, V., et al. 2011, *The Astrophysical Journal Supplement Series*, 194, 29, doi: [10.1088/0067-0049/194/2/29](https://doi.org/10.1088/0067-0049/194/2/29)
- Ritt, S. 2008, in *2008 IEEE Nuclear Science Symposium Conference Record*, 1512–1515, doi: [10.1109/NSSMIC.2008.4774700](https://doi.org/10.1109/NSSMIC.2008.4774700)
- Rybicki, G. B., & Lightman, A. P. 1986, *Radiative Processes in Astrophysics*
- Scargle, J. D. 1998, *The Astrophysical Journal*, 504, 405, doi: [10.1086/306064](https://doi.org/10.1086/306064)
- Schachter, J. F., Stocke, J. T., Perlman, E., et al. 1993, *apj*, 412, 541, doi: [10.1086/172942](https://doi.org/10.1086/172942)
- Schweizer, T., Lorenz, E., Martinez, M., Ostankov, A., & Paneque, D. 2002, *IEEE Transactions on Nuclear Science*, 49, 2497, doi: [10.1109/TNS.2002.803867](https://doi.org/10.1109/TNS.2002.803867)
- Smith, A. J. 2015, *HAWC: Design, Operation, Reconstruction and Analysis*, arXiv, doi: [10.48550/ARXIV.1508.05826](https://doi.org/10.48550/ARXIV.1508.05826)
- Sreekumar, P., Bertsch, D. L., Dingus, B. L., et al. 1998, *The Astrophysical Journal*, 494, 523, doi: [10.1086/305222](https://doi.org/10.1086/305222)
- Tagliaferri, G., Ravasio, M., Ghisellini, G., et al. 2003, *A&A*, 412, 711, doi: [10.1051/0004-6361:20034051](https://doi.org/10.1051/0004-6361:20034051)
- Tridon, D. B., Goebel, F., Fink, D., et al. 2009, *Performance of the Camera of the MAGIC II Telescope*, arXiv, doi: [10.48550/ARXIV.0906.5448](https://doi.org/10.48550/ARXIV.0906.5448)
- Vaughan, S., Edelson, R., Warwick, R. S., & Uttley, P. 2003, *Monthly Notices of the Royal Astronomical Society*, 345, 1271, doi: [10.1046/j.1365-2966.2003.07042.x](https://doi.org/10.1046/j.1365-2966.2003.07042.x)
- Wood, M., Caputo, R., Charles, E., et al. 2017, in *International Cosmic Ray Conference*, Vol. 301, 35th International Cosmic Ray Conference (ICRC2017), 824, doi: [10.22323/1.301.0824](https://doi.org/10.22323/1.301.0824)
- Wu, X.-B., Liu, F. K., & Zhang, T. Z. 2002, *AAP*, 389, 742, doi: [10.1051/0004-6361:20020577](https://doi.org/10.1051/0004-6361:20020577)

## Acknowledgement

I acknowledge all the people who support, communicate, and involved in my life. I have no word to my mother who took care during the Ph.D course. I was not able to conduct my research without supervising by Masahito Teshima, and support by Midori Sugahara. Members who belongs to the CTA group in ICRR are also critical for my research and daily life. I would like to thank you all who gave me words during my long doctoral history in ICRR, Kashiwa, Chiba, Japan. I decided to continue science for a while and do know how long it last. In any case, the experience I got through the thesis will play a significant role in the future.

As mentioned in the text, I used a lot of software in the study. I appreciate developers of those programs, MARS, ftools, fermipy, HEASoft, xspec, astropy, and Agnpy so on.